Coherent structures, their interactions, and their effects on passive scalar transport and aero-optic distortion in a turbulent boundary layer

Thesis by
Theresa Saxton-Fox

In Partial Fulfillment of the Requirements for the
degree of
Doctorate of Philosophy in Mechanical Engineering

CALIFORNIA INSTITUTE OF TECHNOLOGY
Pasadena, California

2018
Defended (October 23, 2017)

Theresa Saxton-Fox
ORCID: 0000-0003-1328-4148

ACKNOWLEDGEMENTS

I am very grateful to many people for their contribution to and support of the work in this thesis.

My advisor, Beverley McKeon, was both a mentor and a role model throughout my time at Caltech. She was a source of steady strength throughout the process of acquiring, analyzing, and interpreting the data shown in this thesis. Her excitement and insight when advancing new ideas, her calm in the face of experimental setbacks, and her compassion for her students have all made my graduate school experience a positive one, and have taught me about the type of researcher I want to be. I am extremely grateful for her influence on the research and on me.

I would also like to thank the members of my thesis committee for their technical insights and their encouraging attitude throughout my graduate career. All of my committee members contributed to my work through insightful questions at my Candidacy Exam, Tuesday Talks and / or in private conversations. They also all contributed to my enjoyment of my time at Caltech and to my larger career goals. In particular, I would like to thank Tim for welcoming me into so many of his group events and being so supportive of my aspirations after Caltech. I would like to thank Guillaume for the many entertaining conversations over the years and for his support of my application for the NDSEG fellowship. And I would like to thank Tony for his questions during Tuesday Talks, the helpful conversations over the years, and for supporting my and my fellow students' growth through his participation in the Caltech Y.

I want to thank the members of the McKeon group, both past and present, for their technical support and friendship throughout these five years. Thank you to Jamie, Rebecca, Mitul, Rashad, Subbu, Reeve, Esteban, Jonathan, Kevin, Sean, David, Ryan, Simon, Morgan, Ben, Scott, and Angeliki. Special thanks to Scott for his work on the passive scalar resolvent framework, to Kevin for the discussions while at the CTR summer program in 2016, and to Rebecca for laying the framework for the work done in this thesis. I would also like to thank the non-group members who I have had the pleasure of working closely with over the years, either during their time visiting the group, or through their attendance at the CTR summer program. Many thanks to Peter Schmid for his keen technical eye and the many invigorating chats, and to Adrian Lozano-Duran and Aaron Towne for hosting us at CTR and

contributing ideas and perspectives on turbulence with us throughout the summer.

Several people helped with the development and improvement of the experimental set up. Our collaborators at the University of Notre Dame, Stas Gordeyev, Adam Smith, and Nick DeLucca, introduced us to the aero-optical techniques used in this thesis and were extremely valuable in the execution of many experiments over the years. Additionally, Ali Kiani from the GALCIT shop, Bahram Valiferdowsi in GALCIT, and Steve Anderson from LaVision all aided in very helpful modifications to the experimental set up.

I want to thank the Department of Defense for funding my National Defense Science and Engineering Graduate (NDSEG) fellowship that supported me for three years of my graduate career, and the Air Force for funding all of the work shown in this thesis.

I want to thank all of my friends from Caltech, from MIT, and from Wayland for teaching me so much and making my life a happy one. I cannot list them all by name, but they should know that they have shaped me and supported me immeasurably, both academically and personally, and I am very grateful for their friendship and for their influence on my value system, my curiosity, and my ambition. I want to thank my family for being there for the highs and lows – for being equally understanding when they didn't hear from me for weeks as they were when I was calling several times a day. I cannot adequately acknowledge their contribution, but suffice it to say that they have shaped my worldview, my discipline, and my self-confidence over decades, and I continue to learn from every member of my family in ways that constantly amaze me. I would also like to thank my adopted family, the Rocco-Goza's, for their boundless enthusiasm and love. They have brightened and enriched my life.

Finally, I would like to thank Andres, who started out as my p-set and quals study buddy, and ended up as my life partner. He shared the full graduate school experience with me, brought genuine joy into my life every day, and supported me intellectually and emotionally in ways that I never would have expected a single person to be able to do. I am grateful for the partnership and laughter that he brought to my experience at Caltech, and am looking forward to a lifetime of partnership and laughter together.

ABSTRACT

This thesis focused on the characterization of coherent structures and their interactions in a turbulent boundary layer using data from particle image velocimetry (PIV) measurements performed at Caltech and from a direct numerical simulation (DNS) of Wu et al. (2017). Connections were identified between instantaneous and statistical descriptions of coherent velocity structures, through the analysis of representative models for their structures derived from the resolvent analysis of McKeon and Sharma (2010). The representative models were used in a novel conditional averaging technique to identify the average behavior of small scales about variations in the large-scale streamwise velocity field. Based upon the results of this analysis, a hypothesis for a scale interaction mechanism was proposed involving three-dimensional critical layers. The modeling and analysis methods were then applied to the aero-optic problem in which optical beams are observed to be distorted after passing through variable-density turbulent flows. Measurements using simultaneous PIV and an aero-optic sensor called a Malley probe (Malley, Sutton, and Kincheloe, 1992) were conducted in an incompressible, mildly-heated turbulent boundary layer with Prandtl number of 0.7. A conditional averaging analysis of the data identified that the nonlinear interaction of two scales was most correlated to the aero-optic distortion. The modeling of this interaction using resolvent modes led to new insights regarding the instantaneous relationship between the velocity and scalar fields over a range of Prandtl numbers.

PUBLISHED CONTENT AND CONTRIBUTIONS

Saxton-Fox, T. and B. J. McKeon (2017). "Coherent structures, uniform momentum zones and the streamwise energy spectrum in wall-bounded turbulent flows". In: *Journal of Fluid Mechanics* 826. DOI: 10.1017/jfm.2017.493

Performed the experiments, analyzed the experimental and modeled results, created the figures, and was the primary author of the paper.

Saxton-Fox, T. and B. J. McKeon (2017). "Modeling momentum and scalar transport in a wall-bounded turbulent flow". In: *Proceedings of the International Symposium of Turbulence and Shear Flow Phenomena* 10. http://resolver.caltech.edu/CaltechAUTHORS:20171128-103322689

Performed the experiments, identified appropriate scales to model, used an existing resolvent formulation to create models of the velocity field, analyzed the experimental and modeled results, created the figures, and was the primary author of the paper.

Rosenberg, K., T. Saxton-Fox, A. Lozano-Duran, A. Towne, and B. J. McKeon (2016). "Towards low order models of wall turbulence using resolvent analysis". In: *Proceedings of the Summer Program 2016, Center for Turbulence Research*. http://resolver.caltech.edu/CaltechAUTHORS:20171128-094432410

Created instantaneous visualizations of the velocity field from an existing DNS database, was the primary author of section 4 and collaborated in the writing of the introduction and conclusion of the paper.

Saxton-Fox, T. and B. J. McKeon (2016). "Scale interactions and 3D critical layers in wall-bounded turbulent flows". In: *Proceedings of the International Congress of Theoretical and Applied Mechanics* 24. http://resolver.caltech.edu/CaltechAUTHORS:20171128-101726402

Performed the experiments, analyzed the experimental data, created the figures, and was the primary author of the paper.

S. Gordeyev, A. E. Smith, B. J. McKeon, and T. Saxton-Fox (2015). "Studies of the large-scale structure in adiabatic and moderately-wall-heated subsonic boundary layers". In *Proceedings of the Symposium on Turbulence and Shear Flow Phenomena*, 9. http://resolver.caltech.edu/CaltechAUTHORS:20171128-113834714

Performed the experiments carried out at Caltech, analyzed the Caltech results, was the primary author of the Caltech, incompressible boundary layer portions of the Experimental Set Up and Results sections.

T. Saxton-Fox, B. J. McKeon, S. Gordeyev, and A. E. Smith (2015). "Aero-optical distortion as a marker of turbulent structure". In: *Proceedings of the International Symposium on Particle Image Velocimetry* 11.

Performed the experiments, analyzed the results, created the figures, and was the primary author of the paper.

A. E. Smith, S. Gordeyev, T. Saxton-Fox, and B. J. McKeon (2014). "Subsonic boundary-layer wavefront spectra for a range of Reynolds numbers". In: *AIAA Aviation and Aeronautics Forum and Exposition*. DOI: 10.2514/6.2014-2491

Contributed data for the incompressible, heated boundary layer, and aided in the creation of the figure showing the compared spectra for incompressible and compressible cases.

TABLE OF CONTENTS

LIST OF ILLUSTRATIONS

LIST OF TABLES

Chapter 1

INTRODUCTION

Wall-bounded turbulent flow contributes to many engineering challenges, affecting drag on transportation technologies, advancing material-degradation of surfaces in high-temperature flows, and distorting optical beams passing through variable-density flows. It is also one of the great unsolved problems of classical physics. This combination of engineering importance and scientific challenge provides great opportunity for contribution to science and the world. This thesis contributes to four challenges in the field: connecting existing descriptions of coherent structures, identifying interaction mechanisms between scales, understanding the relationship between velocity and scalar fields, and isolating the turbulent dynamics responsible for aero-optic distortion.

1.1 The ubiquity and complexity of turbulence

The environment in which most technology operates is filled with fluid, whether that fluid is air, water, oil, or even biological fluids like blood. Many technologies must therefore move through fluid to operate, and for many large-scale or high-speed applications, the associated fluid flow is turbulent, behaving chaotically near the surface of the application in question. Turbulence coats or fills many of the technologies that define the modern age: cars, trains, ships, planes, rockets, car engines, jet engines, steam and gas turbines, water turbines, and wind turbines. Turbulence contributes to many critical engineering challenges including drag reduction for transportation technologies, material degradation in high-temperature environments, and the mixing of pollutants in the atmospheric turbulent boundary layer. Its prevalence and its impact on the modern world make turbulence a critical topic of engineering research.

Turbulence has been noticed peripherally for centuries, observable in drawings of da Vinci (sketch of turbulence in a water fall, c.1508) and Hokusai (*The Great Wave Off Kangawa* c.1832), and has been studied in earnest by many brilliant scientists and engineers for decades. The equation for incompressible fluid flow,

$$\frac{\partial \boldsymbol{U}}{\partial t} + \boldsymbol{U} \cdot \nabla \boldsymbol{U} = -\frac{1}{\rho}\nabla P + \nu \nabla^2 \boldsymbol{U} + \boldsymbol{g}, \tag{1.1}$$

can be solved numerically and demonstrates turbulent behavior. $\boldsymbol{U}$ is the velocity

vector: $\boldsymbol{U} = (U, V, W)^T$, where U is the velocity in the streamwise direction, x, V is the velocity in the wall-normal direction, y, and W is the velocity in the spanwise direction, z. Here t is time, ρ is density, P is pressure, ν is the kinematic viscosity, and $\boldsymbol{g}$ is a body force, such as gravity.

And yet, even with known equations of motion and decades of study, turbulence is still, in fundamental ways, a mystery. It eludes many of our attempts to efficiently model it, control it, and understand it. The intersection of importance and challenge in the turbulent problem is incredibly exciting. Turbulence offers a scientific engineer the opportunity to affect the world by uncovering some of nature's most fiercely-guarded secrets.

1.2 Background on the study of wall-bounded turbulent flows

Several key findings from the literature that are relevant to this thesis are summarized. The summary is broken into four parts, consistent with the major topics focused on in the present work: the energetic coherent structures of wall-bounded turbulent flows, the nonlinear interactions of velocity scales, the transport of a scalar in a turbulent boundary layer, and the distortion of an optical beam by a variable-density turbulent flow. Finally, a brief introduction to the resolvent framework for modeling turbulent wall-bounded flows will be given. At the end of the chapter, some of the specific challenges remaining in wall-bounded turbulence will be outlined, and the contributions of this thesis to those challenges will be highlighted.

Coherent structures

One of the frameworks for understanding turbulence that has been developed in the past sixty to seventy years is that of coherent structures. A coherent structure is a pattern that is repeatedly observed in a turbulent flow that has some coherence or consistency in space and time. Thinking of turbulence through the lens of coherent structures allows for the breaking down of complicated phenomena into the superposition and interaction of many smaller patterns that can be independently studied.

Many different types of coherent structures have been identified over the decades. Some coherent structures have been defined from their instantaneous appearance, others from statistical findings. Experimental observation, computation, and conceptual models have all been used to characterize coherent structures. Features observed at a single snapshot have been observed using visualization of the transport of smoke, dye, and bubbles (Kline et al., 1967; Chen and Blackwelder, 1978),

using particle image velocimetry (PIV) (Adrian, Meinhart, and Tomkins, 2000), and using computation including direct numerical simulation (DNS) (Wu et al., 2017). Coherent structures have also been identified in a statistical sense using many methods, including the calculation of the energy spectrum, two-point correlations, and conditional averaging. Specific length scales have been observed to be most energetic in the streamwise energy spectrum, pointing to the common appearance of a structure of that length scale in the flow (Kim and Adrian, 1999; Monty et al., 2009). Two-point correlations and conditional averages have been used to find the average length scales over which the flow field is correlated, identifying the size and shape of structures that move cohesively (Kovasznay, Kibens, and Blackwelder, 1970; Sillero, Jimenez, and Moser, 2014). Coherent structures have also been consistently identified over a wide range of Reynolds numbers, defined throughout the thesis as either $Re_\tau \equiv \frac{u_\tau \delta}{\nu}$, where u_τ is the friction velocity and δ is the 99% boundary layer thickness, or as $Re_\theta \equiv \frac{U_\infty \theta}{\nu}$, where U_∞ is the free-stream velocity outside of the boundary layer and θ is the momentum thickness.

Through these methods, many 'coherent structures' have been identified. Some have been identified in the instantaneous velocity field, including near-wall streaks (Kline et al., 1967), large-scale bulges (Falco, 1977; Kovasznay, Kibens, and Blackwelder, 1970), uniform momentum zones (Meinhart and Adrian, 1995), and superstructures or VLSMs (Kim and Adrian, 1999). Others have been seen in the instantaneous vorticity field, including near-wall streamwise vortices (Blackwelder and Eckelmann, 1979), hairpin vortices (Theodorsen, 1952; Head and Bandyopadhyay, 1981), and concentrated shear layers (Adrian, Meinhart, and Tomkins, 2000; Morrill-Winter and Klewicki, 2013; Eisma et al., 2015). Still others are observed in the streamwise energy spectrum, including the near-wall streaks (NWS), large-scale motions (LSMs), and very-large-scale motions (VLSMs) (Kim and Adrian, 1999; Monty et al., 2009; Rosenberg et al., 2013). A brief overview will be taken of these various structures in their instantaneous and statistical representations.

Near-wall structures

Near the wall, there is fairly good community consensus on the structures and the cycle of their growth, breakdown, and regeneration. The primary structures observed in the near-wall region are the near-wall streamwise streaks (Kline et al., 1967) and streamwise rolls (Blackwelder and Eckelmann, 1979). These structures have been instantaneously observed and found statistically in the pre-multiplied streamwise energy spectrum as an energetic peak near the wall (Monty et al., 2009).

The structures near the wall scale in 'inner-units', which are dictated by friction at the wall (Tennekes and Lumley, 1972). All dimensions near the wall are normalized using these inner-units, denoted using a +. The near-wall streamwise coordinate is therefore normalized as $x^+ \equiv \frac{xu_\tau}{\nu}$, where u_τ is the friction velocity and is defined as $\tau_w^{1/2}$ and τ_w is the shear stress at the wall. In wavenumber space, the near-wall streamwise streaks have a streamwise wavelength of $x^+ \approx 1000$, a spanwise wavelength of $z^+ \approx 100$, and a phase speed of $c^+ \approx 10$ (Kline et al., 1967; Robinson, 1991).

Logarithmic-layer structures

The consensus in the community is less firm in the logarithmic layer. For decades it has been argued that structures in this region should be self-similar and 'attached' to the wall (Townsend, 1976; Perry and Chong, 1982). This means that the size of the structure should scale with distance from the wall. Thus, structures at higher heights are longer and wider.

In experiments and computations, recently there has been building evidence for very long structures in the logarithmic region. Some of this evidence comes from instantaneous visualizations or reconstructed visualizations built using Taylor's hypothesis, which states that structures convect much more quickly than they deform, and that they convect with the local mean velocity. Long structures that possibly meander in the spanwise direction have been identified at up to 20δ in length, where δ is defined as the height where, on average, the flow is within 99% of the free-stream value. Much of the evidence for the VLSMs and superstructures comes from the streamwise energy spectrum of experimental flows (Kim and Adrian, 1999; Monty et al., 2009; Rosenberg et al., 2013). Energy peaks are observed at $x/\delta \approx 6$ in boundary layers and $x/\delta \approx 10 - 14$ in pipes and channels.

Hairpin vortices and hairpin packets have also been reported in the logarithmic layer (Adrian, Meinhart, and Tomkins, 2000). Hairpin vortices are specific vorticity patterns, very similar to the horseshoe vortices reported by Theodorsen (1952). They are characterized by streamwise vorticity near the wall at the 'legs', transitioning to spanwise-oriented vorticity at the 'head' of the hairpin, farthest from the wall.

Outer region structures

In the outer region of the flow, particle image velocimetry and flow visualization have allowed for the study of instantaneous structures. Large-scale bulges have been observed in the outer-region of boundary layers using smoke-visualization (Falco,

1977; Kovasznay, Kibens, and Blackwelder, 1970). The coherence of these bulges was measured and was found to be approximately $x/\delta \approx 3$ and $z/\delta \approx 1$ using a two-point correlation from hot wire data. More recently, uniform momentum zones (UMZs), regions of relatively similar streamwise velocity with coherence in the streamwise and wall-normal directions, were identified in the outer region of the boundary layer (Meinhart and Adrian, 1995; Adrian, Meinhart, and Tomkins, 2000). UMZs have been found to be ubiquitous in wall-bounded turbulent flows, with an average number across the wall-normal height of the flow ranging between three at $Re_\tau = 10^3$ to five at $Re_\tau = 10^4$ (de Silva, Hutchins, and Marusic, 2016). Statistically, large-scale motions (LSMs), with a characteristic streamwise wavelength of approximately $2-5\delta$ are observed to dominate the outer region (Monty et al., 2009).

In the vorticity field, a number of features can be observed in the outer region of the boundary layer. Thin shear layers have been associated with the backs of bulges (Kovasznay, Kibens, and Blackwelder, 1970) and with the edges of UMZs (Adrian, Meinhart, and Tomkins, 2000; Eisma et al., 2015; Morrill-Winter and Klewicki, 2013). In addition, hairpin, horseshoe, or cane vortices have been reported in the outer boundary layer as well as the logarithmic layer (Theodorsen, 1952; Adrian, Meinhart, and Tomkins, 2000; Bernard, 2013).

Scale interaction

The interaction of the previously-mentioned structures is intimately related to some of turbulence's greatest mysteries and challenges. A very-large-scale disturbance, like a plane passing through quiescent flow, leads to the generation of a cascade of disparate scales. These scales are able to interact, leading to significant challenges in understanding and simulating the flow. Some key unresolved topics in the field include the influence of scales on one another, the mechanisms of self-sustaining behavior, and the selection of scales that are energetic in the flow.

The regeneration cycle of near-wall streaks and rolls has been studied extensively, as it is accessible at fairly low Reynolds numbers and remains a consistent feature of turbulence at high Reynolds numbers. The near-wall cycle is a good testbed to understand nonlinear interactions, as it is self-sustaining, as has been shown by Jimenez and Moin (1991) through the use of a minimal channel. Schoppa and Hussain (2002) connected some of the physical mechanisms of regeneration of near-wall streaks explored by (Kline et al., 1967; Blackwelder and Eckelmann, 1979) to mathematical understandings of transient growth. They defined the near-wall streaks

and mean profile as a base flow about which secondary instabilities were identified.

Additionally, significant work has been done to understand the exchange of energy from large to small scales, a key component of scale interaction in wall-bounded turbulent flows (Jimenez, 2012). Some previous findings regarding the general influence of the large scales on the small scales will now be considered in further detail.

Influence of large scales on small scales

The influence of large scales in turbulent wall-bounded flows (u_l) on the small scales (u_s) has been a topic of interest for several decades. Rao, Narasimha, and Narayanan (1971) first identified that the 'bursting' of the near-wall flow behavior, in which intense activity is seen near the wall, occurred on a mean time scale that scaled with outer units, rather than inner units. This suggested that large scales from the outer region of the flow were able to influence near-wall, smaller-scale behavior. The phase relationship between large scales and the envelope of small scales was first measured by Bandyopadhyay and Hussain (1984), who found that the envelope of small-scale activity was largest at particular phases with respect to the large scale, depending on the height in the boundary layer.

Evidence for a specific type of influence of large scales on small scales has been found, termed 'amplitude modulation'. Hutchins and Marusic (2007) found that the envelope of the small-scale component of a hot wire velocity signal was modulated by the local presence of a large-scale signal. The relationship between the large scale and the envelope of the small scale varied as a function of the wall-normal height with a correlation coefficient (Mathis, Hutchins, and Marusic, 2009) given by

$$R = \frac{\overline{u_l^+ E_l(u_s^+)}}{\mathrm{RMS}(u_l^{+2})\mathrm{RMS}(E_l(u_s^+)^2)}, \tag{1.2}$$

where RMS stands for root-mean-squared and E_l is a filtered envelope of the small-scale signal derived using a Hilbert transform and a spectral filter. The large and small scales, u_l and u_s, were defined using the same spectral filter with a cutoff frequency of $x/\delta = 1$. The correlation coefficient, R, was found to vary across the boundary layer from a positive value near the wall to a negative value away from the wall. Chung and McKeon (2010) showed this correlation coefficient was formally related to the phase between large scales and the envelope of small scales, connecting

the concept of amplitude modulation and phase relationships in the boundary layer, and allowing for direct comparison to the work of Bandyopadhyay and Hussain (1984).

The influence of large scales away from the wall on the near-wall flow was used to formulate a model of small-scale activity near the wall based on the behavior of the large scales in the logarithmic region. This model, termed the predictive inner-outer model, constructs a predicted streamwise velocity signal, u_p, near the wall from a measured time history of velocity taken at a single point in the logarithmic layer, u_{OL}. A statistical 'universal small scale', u^*, is identified that is modified by the large scale signal. Both amplitude modulation and superposition effects are accounted for in the model (Marusic, Mathis, and Hutchins, 2010; Mathis, Hutchins, and Marusic, 2011)

$$u_p^+(y^+) = u^*(y^+)\left(1 + \beta u_{OL}^+(y_O^+, \theta_l)\right) + \alpha u_{OL}^+(y_O, \theta_l). \tag{1.3}$$

The terms α and β are identified experimentally. This model has been successfully implemented in LES of wall-bounded turbulent flows and has been shown to improve the estimates of skin friction (Chung and Pullin, 2009; Inoue et al., 2012), demonstrating the potential for including scale-interaction information in wall models for LES.

Conditional averaging techniques have also been usefully applied to understand the relationship between the large scales and the strength of the small scales in the velocity field. In the presence of a large scale with velocity larger than the mean or near-wall shear stress signal larger than the mean, the small scales were observed to be strongest near the wall and weakest away from the wall, while the reverse small-scale pattern was observed for large scales with velocity less than the mean or near-wall shear stress less than the mean (Hutchins and Marusic, 2007; Chung and McKeon, 2010; Hutchins et al., 2011). This behavior was observed for all three components of small-scale velocity (Talluru et al., 2014). The flow field was also conditionally averaged on the presence of spanwise-meandering large-scales, identified using the simultaneous measurement of the wall shear stress at five points at the wall. The same trends were visible in the small-scale intensity, with some additional variation in the spanwise direction (Hutchins et al., 2011). The small scales were also conditioned on gradients in the streamwise velocity field at a point and on gradients in the shear stress at a point at the wall, leading to the observation that small scales were strongest along regions of high shear in the streamwise

velocity field (Chung and McKeon, 2010; Hutchins et al., 2011; Baars, Hutchins, and Marusic, 2017). The spatial organization and amplitude modulation trends were observed to occur across large ranges of Reynolds numbers by Baars, Hutchins, and Marusic (2017).

This spatial correlation between large scales and the envelope of small scales has been demonstrated to be consistent with a phase relationship between the different scales (Jacobi and McKeon, 2011; Duvvuri and McKeon, 2015; Duvvuri and McKeon, 2017; McKeon, 2017). The fluctuating velocity field,

$$\boldsymbol{u} = \boldsymbol{U} - \bar{\boldsymbol{U}}, \tag{1.4}$$

where $\boldsymbol{U}$ is the original field and $\boldsymbol{u}$ is the fluctuation about a mean, $\bar{U}$, can be decomposed with a Fourier decomposition in the streamwise, spanwise, and temporal variables, leading to the expression

$$\boldsymbol{u}(x, y, z, t) = \int \int \int_{-\infty}^{\infty} \hat{\boldsymbol{u}}_{\boldsymbol{K}}(y) \exp\left(i(k_x x + k_z z - \omega t)\right) dk_x dk_z d\omega. \tag{1.5}$$

$\hat{\boldsymbol{u}}_{\boldsymbol{K}}(y)$ is the wall-normal coherence for each wavenumber triplet $\boldsymbol{K} = (k_x, k_z, \omega)$. In this decomposition, the nonlinear term of the Navier-Stokes equations only admits direct interaction between scales that are triadically consistent, in which two of the wavenumbers sum to the third: $\boldsymbol{K_1} + \boldsymbol{K_2} = \boldsymbol{K_3}$ (McKeon and Sharma, 2010). The experimental observations of scale interaction were shown to be consistent with specific types of triadic interactions. These triadic interactions were experimentally triggered and measured using a novel experimental set up and were shown to interact in the predicted fashion (Duvvuri and McKeon, 2015; Duvvuri and McKeon, 2016).

Conceptual models of scale interaction

Conceptual models have been suggested for scale interaction for decades. Energy cascades were among the first such models and remain a useful framework for understanding turbulence (Jimenez, 2012). Far from the wall, one of the recent conceptual models for scale interaction is the concept of a hairpin packet (Adrian, Meinhart, and Tomkins, 2000). A hairpin packet is an aligned set of hairpin vortices that sit atop a region of low-momentum fluid. The low-momentum fluid is argued to be created or strengthened by the induced flow of the many small-scale vortices. In this conception, small-scale vortices are able to strengthen or create larger scales.

Another type of conceptual model springs from mathematical rather than experimental roots. This conceptual model revolves around a critical layer, which has its

basis in stability theory of shear flows. A critical layer is a region of a flow where a perturbation grows due to its phase speed matching the local base flow velocity. The concept of critical layers has recently been extended to base flows and mean flows that vary in both the wall-normal and spanwise directions (Hall and Sherwin, 2010; Wang, Gibson, and Waleffe, 2007; Park and Graham, 2015). In these examples, smaller-scale velocity features appear to be strongest along spatially-undulating layers that follow streamlines of the base or streamwise-averaged flow field. These critical layers have been observed in exact coherent solutions of the Navier-Stokes equations, which are hypothesized to form the backbone of the chaotic dynamics of turbulent flows (Wang, Gibson, and Waleffe, 2007; Park and Graham, 2015).

The transport of scalars in wall-bounded turbulent flow

The mixing of a scalar by wall-bounded turbulence has implications for many critical engineering and environmental applications. Heat transfer is increased in the presence of turbulent flow compared to laminar flow, leading to increased surface temperatures for technologies in the field of combustion, jet turbine blades downstream of combustion events, and re-entry vehicles. The mixing of particulates is of interest in environmental flows in which turbulence can transport pollutants across continents and oceans.

Scalar mixing has been used to great effect to learn about turbulence itself. Smoke and dye visualizations are both examples of the mixing of scalars, and have been used to identify coherent structures for decades. Seeding the flow with a temperature contaminant through the mild heating of the wall over which the turbulent boundary layer developed was used to identify sharp shear layers and bulges in the outer boundary layer by Chen and Blackwelder (1978).

Passive scalar transport

A passive scalar is one that does not affect the velocity field through its inclusion in the flow. Many scalars are not passive. In flow past a hot plate, for example, the air nearest to the plate becomes warm and more buoyant. The gravity force in equation 1.1 becomes dominant, creating upward motion of warm air in ways that would not have occurred without the inclusion of heat. However, the inclusion of heat can be considered passive if the heating is sufficiently mild such that the gravitational forces are negligible compared with any other force. This work will focus on one such flow, in which mild heating is applied at the wall.

A passive scalar obeys

$$\frac{\partial T'}{\partial t} + \boldsymbol{U} \cdot \nabla T = (RePr)^{-1} \nabla^2 T \tag{1.6}$$

with the velocity term $\boldsymbol{U}$ coming from equation 1.1. T represents the temperature, T' is the fluctuating temperature, defined as $T' = T - \bar{T}$, and $Pr = \frac{\nu}{\alpha}$ is the Prandtl number, the ratio between the kinematic viscosity and the thermal diffusivity. The Prandtl number varies by the type of fluid; e.g. $Pr = 0.7$ for air and $Pr = 7$ for water at standard conditions. A Prandtl number of 1 indicates that momentum and heat diffuse at the same rate, which also means that the scalar and velocity fields will be most similar. Because of the passivity of the scalar, equation 1.1 affects equation 1.6, but equation 1.6 does not feed back to affect equation 1.1.

When heat is added at the wall of a turbulent boundary layer, a thermal boundary layer develops (Antonia, Danh, and Prabhu, 1977) within which, on average, the temperature is higher than that of the free stream. The behavior of the scalar is generally quite similar to the behavior of the streamwise velocity field. In some cases, useful approximations can be made for the temperature field given a velocity field, such as the Strong Reynolds Analogy (Favre, 1964),

$$\begin{aligned} c_p(\bar{T} - T_w) &= Pr_w \frac{\bar{q}_w}{\bar{\tau}_w} \bar{U} \\ c_p T' &= Pr_w \frac{\bar{q}_w}{\bar{\tau}_w} u, \end{aligned} \tag{1.7}$$

where the subscript w indicates the wall, q is the heat transfer rate, c_p is the specific heat capacity of air, and τ is the shear stress. This relation says that the fluctuating temperature field T' is proportional to the streamwise velocity field, u. It is not believed that this holds instantaneously, but it is a useful approximation for comparing the velocity and scalar field (Spina, Smits, and Robinson, 1994).

There are, however, interesting and important differences between the velocity field and the passive scalar field statistically and instantaneously, even in unity Prandtl number flows. The tails of the probability density function of the scalar field are exponential rather than Gaussian (Warhaft, 2000), the scalar behavior is anisotropic (Sreenivasan, 1991), and the gradients are sharper, known as the 'unmixedness of the scalar' (Guezennec, Stretch, and Kim, 1990). Additionally, the instantaneous features of the velocity and scalar fields, as well as their gradients, do not appear equivalent in visualization and analysis of recent DNS of heated turbulent channel flow (Antonia, Abe, and Kawamura, 2009; Abe, Antonia, and Kawamura, 2009).

Thus, open questions remain regarding the estimation of a passive scalar field based upon the velocity field of a flow without computing the answer directly from equation 1.6. Just as is true for the velocity field, efficient models are of interest in the scalar field to be able to predict its behavior for realistic applications. Models of the scalar field are also of scientific interest, as understanding the mixing of a passive scalar can give insight into the dynamics and interaction of turbulent scales.

Aero-optics

One important application of the transport of scalars in a wall-bounded turbulent flow is the problem of aero-optics. When light is passed through a turbulent boundary layer with density variation, the wavefront of the light becomes distorted due to coupling between the index of refraction, n, and the density, ρ, in the fluid. The two are linearly related through the Gladstone-Dale relation,

$$n = 1 + K_{GD}\rho, \tag{1.8}$$

where K_{GD} is the Gladstone-Dale constant, which is a function of the fluid in question. As the beam passes through the variations in density in the fluid, it is also passing through variations in the index of refraction field, causing wavefront and beam path aberrations. In aircraft laser-based communication applications, this results in signal-dropout due to the rapid distortion of the beam in time. Understanding the fundamental physics behind these distortions opens the possibility of active control that mitigates the distortion.

Due to the application of interest in the problem, most of the work in aero-optics has been done in compressible flows, where the energy equation is coupled to the momentum equations. In compressible flows, the scalar is generally not passive, but comparisons can be made to the incompressible, heated case. The Strong Reynolds Analogy is often used for this purpose (Spina, Smits, and Robinson, 1994).

Study of the distortion of an optical beam has been done in boundary layers, shear flows, and over more complex application-specific geometries (Jumper and Fitzgerald, 2001; Dimotakis, Catrakis, and Fourguette, 2001; Gordeyev et al., 2014). Several measurement techniques were developed to study this problem including the Malley probe (Malley, Sutton, and Kincheloe, 1992) and the Shack-Hartmann sensor (Wyckham and Smits, 2009).

The distortions of the optical beam were observed to 'convect' with a particular speed in turbulent boundary layers (Gordeyev et al., 2014) by correlating the distortion

signals at two locations, separated by a small distance in the streamwise direction. This speed, approximately $0.82U_\infty$ (Gordeyev et al., 2014) indicated that something in the outer region of the boundary layer was responsible for the deflections. The distortion was observed to have a consistent spectral content that collapsed when normalized appropriately across Mach numbers and Reynolds numbers (Gordeyev et al., 2014; Smith et al., 2014), suggesting that a particular range of length scales was consistently correlated to the distortion. These findings suggested that the aero-optic measurement was responding to some specific turbulent behavior. Open questions remained about what turbulent phenomena were correlated to the deflection, and how to mitigate their effects on the signal-dropout problem.

An additional complexity of understanding the aero-optic measurement is that it is inherently an integral measurement. The beam passes through the full turbulent boundary layer before its distortion is measured. This would generally mean that a number of turbulent phenomena could influence the beam before its distortion was measured, complicating any analysis of the source of distortion. However, evidence from turbulent shear layers suggested that a single interface in the density field could dominate aero-optic distortion signals (Dimotakis, Catrakis, and Fourguette, 2001), offering the possibility that the integral measurement in turbulent boundary layers could also be correlated to a single event. This possibility warranted further study.

Modeling with the resolvent operator

Modeling was used in this thesis to aid in the understanding of coherent structures, their interactions, and their relevance to the passive scalar field and the aero-optic problem. The fluctuating field (equation 1.4) was decomposed in a Fourier decomposition as shown in equation 1.5, and the resolvent analysis of the Navier-Stokes equations was used to identify the wall-normal coherence of models for specific scales, using the formulation of McKeon and Sharma (2010). The interaction of these coherent structure models was also explored to capture scale interaction, building off of the work of Sharma and McKeon (2013) and McKeon (2017).

Resolvent analyses formulate the non-dimensionalized Navier-Stokes equations as an input-output system between an input and the velocity field with the linear dynamics acting as a transfer function between the two. The linear transfer function

is termed the resolvent operator

$$\boldsymbol{\mathcal{H}} \equiv (-i\omega - \boldsymbol{\mathcal{L}})^{-1}$$
$$= \begin{bmatrix} -i\omega + ik_x\bar{U} + Re_\tau^{-1}\Delta & D_y\bar{U} & 0 & ik_x \\ 0 & -i\omega + ik_x\bar{U} + Re_\tau^{-1}\Delta & 0 & D_y \\ 0 & 0 & -i\omega + ik_x\bar{U} + Re_\tau^{-1}\Delta & ik_z \\ ik_x & D_y & ik_z & 0 \end{bmatrix}^{-1}, \tag{1.9}$$

where D_y is the partial derivative in the wall-normal direction and $\Delta = D_{yy} - k_x^2 - k_z^2$ such that

$$\begin{bmatrix} \tilde{\boldsymbol{u}} \\ \tilde{p} \end{bmatrix} = \boldsymbol{\mathcal{H}} \begin{bmatrix} \tilde{\boldsymbol{f}} \\ 0 \end{bmatrix}, \tag{1.10}$$

where $\boldsymbol{f} = -\boldsymbol{u} \cdot \boldsymbol{\nabla} \boldsymbol{u}$ is the nonlinear forcing term and $\tilde{\boldsymbol{f}}$ is the forcing for a particular scale, defined by its streamwise, spanwise, and temporal wavenumbers. Many velocity scales, not just $\tilde{\boldsymbol{u}}$, contribute to $\tilde{\boldsymbol{f}}$. Note that the mean velocity field $\bar{U}$ is needed to formulate the resolvent operator.

A singular value decomposition is performed on the resolvent operator to determine the right ($\boldsymbol{\Phi}$) and left ($\boldsymbol{\Psi}$) singular vectors for each wavenumber triplet (streamwise, spanwise, and temporal). In this formulation

$$\boldsymbol{\mathcal{H}}(k_x, k_z, \omega) = \boldsymbol{\Psi\Sigma\Phi}, \tag{1.11}$$

where $\boldsymbol{\Sigma}$ is the matrix of singular values. The operator has been observed to be low-rank (McKeon and Sharma, 2010), such that the first singular vector is much more amplified by the linear dynamics at a given wavenumber triplet than the second singular vector. The first singular vector is used as an approximation of the wall-normal coherence for the model such that

$$\hat{\boldsymbol{u}}(y) = \chi \boldsymbol{\psi}(y), \tag{1.12}$$

where χ is the weighting of the mode and ψ is the first singular vector. The scaling with Reynolds number of the singular value and geometry of modes throughout the boundary layer has been reported by (Moarref et al., 2013), while the scaling of the full weighting χ is the subject of ongoing work within the research group of Dr. Beverley McKeon. The value of χ was defined through analysis of the data in chapters 4 and 5.

A key finding of McKeon and Sharma (2010) was the importance of critical layers in wall-bounded turbulent flows. The first singular vector, from here referred to as a resolvent mode, was observed to be localized about its critical layer in the mean flow field: the height where

$$\begin{aligned} c &= \bar{U}(y), \\ c &= \omega/k_x. \end{aligned} \tag{1.13}$$

The concept of critical layers in turbulence plays an important role throughout the thesis, with particular emphasis in chapters 4 and 5.

1.3 Open questions and challenges

There are many remaining challenges in the study of turbulent wall-bounded flows. Within engineering, there is a great need to be able to efficiently model turbulence near walls. Currently, while the Navier-Stokes equations can be solved on computers, the range of scales involved are very large in realistic applications, making the direct computation too large to be feasible. Instead, many current efforts focus on exactly computing the largest scales, and modeling the smallest scales using physics-based models. This coupling allows for the simulation of large-scale engineering applications, which improves the design process of modern technologies. However, current models are often inaccurate, especially in non-canonical geometries. Critical parameters at the wall, including skin friction and heat transfer, are often incorrectly estimated (Park and Moin, 2016). There is a need for better models of turbulent dynamics that can interface with the computation of the Navier-Stokes equations. The work of Marusic, Mathis, and Hutchins (2010) demonstrates the utility of such an approach, in which the small-scale velocity field is modulated by the action of the large scales in the logarithmic layer. Further work is needed to create models that can couple to the LES to allow the small scales to influence the large scales, as well as to create models that are applicable in a wide variety of non-equilibrium flow conditions.

There is also a desire in the engineering world to do more than just model turbulence: there is an interest in modifying it. The application of closed-loop control to turbulent boundary layers could allow for some of the damaging effects of turbulence on the engineering variables of interest (drag, heat transfer) to be mitigated by continuously changing the behavior of the fluid to a state with better engineering characteristics. But to implement closed-loop control, one has to be able to do many things that are not currently possible. One has to be able to quickly measure the flow

field and use that measurement to estimate the state of a reasonably large area of the fluid. Currently, most instantaneous measurements are local, while most global measurements require post-processing time, offering complexity in state estimation from local measurements, and in processing speed for global measurements. Then, one has to be able to use the estimation of the current state of turbulence to quickly predict what the turbulence is about to do, requiring efficient modeling of the flow dynamics. One also has to know what one would prefer the turbulence to do, and how to change its behavior towards that goal, which is an area of active research in the community. And finally, one has to be able to actuate the turbulence in such a way as to change its behavior. The implementation of a closed-loop control system that reduces drag is a significant challenge that requires a community of people all working on pieces of the puzzle.

The present approach

There are many useful and valid perspectives to take when studying a problem as complex as turbulence. The approach taken here is experimental and data-driven, and has a strong interest in uniting the statistical and instantaneous perspectives of turbulence. It attempts to stay in physical space as much as possible, in order to try to understand the physical and instantaneous structure of turbulence, including how different scales are organized in relation to one another. This rooting in the physical world is chosen with the belief that the spatial structure and organization of turbulence is central to its character and its ability to self-sustain. The approach seeks to build models that instantaneously, physically resemble turbulent flows while maintaining a clear connection to the energetic statistics that have been identified as universal across many experiments. These models serve both the engineering purpose of advancing the useful predictive abilities of reduced-order models, and the scientific purpose of clarifying and simplifying turbulent dynamics towards a system that can be understood.

Contributions of the thesis

Some key challenges to which this thesis contributes:

- The connection between instantaneous and statistical descriptions of turbulence
- The identification of mechanisms through which scales influence one another

- The clarification of the instantaneous relationship between velocity and scalar fields
- The isolation of the turbulent dynamics that are correlated to aero-optic distortion

After a discussion of the experimental methods, DNS database, modeling methods, and analysis methods used in chapter 2, the thesis focuses on the description of coherent structures, with specific contributions to the first of the four listed challenges in chapter 3. Representative models for a number of energetic scales in turbulence are proposed and compared to instantaneous velocity fields through visualization and instantaneous streamwise histogram techniques.

The thesis then uses these modeled representations of the energetic scales to probe the second challenge, the identification of scale interaction mechanisms, in chapter 4. A novel conditional averaging technique is implemented that uses the models of energetic scales to phase average the small-scale velocity intensity on the large scale flow field. A localization of small-scale intensity is observed at particular isocontours of the large-scale flow, leading to a hypothesis for an interaction mechanism. It is hypothesized that the large scale superimposed with the mean velocity profile acts as a pseudo-base flow, while the small scales act as perturbations about that base flow, showing strongest growth and presence along isocontours of the pseudo-base flow corresponding to the small-scale phase velocity.

Further work is done to contribute to the challenge of identifying scale interaction mechanisms in chapter 5, where the conditional averaging technique just described is combined with a second conditional averaging technique that allows for a phase average on both the large and small scales. A single small scale is observed to dominate much of the outer region of the boundary layer, appearing to sit at a variety of heights from the wall as a function of the phase of the large scale. This experimentally-observed phenomenon is argued to support the critical layer hypothesis. Modeling of this phenomenon is shown to be possible with a linear superposition of resolvent modes.

The model of scale interaction in the velocity field is extended to model the scalar field using a passive scalar resolvent code in chapter 5. This model allows for the comparison of the predicted instantaneous structure of the velocity and scalar fields as a function of Prandtl number, contributing to the third challenge. Finally, the interaction of only two scales is shown to be strongly correlated to the distortion of

an optical beam passing through a variable-density flow field, offering an answer to the fourth challenge in the context of incompressible flows.

In chapter 6, the work is summarized and some avenues for future work are outlined.

Chapter 2

METHODS

2.1 Experimental methods

Heated flat plate

Experiments were run in the Merrill wind tunnel at Caltech. The tunnel is an incompressible, recirculating flow facility with a 0.6 m x 0.6 m test section. The test section used for the experiments described in this thesis had an aluminum flat plate along its center with rubber resistance heaters embedded inside such that the flat plate could be heated (Rought, 2013). At the upstream edge of the flat plate, a small wire tripped the flow into turbulence. At the downstream edge of the flat plate a fin adjusted the flow to secure the stagnation point location at the leading edge.

The flat plate itself included heated and unheated portions, shown schematically in figure 2.1. The unheated portions included glass and acrylic inserts through which light could pass. These inserts were used both to allow for a high quality light sheet for PIV, and to allow for the use of optical devices including a Malley probe and a Shack-Hartmann sensor. In the heated portions, the heating elements extended through the span of the flat plate and heated a total of 1.25 m in the streamwise direction, composed of two 0.63 m sections with a 0.14 m unheated length between them. The first heated portion of the plate started 0.3 m downstream of the boundary layer trip and ended 0.2 m before the measurement location. In figure 2.1, the lengths of the plates are noted in dimensional units. The dimensionless lengths of the final heated and unheated plates, nondimensionalized by the 99% boundary layer thickness at measurement location B, were 18δ and 10δ respectively.

Two thermocouples, embedded with the heaters in the flat plate, measured the temperature of each heated section at its centerpoint (Rought, 2013). A thermal camera (FLIR A325sc #48001 – 1001) was used to examine the spatial variation of the temperature across the plate, which was found to vary by about 3°C. The resolution of the thermal camera was ±0.8°C. The hottest location was found at the center of each plate and the coolest near the edges, where conduction to the unheated portions of the wind tunnel decreased the equilibrium temperature.

The temperature difference between the free stream and plate was held constant at 22°C such that the flow was moderately heated. The statistics of the temperature

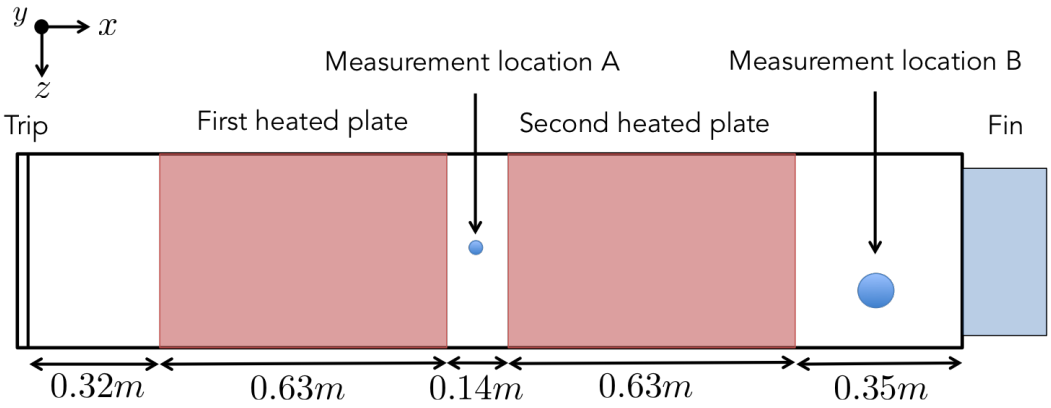

(a)

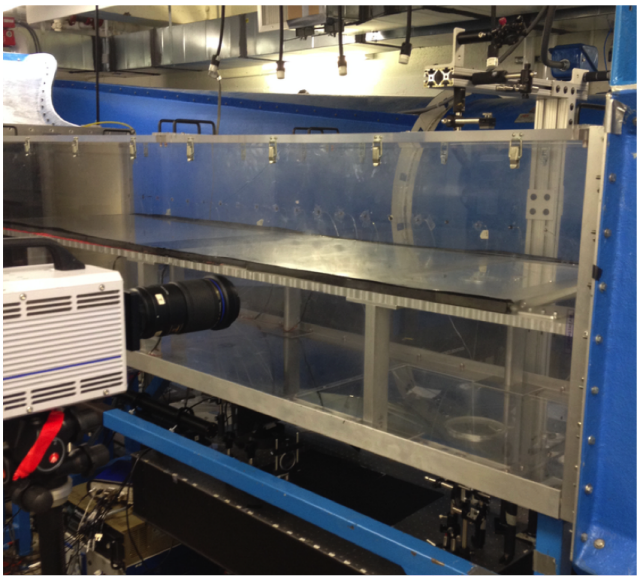

(b)

Figure 2.1: Schematic from a bird's eye view of the flat plate in the Merrill wind tunnel (a), and image of the Merrill wind tunnel (b). Dimensional length scales are shown for each of the segments of the flat plate in (a). Red shading indicates heated portions of the plate. In (b), the flat plate is observed as the shiny, aluminum surface in the center of the test section. A camera used for velocimetry is also shown. Flow moves from left to right in both panels.

field will be described in the the subsection *Relevant flow statistics*.

Velocity field measurement

Particle image velocimetry (PIV) was used to acquire streamwise and wall-normal velocity data from a turbulent boundary layer at measurement location B in figure 2.1(a). The flow was seeded with an aerosol of bis(2-ethylhexyl)sebacate (DEHS) (0.25 μm modal size, LaVision Aerosol Generator #1108926) and was illuminated in

the wall-normal, streamwise plane using a double-pulsed YLF laser with a frequency of 1.5 kHz and a pulse separation of 35 μs. A Photron Fastcam APX-RS camera with a 17 mm Tamron macro lens was used to record images at a resolution of 1024×1024 pixels. The field of view was $1.4\delta \times 1.7\delta$ (50 mm $\times$ 60 mm). Davis software from LaVision was used to process the data, using a double pass approach with windows of first 32 and then 16 pixels with 50% overlap. The resolution per vector was 0.013×0.013 outer units or 14.5×14.5 inner units.

The Reynolds number was found to be Re_θ = 3,300 or Re_τ = 910. The 99% boundary layer thickness, δ, was found to be 35 mm in the center of the measurement, with a change of less than 7% over 1.7δ of streamwise extent. Note that the expression for boundary layer thickness as a function of the streamwise variable is approximated as

$$\delta \approx 0.37 \frac{x^*}{Re_{x^*}^{1/5}}, \tag{2.1}$$

where $Re_x^* = \frac{U_\infty x^*}{\nu}$ and x^* is the distance downstream from the virtual origin, the location where the boundary layer would have begun had it not been tripped (Schlichting, 1979). Given the rate of growth observed, this suggests an approximate location of the virtual origin of $x^* = 3.8$ m.

The measured free stream velocity from PIV was U_∞ = 12.15 m/s, which was within 2% of that measured by a pitot probe placed upstream of the measurement location. The friction velocity u_τ was determined using the Clauser method and was identified to be 0.47 m/s. There was a slightly favorable pressure gradient in the tunnel due to its constant rectangular cross section in the presence of a growing boundary layer. This pressure gradient was sufficiently small such that the flow can still be characterized as a zero pressure gradient flow, with an acceleration parameter of $K = 6.7 \times 10^{-7}$ (Rought, 2013). The acceleration parameter is defined as

$$K = -\frac{\nu}{\rho U_\infty^2} \frac{dP}{dx} \tag{2.2}$$

and has an upper threshold of $1.6x10^{-6}$ for a pressure gradient that causes deviation from standard statistics (DeGraaff and Eaton, 2000).

Relevant flow statistics

The mean and root mean squared (RMS) velocity statistics were found from the PIV data and compared to data from DeGraaff and Eaton (2000) at similar Reynolds numbers. The data was found to agree well above a y^+ of about 40 or equivalently

$y/\delta = 0.05$. Figure 2.2 shows the mean (a) and RMS (b) of the streamwise velocity field compared to the DeGraaff and Eaton data. The discrepancy near the wall is caused by reflections from the laser light sheet shining down onto the aluminum flat plate from above.

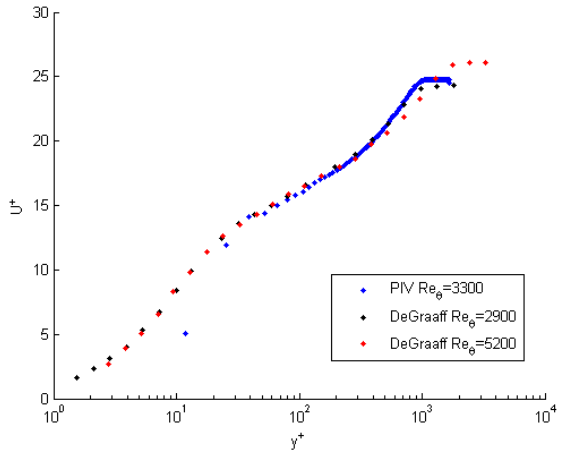

(a)

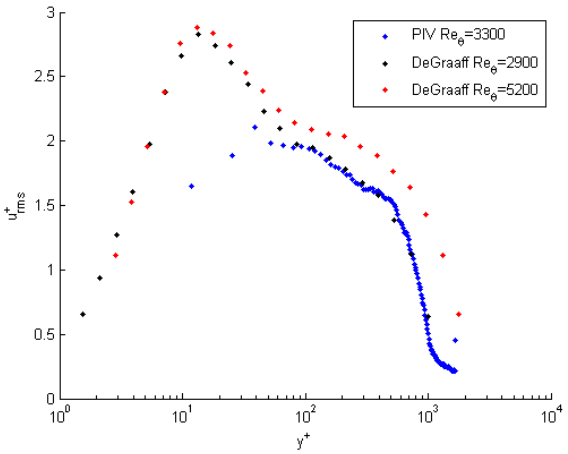

(b)

Figure 2.2: Mean profile (a) and RMS (b) as a function of distance from the wall. Blue points indicate data from PIV measurements in this study. Black and red points indicate data from DeGraaff and Eaton (2000) at similar Reynolds numbers for comparison. Data was seen to agree above $y^+ \approx 40$. Discrepancies near the wall are due to glare from the PIV light sheet.

The mean temperature profile in the tunnel was determined through measurement with a cold wire, collected by Rebecca Rought. The temperature was measured both directly over a heated plate and at measurement location A of figure 2.1. The temperature measurements were non-dimensionalized using a friction temperature

defined as

$$T_\tau = \frac{q_w}{\rho C_p u_\tau}, \tag{2.3}$$

where q_w is the heat flux at the wall and C_p is the specific heat capacity of air. The plotted temperature in figure 2.3 is non-dimensionalized as

$$T^* = \frac{T_{w,h} - T}{T_\tau}, \tag{2.4}$$

where $T_{w,h}$ is the temperature of the heated wall. The ambient temperature in the room was held at approximately $21°C$, while the wall was heated to approximately $43°C$, leading to a difference in temperature of approximately $22°C$.

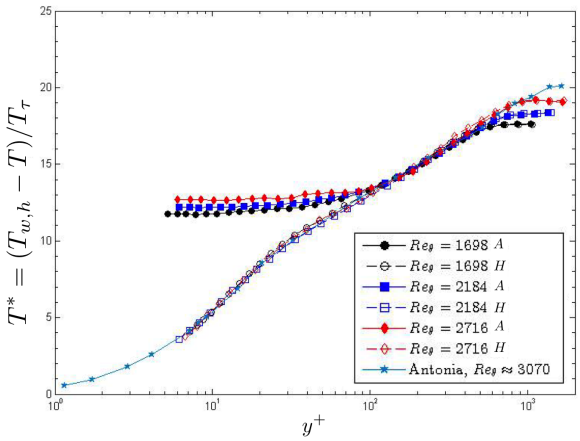

Figure 2.3: Mean temperature profiles as a function of distance from the wall for a variety of Reynolds numbers and measurement locations. *H* indicates that the measurement was taken directly over the heated plate, 5 cm before the end of the first heated section, while *A* indicates the measurement location *A* in figure 2.1. The blue starred curve indicates data from Antonia, Danh, and Prabhu (1977) for a passively heated turbulent boundary layer. Cold wire data was collected by Rebecca Rought. Plot adapted from Rought (2013).

The mean temperature profiles in figure 2.3 are observed to agree with that of Antonia, Danh, and Prabhu (1977) over the heated wall. At measurement location A, the mean temperature profile is observed to depart from the canonical thermal boundary layer at a $y^+ \approx 100$, or $y/\delta \approx 0.1$. This internal cool layer is a result of the heated plate ending upstream of the measurement location due to experimental constraints. At a step change in the temperature boundary condition that decreases the wall heat flux, a new thermal boundary layer begins to develop that is cooler than the first (Antonia, Danh, and Prabhu, 1977). The measured height of the internal

cool layer (the point of deviation from the fully-heated case) is deemed acceptable, as the focus of the analysis using the scalar field is on the outer boundary layer above $y/\delta \approx 0.2$.

The agreement of the velocity statistics with an unheated boundary layer (figure 2.2 and the temperature statistics with a passive thermal boundary layer (figure 2.3) demonstrates that the heating in this experiment is sufficiently small that no dynamic effects are statistically observed. The scalar is therefore assumed to be a passive contaminant in the flow for the remainder of the work. This also means that the internal cool layer is not associated with any change in the velocity field. This observation coupled with the lack of a pressure gradient allows this flow to be considered a canonical turbulent boundary layer.

Scalar measurement overview

The scalar field was measured using a Malley probe (Malley, Sutton, and Kincheloe, 1992) at measurement location B in figure 2.1. The Malley probe consists of two 1 mm diameter laser beams aligned in the streamwise direction. In this work, a single beam is first passed through a spatial filter before it is split into two equal beams by a beam splitter. The beams are then passed through the flow field along the wall-normal direction, as in figure 2.4(a). An experimental image of the two beams, aligned in the streamwise direction, is shown in figure 2.4(b). After passing through the flow field once, the beams hit a mirror and pass back down through the flow a second time along the same path to increase the strength of the final signal. Finally, each beam impinges on a position sensor that measures its centroid position. The final angle of each beam is deduced from its centroid position, illustrated in figure 2.4(c).

The beam angle is found to be time varying when the beam is passed through a variable-density flow, due to a relationship between index of refraction and density (Gordeyev et al., 2014). The index of refraction is in general a function of time and space

$$n(x, y, z, t) = 1 + K_{GD}\rho(x, y, z, t), \tag{2.5}$$

where K_{GD} is the Gladstone-Dale constant and ρ is the density field. In the schematic in figure 2.4(c) a streamwise density gradient is modeled using a single interface in the density field, illustrated using a dark red inclined line.

In this study, the Malley probe is used to study a low Mach number flow ($M = 0.05$) with heat addition, such that the only source of density fluctuations comes from

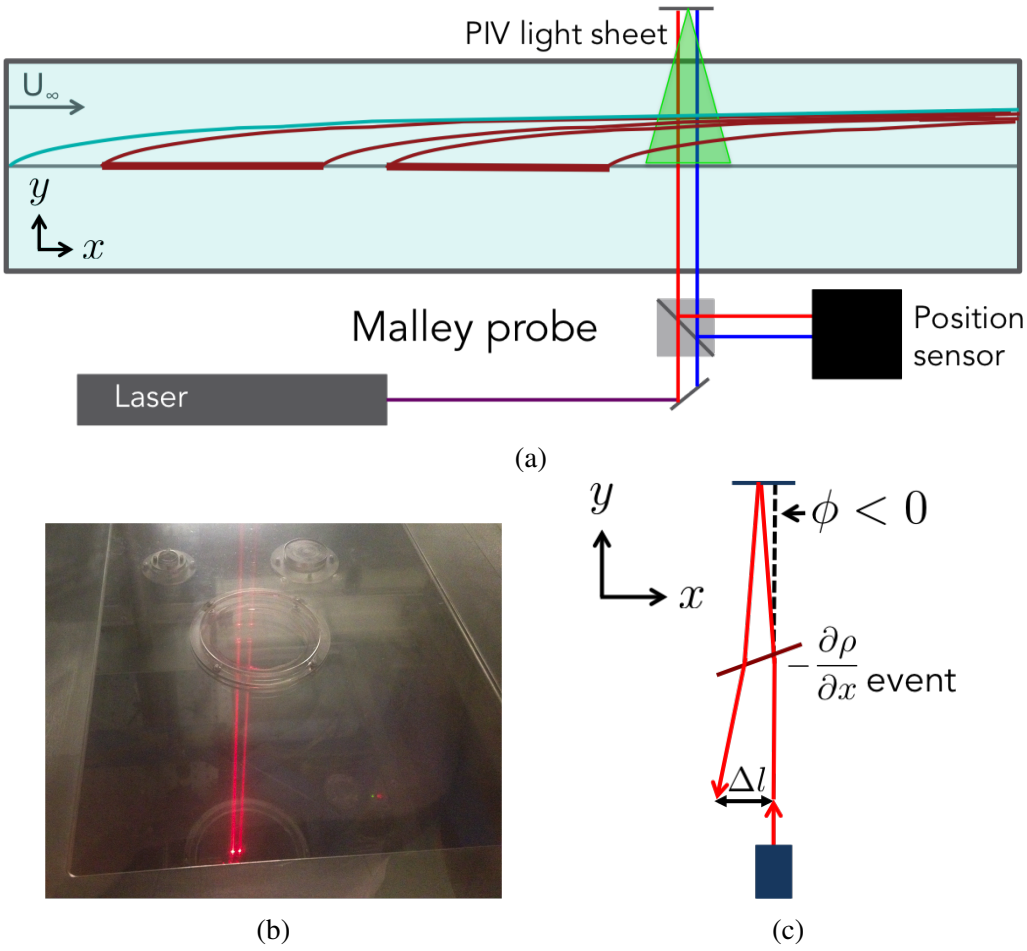

Figure 2.4: Schematic of the PIV and Malley probe simultaneous measurements in a heated, turbulent boundary layer (a), an experimental image of the two Malley probe beams passing through the flow at measurement location B, aligned in the streamwise direction (b), and a simplified representation of the Malley probe optical measurement for a single beam (c). Schematics (a) and (c) are not to scale.

the heated flat plate (Gordeyev et al., 2015). The beam is deflected in both the streamwise and spanwise directions and both final angles are measured. The work in this thesis will focus on the streamwise angle, with the analysis of the spanwise angle identified as a source of future work. The standard deviation of the final streamwise angle, $\phi(t)$, was found to be 7 mrad. Thus the beam deflections are sufficiently small that the double-pass approach used in this implementation of the Malley probe measures the effect of the same fluid phenomena in both passes. Positive values of ϕ will be used to denote downstream inclinations relative to the vertical, while negative values of ϕ will denote upstream inclinations.

Synchronization

To be able to identify the relationship between the scalar and velocity measurements, the two measurements had to be properly synchronized. To do this, a signal (RecordPost) was recorded from the PIV system using the same sampling and recording system that the Malley probe used. The relationship of this signal to the other PIV signals is shown in figure 2.5. RecordPost jumped from 0 to 5 volts at the beginning of the first exposure of the first recorded image pair. The start time of the PIV data was then taken as one exposure time after the RecordPost signal increased to 5 V, such that the moment between the two images of the first image pair was taken as $t = 0$.

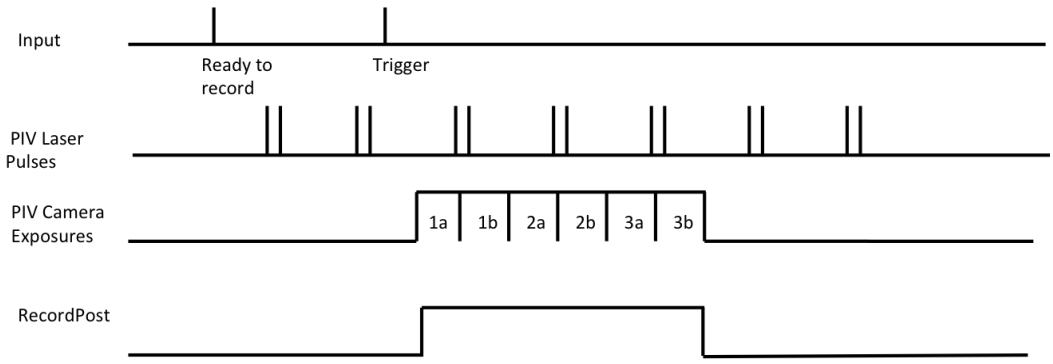

Figure 2.5: Timing diagram shown for PIV system. The RecordPost signal was outputted from the PIV system and was read by the same measurement system recording the Malley probe deflection signal. Exposures 1a and 1b comprised the first recorded image pair that was correlated to identify the velocity field.

Analysis of optical path length and deflection

The goal of this section is to derive the relationship between a scalar field and the measurement of the Malley probe. The relevant optical terms will be defined and their relationships will be clarified to arrive at the final expression for the Malley probe angle, ϕ, as a function of the density field, ρ.

Optical path length

The optical path length is the geometric product of the path that the light follows with the local index of refraction of the medium. It is defined as

$$S = \int n ds, \tag{2.6}$$

where s is the path along which the beam travels. Define ζ as a parameterization variable for the path s, such that $s = s(x'(\zeta), y'(\zeta), z'(\zeta))$ where the primes indicate that $x'(\zeta)$, $y'(\zeta)$, and $z'(\zeta)$ are the coordinates of the beam in space, rather than the independent spatial variables x, y, and z. Note that $ds = \sqrt{dx'^2 + dy'^2 + dz'^2}$ and $\frac{ds}{d\zeta} = \sqrt{\dot{x}'^2 + \dot{y}'^2 + \dot{z}'^2}$, where $\dot{x}'(\zeta) = \frac{dx'}{d\zeta}$, $\dot{y}'(\zeta) = \frac{dy'}{d\zeta}$, $\dot{z}'(\zeta) = \frac{dz'}{d\zeta}$, such that

$$\begin{aligned} S(\zeta) &= \int n(x', y', z') \frac{ds}{d\zeta} d\zeta \\ S(\zeta) &= \int n(x', y', z') \sqrt{\dot{x}'^2 + \dot{y}'^2 + \dot{z}'^2} d\zeta. \end{aligned} \tag{2.7}$$

This indefinite integral will give a value of S for all ζ. Curves of constant optical path length in space are called wavefronts. The final value of the optical path length along a particular path is then

$$S(\zeta_f) - S(\zeta_i) = \int_{\zeta_i}^{\zeta_f} n(x', y', z') \sqrt{\dot{x}'^2 + \dot{y}'^2 + \dot{z}'^2} d\zeta. \tag{2.8}$$

Finally, using equation 2.5 to relate index of refraction to density leads to the final expression for the optical path length as a function of density,

$$S(\zeta_f) - S(\zeta_i) = \int_{\zeta_i}^{\zeta_f} \left(\rho(x', y', z') K_{GD} + 1\right) \sqrt{\dot{x}'^2 + \dot{y}'^2 + \dot{z}'^2} d\zeta. \tag{2.9}$$

Optical momentum

To identify the relationship between the beam angle and the density field, the optical momentum vector will be used. The optical momentum vector is everywhere tangent to the ray of light and has magnitude equal to the local index of refraction. It is defined as

$$\begin{aligned} \mathbf{p} &= (p_x, p_y, p_z) \\ p_x &= n \frac{dx'}{ds} \\ p_y &= n \frac{dy'}{ds} \\ p_z &= n \frac{dz'}{ds}. \end{aligned} \tag{2.10}$$

Note that $||\mathbf{p}|| = n$. The gradient of the optical path length is the optical momentum,

$$\mathbf{p} = \nabla S. \tag{2.11}$$

Levelsets of S (wavefronts) are perpendicular to levelsets of the optical momentum (optical rays). This relationship can also be written as

$$S = \int \mathbf{p} \cdot \mathbf{ds}, \tag{2.12}$$

where $\mathbf{ds} = (dx', dy', dz')$.

Finding ϕ along beam path

A simple relationship is sought between the measured streamwise angle in the aero-optical distortion experiment and the index of refraction field. The relationship between $\mathbf{p}$ and S will be used. First, note that

$$\mathbf{p} = (n\cos\alpha_x, n\cos\alpha_y, n\cos\alpha_z), \tag{2.13}$$

where both n and α are functions of ζ and each α is defined relative to the axis it specifies, as seen in Figure 2.6.

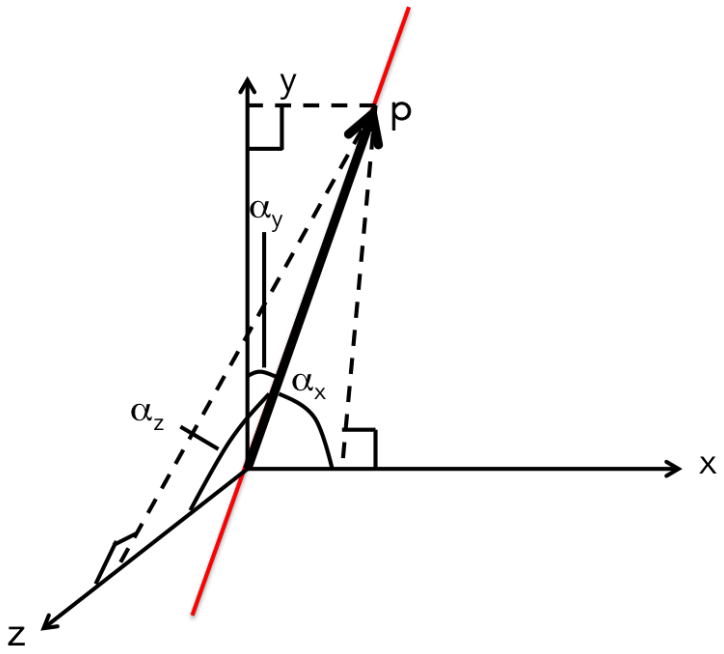

Figure 2.6: Schematic shows the definition of three angles that define the orientation of the optical momentum vector.

The analysis in this thesis focuses exclusively on the streamwise deflection angle of the Malley probe, allowing for a focus on the x-component of the $\mathbf{p}$ vector. Using

the relationship between $\mathbf{p}$ and S, one finds

$$p_x(\zeta) = n(x', y', z') \cos \alpha_x(\zeta) = \frac{\partial}{\partial x'} S(\zeta). \tag{2.14}$$

Using the expression for S in equation 2.9, this gives

$$p_x(\zeta) = n(\zeta) \cos \alpha_x(\zeta) = \frac{\partial}{\partial x'} \int n(x', y', z') \sqrt{\dot{x}'^2 + \dot{y}'^2 + \dot{z}'^2} d\zeta. \tag{2.15}$$

The angle defined for the ensuing experiments is measured relative to the y-axis rather than the x-axis, so our angle ϕ is defined as $\frac{\pi}{2} - \alpha_x$ such that

$$n(\zeta) \sin \phi(\zeta) = \frac{\partial}{\partial x'} \int n(x', y', z') \sqrt{\dot{x}'^2 + \dot{y}'^2 + \dot{z}'^2} d\zeta. \tag{2.16}$$

Pulling the derivative inside the integral and noting that $\frac{ds}{d\zeta} = \sqrt{\dot{x}'^2 + \dot{y}'^2 + \dot{z}'^2}$ is not a function of x', one identifies that

$$n(\zeta) \sin \phi(\zeta) = \int \frac{\partial n}{\partial x'}(x', y', z') \sqrt{\dot{x}'^2 + \dot{y}'^2 + \dot{z}'^2} d\zeta. \tag{2.17}$$

Using the relationship between density and index of refraction, one finds

$$n(\zeta) \sin \phi(\zeta) = K_{\mathrm{GD}} \int \frac{\partial \rho}{\partial x}(x', y', z') \sqrt{\dot{x}'^2 + \dot{y}'^2 + \dot{z}'^2} d\zeta. \tag{2.18}$$

The final angle measured simply requires a change to a definite integral, where ζ_i is taken as the value of ζ at the initial location of the beam, and ζ_f is taken as the value of ζ at the final location of the beam.

$$n(\zeta_f) \sin \phi(\zeta_f) - n(\zeta_i) \sin \phi(\zeta_i) = K_{\mathrm{GD}} \int_{\zeta_i}^{\zeta_f} \frac{\partial \rho}{\partial x}(x', y', z') \sqrt{\dot{x}'^2 + \dot{y}'^2 + \dot{z}'^2} d\zeta. \tag{2.19}$$

Both the density field and the path are functions of time, so this can be written as

$$\begin{aligned} &n(\zeta_f, t) \sin \phi(\zeta_f, t) - n(\zeta_i, t) \sin \phi(\zeta_i, t) = \\ &K_{\mathrm{GD}} \int_{\zeta_i}^{\zeta_f} \frac{\partial \rho}{\partial x}(x', y', z', t) \sqrt{\dot{x}'^2 + \dot{y}'^2 + \dot{z}'^2} d\zeta, \end{aligned} \tag{2.20}$$

where x', y', z', $\dot{x}'$, $\dot{y}'$, and $\dot{z}'$ are all functions of ζ and t.

Some approximations can be made to simplify this expression. First, the index of refraction at ζ_i and ζ_f can be taken to be the same value associated with the ambient conditions, n_a, as the beam path begins and ends outside of the tunnel, where no

substantial density variation is present. Additionally, the initial angle can be taken to be a constant, rather than a function of time, such that $\phi(\zeta_i, t) = \phi(\zeta_i)$. The standard deviation of the measured angle is only 7 mrad, allowing the use of the small angle approximation, which also identifies that $\dot{y}'$ is significantly larger than $\dot{x}'$ or $\dot{z}'$. These assumptions lead to equations 2.21 and 2.22.

$$n_a \left(\phi(\zeta_f, t) - \phi(\zeta_i)\right) = K_{\mathrm{GD}} \int_{\zeta_i}^{\zeta_f} \frac{\partial \rho}{\partial x}(x', y', z', t)\dot{y}' d\zeta \tag{2.21}$$

or

$$\phi(y_f, t) - \phi(y_i) = \frac{K_{\mathrm{GD}}}{1 + K_{\mathrm{GD}}\rho_a} \int_{y_i}^{y_f} \frac{\partial \rho}{\partial x}(x_0, y, z_0, t) dy, \tag{2.22}$$

where ρ_a is the ambient air density and ϕ_x is the measured angle in the experiments.

2.2 Direct numerical simulation

Data was extensively analyzed from a direct numerical simulation (DNS) of a zero pressure gradient turbulent boundary layer from Dr. Xiaohua Wu of the Royal Military College of Canada (Wu, Moin, and Hickey, 2014; Wu et al., 2017). The boundary layer was simulated from its initial laminar state through a bypass transition to a fully canonical turbulent state. The portion of the boundary layer considered in this thesis is the region farthest downstream, where $Re_\theta \approx 3,000$ and $Re_\tau \approx 1,000$. The friction velocity is estimated using the Clauser method and is found to be 0.0384 relative to the maximum velocity of 1 in the simulation. In the region of interest, the spanwise extent of the simulation is approximately 2.6δ. The boundary layer thickness varies by less than 8% over a 1.6δ streamwise extent in the region of interest, closely matching the change in boundary layer height of the PIV data, which was less than 7% over 1.7δ. The mean velocity profile is shown in figure 2.7.

2.3 Modeling methods

Throughout the thesis, a Reynolds-decomposition will be applied to the velocity field, $\boldsymbol{U}$, such that

$$\boldsymbol{U}(x, y, z, t) = \bar{\boldsymbol{U}}(x, y) + \boldsymbol{u}(x, y, z, t), \tag{2.23}$$

where $\bar{\boldsymbol{U}}$ is the temporal mean of the flow field and $\boldsymbol{u}$ represents the fluctuation about that mean. The fluctuation can be further decomposed into a representative scale of interest, $\tilde{\boldsymbol{u}}$, and other fluctuations that are not coherent at that scale, $\boldsymbol{u'}$, to arrive at a triple-decomposition (Hussain and Reynolds, 1970; Jacobi and McKeon, 2011)

$$\boldsymbol{U}(x, y, z, t) = \bar{\boldsymbol{U}}(x, y) + \tilde{\boldsymbol{u}}(x, y, z, t) + \boldsymbol{u'}(x, y, z, t). \tag{2.24}$$

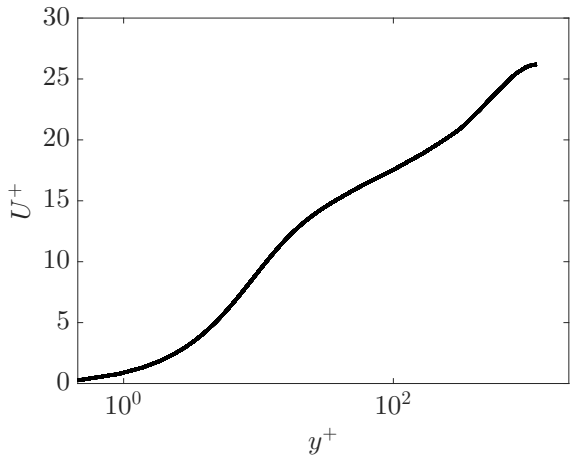

Figure 2.7: Mean profile as a function of distance from the wall for the DNS data of Wu et al. (2017).

In general, a representation of a scale of interest, $\tilde{u}$, can be identified from experimental or computational data by filtering, conditionally averaging on a strong event, or performing a modal analysis. In this work, the scale of interest, $\tilde{\boldsymbol{u}}$ is identified from length and time scales that are associated with maxima in the streamwise energy spectrum. Because turbulent spectra are not sharply peaked, $\tilde{\boldsymbol{u}}$ is interpreted as a representative model of the class of structures within the broad energetic peak in the spectrum, with the understanding that slight variation about the representative spatial and temporal scales would be expected in a fully-turbulent flow.

For simplicity in modeling, the mean velocity field is assumed to be constant in the streamwise direction: $\bar{\boldsymbol{U}} = \bar{U}(y)$, invoking the parallel-flow assumption for turbulent boundary layers. A Fourier transform is then applied in the streamwise, spanwise, and temporal variables such that the model for a particular scale $\tilde{\boldsymbol{u}}$ takes the form of a traveling wave in the fluctuating velocity field, periodic in both the streamwise, x, and spanwise, z, directions. This choice of representation allows for a clear connection between the model and the streamwise velocity spectrum, as the model can be associated with a single point in streamwise and spanwise wavenumber space. Right and left propagating waves are summed to isolate a downstream propagating wave

$$\tilde{\boldsymbol{u}}(x, y, z, t) = \mathrm{Re}[\hat{\boldsymbol{u}}(y)(e^{i(k_x x + k_z z - \omega t)} + e^{i(k_x x + (-k_z) z - \omega t)})], \tag{2.25}$$

where k_x, k_z, and ω are the streamwise, spanwise, and temporal wavenumbers respectively and here Re indicates real part. The triple decomposition can therefore

be written as

$$\boldsymbol{U}(x,y,z,t) = \bar{\boldsymbol{U}}(x,y) + \mathrm{Re}(\hat{\boldsymbol{u}}(y)(e^{i(k_x x + k_z z - \omega t)} + e^{i(k_x x + (-k_z) z - \omega t)})) + \boldsymbol{u'}(x,y,z,t). \tag{2.26}$$

The streamwise wavelengths for structures of interest are identified based on energetic scales in the streamwise energy spectrum, or from experimental evidence from conditional averaging analysis. The spanwise wavelengths and the phase velocity $c = \omega/k_x$ are drawn from commonly used values in the literature or from experimental observations. These values are drawn from the literature rather from the present data due to their common acceptance in the literature and the difficulty of deriving them from data that is not time resolved and is restricted in its spatial extent. To determine the model's wall-normal coherence, $\hat{\boldsymbol{u}}(y)$, the resolvent formulation for wall-bounded turbulent flows is used for the boundary layer geometry with a parallel flow assumption. The boundary layer resolvent code written by Dr. Ian Jacobi, Dr. Beverley McKeon, and Dr. Scott Dawson is used throughout the thesis. For a more complete discussion of the resolvent formulation, the reader is pointed to McKeon and Sharma (2010), Jacobi and McKeon (2011), and Sharma and McKeon (2013).

In addition to the velocity resolvent formulation described in chapter 1, a passive scalar resolvent code formulated and executed by Dr. Scott Dawson is used to model the passive scalar field in a mildly-heated, turbulent boundary layer. The passive scalar resolvent code is a modification to the existing resolvent boundary layer code. Due to the decoupling between the passive scalar and velocity fields, the passive scalar resolvent can be used after the identification of a velocity mode of interest, $\tilde{\boldsymbol{u}}$.

To identify the scalar modes, a new form of the resolvent operator is constructed, including the passive scalar equation. This new resolvent operator is here termed $\boldsymbol{\mathcal{H}_T}$ (T for temperature, though the formulation is general for any scalar). This resolvent operator is defined below.

$$\boldsymbol{\mathcal{H}_T} = \begin{bmatrix} -i\omega + ik_x\bar{U} + Re^{-1}\Delta & D_y\bar{U} & 0 & ik_x & 0 \\ 0 & -i\omega + ik_x\bar{U} + Re^{-1}\Delta & 0 & D_y & 0 \\ 0 & 0 & -i\omega + ik_x\bar{U} + Re^{-1}\Delta & ik_z & 0 \\ ik_x & D_y & ik_z & 0 & 0 \\ 0 & D_y\bar{T} & 0 & 0 & -i\omega + ik_x\bar{U} + (RePr)^{-1}\Delta \end{bmatrix}^{-1}, \tag{2.27}$$

where $\bar{T}$ is the mean temperature field and Pr is the Prandtl number.[1] Here the resolvent operator acts on the vector $[f_u, f_v, f_w, 0, f_T]^T$ to give the vector $[u, v, w, P', T']^T$ and $f_T = -\boldsymbol{u} \cdot \boldsymbol{\nabla} T'$.

[1] The formulation of the passive scalar resolvent is credited to Dr. Scott Dawson.

The mean velocity field $\bar{U}$ is needed to formulate the resolvent operator, shown in chapter 1 and that the mean temperature field is additionally needed to formulate the passive scalar resolvent operator. Two different mean velocity profiles are used to identify resolvent modes in this thesis. In chapter 3 the DNS mean velocity profile is used to formulate the resolvent operator, while in chapters 4 and 5 the experimental mean velocity profile from PIV measurements is used. A nominally constant temperature is used as the thermal boundary condition at the wall for both cases. In chapter 3 near-wall structures are modeled, requiring a mean that is well-resolved to the wall, whereas in chapters 4 and 5 only structures in the outer region of the boundary layer are modeled. The use of the experimental mean in chapter 5 also allows for the use of the corresponding mean temperature profile in the modeling of the scalar field, which will be discussed shortly. The flows that produced the two means are at similar Reynolds numbers, allowing for comparison between the models derived from the different means.

2.4 Analysis methods

Filtering

An interest in understanding particular large and small scales motivates the use of spatial filtering methods throughout the thesis work. Low-pass filters are used in chapter 3 to approximate from data the weighting χ of particular scales in the boundary layer. High-pass filters are used in chapters 4 and 5 to isolate and study small spatial scales throughout the boundary layer.

A Gaussian filter is used for each of these applications, defined as the convolution of the data with a Gaussian kernel. This filter is chosen for its excellent spatial filtering characteristics and its widespread use in the computer vision community as part of the scale-space theory, which is a framework to analyze distinct scales in images (Lindeberg, 1994). A key feature of the Gaussian filter is that it does not add spurious effects to the image. Filters that are sharp in the frequency domain have oscillations when transformed into the spatial domain, which can cause the spurious creation of halos around objects (Davies, 2004). A Gaussian filter is nonoscillatory in both the frequency and spatial domain, and in fact has an identical form in the spatial and spatial frequency domains (Marr and Hildreth, 1980). The Gaussian filter is also easily implementable on multi-dimensional data, as it can be applied exactly through sequential convolutions in each dimension (Davies, 2004). The Gaussian kernel is defined as

$$F_G(x) = \frac{1}{\sigma_G\sqrt{\pi}}\exp\left(-\left(\frac{x^2}{(2\sigma_G)^2}\right)\right), \tag{2.28}$$

where σ_G is the standard deviation of the Gaussian and x is the spatial dimension along which the data is being filtered. The filtering is then performed by convolving the kernel with the data and normalizing by the integral of the kernel itself.

$$u_l(x) = \frac{\int_{x_i^*}^{x_f^*} u(x^*)\exp\left(-\left(\frac{(x-x^*)^2}{(2\sigma_G)^2}\right)\right)dx^*}{\int_{x_i^*}^{x_f^*} \exp\left(-\left(\frac{(x-x^*)^2}{(2\sigma_G)^2}\right)\right)dx^*}. \tag{2.29}$$

The normalization by the integral of the Gaussian kernel improves the behavior of the filter near the edges of the domain. Without the normalization, the filter inaccurately decreases the power of the original signal near the edges. Even with the normalization, edge effects occur near the edges of the domain; an analysis of the impact of these edge effects on the results is a topic of on-going work. Future work may include strategies to minimize these effects, including mirroring of the data across boundaries.

As the Gaussian filter is also a Gaussian in frequency space, it has a smooth cutoff condition in frequency space with standard deviation given by

$$\sigma_{G,f} = \frac{1}{2\pi\sigma_G}, \tag{2.30}$$

where the standard deviation in spatial frequency space is here in units $1/m$. The approximate cutoff frequency can be identified by the point where the filter response is half of its maximum in the power spectrum. This frequency is given by the expression

$$f_c = \sqrt{2\ln(2)}\sigma_{G,f} \tag{2.31}$$

$$f_c = \frac{\sqrt{2\ln(2)}}{2\pi\sigma_G}, \tag{2.32}$$

but this is an approximate cutoff rather than a sharp cut-off. This smoothness in the filter is distinct from the filtering practices that have previously been used to study scale interaction in turbulence, which are often defined using spectral filters with sharp cutoffs (Mathis, Hutchins, and Marusic, 2009; Ganapathisubramani et al., 2012) or top-hat spatial filters with sharp spatial cutoffs (Chung and McKeon, 2010). The smooth cutoff used in this work in both the space and frequency domains has some drawbacks, as it is less clear exactly which spatial frequencies are included in the large scales versus the small scales. However, this drawback is considered to

be a worthwhile trade for the optimally smooth behavior of the filter in the spatial and frequency domains.

To identify the small scales, the remainder from subtracting the filtered data from the original data is used,

$$u_s = u - u_l. \tag{2.33}$$

For multi-dimensional data, the filtering is done along all three dimensions with the same standard deviation in each. The sensitivity of the results to the standard deviation of the filtering method is explored in each relevant chapter.

Conditional averaging overview

Conditional averaging techniques are used in this thesis to probe two distinct relationships: the relationship between large and small velocity scales, and the relationship between the aero-optic measurement and the velocity field. For each relationship of interest, a condition is defined on which the other relevant variables are averaged. Table 2.1 shows the conditions used for conditional averaging in chapters 4 and 5. Four types of conditional averaging are used. The details of each condition will be specified throughout this section.

Name	Condition 1	Condition 2	Condition 3
MP	$\lvert\phi\rvert > 0.5\sigma$		
P_{2D}	$\gamma^* = \arg\max R_{P_{2D}}(\tilde{\gamma})$	$R^*_{P_{2D}}(\gamma^*) > 0.4$	
P_{1D}	$\gamma^* = \arg\max R_{P_{1D}}(\tilde{\gamma})$	$R^*_{P_{1D}}(\gamma^*) > 0.4$	
MP / P_{1D}	$\lvert\phi\rvert > 0.5\sigma$,	$\gamma^* = \arg\max R_{P_{1D}}(\tilde{\gamma})$	$R^*_{P_{1D}}(\gamma^*) > 0.4$

Table 2.1: The conditions for the conditional averaging methods used in this thesis are specified and given short names for reference. The four types of conditions used for averaging are the Malley probe (MP) condition, the 2D projection condition (P_{2D}), the 1D projection condition (P_{1D}) and the combined Malley probe, 1D projection condition (MP / P_{1D}).

Conditional averaging: aero-optics and velocity field

To identify the relationship between the Malley probe measurement and the velocity field, conditional averaging will be used. The condition is an excursion of the Malley probe deflection angle, $|\phi| > 0.5\sigma$, where here σ is the standard deviation of $\phi(t)$. The velocity field is separately averaged for Malley probe deflections of positive and negative sign. A flow quantity q averaged on upstream deflections is given by

$$< q >_{\bar{MP}} = \frac{1}{N} \sum_{t_i} q(x, y, t_i) \qquad \forall t_i \text{ s.t. } \phi(t_i) < -0.5\sigma \tag{2.34}$$

while q averaged on downstream deflections is given by

$$< q >^{+}_{MP} = \frac{1}{N} \sum_{t_i} q(x, y, t_i) \qquad \forall t_i \text{ s.t. } \phi(t_i) > 0.5\sigma. \tag{2.35}$$

A sample algorithm for calculating the conditionally-averaged velocity field for a downstream deflection is provided in the appendix in algorithm 7.

Conditional averaging: large and small scales, condition on streamwise fluctuating field

To study the relationship between the large and small velocity scales, a condition is defined in the fluctuating velocity field and the filtered small-scale velocity field is averaged. Conditional averaging has already been used to great effect to study the interaction of scales by a number of researchers. Some of their findings are highlighted in chapter 1.

In order to condition on the presence and location of large scale flow features, one has to be able to identify large scales in a given instantaneous snapshot of the flow. To accomplish this, a projection method is used here in which instantaneous velocity data is projected onto models for the large scale of interest.

Projection method

The goal of this method is to identify the average of some flow quantity, q, given the presence of a large-scale streamwise velocity structure. This is achieved by averaging the flow quantity only when the projection of the instantaneous streamwise velocity field onto a model of the structure gives a sufficiently good projection. The result that is being sought is therefore (in general)

$$< q >_{P,\tilde{t}} (x, y, z) \equiv \frac{1}{N} \sum_{t_i} q(x, y, z, t_i) \qquad \forall t_i \text{ s.t. } \left(\frac{u(x, y, z, t_i) \cdot \tilde{u}(x, y, z, \tilde{t})}{|u(x, y, z, t_i)||\tilde{u}(x, y, z, \tilde{t})|} \right) > R_{th}, \tag{2.36}$$

where the subscript P indicates that this is a projection-based conditional average, N represents the number of temporal snapshots for which the projection is sufficiently good, $\tilde{u}$ is the model of the large-scale structure, $\tilde{t}$ is one chosen time for which the model is evaluated, and R_{th} is a threshold on the value of the projection coefficient.

One could use equation 2.36 to directly compute the results shown in chapters 4 and 5. However, because of limitations in the amount of data and the field of view, a more complex algorithm is used to arrive at the value described in equation 2.36. In

equation 2.36, the streamwise velocity field is projected onto a model at a fixed time $\tilde{t}$. We can also describe this time through a phase, defined as $\tilde{\gamma} = -\omega\tilde{t}$. Because structures convect through the field of view and because the model chosen in this study convects downstream without deforming, one can use more of the data by repeating the projection procedure at multiple model phases, $\tilde{\gamma}$. By shifting the data back in post-processing such that the phases of the models line up, one arrives at a result that represents the projection one would attain using a single time, $\tilde{t}$, or phase, $\tilde{\gamma}$, of the model, but with improved convergence behavior.

The algorithm used in this thesis also allows for the use of fields of view that are shorter than the length scale of the model $\tilde{u}$. Multiple phases of the model can be stitched together in post-processing to arrive at a final result with an effective field of view that is larger than the original. The algorithm used in this thesis considers phases $\tilde{\gamma} \in \tilde{\Gamma}$ with $\tilde{\Gamma} = [0, 2\pi)$ for the model. An additional condition is added to prevent particular data frames from being used for multiple phases of the data. This condition requires that the value of R is the maximum value of R across the phases considered. Define the maximum of R as $R^* \equiv \max_{\tilde{t}} R$ at a given data time t_i. As mentioned previously, one can carefully average over $\tilde{t}$ to collapse the data onto a single figure, with phase information varying between 0 and 2π. The specifics of this averaging are discussed later in this section and in appendix A. For conciseness, here it will simply be written as a sum over $\tilde{t}$.

$$< q >_P (x, y, z) \equiv \frac{1}{\tilde{n}} \sum_{\tilde{t}} \left(\frac{1}{N} \sum_{t_i} q(x, y, z, t_i) \right. \\ \left. \forall t_i \text{ s.t. } R(\tilde{t}) \equiv \left(\frac{u(x, y, z, t_i) \cdot \tilde{u}(x, y, z, \tilde{t})}{|u(x, y, z, t_i)||\tilde{u}(x, y, z, \tilde{t})|} \right) = R^* > R_{th} \right). \tag{2.37}$$

Note that both conditions are now listed and that $\tilde{n}$ is the number of values of $\tilde{t}$ for which a nonzero number of data frames, t_i, satisfied the conditions.

Depending on specifics of the implementation, which will be described below, the class of flow features on which the data is conditioned changes slightly. The method can either act to condition on the global behavior of a low-pass filtered velocity field, or can condition on the location and existence of one particular length scale in the flow. More detail regarding the procedure used to calculate the value of equation 2.37 is provided below and in appendix A.

Simple sinusoidal example – There is a natural question of whether maximizing the projection coefficient over multiple phases effectively identifies the appropriate phase, $\tilde{\gamma}$, or model time, $\tilde{t}$, that each frame of data should be associated with. To

investigate this, consider a simple system of sinusoids on which this approach can be demonstrated. Define a signal that will be used as the 'data' as $a(\xi) = \sin(\frac{2\pi}{\lambda}\xi + \gamma)$. The model is also defined as a sinusoid, $\tilde{a}(\xi, \tilde{\lambda}, \tilde{\gamma}) = \sin(\frac{2\pi}{\tilde{\lambda}}\xi + \tilde{\gamma})$. The original signal, a is projected onto each modeled signal, with the intention of maximizing the value of R over the considered values of $\tilde{\gamma}$. The projection coefficient is defined as

$$R(\lambda, \tilde{\gamma}) = \frac{a \cdot \tilde{a}}{|a||\tilde{a}|}. \tag{2.38}$$

In this case, maximizing R over $\tilde{\gamma}$ should identify a maximizing modeled phase γ^* that is the same or close to the original phase, γ, of the data. Figure 2.8 demonstrates that if the wavelength of the signal and the model are the same ($\lambda = \tilde{\lambda}$) then depending on whether the phase of the signal is contained in the set of phases considered by the model, $\gamma \in \tilde{\Gamma}$, the method either exactly identifies or closely approximates the phase of the starting sinusoid, such that $\gamma^* = \gamma$ or $\gamma^* \approx \gamma$. This is true even when the length of signal one has available is less than the wavelength of the sinusoid λ (see figure 2.8). This is an important characteristic, as this method will be used on data for which the wavelength of the large scale of interest is two to three times that of the available data window.

Future work includes using a more complex model, such as a resolvent-based model with added noise, to continue to test the projection method's robustness in consistently identifying the appropriate phase of the local large-scale structure.

Implementation with PIV and DNS data

Models – Two classes of model are used for the projection method: 2D models and 1D models. In the case using a 2D model (referred to as the P_{2D} case), streamwise velocity data in the $x-y$ or $z-y$ plane is projected onto a 2D model of the large scale of interest. In this thesis, that model will be derived from a resolvent analysis of the Navier-Stokes equations described earlier in this chapter. A 2D slice of a resolvent mode in either the $x-y$ or $z-y$ plane is used as the model in this case, such that the average is defined for 2D data as

$$< q >_{P_{2D}} (x, y) \equiv \frac{1}{\tilde{n}} \sum_{\tilde{t}} \left(\frac{1}{N} \sum_{t_i} u(x, y, t_i) \forall t_i \text{ s.t. } \left(\frac{u(x, y, t_i) \cdot \tilde{u}(x, y, \tilde{t})}{|u(x, y, t_i)||\tilde{u}(x, y, \tilde{t})|} \right) = R^* > R_{th} \right) \tag{2.39}$$

and in practice, a number of values of $\tilde{t}$ are considered by equivalently changing the phase ($\tilde{\gamma} = -\omega\tilde{t}$) of the model. Figure 2.9 shows a schematic of the projection

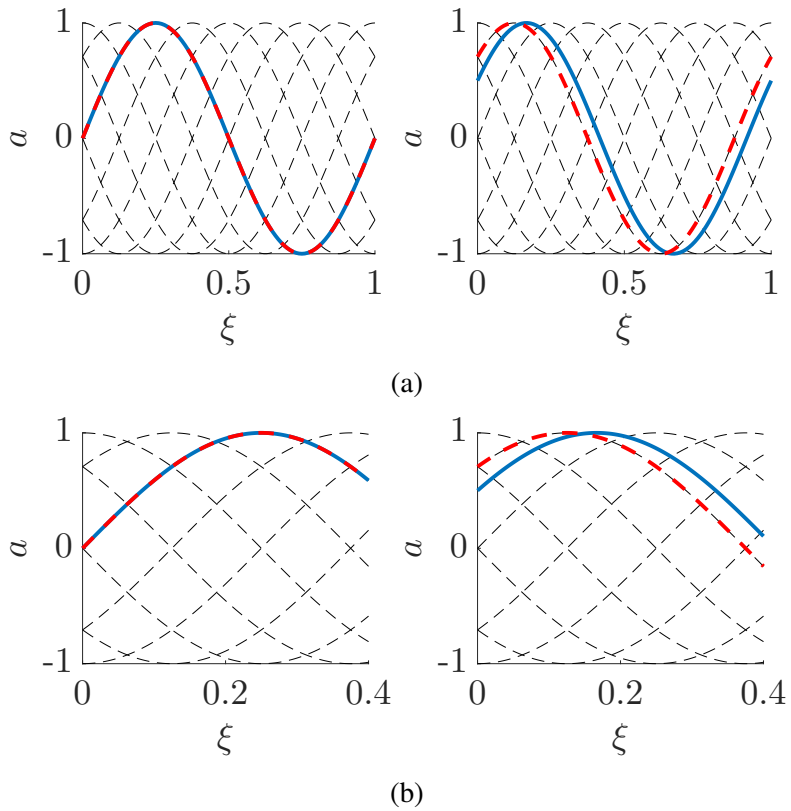

Figure 2.8: The original (blue, solid) and approximated (red, dashed) sinusoidal signals are shown for the case of a projection length $\Lambda/\lambda = 1$ (a) and $\Lambda/\lambda = 0.4$ (b). Black dashed lines show all model signals considered with phases $\tilde{\gamma} \in \tilde{\Gamma} = [0, 2\pi)$ with increments of $\pi/4$. For the original signal, $\gamma \in \Gamma = [0, \pi/6]$ (left, right). When $\gamma \in \tilde{\Gamma}$, the method exactly identifies the phase in both (a) and (b). When $\gamma \notin \tilde{\Gamma}$, the projection method identifies the closest phase considered in both (a) and (b).

process for the P_{2D} case. One frame of PIV data, illustrated using the black box of figure 2.9(a) is projected onto a model, schematically illustrated in figure 2.9(b) at a number of phases. For conciseness, only four phases are shown in figure 2.9, but in general eight to sixteen phases are used. More details on the implementation of the P_{2D} case are given in algorithm 2 in the appendix.

When using the projection model with a 1D model, referred to as the P_{1D} case, streamwise velocity data is extracted along a line in the x or z dimension, depending on the dimension of interest. Data is extracted at the critical layer of the modeled large scale, the height where $c = \bar{U}$ and c is the phase speed of the model of the large scale. In this case, the data will be projected onto a sinusoidal signal with wavelength equal to that of the large scale of interest, such that the average is defined

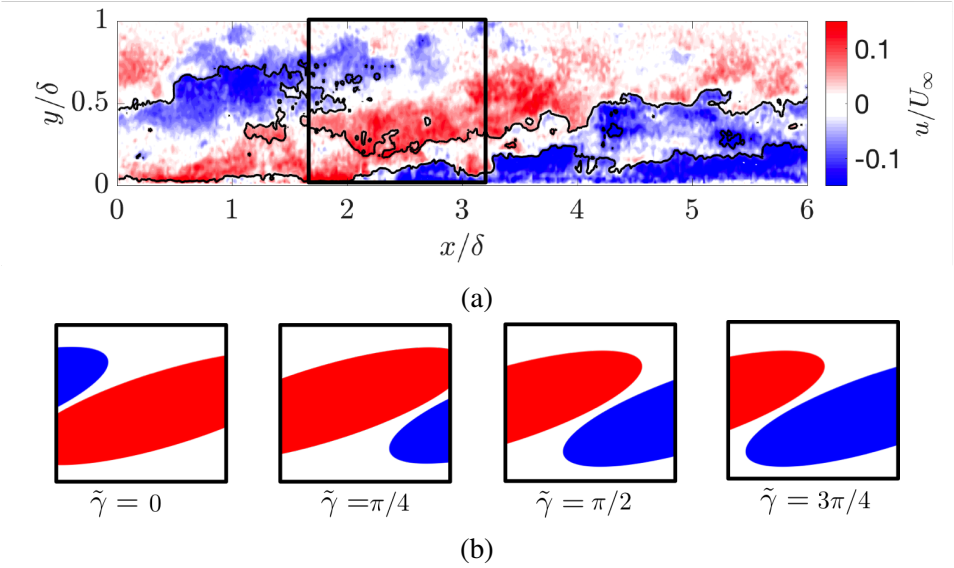

Figure 2.9: Schematic of the P_{2D} projection method is shown. In (a), a visualization of the fluctuating streamwise velocity field is shown for illustration. The black box outlines the approximate size of a single PIV frame. In (b), illustrations of a model of a large-scale structure is shown at four phases $\tilde{\gamma}$. In the P_{2D} projection method, the highlighted data is projected onto the model at each of the phases. The phase at which the projection is best is taken as an estimate of the phase of the structure in the data, γ^*.

for 2D data as

$$< q >_{P_{1D}} (x, y) = \frac{1}{\tilde{n}} \sum_{\tilde{t}} \left(\frac{1}{N} \sum_{t_i} q(x, y, t_i) \forall t_i \text{ s.t. } \left(\frac{u(x, y_c, t_i) \cdot \tilde{u}(x, y_c, \tilde{t})}{|u(x, y_c, t_i)||\tilde{u}(x, y_c, \tilde{t})|} \right) = R^* > R_{th} \right). \tag{2.40}$$

Figure 2.10 illustrates this process for two different data lengths, meant to roughly represent the length of data used for the PIV and DNS data respectively. Data is extracted from one height in the boundary layer, illustrated using a narrow black box, in one frame of PIV or DNS data. In figure 2.10 this is illustrated in the streamwise – wall-normal plane, but can also be executed in the spanwise – wall-normal plane. The extracted data is then projected onto a sinusoidal model at a variety of phases. Four phases are shown in each figure for conciseness, but eight (DNS) to sixteen (PIV) phases are used in the method. More detail on the implementation of the P_{1D} projection method for 2D data is given in algorithm 3 in the appendix.

Models of three distinct coherent structures are implemented: the large-scale motions (LSMs) of the outer boundary layer, the very-large-scale motions (VLSMs) of

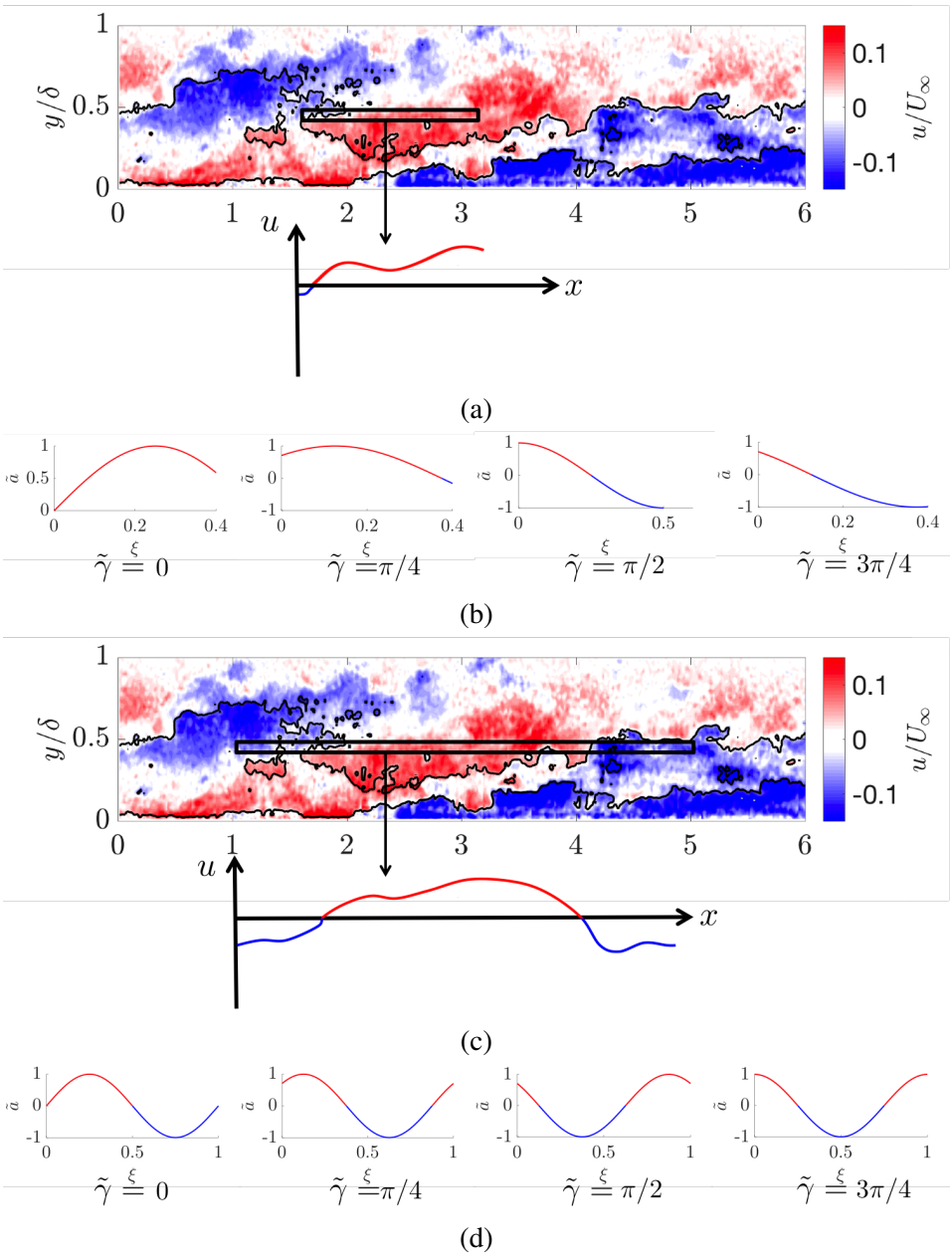

Figure 2.10: Schematic of the P_{1D} projection method is shown. In (a) and (c), visualizations of the fluctuating streamwise velocity field are shown for illustration in the streamwise – wall-normal plane. The black box in each illustrates the extraction of data along a line in the streamwise direction, while the colored line below indicates the extracted data, $u(x)$. Two different extraction lengths are shown, $\Lambda \approx 0.4\tilde{\lambda}$ and $1\tilde{\lambda}$, which approximately represent the extraction lengths used for PIV and DNS for the LSM model. In (b,d), illustrations of the 1D model for a large-scale structure is shown at four phases $\tilde{\gamma}$ for the two data lengths. The extracted data is projected onto the model at each of the phases. The phase at which the projection is best is taken as an estimate of the phase of the structure in the data, γ^*.

the logarithmic layer, and the near-wall streaks (NWSs) of the inner region. Each has its own streamwise and spanwise wavlength as well as its own phase velocity. The details of these models are given in chapter 4.

Handling of 3D data – For the DNS, both $x-y$ and $z-y$ conditional averaging will be performed. For the $x-y$ plane conditional averaging, the 1D projection method will be implemented along the x dimension of the field of view at every spanwise point in the domain, z. Each spanwise point is conditioned and averaged separately, as if it were an independent realization. The reverse practice is used for the $z-y$ planes. At every x point in the field of view, the projection method is applied to the data along the z dimension. More detail on the implementation of the P_{1D} projection method for 3D data is given in algorithm 5 in the appendix. A projection method that simultaneously accounts for streamwise and spanwise phase is a topic of current and future work.

Projection length – The length of signal available in physical space is a function of the data type being used: shorter windows are available in the PIV data than in the DNS data. In addition, the relative size of signal length versus the wavelength of interest is a function of the scale being considered. Considering both of these effects, the projection length, Λ, is shown relative to the wavelength of the model used in each conditional averaging case in table 2.2.

Data type	Spatial plane	Model	$\Lambda/\tilde{\lambda}$
PIV	$x-y$	LSM	0.4
DNS	$x-y$	LSM	1
DNS	$z-y$	LSM	2
DNS	$x-y$	VLSM	0.7
DNS	$z-y$	VLSM	2
DNS	$x-y$	NWS	2
DNS	$z-y$	NWS	20

Table 2.2: Projection length Λ used for a variety of models used in chapters 4 and 5, normalized by the model's streamwise wavelength, $\tilde{\lambda}$.

Having a short field of view does not prohibit the model from approximating the local phase of the large scale, but it does lead to difficulty distinguishing between different length scales. This can be illustrated using the sinusoidal system with a model wavelength, $\tilde{\lambda}$, that is not equal to the signal wavelength, λ. The maximum value of the projection coefficient, R, maximized over $\tilde{\gamma}$ for varying λ is shown in figure 2.11.

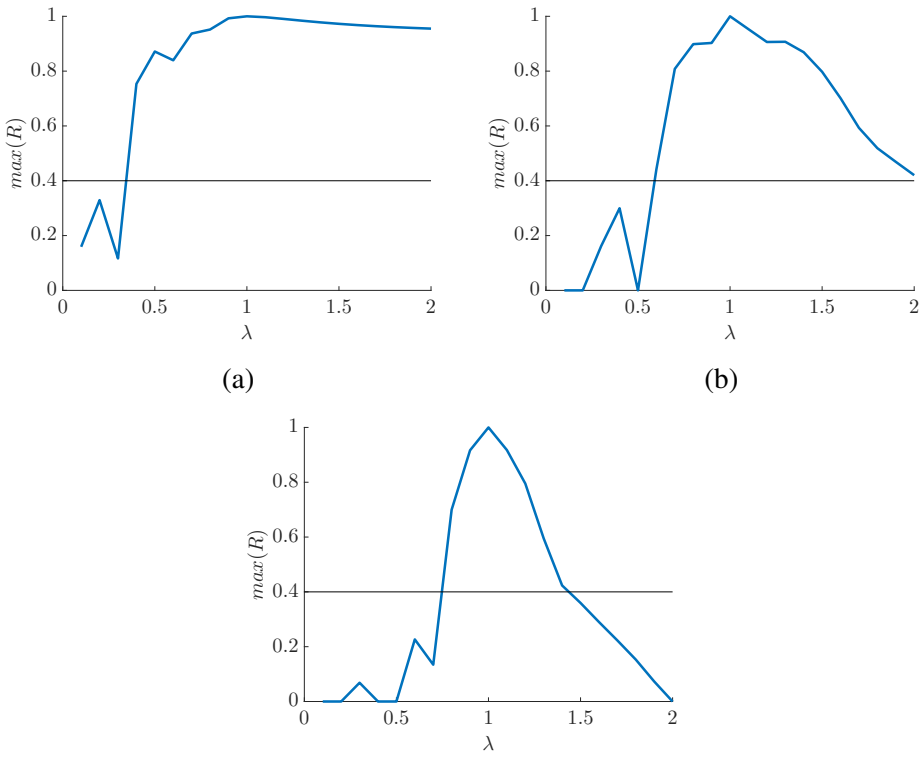

Figure 2.11: Maximum projection coefficient, R^*, shown for a variety of signal wavelengths λ assuming a constant model wavelength of $\tilde{\lambda} = 1$. The projection length $\Lambda/\tilde{\lambda}$ is 0.4 (a), 1 (b), and 2 (c). The black isocontour represents the threshold value $R_{th} = 0.4$.

Figure 2.11 demonstrates a difference in interpretation of the method for short projection lengths than for long projection lengths. For short projection lengths, figure 2.11(a) suggests that one of the functions of the projection method is to act as a long-pass filter on the scales that can be used to average. By implementing a threshold above which the signal is accepted (0.4 in this case), one cuts off averaging on the position of any scales smaller than $0.4\tilde{\lambda}$. As one increases the projection lengths, the method is observed to act as a band-pass filter, preventing the averaging on the position of scales smaller than about $0.75\tilde{\lambda}$ and $1.5\tilde{\lambda}$ for the largest signal length considered in the simple sinusoid system here, $2\tilde{\lambda}$. Thus the method offers slightly different interpretations depending on the amount of data available to project over.

In the implementation of this approach on real data, the wavelength of the model is deduced from the most energetic scales in the streamwise energy spectrum of the flow in question, which is dominated by isolated bands of energetic structures at

different heights from the wall. This is done to maximize the similarity between the model wavelength and the wavelength of the structure of interest on average. Thus, in the current implementation there is an incoming assumption that there is a specific large scale that is dominant in the region of the flow of interest.

Increasing projection lengths are helpful for distinguishing length scales, but can be problematic in boundary layers, where relevant flow parameters including the boundary layer thickness can vary significantly if one requires 2λ for a healthy projection, as that can be up to 12δ depending on the structure. Other approaches to improve the ability of the method to distinguish between large scales are being explored, including the implementation of a Fourier transform to approximate the locally dominant wavelength in fairly short windows of data, and the use of models $\tilde{u}$ that consider a range of both wavelengths and phases with the maximum of R identified over both variables.

Effect of mismatched wavelength on identified phase – If the assumed wavelength is incorrect, the method still identifies the best approximation of the location of the signal, as shown in figure 2.12, where the wavelength of the signal of interest is varied and the modeled wavelength is held fixed. The projection method is seen to identify the closest approximation to the local position of the signal in both the 1λ and 0.4λ signal length cases.

The method will therefore average together regions of the flow in which the fluctuating amplitude of the large-scale velocity field varies smoothly with approximately the variation specified by the model. This will be shown to lead to smooth variation in the averaged fluctuating ($< u >$) and laboratory-frame ($< u > +\bar{U}$) large-scale velocity fields, allowing one to explore the behavior of other flow phenomena about such smooth variations in the large-scale flow.

However, the ability of the model to identify the best approximation of the instantaneous position is not equivalent to identifying the true phase γ. Consider the simplified sinusoidal system. The difference between the true and modeled wavelengths, λ and $\tilde{\lambda}$, leads to a difference between the phase that best estimates the location of the structure, γ^*, and the original phase of the signal, γ. To illustrate this, the modeled signal that has the phase γ is highlighted in figure 2.12(a) in green, and is observed to be less accurate in capturing the physical location of the signal than the model with γ^*, shown in red.

Because of this distinction between the phase that best estimates the instantaneous

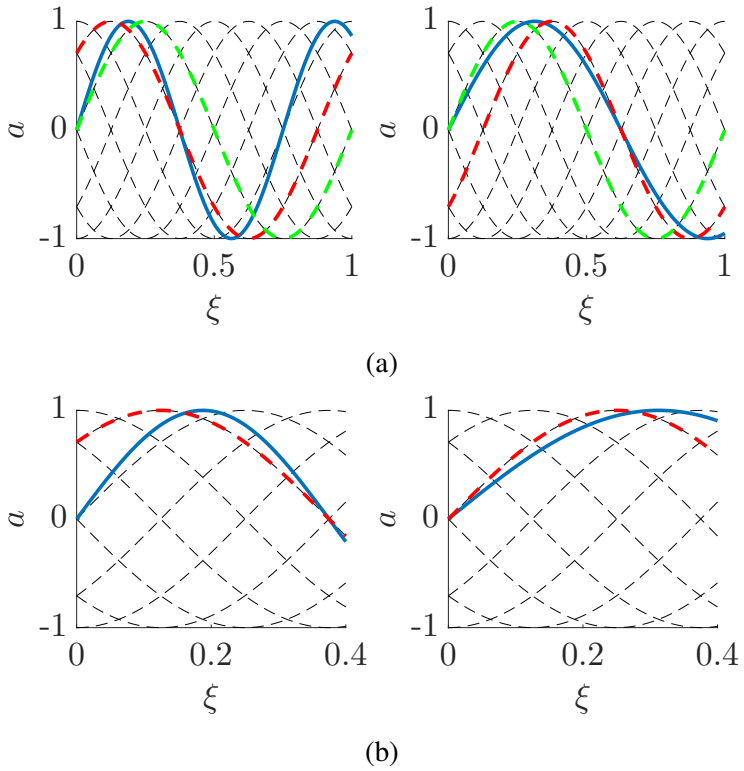

Figure 2.12: The original (blue, solid) and approximated (red, dashed) sinusoidal signals are shown for projection lengths $\Lambda/\tilde{\lambda} = 1$ (a) and 0.4 (b). Black dashed lines show all model signals considered over the phases $\tilde{\gamma} \in \tilde{\Gamma} = [0, 2\pi)$ in increments of $\pi/4$. The phase of the original signal, γ, is held constant at 0, but its wavelength is varied from $\lambda/\tilde{\lambda} = 0.75$ (left) to 1.25(right). The green curves in (a) show the sinusoid $\tilde{a} = \sin(\tilde{\lambda}x + \gamma)$, representing the modeled signal with the exact phase as the original signal.

location γ^* and the true phase of the signal γ for signals with mismatched wavelengths, the phases identified by the method, Γ^* may not be uniformly distributed, even for an incoming uniform distribution of $\gamma \in \Gamma$. This is shown in figure 2.13, where the distribution of estimated phases PDF(Γ^*) are shown after the estimation of a signal with a starting phase evenly distributed between 0 and 2π.

The distribution of estimated phases is essentially uniform for the case where the wavelength of the model matches that of the signal (figure 2.13a), but in the case where the true signal is of a shorter wavelength than the model (figure 2.13b), or when the true signal has a longer wavelength than the model (figure 2.13c), the distribution PDF(Γ^*) is biased. For cases where $\lambda/\tilde{\lambda} < 0.8$, phases of $\pi/2$ and $3\pi/2$ are more common, while for cases where $\lambda/\tilde{\lambda} > 1.2$, phases of 0 and π are more common.

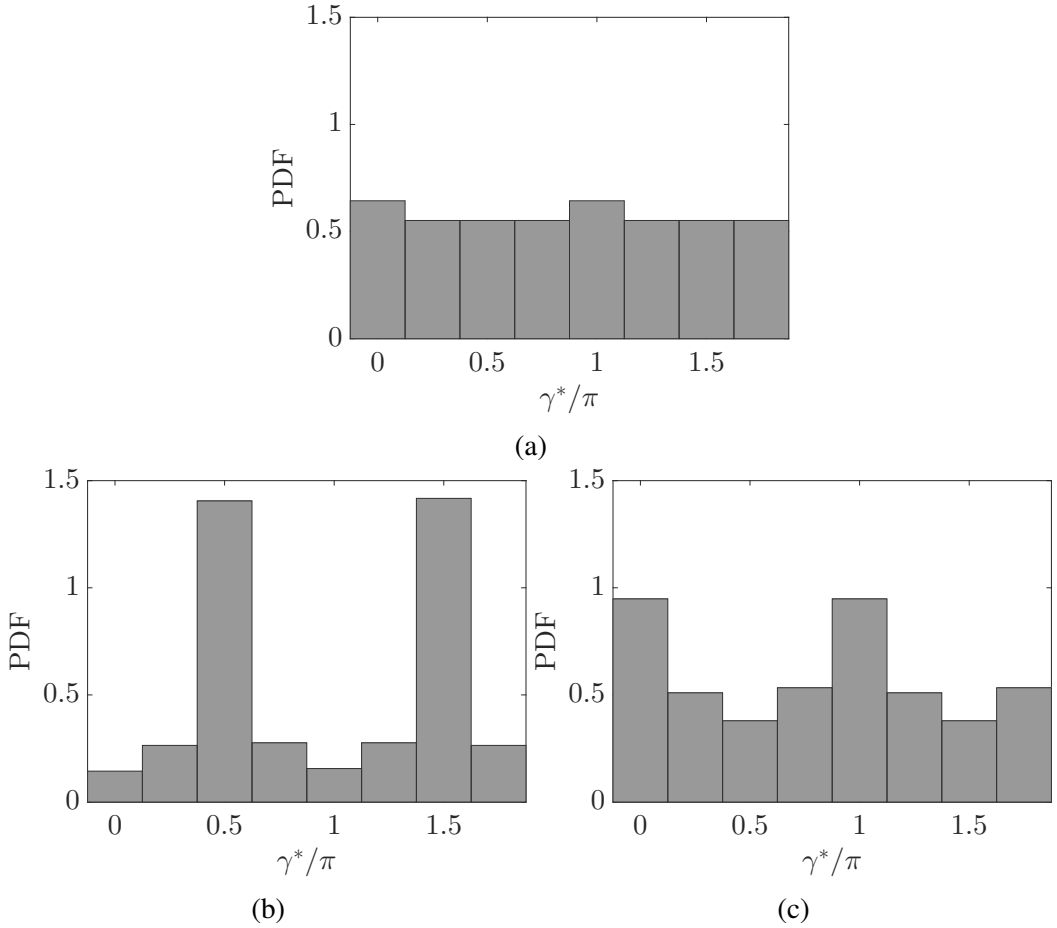

Figure 2.13: The probability density function of estimated phases Γ^* is shown when the modeled and true wavelengths of the signal are the same (a), over all cases where $\lambda/\tilde{\lambda} = 0.1 : 0.1 : 0.8$ (b), and over cases with $\lambda/\tilde{\lambda} = 1.2 : 0.1 : 2.0$ (c). Each case has a projection length of $\Lambda = 1\tilde{\lambda}$, though the observed behavior is observed to persist across differing values of Λ.

This observation may provide a way to evaluate the similarity between estimated wavelength and the modeled wavelength. If the distribution of the experimentally identified phases is skewed towards one of the behaviors observed in figure 2.13(b,c), this could indicate that either smaller or longer average wavelengths are present in the data than are being modeled.

Averaging based upon the projection condition

In general, when averaging on a condition, one ends up with an averaged result for each condition considered. For the P_{2D} and P_{1D} methods (see table 2.1 for complete list of conditions), this would yield a distinct 2D averaged velocity field for each phase $\gamma^* \in \Gamma^*$, which in practice is equivalently $\gamma^* \in \tilde{\Gamma}$, decreasing the

convergence of behavior as one increases the resolution of phases considered in $\tilde{\Gamma}$. However, because the P_{2D} and P_{1D} conditional averaging methods are essentially phase averages, each averaged result should contain the same data shifted by the phase γ^*. This allows for a more efficient averaging process, in which the data is broken up into phase bins based upon the assumed wavelength and approximated phase of the large scale. All of the data is then able to be averaged into a single image, composed of panels associated with each phase bin. A schematic of this averaging process is shown in figure 2.14. This means that the final averaged result is predetermined to appear periodic with the assumed wavelength of the model. The interest will not be in the periodicity of the result, but rather the variation of behavior across the phase of the large scale.

Figure 2.14 illustrates the process through which data is extracted to phase average. The data is broken up into phase bins: one such phase bin is shown as a black box highlighting a particular portion of each of the models, which are shown at a variety of starting phases $\tilde{\gamma}$. The data associated with each black box is averaged together because they identify the same phase range of the large scale. This is done over eight (DNS) or sixteen (PIV) phase bins. If one has a data window that is at least $1\tilde{\lambda}$ long, data from frames associated with every phase γ^* will contribute to every panel in the final averaged figures. At the end of this process, one has one image that is the same length as $\tilde{\lambda}$ that is composed of panels associated with each phase bin, illustrated in figure 2.14(b). More detail on the implementation of this method is provided in algorithms 4 and 6 for 2D and 3D data respectively.

Conditional averaging: scale interaction and aero-optics

It will also be of interest to study the interaction of the two relationships described in this section: the relationship between large and small velocity scales and the relationship between the aero-optic signal and the velocity field. By averaging on both sets of conditions already described, one can identify how scale interaction affects the scalar field and the aero-optic distortion. In that case, a paneled averaging method is used to consolidate the phase information of the large scale, and the location of the Malley probe relative to the velocity field is centered within each

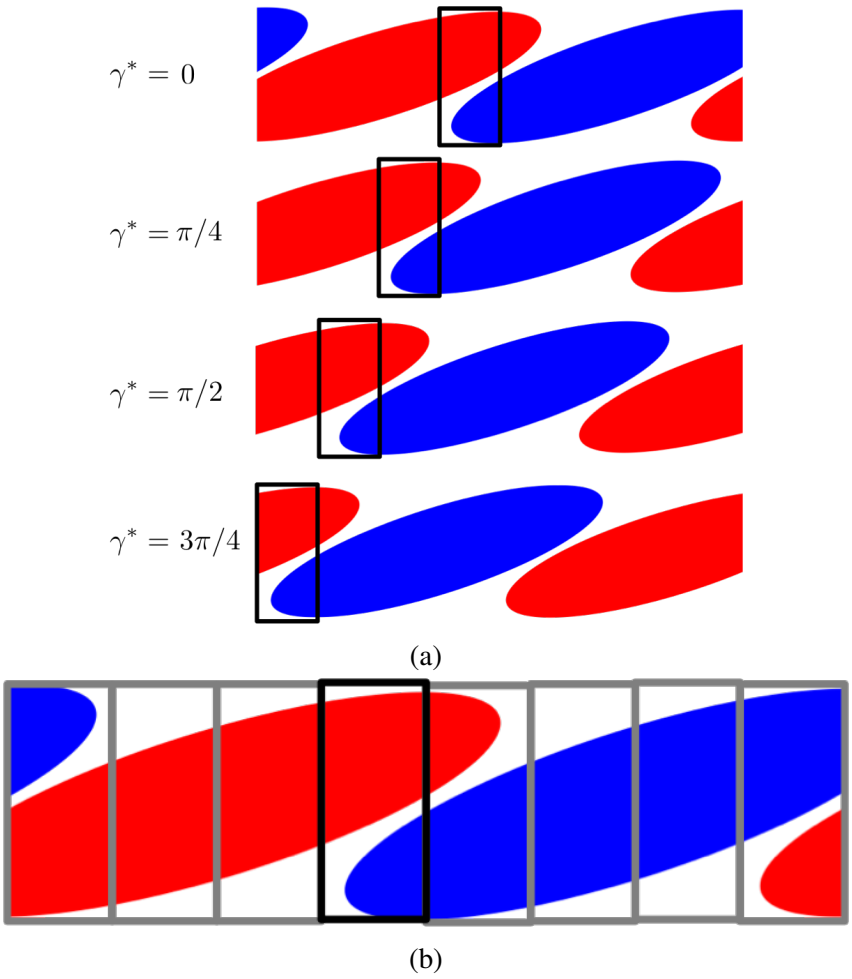

Figure 2.14: Schematic showing the averaging of phase bins after application of the P_{2D} or P_{1D} projection method. In (a), each group of data, which has been grouped by their starting phase, γ^*, is broken up into bins; one such bin is highlighted in black in each of the four phase groups shown. The data of each bin is then averaged together, leading to a single figure composed of panels of each bin (b).

panel. This averaging process can be generally represented as

$$< q >_{MP/P}(x,y,z) \equiv \frac{1}{\tilde{n}} \sum_{\tilde{t}} \left(\frac{1}{N} \sum_{t_i} q(x,y,z,t_i) \right.$$
$$\left. \forall t \text{ s.t. } |\phi(t_i)| > 0.5\sigma \text{ and } \left(\frac{u(x,y,z,t_i) \cdot \tilde{u}(x,y,z,\tilde{t})}{|u(x,y,z,t_i)||\tilde{u}(x,y,z,\tilde{t})|} \right) = R^* > R_{th} \right). \tag{2.41}$$

Within this thesis, the 2D P_{1D} method is used to evaluate this conditional average, referred to as the MP / P_{1D} method. The averaging conditions are listed in table 2.1. More detail on the implementation of this method is provided in algorithm 8 in the appendix.

Chapter 3

COHERENT STRUCTURES

While the description of coherent structures has been a focus of many for decades, we focus here on the description and modeling of specific energetic features of the streamwise velocity field. The scales in question are those identified as energetic in the streamwise energy spectrum: the near-wall streaks of the inner region, the very-large-scale motions or superstructures of the logarithmic layer, and the large-scale motions of the outer region. While these features cover a wide range of scales, each will be considered as a 'large-scale structure' in its particular region of the flow.

This work uses a model for the wall-normal coherence of each structure to connect the spectral representation to the structural representation. A traveling wave is used as the basis for the model, consistent with spectral representations, and is shown to capture experimentally observable structural features both visually and in instantaneous streamwise velocity histograms. The model is compared to instantaneous velocity data from PIV measurements of a turbulent boundary layer. Analytic developments are used to clarify how the model, which is derived in the fluctuating velocity field, relative to a temporal mean, reproduces asymmetric structural features and UMZ characteristics in the laboratory-frame velocity field, in which the mean is included.[1]

3.1 Data visualization

The velocity field in the streamwise – wall-normal plane was measured in the wind tunnel and PIV technique described in chapter 2. For visualization, the PIV data was extended beyond the experimental field of view to allow for the study of the scales of interest. Following the work of (Zaman and Hussain, 1981), a fixed convection velocity was used to 'convect' the PIV snapshots. Zaman and Hussain (1981) noted that, in the case of an isolated coherent structure in a turbulent flow, convecting the full shear flow with a single convection velocity equal to the structure's centerline velocity maintained the closest approximation of the later shape of the structure. The data is not fully time-resolved, so a mixed spatial - temporal visualization technique is used. Each frame is convected with a convection velocity of $0.8U_\infty$, corresponding

[1] The analysis of the large scale motions described in this chapter has been published as part of Saxton-Fox and McKeon (2017a).

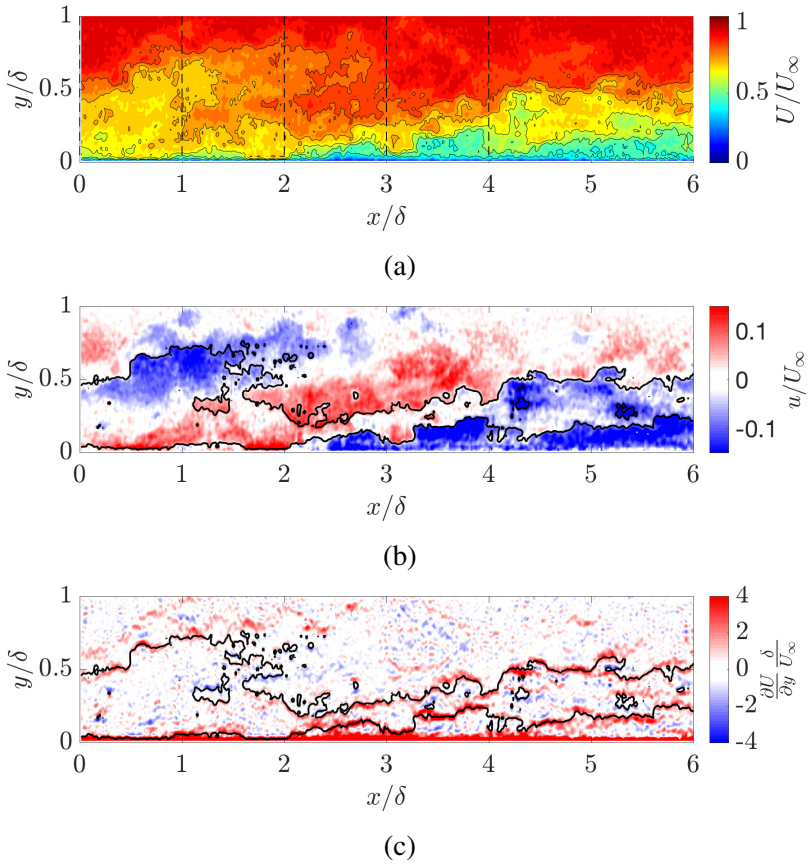

Figure 3.1: A visualization of the instantaneous streamwise velocity field is shown from PIV data in the wall-normal – streamwise plane. Contours of the velocity field in the laboratory frame are shown in (a) at the values $U/U_\infty = 0 : 0.05 : 1$ with every other isocontour outlined in black for visual clarity. Two isocontours of the laboratory-frame velocity field, $U/U_\infty = 0.6, 0.8$ are overlaid on (b) and (c) to illustrate the relationship between panels. Contours of the fluctuating velocity field are shown in (b) at the values $u/U_\infty = -0.15 : 0.01 : 0.15$ in the wall-normal – streamwise plane. The wall-normal derivative of the laboratory-frame velocity field is shown in (c) at values of $\frac{\partial U}{\partial y}\frac{\delta}{U_\infty} = -4 : 0.4 : 4$. Flow moves from left to right.

to the approximate speed of large scale motions in the outer boundary layer (Brown and Thomas, 1977; Cantwell, 1981). A small window of spatial data (0.2δ) in the center of each PIV frame is stitched together to create a large visualization. Figure 3.1 shows the extended visualization of the instantaneous streamwise velocity and its wall-normal derivative. The features at various regions of the flow will have distinct convection velocities, and this choice of velocity will most accurately represent the spatial scale in the outer region of the flow. Nearer to the wall, the structure will appear more elongated than its true size.

3.2 Models of coherent structures

The resolvent analysis described in chapter 2 was used to generate models of three structures: large scale motions (LSMs), very-large-scale motions (VLSMs), and near wall streaks (NWSs). Due to the interest in structures near the wall (VLSMs and NWSs), the mean velocity profile of the DNS data of Wu et al. (2017) was used in the formulation of the resolvent. In section 2, the modeling framework was built around a triple decomposition, where a single scale was of interest and the rest was considered a fluctuation: $\boldsymbol{U}(x,y,z,t) = \bar{\boldsymbol{U}}(x,y) + \tilde{\boldsymbol{u}}(x,y,z,t) + \boldsymbol{u'}(x,y,z,t)$. In this section, three distinct scales are considered. This leads to a quintuple decomposition: $\boldsymbol{U}(x,y,z,t) = \bar{\boldsymbol{U}}(x,y) + \tilde{\boldsymbol{u}}_{LSM}(x,y,z,t) + \tilde{\boldsymbol{u}}_{VLSM}(x,y,z,t) + \tilde{\boldsymbol{u}}_{NWS}(x,y,z,t) + \boldsymbol{u'}(x,y,z,t)$. As with the triple decomposition described in chapter 2, the single scales, $\tilde{u}_{LSM}, \tilde{u}_{VLSM}$, and $\tilde{u}_{NWS}$, are taken as representative of distinct classes of energetic structures. The use of representative models allows for a very-reduced-order representation of realistic turbulent behaviors. In a fully-turbulent flow, slight deviation would be expected about the modeled forms of each of the scales of interest.

The quintuple decomposition can be expanded to account for an assumed periodicity of the modes in the streamwise, spanwise, and temporal variables, as described in chapter 2. For the expanded representation in equation 3.3, subscripts L, V, and N will be used in lieu of LSM, $VLSM$, and NWS for the spatial wavenumbers and the temporal frequency for conciseness.

$$\begin{aligned} U(x,y,z,t) = \bar{U}(x,y) \\ &+\mathrm{Re}\Big[\hat{u}_{LSM}(y)\left(e^{i(k_{x,L}x+k_{z,L}z-\omega_L t)} + e^{i(k_{x,L}x-k_{z,L}z-\omega_L t)}\right) \\ &\quad + \hat{u}_{VLSM}(y)\left(e^{i(k_{x,V}x+k_{z,V}z-\omega_V t)} + e^{i(k_{x,V}x-k_{z,V}z+\omega_V t)}\right) \\ &\quad + \hat{u}_{NWS}(y)\left(e^{i(k_{x,N}x+k_{z,N}z-\omega_N t)} + e^{i(k_{x,N}x-k_{z,N}z+\omega_N t)}\right)\Big] \\ &+u'(x,y,z,t). \end{aligned} \tag{3.1}$$

Re indicates real part and each $\hat{\boldsymbol{u}}$ is defined from a resolvent analysis of the Navier-Stokes equations, with

$$\hat{\boldsymbol{u}}(y) = \chi\boldsymbol{\psi}(y), \tag{3.2}$$

as discussed in chapter 1.

For convenience, we define a phase, $\gamma \equiv -\omega t$, such that this decomposition can be written as

$$\begin{aligned} U(x,y,z,t) = \bar{U}(x,y) \\ &+\mathrm{Re}\Big[\hat{u}_{LSM}(y)\left(e^{i(k_{x,L}x+k_{z,L}z+\gamma_L)} + e^{i(k_{x,L}x-k_{z,L}z+\gamma_L)}\right) \\ &\quad + \hat{u}_{VLSM}(y)\left(e^{i(k_{x,V}x+k_{z,V}z+\gamma_V)} + e^{i(k_{x,V}x-k_{z,V}z+\gamma_V)}\right) \\ &\quad + \hat{u}_{NWS}(y)\left(e^{i(k_{x,N}x+k_{z,N}z+\gamma_N)} + e^{i(k_{x,N}x-k_{z,N}z+\gamma_N)}\right)\Big] \\ &+u'(x,y,z,t). \end{aligned} \tag{3.3}$$

In this representation, setting γ to a single value is equivalent to choosing a single value of time. Because the different structures have different temporal frequencies, a value of t can be found that allows for three phases γ_{LSM}, γ_{VLSM}, and γ_{NWS}, such that one can choose them independently. Because the phase γ is unchanged by additions of 2π, the system of equations one needs to solve to find the value of t for a given set of γ values is

$$\begin{aligned} -\omega_{LSM}t &= \gamma_{LSM} + 2\pi n_{LSM} \\ -\omega_{VLSM}t &= \gamma_{VLSM} + 2\pi n_{VLSM} \\ -\omega_{NWS}t &= \gamma_{NWS} + 2\pi n_{NWS}. \end{aligned} \tag{3.4}$$

The system of three equations has four unknowns: t, n_{LSM}, n_{VLSM}, and n_{NWS}, indicating that there are infinite solutions for the value of t. Adding more scales will add another variable n such that the number of variables is always one more than the number of equations.

It is more convenient to set the phases of each scale independently than to set a value of t, which has to be set across all scales. The value of γ will be set to match the instantaneous location of structures observed in real turbulent flows.

For each scale, spatial and temporal information (k_x, k_z, ω) were identified from statistical findings in the literature. These scales are relatively well known in the literature, and would be challenging to directly compute from the data used in this study; a lack of temporal resolution in the available data would prevent a clean calculation of the streamwise energy spectrum, for example. The value of χ, however, is not available in the literature, and so is approximated from the present data using filtered, instantaneous data. Other more statistical methods to identify χ are a topic of continuous work in the McKeon group (Moarref et al., 2013; Moarref et al., 2014; McKeon, 2017). The spatial and temporal characteristics of the scales used are highlighted in table 3.1, written as wavelengths and wave speeds, which

are the more common representations in the literature. These values are related to those in equation 3.3 through $k = \frac{2\pi}{\lambda}$ and $\omega = ck_x$.

For the LSMs, the streamwise wavelength was determined from the band of energetic wavelengths associated with LSMs in Monty et al. (2009), the spanwise wavelength was determined from the coherence length of bulges observed by Kovasznay, Kibens, and Blackwelder (1970), and the convection velocity was identified from the observations of Brown and Thomas (1977) and Cantwell (1981). A data-based approach was used to approximate χ. Using the filtering method described in chapter 2 with a standard deviation of 0.5δ, the peak-to-peak amplitude of the large-scale filtered streamwise velocity field in the outer region of figure 3.1 ($y/\delta > 0.2$) was computed. The large-scale streamwise velocity field was defined as

$$u_l(x,y) = \frac{\int_{x_j^*}^{x_f^*}\int_{y_i^*}^{y_f^*} u(x^*,y^*,t_0)\exp\left(-\left(\frac{(x-x^*)^2+(y-y^*)^2}{(2\sigma_G)^2}\right)\right)dx^*dy^*}{\int_{x_j^*}^{x_f^*}\int_{y_i^*}^{y_f^*}\exp\left(-\left(\frac{(x-x^*)^2+(y-y^*)^2}{(2\sigma_G)^2}\right)\right)dx^*dy^*}. \tag{3.5}$$

The value of χ_{LSM} was defined such that the maximum value of the model of the streamwise velocity field, $\hat{u}$, was half of the data's peak-to-peak amplitude.

$$\begin{aligned}\max(\hat{u}_{LSM}) =& \frac{1}{2}\left(\max(u_l(x,y)) - \min(u_l(x,y))\right)\\ & 0 < x/\delta < 4\\ & 0.2 < y/\delta < 1.\end{aligned} \tag{3.6}$$

The maximum and minimum values of u_l were not exactly symmetric about zero. The difference in their absolute values was

$$\epsilon = \left|\frac{|\max(u_l)| - |\min(u_l)|}{|\max(u_l)|}\right| = 17\%. \tag{3.7}$$

This difference may come from an incomplete scale separation from the filtering process leading to a lingering superposition of multiple scales. The value of γ_{LSM} was chosen to approximate the phase of the structure in the outer region of in figure 3.1, for convenience in comparing the model to the data.

The streamwise wavelength of the VLSMs were identified from the energetic bands of the streamwise energy spectrum for boundary layers in Monty et al. (2009), the spanwise coherence was identified from Hutchins et al. (2011), and the convection velocity was identified from Del Alamo and Jimenez (2009) and Hutchins et al. (2011). To identify χ, equation 3.5 was used to define the large-scale streamwise

	λ_x/δ	λ_z/δ	c	χ	γ
LSM	4δ	1δ	$0.8U_\infty$	$0.12U_\infty$	$-\pi/2$
VLSM	6δ	1δ	$0.6U_\infty$	$0.15U_\infty$	π
NWS	1000^+	100^+	10^+	$0.05U_\infty$	0

Table 3.1: The physical parameters used to build representative models of three energetic large scales (large-scale motions, very-large-scale motions, and near-wall streaks) in a turbulent boundary layer. The streamwise and spanwise wavelengths, the phase speed, the amplitude, and the phase to set their instantaneous positions are given for each structure.

velocity field, and the peak-to-peak value near the wall was used to define $\hat{u}_{VLSM}$.

$$\begin{aligned} \max(\hat{u}_{VLSM}) =& \frac{1}{2}\left(\max(u_l(x,y)) - \min(u_l(x,y))\right) \\ & 0 < x/\delta < 6 \\ & 0 < y/\delta < 0.2. \end{aligned} \tag{3.8}$$

The difference in the absolute values of the minimum and maximum of u_l nearer to the wall was less symmetric than far from the wall, with an ϵ defined using equation 3.7, of 65%. This may indicate the superposition of multiple scales that were not distinguished by the filter, and does indicate a difference between the model and the data. The value of γ_{VLSM} was chosen to approximately match the location where the near-wall structure changed sign in figure 3.1, for convenience in comparing the model to the data.

The streamwise and spanwise wavelengths of the NWSs were identified from Kline et al. (1967) and Robinson (1991), and the convection velocity was approximated from Del Alamo and Jimenez (2009) and Hutchins et al. (2011). The relevant values for each structure are shown in table 3.1. The value of χ_{NWS} was more difficult to estimate, as the PIV data was not able to fully resolve the near wall streaks. The value was chosen to approximate the amount of small-scale fluctuation visible near the wall in the under-resolved PIV data. The value of γ_{NWS} was left at 0 because the structures could not be fully resolved by the PIV data.

The streamwise velocity field of the representative model of the LSM, VLSM, and NWS models is shown in figures 3.2 (LSM), 3.3 and 3.4 (VLSM), and 3.5 and 3.6 (NWS). The velocity field relative to the mean (fluctuating, $\tilde{u}$) and including the mean (laboratory frame, $\tilde{U} \equiv \tilde{u} + \bar{U}$) is shown for each structure. In addition, the wall-normal derivative of the laboratory-frame streamwise velocity field is shown for each.

To compare the model and the data, any velocity field that includes the mean is referred to as a laboratory-frame velocity field, while the velocity fields that do not include the mean are referred to as fluctuating velocity fields. This is done with acknowledgement of the distinction between the PIV data, which includes all three scales of interest and the fluctuations that are not coherent with those scales, and the velocity fields of the models, which only include one scale and do not include u'.

In figure 3.2, 3D representations of laboratory-frame (a) and fluctuating (b) streamwise isocontours of the LSM representative model are shown. In figure 3.2(a), bulges are observed in the isocontour, lifting above the mean height of the isocontour, shown in black. In figure 3.2(b), the faster and slower fluctuations are observed to be equally strong and take the form of a traveling wave. In comparing figure 3.2(a) and figure 3.2(b), the slower fluctuations are observed to coincide with the bulges in the laboratory frame isocontour, while the faster fluctuations are observed to correspond to depressions in the height of the laboratory frame isocontour. In figure 3.2(c-g), a wall-normal – streamwise plane is shown for the LSM representative model for the laboratory frame (figure 3.2c) and fluctuating (figure 3.2d) streamwise velocity field. The same relationship between the laboratory-frame and fluctuating velocity fields is apparent as that which was observed in the 3D results. In figure 3.2(c), the wall-normal derivative of the laboratory-frame streamwise velocity field is shown, where strong shear layers are observable along the 'backs' of the bulges, sitting along the isocontour $\tilde{U}_{LSM} = 0.8U_\infty$. Regions of negative shear lie between the positive shear layers, coinciding with the laboratory frame isocontour folding under itself. The shear observed is the sum of the mean shear, $\partial\bar{U}/\partial y$, and the fluctuating shear, $\partial\tilde{u}/\partial y$.

In figure 3.3, the streamwise velocity field of the representative model for the VLSM is shown in the streamwise – wall-normal plane. The VLSM sits nearer to the wall, as its convection velocity is less than that of the LSM. The relationship between the laboratory-frame (figure 3.3a) and fluctuating (figure 3.3b) velocity fields are observed to be consistent with that seen for the LSM: slow fluctuations correspond to an elevation in the laboratory-frame isocontour, while fast fluctuations correspond to a downward protrusion of the isocontour. A shear layer is observed in figure 3.3(c) along the 'back' of the bulge, sitting along the isocontour $\tilde{U}_{LSM} = 0.6U_\infty$. The mean shear nearer to the wall is stronger such that the wall-normal derivative of the laboratory-frame velocity field of the VLSM is asymmetrically positive throughout the field, rather than showing both positive and negative shear as was observed for

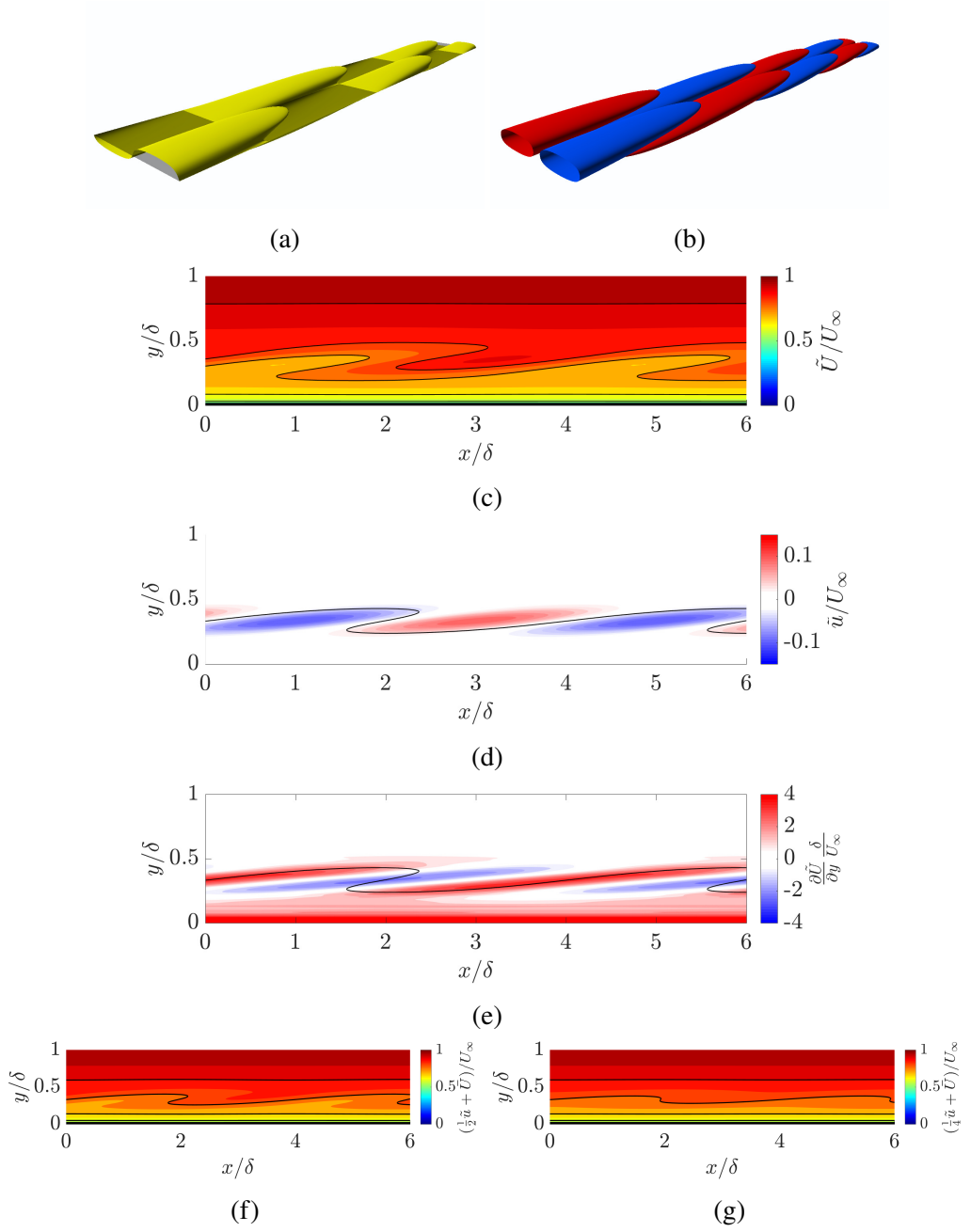

Figure 3.2: The structure of the LSM representative model is shown for the laboratory-frame streamwise velocity field $\tilde{U}$ and fluctuating velocity field $\tilde{u}$. Three-dimensional representations of streamwise velocity isosurfaces are shown in (a) $\tilde{U}_{LSM}/U_\infty = 0.8$ (yellow), $\bar{U}_{LSM}/U_\infty = 0.8$ (black), and (b) $\tilde{u}_{LSM}/U_\infty = 0.03$ (red) and -0.03 (blue). In (c), a wall-normal – streamwise slice of the laboratory-frame velocity field is shown with the contour range $\tilde{U}_{LSM}/U_\infty = 0 : 0.05 : 1$ and every other isocontour outlined in black for visibility. A single isocontour of $\tilde{U}_{LSM}/U_\infty = 0.8$ is overlaid on (d) and (e) to illustrate the relationship between panels. Contours of the fluctuating velocity field are shown in (d) at the values $\tilde{u}_{LSM}/U_\infty = -0.15 : 0.01 : 0.15$, while the wall-normal derivative of $\tilde{U}_{LSM}$ is shown in (e) at the values $\frac{\partial \tilde{U}_{LSM}}{\partial y}\frac{\delta}{U_\infty} = -4 : 0.4 : 4$. The laboratory frame streamwise velocity field (same contour values as c) is shown with the fluctuating amplitude of the LSM representative model halved in (f) and quartered in (g). Flow moves from left to right.

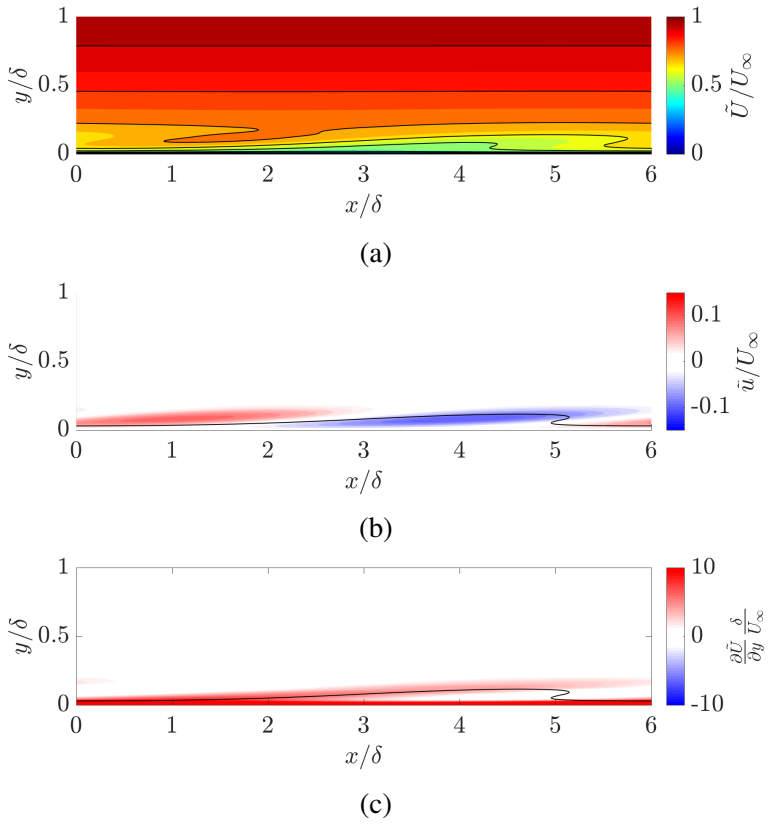

Figure 3.3: The structure of the VLSM representative model is shown for the laboratory frame streamwise velocity field $\tilde{U}_{VLSM}$ (a) and fluctuating velocity field $\tilde{u}_{VLSM}$ (b). The same contour levels are used in (a,b) as those in figure 3.2(c,d). In (c), the wall-normal derivative of $\tilde{U}_{VLSM}$ is shown at the values $\frac{\partial \tilde{U}_{LSM}}{\partial y}\frac{\delta}{U_\infty} = -10 : 0.1 : 10$. A single isocontour of $\tilde{U}_{VLSM}/U_\infty = 0.6$ is overlaid on (b) and (c) to illustrate the relationship between panels. Flow moves from left to right.

the LSM. To see more detail, these plots are shown again with a small wall-normal extent in figure 3.4.

In figure 3.5, the representative model for the NWSs are shown with the same field of view shown for those of the LSMs and VLSMs, to indicate relative scale. Figure 3.6 shows more detail, showing one period of the representative model (all axes have a linear scale). Bulges are again observed in the laboratory frame, with the same relationship with the fluctuating field that was observed in the LSM and VLSM models. Distinct shear layers are no longer visible, but the contours of shear are observed to protrude above slow fluctuations and below fast fluctuations, as the mean shear dominates the fluctuating shear near the wall.

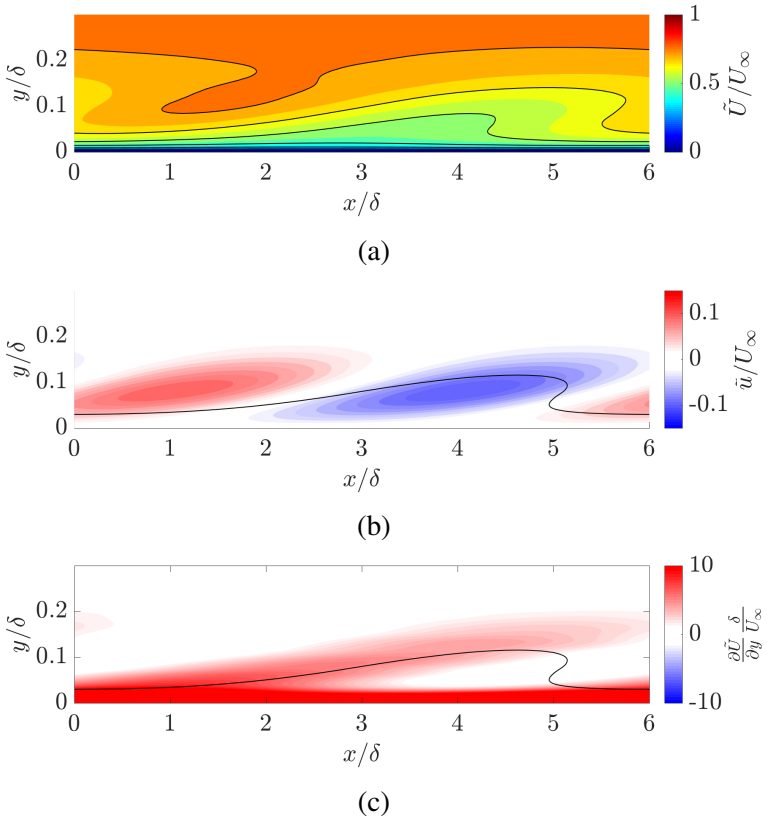

Figure 3.4: The structure of the VLSM representative model is shown for the laboratory frame streamwise velocity field $\tilde{U}_{VLSM}$ (a) and fluctuating velocity field $\tilde{u}_{VLSM}$ (b) in the region $0 < y/\delta < 0.3$. The same contour levels are used as those in figure 3.3. A single isocontour of $\tilde{U}_{VLSM}/U_\infty = 0.6$ is overlaid on (b) and (c) to illustrate the relationship between panels. Flow moves from left to right.

3.3 Results and discussion

Connecting the streamwise energy spectrum to bulges

The streamwise velocity fields of the representative models in the wall-normal – streamwise plane are observed to have common traits across the structures considered. Equally strong positive and negative inclined structures are observed in the fluctuating streamwise velocity field, while bulges are observed in the laboratory-frame velocity field. In the laboratory-frame velocity field, a positive fluctuating structure corresponds to the absence of a visible structure (downward protrusion of isocontours), and the streamwise length scale of the structure, which is constant in the fluctuating field, is observed to change as a function of wall-normal height.

The values of χ were deduced from a single frame of PIV, and are therefore the largest sources of uncertainty in the model. Figure 3.2(f,g) demonstrates the effect on the laboratory-frame velocity field of halving and quartering the fluctuating amplitude of

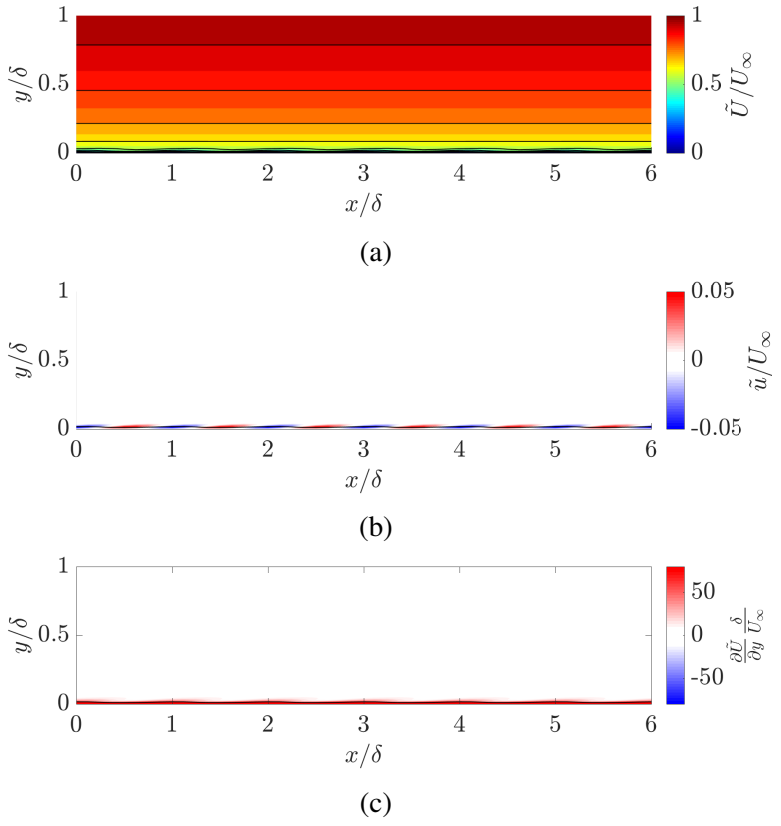

Figure 3.5: The structure of the NWS representative model is shown for the laboratory frame streamwise velocity field $\tilde{U}_{NWS}$ and fluctuating velocity field $\tilde{u}_{NWS}$. Unlike figures 3.2 and 3.3, axes are shown in inner units with a logarithmic wall-normal scale. In (a), a wall-normal – streamwise slice of the laboratory-frame velocity field is shown with the contour range $\tilde{U}_{NWS}/U_\infty = 0 : 0.05 : 1$ and every other isocontour outlined in black for visibility. A single isocontour of $\tilde{U}^+_{NWS} = 10, \tilde{U}_{NWS}/U_\infty = 0.4$ is overlaid on (b) and (c) to illustrate the relationship between panels. Contours of the fluctuating velocity field are shown in (b) at the values $\tilde{u}_{NWS}/U_\infty = -0.05 : 0.001 : 0.05$, while the wall-normal derivative of $\tilde{U}_{NWS}$ is shown in (c) at the values $\frac{\partial \tilde{U}_{NWS}}{\partial y}\frac{\delta}{U_\infty} = -80 : 5 : 80$. Flow moves from left to right.

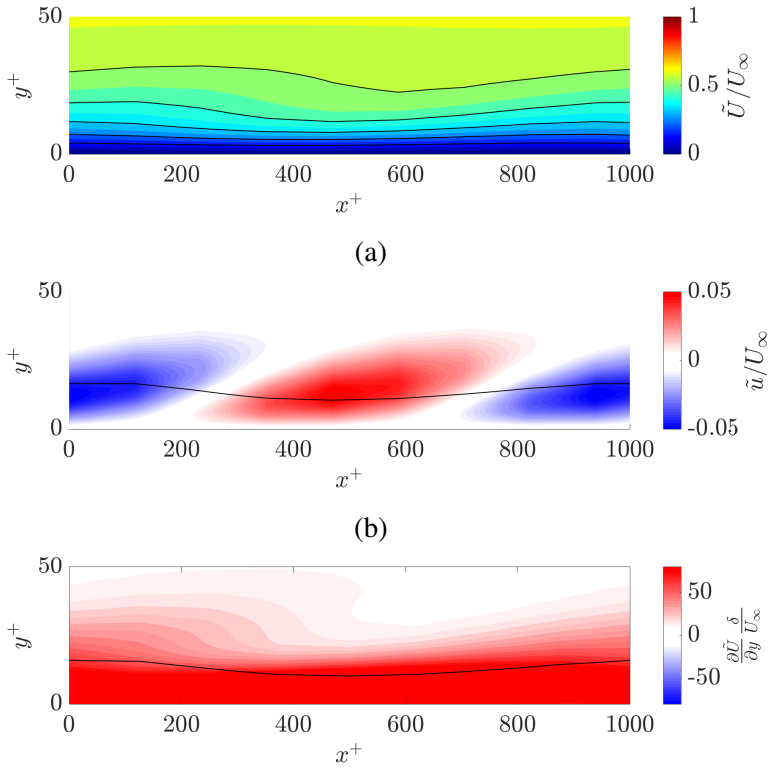

Figure 3.6: The structure of the NWS representative model is shown for the laboratory frame streamwise velocity field $\tilde{U}_{NWS}$ and fluctuating velocity field $\tilde{u}_{NWS}$ in a small field of view. In (a), a wall-normal – streamwise slice of the laboratory-frame velocity field is shown with the contour range $\tilde{U}_{NWS}/U_\infty = 0 : 0.05 : 1$ and every other isocontour outlined in black for visibility. A single isocontour of $\tilde{U}^+_{NWS} = 10, \tilde{U}_{NWS}/U_\infty = 0.4$ is overlaid on (b) and (c) to illustrate the relationship between panels. Contours of the fluctuating velocity field are shown in (b) at the values $\tilde{u}_{NWS}/U_\infty = -0.05 : 0.001 : 0.05$, while the wall-normal derivative of $\tilde{U}_{NWS}$ is shown in (c) at the values $\frac{\partial \tilde{U}_{NWS}}{\partial y}\frac{\delta}{U_\infty} = -80 : 5 : 80$. Flow moves from left to right. Axes are shown with a linear scale.

the LSM representative model relative to its strength in figure 3.2(d). The presence of an asymmetric bulge shape is consistent through these large changes in fluctuating amplitude, but changes in the apparent height, width, and inclination angle of the laboratory-frame velocity structure are observed. The same phenomenon repeats for the VLSM and NWS and is not repeated for conciseness.

In figure 3.7, all three structures are superimposed to show a representative complete 'large scale' velocity field. The superposition of the three structures is observed to lead to a velocity field that shows reasonable agreement with the PIV visualization in figure 3.1 (though the visualization convection velocity was chosen to best represent the outer region, above $y/\delta \approx 0.2$). In particular, large bulges are observed in the outer region of the boundary layer, while smaller bulges are observed near the wall in figure 3.7(a). Shear is observed along the 'backs' of the bulges associated with LSMs, in addition to shear layers nearer to the wall associated with the VLSMs in figure 3.7(c). However, there are a number of differences in the appearance of the model from the instantaneous visualization. The LSM structures appear shorter in the model than the instantaneous structures observed in the instantaneous visualization. The scales that are not coherent with the three modeled structures, u', also play a key role in the PIV data, leading to much more corrugated laboratory frame isocontours and a dimpled appearance of the structures in the fluctuating velocity field in the data than in the model.

The black curves in all previous figures represent the height of laboratory frame streamwise velocity isocontours, $h_U(x, z, t)$, defined as the set of wall-normal locations where the laboratory frame streamwise velocity field is equal to some particular value, $U(x, h_U, z, t) = U^*$. The analytical relationship between a laboratory frame streamwise velocity isocontour and the fluctuating velocity field can be derived to clarify the trends observed in figures 3.1 - 3.7. Define the height of the mean streamwise velocity isocontour, $h_{\bar{U}}(x)$, as the set of wall-normal locations where the mean velocity field is equal to the same value, $\bar{U}(x, h_{\bar{U}}) = U^*$, where x-dependence of the mean is retained for generality in the following derivation. In general, fluctuations relative to a mean appear in laboratory-frame velocity isocontours as differences between h_U and $h_{\bar{U}}$. The relationship between a fluctuating velocity field, $u(x, y, z, t)$, and the change in laboratory frame isocontour height, $\Delta h_U \equiv h_U - h_{\bar{U}}$, can be defined for laboratory-frame velocity fields with monotonic variation in y (equivalently $|\partial u/\partial y| < \partial \bar{U}/\partial y$) by expanding U in a Taylor series about the height $h_{\bar{U}}$.

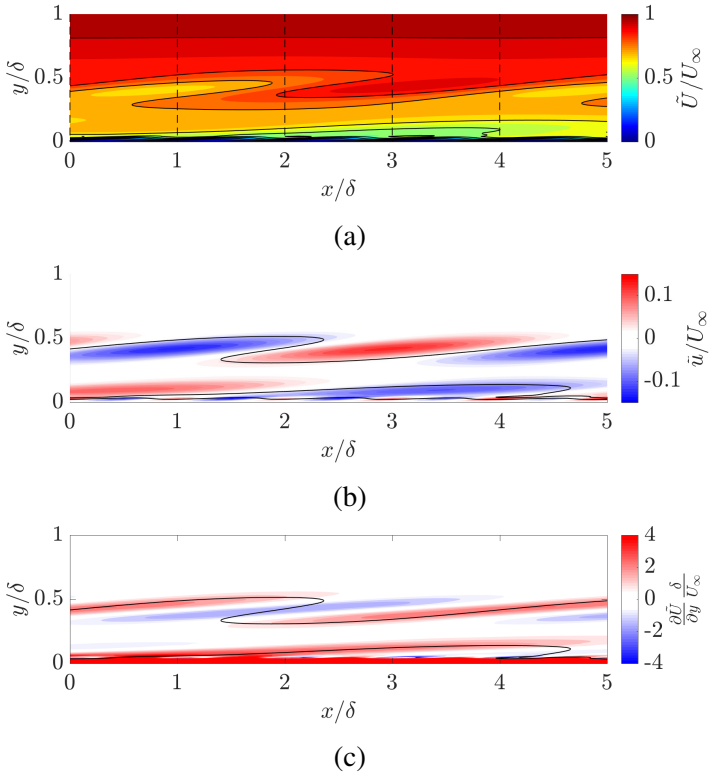

Figure 3.7: The superposition of all three representative models is shown to demonstrate their relative spacing in the height of the boundary layer. The streamwise velocity field is shown in the laboratory frame ($\bar{U} + \tilde{u}_{LSM} + \tilde{u}_{VLSM} + \tilde{u}_{NWS}$) (a) and in the fluctuating field ($\tilde{u}_{LSM} + \tilde{u}_{VLSM} + \tilde{u}_{NWS}$) (b). In (c), the wall-normal gradient of the field in (a) is shown. The phases of the modes are chosen to roughly correspond to those observed in the PIV visualization in figure 3.2. Contour levels are the same as those shown for figure 3.2. In (b,c), two isocontours are shown at values of $\tilde{U}/U_\infty = 0.8$ and $\tilde{U}/U_\infty = 0.6$.

$$\Delta h_U(x,z,t) = h_U(x,z,t) - h_{\bar{U}}(x) \approx -\left[u/\left(\frac{\partial U}{\partial y}\right)\right]_{(x,h_{\bar{U}},z,t)}. \tag{3.9}$$

In a geometry where the mean shear is defined as positive, equation 3.9 demonstrates that a negative velocity fluctuation corresponds to an upward protrusion of the laboratory frame isocontour relative to its position in the mean velocity field, while a positive fluctuation is consistent with the downward protrusion of the isocontour. Though the monotonic condition on U does not hold everywhere in the data or the model, the relationship between the height of laboratory-frame velocity isocontours and the sign of fluctuating velocity structures can still be observed. From equation 3.9, one also sees that the strength of the wall-normal derivative of the laboratory

frame streamwise velocity field or 'shear' field is inversely proportional to the isocontour height change. This relationship coupled with the consistent spatial relationship between the velocity and shear fields leads to gradual increases in isocontour height with x, known as 'ramps', and rapid decreases in isocontour height with x, known as 'cliffs', in the laboratory-frame velocity fields of the model and the data. It also leads to larger bulges in the outer region of the flow than near the wall.

Equation 3.9 sheds light on a fundamental equivalency between symmetry in the fluctuating velocity field and asymmetry in the laboratory-frame velocity field that allows the statistical and structural perspectives to be consistent and representable by the representative models. This equivalency also clarifies the focus on low-speed structures in the structural turbulence community. Fluctuating structures with amplitude less than the mean correspond to visually identifiable bulges in the isocontours of the laboratory frame streamwise velocity field. The fluctuating structures with amplitude larger than the mean have an equally strong relationship with the shape of the laboratory frame isocontours, but their impact (the downward protrusion of isocontours) is less visually identifiable.

Connecting the streamwise energy spectrum to uniform momentum zones

The representative models also reproduce the UMZ behavior observed by (Meinhart and Adrian, 1995) using the instantaneous streamwise velocity histogram technique. In this technique, a discrete approximation of the probability density function of an instantaneous laboratory frame streamwise velocity field is calculated, identifying the most and least common velocity values in the instantaneous field. To calculate the histogram, one divides the total range of observed streamwise velocity values into a set number of equally-spaced bins. U_b^* is defined as the velocity at the center of a given bin, with the range of velocities in the bin given by

$$U_b = \left[U_b^* - \frac{\Delta U}{2n_b}, U_b^* + \frac{\Delta U}{2n_b} \right), \tag{3.10}$$

where $\Delta U = \max(U(x,y,t)) - \min(U(x,y,t))$ is the difference between the maximum and minimum velocity values observed in the data, and n_b is the number of velocity bins. For a given bin, the value plotted in the histogram is

$$m_b = \frac{n_b}{\Delta U \sum_{b=1}^{n_b} m_b} \mathcal{N}\left(U(x,y) \in U_b\right), x \in X, y \in Y, \tag{3.11}$$

where $\mathcal{N}$ represents a count of the number of grid points at which the conditions are satisfied. The value m_b is normalized such that the integral over the final distribution gives a value of one. A restricted spatial range, X, in the streamwise variable is used to identify features of localized structures: if it were not restricted, the result would be equivalent to a histogram of the mean velocity field. The range Y is generally taken as the full height of the boundary layer.

Instantaneous streamwise velocity histograms of turbulent boundary layers have been shown to have discrete minima and maxima, meaning that some bins have substantially larger numbers than others. Thus, some values of velocity are more common than others in a particular region of the flow at an instant in time. These minima and maxima in the flow which have been correlated to the presence of regions of almost constant velocity (uniform momentum zones) bordered by thin regions of rapidly changing velocity (shear layers) (Adrian, Meinhart, and Tomkins, 2000; de Silva, Hutchins, and Marusic, 2016) in the velocity field.

This histogram technique was applied to the experimental data and the superposition of all three representative models over four different streamwise ranges. The dashed lines in figures 3.1(a) and 3.7(a) demarcate the regions of data used for the histograms, though the equivalent spatial data from the appropriate instantaneous snapshot was used for the experimental histograms, rather than the temporally-reconstructed representation shown in figure 3.1(a). Because instantaneous images were used with no convection velocity assumption, the near-wall region of the PIV data and the model could be directly compared in this section. The histograms were calculated using a 1δ range in the streamwise direction and 50 velocity bins, with the free stream masked following the procedure from (de Silva, Hutchins, and Marusic, 2016). The turbulent/non-turbulent interface (TNTI) was identified using a turbulence intensity threshold (Chauhan et al., 2014) with a value of $k_{th} = 0.5$ for the PIV data and $k_{th} = 2$ for the model. These values of k_{th} were chosen such that the mean height of the TNTI, $\bar{Z}/\delta$, was 0.8 for both the PIV and LSM representative model, matching previous studies (Chen and Blackwelder, 1978). The modeled and experimental velocity fields were represented on identical grids for the calculation of the histograms.

Figures 3.8 and 3.9 show the instantaneous streamwise histograms for the PIV data (figures 3.8(a,b) and 3.9(a,b)) and for the modeled velocity field (figures 3.8(c,d) and 3.9(c,d)) for the streamwise ranges $0 < x/\delta < 2$ (figure 3.8) and $2 < x/\delta < 4$ (figure 3.9). At least two distinct maxima are present in each histogram, shown in figures

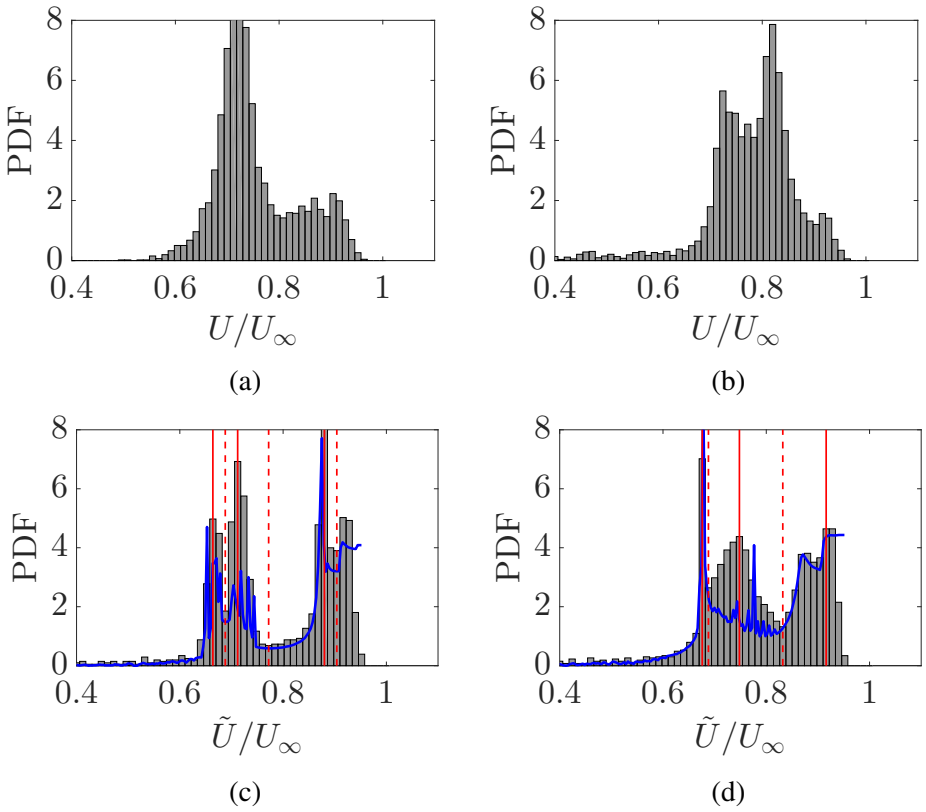

Figure 3.8: Histograms of the laboratory frame streamwise velocity field of instantaneous PIV data (a,b) and the superposition of the three representative models (c,d). Histograms are derived from data in figures 3.1(a) and 3.7(c) in the streamwise ranges: (a,c) $0 < x/\delta < 1$, (b,d) $1 < x/\delta < 2$. Solid red lines indicate local maxima in the histograms, while dashed red lines indicate local minima. The blue curves represent an estimate of the probability density function derived from the wall-normal derivative of the streamwise velocity field (equation 3.14).

3.8 and 3.9, indicating uniform momentum zone behavior in the laboratory-frame streamwise velocity field of the data and the model (Adrian, Meinhart, and Tomkins, 2000).

Good agreement is seen in the location of local maxima at $U/U_\infty \approx 0.7$ and $U/U_\infty \approx 0.9$ and the location of a local minimum at $U/U_\infty \approx 0.8$ in all panels of figures 3.8 and 3.9 but figure 3.8(b,d). Less favorable agreement is seen in the amplitude of the peaks. In figure 3.8(a,c) reasonable agreement is seen for the amplitude of one of the peaks ($U/U_\infty \approx 0.7$), while poor agreement is seen for the amplitude of the other. In figure 3.8(b,d), reduced peaks are observed in both the PIV and model, but little quantitative agreement is seen.

In figure 3.9(a,c) and figure 3.9(b,d), the amplitudes of both peaks show some

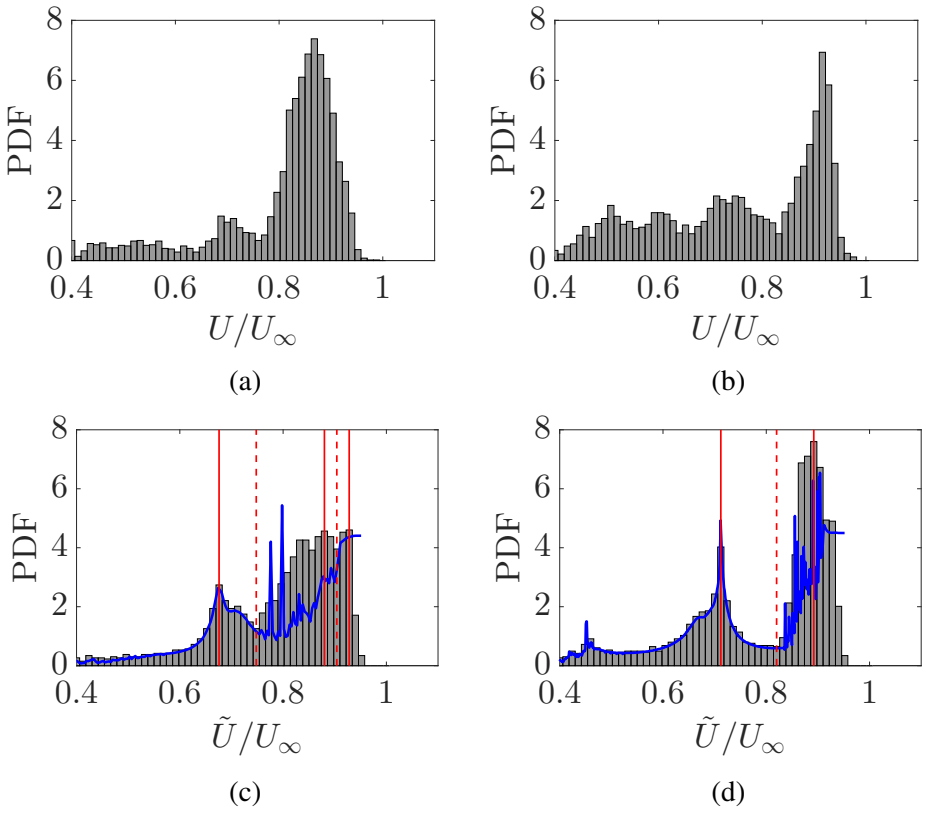

Figure 3.9: Histograms of the laboratory frame streamwise velocity field of instantaneous PIV data (a,b) and the superposition of the three representative models (c,d). Histograms are derived from data in figures 3.1(a) and 3.7(c) in the streamwise ranges: (a,c) $2 < x/\delta < 3$, (b,d) $3 < x/\delta < 4$. Solid red lines indicate local maxima in the histograms, while dashed red lines indicate local minima. The blue curves represent an estimate of the probability density function derived from the wall-normal derivative of the streamwise velocity field (equation 3.14).

agreement. In addition, activity is observed at low streamwise velocity values in both the PIV data and the model in figure 3.9, which is associated with the presence of a VLSM with locally low-momentum. Though additional work is needed to achieve quantitative prediction, figures 3.8 and 3.9 demonstrate that periodic, symmetric structures in the fluctuating velocity field can yield physically realistic uniform momentum zone behavior in the laboratory-frame velocity field, allowing UMZs and the spectral description of coherent structures to be compatible.

Analytical probability density function of instantaneous streamwise velocity

Previous interpretations of the instantaneous streamwise velocity histograms have argued that maxima in the histograms indicate modal velocities of UMZs, while minima indicate shear layers (Adrian, Meinhart, and Tomkins, 2000). A derivation

of the exact probability density function for a streamwise velocity profile clarifies this relationship and identifies a direct relationship between the instantaneous streamwise velocity histogram and the shear field.

Consider a laboratory frame streamwise velocity profile at a single streamwise, spanwise, and temporal location: $U(x_0, y, z_0, t_0) \equiv U_0(y) = G(y)$. As a simplification, assume G is one-to-one such that one can write down the inverse relationship $y = G^{-1}(U_0)$ (this is equivalent to the monotonic assumption used in the calculation of the streamwise laboratory-frame isocontour height). Then the probability density function for the instantaneous velocity profile, $U_0(y)$, can be analytically written as

$$f(U_0) = \frac{d}{dU_0}\left(\int_{-\infty}^{G^{-1}(U_0)} \phi(y)dy\right), \tag{3.12}$$

where f is the probability density function of U_0 and ϕ is the probability density function of y. For y uniformly distributed between two points y_i and y_f (a uniform grid), one can show that

$$f(U_0) = \frac{c}{\frac{\partial U}{\partial y}\left(x_0, G^{-1}(U_0), z_0, t_0\right)}, \tag{3.13}$$

where $c = \frac{1}{y_f - y_i}$.

Equation 3.13 demonstrates that the probability density function of an instantaneous streamwise velocity profile is the inverse of the local shear with a scaling. This matches the intuitive reasoning of (Adrian, Meinhart, and Tomkins, 2000): maxima in a histogram correspond to low shear events, while minima correspond to high shear events. The inverse function $y = G^{-1}(U_0)$ builds in the idea of locality, requiring that one consider the shear and the velocity at the same point in space. This simplified analysis was performed at a single streamwise and spanwise location because a larger-dimensional analysis complicates the definition of the inverse relationship.

When G is not one-to-one, the relationship highlighted by equation 3.13 retains predictive value. A few modifications are necessary to apply the derived equation to turbulent data, where the magnitude of local shear can be much larger than the mean shear: one must constrain the relationship between the wall-normal coordinate and the streamwise velocity value, the absolute value of shear must be considered rather than its signed value, and, to compare to histograms reported in the literature (Adrian, Meinhart, and Tomkins, 2000; de Silva, Hutchins, and Marusic, 2016) and those shown in figures 3.8 and 3.9, one must approximate the probability density

function over a two-dimensional region of the flow. As an estimate for the 2D probability density function, one can average the probability density function of all measured profiles across a 1δ range in x, consistent with the data range used for the histograms in figures 3.8 and 3.9. Then,

$$f(U_{2D}) \approx \frac{1}{N} \sum_{i=1}^{N} \frac{c}{|\frac{\partial U}{\partial y}\left(x_i, g^{-1}(U_i), z_0, t_0\right)|}, \tag{3.14}$$

where N is the number of streamwise locations considered, U_i is the velocity profile at a given streamwise location x_i, and $y = g^{-1}(U_i)$ is the modified inverse relationship. For the present work, $y = g^{-1}(U_i)$ is defined as the height where the instantaneous velocity profile is closest to the input velocity value. If there is no height where the velocity profile is within 1% of the input velocity value, $f(U_{2D})$ is set to zero. This definition of g^{-1} is found to be a unique mapping in the discrete velocity fields. The result of applying equation 3.14 to the PIV data and the superposition of the representative models is shown in figures 3.8 and 3.9 and is seen to closely match the directly computed histograms, suggesting that the histograms are a measure of local shear in the flow, as intuited by (Adrian, Meinhart, and Tomkins, 2000). The largest discrepancies between the computed histograms and the approximated probability density function are observed at the largest values of the probability density function, where the shear is lowest and the assumption of uniqueness of the velocity field is least valid.

Future work includes studying the predictive abilities of the model, including in capturing the average of three to five uniform momentum zones observed across $Re_\tau = 10^3$ to 10^4 by (de Silva, Hutchins, and Marusic, 2016). The superposition of more modes could also be used to allow for the representation of more complex phenomena, such as the meandering of structures (Sharma and McKeon, 2013) and amplitude modulation of small scales (McKeon, 2017), which could further improve the predictive capabilities.

3.4 Conclusions

Representative models for large-scale motions, very-large-scale motions, and near-wall streaks in wall-bounded turbulent flows were developed, with scale information from the streamwise energy spectrum and wall-normal coherence information from the Navier-Stokes equations. The model was found to naturally capture key structural characteristics of the laboratory-frame velocity field, including bulges in isocontours and distinct minima and maxima in instantaneous streamwise velocity histograms,

indicating uniform momentum zone behavior. The success of this simple model was argued to demonstrate the equivalence of the energetic scales of the energy spectrum and instantaneously observable characteristics of the velocity field.

A key observation towards connecting the statistical and instantaneous descriptions was reconciling characteristics of the fluctuating and laboratory frame streamwise velocity fields in which they were respectively described. Visualizations of the representative models highlighted a nontrivial relationship between instantaneous fluctuating and laboratory-frame velocity fields: symmetry in high- and low- momentum structures and constant streamwise length scales were observed in the fluctuating field while asymmetry between high- and low-momentum structures and varying streamwise length scales were observed in the laboratory frame field. These observations were explained through the development of an analytic expression for the shape of a laboratory frame streamwise velocity isocontour given a fluctuating velocity field. Connecting the statistical description to UMZ behavior required the use of the instantaneous streamwise velocity histogram technique, which has been used to identify UMZ behavior in previous work (Adrian, Meinhart, and Tomkins, 2000; de Silva, Hutchins, and Marusic, 2016). This technique was analyzed by considering the probability density function of a streamwise velocity profile and was shown to be a direct measure of the local shear field.

The success of the representative models supports the use of a traveling wave to understand and model turbulent structures (Sharma and McKeon, 2013). Traveling wave models can act as a bridge between statistics and instantaneous fields: their periodicity allows for a direct connection to spectral descriptions of turbulent statistics, while their wall-normal coherence allows for a direct connection to the instantaneous flow features. Future work will look towards more quantitative prediction, including capturing trends in the number of UMZs with Reynolds number, as well as capturing nonlinear multi-scale interactions, such as hairpin packets.

Chapter 4

STRUCTURE INTERACTION

4.1 Introduction

A key trait of turbulence is the interaction and energy exchange between scales. Here, the modeling insights gained from chapter 3 regarding particular structures are used to examine scale interactions. Interactions are investigated between the large-scale structures described in chapter 3 and 'small scales', defined using a filtering process described in chapter 2. The interactions are studied using a conditional averaging technique that investigates the spatial relationship of the large and small scales. The details of the technique can be found in chapter 2. Velocity data from the PIV measurements undertaken at Caltech and from the DNS database of (Wu et al., 2017) are used. Details on both sets of measurements can be found in chapter 2.[1]

4.2 Visualization of instantaneous scale interaction

The turbulent boundary layer DNS data described in chapter 2 was analyzed to identify the instantaneous spatial organization of large and small scales. Isosurfaces of the unfiltered, fluctuating streamwise velocity field, u, from a single snapshot of DNS of Wu et al. (2017) are shown in figure 4.1. A single isosurface of the laboratory-frame streamwise velocity field U is shown in white. This isocontour corresponds to an estimated instantaneous convection velocity of the local large-scale flow, identified through a correlation between temporal snapshots of the large-scale velocity field. This value was found to be $0.85U_\infty$. This value differs by 6% from the estimated average convection velocity of the LSMs, $0.8U_\infty$, taken from Brown and Thomas (1977) and Cantwell (1981) and used through much of the thesis.

The instantaneous relationship between scales is masked in figure 4.1 by the complexity of the full streamwise velocity; however, a clear spatial organization can be seen after application of the filtering process. To define large and small scales, the Gaussian filter described in chapter 2 was used with a standard deviation of 0.5δ

[1] The visualization results in this chapter were published as part of Rosenberg et al. (2016).

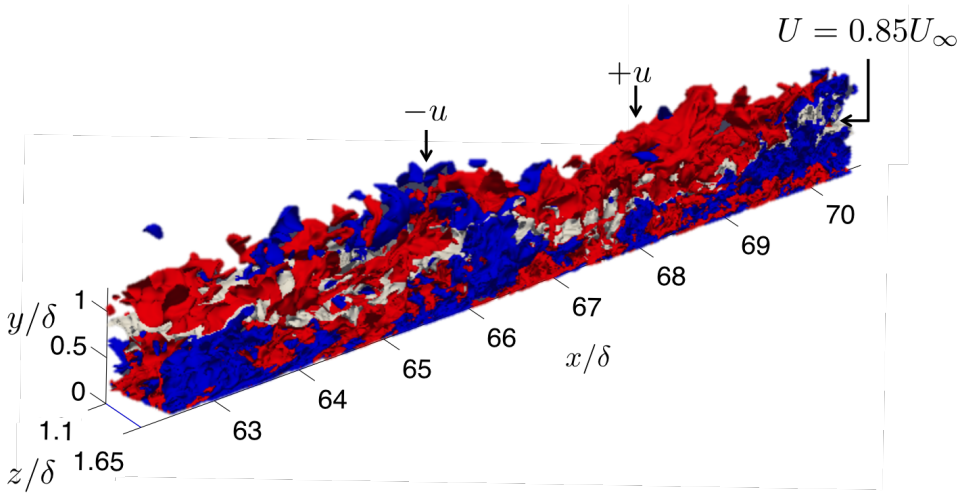

Figure 4.1: Visualization of the streamwise velocity field of DNS of a turbulent boundary layer. Red and blue isosurfaces represent the fluctuating velocity field u at $\pm 0.04U_\infty$. The white isosurface represents a single value of the streamwise velocity field, U, at $0.85U_\infty$.

along all three spatial dimensions, such that

$$u_l(x,y,z,t_0) = \frac{\int_{x_j^*}^{x_f^*}\int_{y_i^*}^{y_f^*}\int_{z_j^*}^{z_f^*} u(x^*,y^*,z^*,t_0)\exp\left(-\left(\frac{(x-x^*)^2+(y-y^*)^2+(z-z^*)^2}{(2\sigma_G)^2}\right)\right)dx^*dy^*dz^*}{\int_{x_j^*}^{x_f^*}\int_{y_i^*}^{y_f^*}\int_{z_j^*}^{z_f^*} \exp\left(-\left(\frac{(x-x^*)^2+(y-y^*)^2+(z-z^*)^2}{(2\sigma_G)^2}\right)\right)dx^*dy^*dz^*} \tag{4.1}$$

is the fluctuating large scale streamwise velocity field with t_0 defined as the frame of interest. The laboratory-frame large-scale streamwise velocity field is defined as

$$U_l(x,y,z,t_0) = u_l(x,y,z,t_0) + \bar{U}(x,y) \tag{4.2}$$

and

$$u_s(x,y,z,t_0) = u(x,y,z,t_0) - u_l(x,y,z,t_0) \tag{4.3}$$

is the small-scale streamwise velocity field. The equivalent procedure is used to define v_l, w_l, v_s, and w_s, the large and small scales in the wall-normal and spanwise velocity fields.

The value $\sigma_G = 0.5\delta$ was used for all results in the chapter unless otherwise specified. This filter size was chosen due to observations that it distinguished large and small scales accurately in the conditional averaging results of the PIV data. The sensitivity and manner of determination of scale separation are discussed in this chapter in the subsection titled *Sensitivity to parameters*. Using the expression

for the cutoff frequency given in chapter 2, one can define the approximate cutoff wavelength of the filter as $\lambda_G/\delta = 2.7$. This approximate cutoff wavelength is slightly larger than the wavelength cutoff used for the spectral filter of Mathis, Hutchins, and Marusic (2009), $\lambda_x/\delta = 1$, and within the range of filter sizes considered by Ganapathisubramani et al. (2012). The exact value of the cutoff wavelength used for the spectral filter was found to have little effect on the results of Ganapathisubramani et al. (2012).

Figure 4.2 shows the filtered streamwise velocity field at the same instant as the field shown in figure 4.1. The large-scale fluctuating streamwise velocity field is shown in the background plane in red and blue contours. A clear correlation between the large-scale streamwise fluctuation, u_l, and the black and white isosurfaces of the small-scale fluctuations, u_s, can be observed. Depending on the sign of the local large-scale velocity structure, the small scales at this particular isocontour are observable far from the wall (negative large scale) or only close to the wall (positive large scale). The location of strong small-scale activity is also closely correlated with the isosurface of the instantaneous velocity, $U_l = 0.85U_\infty$. The wall-normal location of this isosurface is also dictated by u_l, via the preceding equation.

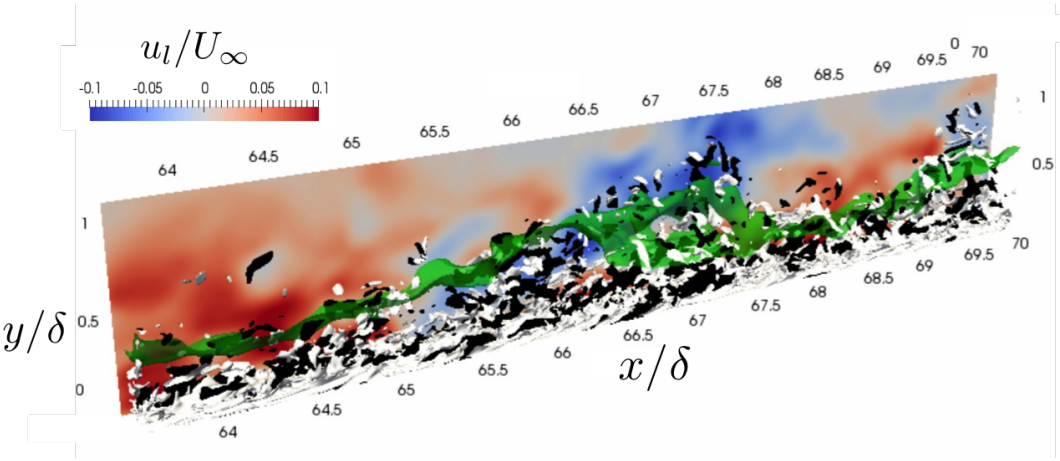

Figure 4.2: Visualization of the filtered streamwise velocity field of a turbulent boundary layer DNS (Wu et al., 2017) between the spanwise locations $z/\delta = 0.3 - 0.8$. Red and blue contours represent the large-scale fluctuation, u_l, defined using the filter described in chapter 2. The white and black isosurfaces represent the small-scale fluctuation, u_s, at $\pm 0.06U_\infty$. The green isosurface represents an isosurface of the large-scale laboratory-frame streamwise velocity field (U_l) at $0.85U_\infty$, which is the approximated convection velocity of the large scale in this snapshot.

The instantaneous behavior of the large and small fluctuating velocity scales shown

in figure 4.2 is compatible with observations of amplitude modulation and phase organization of large and small scales in wall-bounded turbulent flows described in chapter 1 (Hutchins and Marusic, 2007; Mathis, Hutchins, and Marusic, 2009; Jacobi and McKeon, 2013). However, the correlation that is visually identifiable in figure 4.2 between a particular isocontour of the laboratory-frame, large-scale flow and the strength of the small scales had not previously been identified. To probe the importance of this relationship, a more quantitative, statistical assessment was needed.

4.3 Conditional averaging: the spatial organization of large and small scales

To quantify the spatial relationship that was instantaneously observed in figure 4.2 and probe the importance of the isocontour of the large-scale flow, the P_{1D} and P_{2D} conditional averaging techniques described in chapter 2 were implemented.

The organization of small scales about LSMs

Conditional averaging of PIV data

First, the behavior of the small scales about a large-scale motion in PIV data was considered. As discussed in chapter 2, a model of the large-scale motion was required to perform the conditional averaging technique. Two different models were considered when analyzing the PIV results: the first was the representative model of a large-scale motion identified and analyzed in chapter 3, considered in a streamwise – wall-normal plane to match the PIV data (2D model); the second was the same model only sampled along its critical layer height, leading to a sinusoidal amplitude variation of streamwise velocity as a function of the streamwise variable (1D model).

As discussed in chapter 3, the approximate size and speed of a large-scale motion is given by $\lambda_x = 4\delta$, $\lambda_z = 1\delta$, and $c = 0.8U_\infty$. For the 2D results, these parameters were used to identify a resolvent response mode, which was used as the estimated shape of the large-scale motion. The number of 2D planes of data used in each conditional averaging figure (total over the panels) are shown in table 4.1, along with the percentage of the total 2D planes of data considered. For the PIV data, this is equivalent to the number of temporal snapshots used for each total figure.

The P_{2D} conditional averaging method was used to identify the averaged streamwise velocity field and the averaged small-scale streamwise and wall-normal intensity fields given the presence of a large-scale motion. Using the algorithm described in chapter 2 and written in full in Appendix A, one arrives at the results shown in

figure 4.3. Figure 4.3(a) represents the quantity

$$< u >_{P_{2D},LSM}(x,y) = \frac{1}{\tilde{n}} \sum_{\tilde{t}} \left(\frac{1}{N} \sum_{t_i} u(x,y,t_i) \right. \\ \left. \forall t_i \text{ s.t. } \left(\frac{u(x,y,t_i) \cdot \tilde{u}_{LSM}(x,y,\tilde{t})}{|u(x,y,t_i)||\tilde{u}_{LSM}(x,y,\tilde{t})|} \right) = R^* > R_{th} \right), \tag{4.4}$$

the conditionally-averaged, fluctuating streamwise velocity field of the PIV data. The subscript i indicates that the projection is carried out separately for each frame of data. As discussed in chapter 2, the projection coefficient must be the maximum over the considered phases at a given time t_i, R^*, and must be larger than a given threshold, R_{th}. $\tilde{n}$ represents the number of phases considered.

For the small-scale streamwise intensity, the result shown in figure 4.3(b) represents

$$< u_s^2 >_{P_{2D},LSM}(x,y) = \frac{1}{\tilde{n}} \sum_{\tilde{t}} \left(\frac{1}{N} \sum_{t_i} u_s^2(x,y,t_i) \right. \\ \left. \forall t_i \text{ s.t. } \left(\frac{u(x,y,t_i) \cdot \tilde{u}_{LSM}(x,y,\tilde{t})}{|u(x,y,t_i)||\tilde{u}_{LSM}(x,y,\tilde{t})|} \right) = R^* > R_{th} \right), \tag{4.5}$$

and for the small-scale wall-normal intensity, figure 4.3(c) represents

$$< v_s^2 >_{P_{2D},LSM}(x,y) = \frac{1}{\tilde{n}} \sum_{\tilde{t}} \left(\frac{1}{N} \sum_{t_i} v_s^2(x,y,t_i) \right. \\ \left. \forall t_i \text{ s.t. } \left(\frac{u(x,y,t_i) \cdot \tilde{u}_{LSM}(x,y,\tilde{t})}{|u(x,y,t_i)||\tilde{u}_{LSM}(x,y,\tilde{t})|} \right) = R^* > R_{th} \right). \tag{4.6}$$

Large and small scales are defined using the filtering process described in equations 4.1 through 4.3. Note that only the averaged quantity, rather than the condition, changes across the variables. The results in figure 4.3 appear paneled because of the phase averaging process described in chapter 2 and in Appendix A. The phase averaging process allows for an efficient use of the data to maximize the convergence of the result.

The number of temporal snapshots used for the P_{2D} conditional average of figure 4.3 is shown in table 4.1, while the number associated with each estimated large-scale phase γ^* is shown in table 4.2. The PIV results are exclusively temporally averaged as only one spatial plane of data is available. Table 4.1 also shows the statistics for the results of the application of the P_{1D} conditional averaging method on both PIV and DNS data. The DNS data is both temporally and spatially averaged in the manner described in chapter 2.

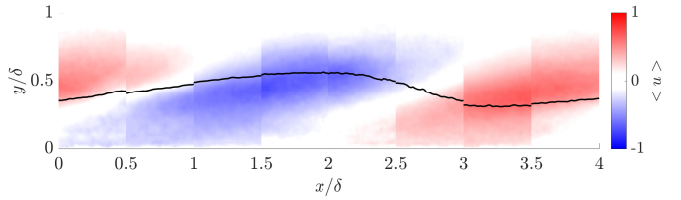

(a)

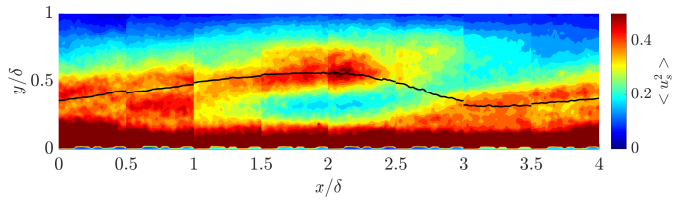

(b)

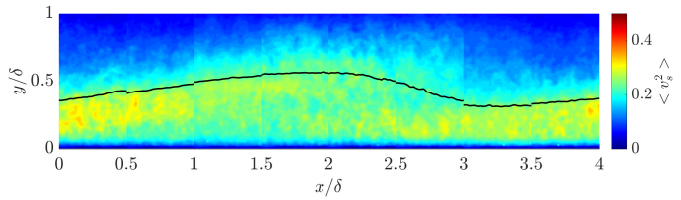

(c)

Figure 4.3: Conditional averaging results using the P_{2D} method with an LSM model in the $x-y$ plane for LSMs in PIV. Large (a) and small (b,c) scales are shown for the streamwise (a,b) and wall-normal (c) velocity fields. The black line in all panels indicates $< u >_{P_{2D},LSM} + \bar{U} = 0.8U_\infty$, the assumed convection velocity of the LSMs. The streamwise small scales are observed to follow this line, while the wall-normal small scales are observed to be bounded by this line.

	N time avg	N time, space avg	% time avg	% time, space avg
LSM, PIV, P_{2D}	5120	n/a	100	n/a
LSM, PIV, P_{1D}	5100	n/a	100	n/a
LSM, DNS, $x-y$	30	8,163	100	54
LSM, DNS, $z-y$	30	30,000	100	100
VLSM, DNS, $x-y$	20	5,529	100	92
VLSM, DNS, $z-y$	30	30,000	100	100
NWS, DNS, $x-y$	28	1,233	93	16
NWS, DNS, $z-y$	30	30,000	100	100

Table 4.1: Table of total number of 2D planes used for conditional averaging.

	1	2	3	4	5	6	7	8
N frames	404	638	946	548	413	655	988	528
% frames	8	12	18	11	8	13	19	10

Table 4.2: The number of frames associated with each estimated phase γ^* for the P_{2D} conditional averaging method applied to PIV data with an LSM model, associated with figure 4.3. The numeric label corresponds to the index of $\gamma^* \in \Gamma^*$, with $\Gamma^* = [0, 2\pi)$ in intervals of $\pi/4$.

The conditionally averaged fluctuating streamwise velocity field $< u >_{P_{2D},LSM}$ is shown in (a). Inclined, alternating large-scale features are observed in the streamwise velocity field, reflecting the input LSM model. The are observed to have a larger wall-normal extent than the resolvent model of figure 3.2 in chapter 3. In (b,c), the conditionally averaged small-scale intensity is shown for the streamwise $< u_s^2 >_{P_{2D},LSM}$ and wall-normal $< v_s^2 >_{P_{2D},LSM}$ velocity fields respectively. The small scales are defined using a Gaussian filter, as described in chapter 2. The black line represents an isocontour of the superposition of the conditionally averaged streamwise velocity field and the mean ($< u >_{P_{2D},LSM} + \bar{U} = 0.8U_\infty$). The small-scale streamwise intensity is seen to be strongly affected by the behavior of the large-scale velocity field. In the presence of the large-scale positive fluctuating structure, the small scales are strong and localized near the wall, while in the presence of the large-scale negative fluctuating structure, the small scales are lifted away from the wall. The streamwise small-scale intensity is seen to be localized along the highlighted isocontour of the large-scale field. The wall-normal small-scale intensity appears to be bounded by the isocontour, rather than localized about it.

The use of a 1D model of an LSM for the projection method yields similar results. For the 1D model, the conditionally-averaged streamwise velocity field is shown in figure 4.4(a), representing

$$\begin{aligned} < u >_{P_{1D},LSM}(x, y) = &\frac{1}{\tilde{n}} \sum_{\tilde{t}} \left(\frac{1}{N} \sum_{t_i} u(x, y, t_i) \right. \\ &\left. \forall t_i \text{ s.t. } \left(\frac{u(x, y_c, t_i) \cdot \tilde{u}_{LSM}(x, y_c, \tilde{t})}{|u(x, y_c, t_i)||\tilde{u}_{LSM}(x, y_c, \tilde{t})|} \right) = R^* > R_{th} \right), \end{aligned} \tag{4.7}$$

where y_c is the critical layer height of the model; the height at which the mean velocity is equal to the assumed phase speed. The P_{1D} conditionally-averaged

small-scale streamwise intensity is shown in figure 4.4(b), representing

$$< u_s^2 >_{P_{1D},LSM}(x,y) = \frac{1}{\tilde{n}} \sum_{\tilde{t}} \left(\frac{1}{N} \sum_{t_i} u_s^2(x,y,t_i) \right. \\ \left. \forall t_i \text{ s.t. } \left(\frac{u(x,y_c,t_i) \cdot \tilde{u}_{LSM}(x,y_c,\tilde{t})}{|u(x,y_c,t_i)||\tilde{u}_{LSM}(x,y_c,\tilde{t})|} \right) = R^* > R_{th} \right). \tag{4.8}$$

The P_{1D} conditionally-averaged small-scale wall-normal intensity is shown in figure 4.4(c), representing

$$< v_s^2 >_{P_{1D},LSM}(x,y) = \frac{1}{\tilde{n}} \sum_{\tilde{t}} \left(\frac{1}{N} \sum_{t_i} v_s^2(x,y,t_i) \right. \\ \left. \forall t_i \text{ s.t. } \left(\frac{u(x,y_c,t_i) \cdot \tilde{u}_{LSM}(x,y_c,\tilde{t})}{|u(x,y_c,t_i)||\tilde{u}_{LSM}(x,y_c,\tilde{t})|} \right) = R^* > R_{th} \right). \tag{4.9}$$

The black line indicating a single isocontour of the laboratory-frame velocity field $< u >_{P_{1D},LSM} + \bar{U} = 0.8U_\infty$ appears slightly more regular and periodic in its shape, as compared to the inclined contour of figure 4.3. The streamwise small-scales are again seen to be strongest along the isocontour of the large scale, stronger near the wall in the presence of a large-scale positive streamwise velocity structure, and strongest away from the wall in the presence of a large-scale negative fluctuating streamwise velocity structure. The wall-normal small scales are again observed to be essentially bounded from above by the large-scale streamwise isocontour.

The proximity of the LSM feature to the edge of the boundary layer begs the question of whether the small scale organization observed in figures 4.3 and 4.4 is associated with the edge of the boundary layer, rather than representing a behavior within the boundary layer itself. To address this question, the turbulent/non-turbulent interface (TNTI) detection scheme of (Chauhan et al., 2014) is used, in the same manner discussed in chapter 3, to identify the edge of the boundary layer. An intermittency variable, I, was defined with the same definition used by Chauhan et al. (2014), such that its value was zero within the boundary layer and one outside of it, with a sharp interface indicating the instantaneous height of the TNTI for each frame of PIV.

$$I(x,y,t) = \begin{cases} 0 & k(x,y,t) > k_{th} \\ 1 & k(x,y,t) < k_{th} \end{cases} \tag{4.10}$$

with $k_{th} = 0.5$ and k defined as

$$k(x,y,t) = \frac{100}{9U_\infty^2} \sum_{m,n=-1}^{1} [(U(x+m,y+n,t) - U_\infty)^2 + V(x+m,y+n,t)^2], \tag{4.11}$$

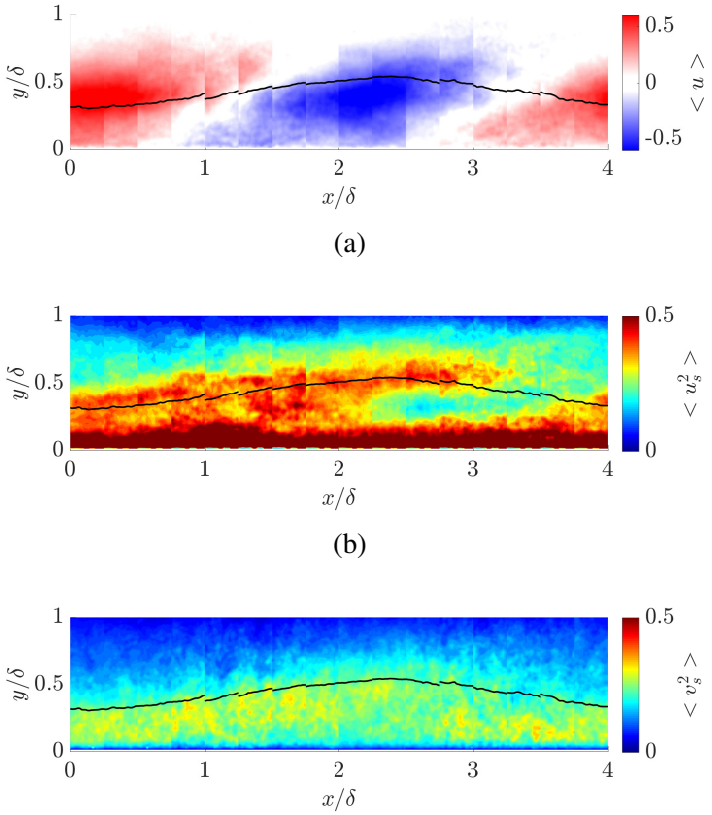

Figure 4.4: Conditional averaging results in the $x-y$ plane using the P_{1D} method with an LSM model in PIV using the 1D projection method. Large (a) and small (b,c) scales are shown for the streamwise (a,b) and wall-normal (c) velocity fields. The black line in all panels indicates $< u >_{P_{1D},LSM} + \bar{U} = 0.8U_\infty$, the assumed convection velocity of the LSMs. The streamwise small scales are observed to follow this line, while the wall-normal small scales are observed to be bounded by this line.

again following Chauhan et al. (2014). The identification of k_{th} is described in chapter 3 in the discussion of the definition of the instantaneous streamwise velocity histogram.

The intermittency variable I was then averaged with the same P_{1D} conditional averaging scheme used on the small scales in figures 4.3 and 4.4 to determine its average height relative to the height of small-scale localization. Figure 4.5 shows

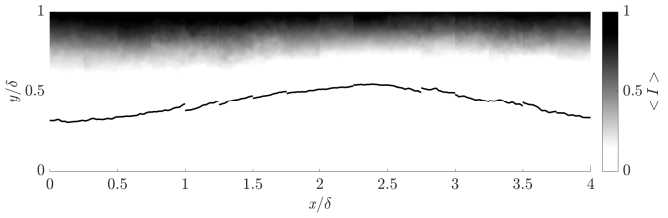

Figure 4.5: The conditionally averaged TNTI is visualized relative to the height of small-scale activity of figure 4.4. The thresholding method of Chauhan et al. (2014) was used to define a variable I, defined to be 0 within the boundary layer, where the instantaneous turbulence intensity is above a given threshold k_{th}, and 1 outside of the boundary layer where the instantaneous turbulence intensity falls below the threshold. The P_{1D} conditional averaging technique was used to average the instantaneous fields $I(x, y, t)$.

the result of this averaging process, which represents

$$< I >_{P_{1D},LSM}(x, y) = \frac{1}{\tilde{n}} \sum_{\tilde{t}} \left(\frac{1}{N} \sum_{t_i} I(x, y, t_i) \right. \\ \left. \forall t_i \text{ s.t. } \left(\frac{u(x, y_c, t_i) \cdot \tilde{u}_{LSM}(x, y_c, \tilde{t})}{|u(x, y_c, t_i)||\tilde{u}_{LSM}(x, y_c, \tilde{t})|} \right) = R^* > R_{th} \right). \tag{4.12}$$

The interface height in figure 4.5 is observed to vary as a function of the phase of the large scale of figure 4.4(a). The average TNTI height is observed to be lower in the presence of a high-speed large-scale structure and higher in the presence of a low-speed large-scale structure. This correlation suggests that the large scale observed in figure 4.4(a) may drive the instantaneous TNTI height. However, the average height of the interface is observed to be substantially above that of the isocontour $< u >_{P_{1D},LSM} + \bar{U} = 0.8U_\infty$, where small scales are observed to be localized in figures 4.3 and 4.4. This suggests that, while the large scales of figure 4.4(a) are correlated to the TNTI, the small scales of figure 4.4(b,c) are not a reflection of the TNTI itself. The total number of snapshots for the P_{1D} conditional average of figure 4.4 is shown in table 4.1, while the number associated with each estimated large-scale phase γ^* is shown in table 4.3.

Due to the similarity in the qualitative nature of the results between the 2D and 1D projections and the relative ease and efficiency of the 1D projection approach, only the 1D projection approach will be used for the remainder of the chapter and the

	1	2	3	4	5	6	7	8	9	10	11	12	13	14	15	16
N frames	547	476	317	227	188	193	223	353	535	540	352	211	189	178	237	334
% frames	11	9	6	4	4	4	4	7	10	11	7	4	4	3	5	7

Table 4.3: The number of frames associated with each estimated phase γ^* for the P_{1D} conditional averaging method applied to PIV data with an LSM model, associated with figure 4.4. The numeric label corresponds to the index of $\gamma^* \in \Gamma^*$, with $\Gamma^* = [0, 2\pi)$ in intervals of $\pi/8$.

dimension of the projection method will no longer be specified in the conditional averaging notation.

Conditional averaging of DNS data

The DNS allows for more comprehensive study of the flow field closer to the wall (allowing the study of VLSMs and the near wall streaks (NWSs)) as well as allowing for the study of the behavior in the spanwise direction and velocity field. It also allows for a larger field of view, increasing the length over which the projection occurs and improving the accuracy of the method. However, as noted in table 4.1, a limited number of temporal snapshots are used for processing the DNS data: on the order of 50, rather than 5000 for PIV. To manage this limited temporal data, the data is temporally and spatially averaged. Each spanwise point is treated as if it were an independent realization for the streamwise – wall-normal projection and average, while every streamwise point is treated as an independent realization for the spanwise – wall-normal projection and average. This leads to large numbers of planes available for averaging; however, these planes are not independent. For the LSMs and VLSMs, averaging is done over approximately 2 wavelengths of the structure in each direction, while for the NWSs, averaging is done over 2 (streamwise-average) or 10 (spanwise-average) wavelengths.

The assumed parameters of the LSMs were $\lambda_x/\delta = 4$, $\lambda_z/\delta = 1.3$, and $c/U_\infty = 0.8$. The streamwise and temporal characteristics are the same as those described in chapter 3, while the spanwise wavenumber is modified slightly to be an integer of the spanwise extent of the simulation. The 1D projection method applied to the DNS data with an LSM model is used to conditionally average the streamwise velocity

field in both the $x-y$ (figure 4.6a) and $z-y$ (figure 4.6b) planes, representing

$$< u >_{P,LSM}\ (x,y) = \frac{1}{\tilde{n}} \sum_{\tilde{t}} \sum_{\tilde{z}} \left(\frac{1}{N} \sum_{t_i} \sum_{z_j} u(x,y,z_j,t_i) \right.$$
$$\left. \forall z_j, t_i \text{ s.t. } \left(\frac{u(x,y_c,z_j,t_i) \cdot \tilde{u}_{LSM}(x,y_c,\tilde{z},\tilde{t})}{|u(x,y_c,z_j,t_i)||\tilde{u}_{LSM}(x,y_c,\tilde{z},\tilde{t})|} \right) = R^* > R_{th} \right) \tag{4.13}$$

and

$$< u >_{P,LSM,}\ (z,y) = \frac{1}{\tilde{n}} \sum_{\tilde{t}} \sum_{\tilde{z}} \left(\frac{1}{N} \sum_{t_i} \sum_{x_j} u(x_j,y,z,t_i) \right.$$
$$\left. \forall x_j, t_i \text{ s.t. } \left(\frac{u(x_j,y_c,z,t_i) \cdot \tilde{u}_{LSM}(\tilde{x},y_c,z,\tilde{t})}{|u(x_j,y_c,z,t_i)||\tilde{u}_{LSM}(\tilde{x},y_c,z,\tilde{t})|} \right) = R^* > R_{th} \right). \tag{4.14}$$

Here again, the subscript i denotes that the projection takes place at one value of that variable, y_c indicates the height where the phase speed of the model matches the mean velocity profile, and $\tilde{n}$ represents the total number of phases for both the temporal variable, $\tilde{t}$ and the spanwise variable, $\tilde{z}$. The averaged small-scale intensity was computed for the streamwise field in both the $x-y$ and $z-y$ planes (figure 4.6c,d), representing

$$< u_s^2 >_{P,LSM}\ (x,y) = \frac{1}{\tilde{n}} \sum_{\tilde{t}} \sum_{\tilde{z}} \left(\frac{1}{N} \sum_{t_i} \sum_{z_j} u_s^2(x,y,z_j,t_i) \right.$$
$$\left. \forall z_j, t_i \text{ s.t. } \left(\frac{u(x,y_c,z_j,t_i) \cdot \tilde{u}_{LSM}(x,y_c,\tilde{z},\tilde{t})}{|u(x,y_c,z_j,t_i)||\tilde{u}_{LSM}(x,y_c,\tilde{z},\tilde{t})|} \right) = R^* > R_{th} \right) \tag{4.15}$$

and

$$< u_s^2 >_{P,LSM}\ (z,y) = \frac{1}{\tilde{n}} \sum_{\tilde{t}} \sum_{\tilde{x}} \left(\frac{1}{N} \sum_{t_i} \sum_{x_j} u_s^2(x_j,y,z,t_i) \right.$$
$$\left. \forall x_j, t_i \text{ s.t. } \left(\frac{u(x_j,y_c,z,t_i) \cdot \tilde{u}_{LSM}(\tilde{x},y_c,z,\tilde{t})}{|u(x_j,y_c,z,t_i)||\tilde{u}_{LSM}(\tilde{x},y_c,z,\tilde{t})|} \right) = R^* > R_{th} \right). \tag{4.16}$$

For both wall-normal and spanwise small-scale intensity fields, only the $x-y$ planes are shown here, with the $z-y$ planes left as future work. Figures 4.6(e) and (f)

represent

$$< v_s^2 >_{P,LSM}(x,y) = \frac{1}{\tilde{n}} \sum_{\tilde{t}} \sum_{\tilde{z}} \left(\frac{1}{N} \sum_{t_i} \sum_{z_j} v_s^2(x,y,z_j,t_i) \right.$$
$$\left. \forall z_j, t_i \text{ s.t. } \left(\frac{u(x,y_c,z_j,t_i) \cdot \tilde{u}_{LSM}(x,y_c,\tilde{z},\tilde{t})}{|u(x,y_c,z_j,t_i)||\tilde{u}_{LSM}(x,y_c,\tilde{z},\tilde{t})|} \right) = R^* > R_{th} \right) \tag{4.17}$$

and

$$< w_s^2 >_{P,LSM}(x,y) = \frac{1}{\tilde{n}} \sum_{\tilde{t}} \sum_{\tilde{z}} \left(\frac{1}{N} \sum_{t_i} \sum_{z_j} w_s^2(x,y,z_j,t_i) \right.$$
$$\left. \forall z_j, t_i \text{ s.t. } \left(\frac{u(x,y_c,z_j,t_i) \cdot \tilde{u}_{LSM}(x,y_c,\tilde{z},\tilde{t})}{|u(x,y_c,z_j,t_i)||\tilde{u}_{LSM}(x,y_c,\tilde{z},\tilde{t})|} \right) = R^* > R_{th} \right) \tag{4.18}$$

respectively. The black curve in all panels represents the isocontour $< u >_{P,LSM} + \bar{U} = 0.8U_\infty$.

As with the PIV data, alternating signed, large-scale streamwise velocity features are observed in the DNS data in the conditionally averaged fluctuating streamwise velocity field (figure 4.6a). The structures appear shorter in the streamwise – wall-normal plane than those observed in the PIV results. The streamwise features appear tall and slightly asymmetric in the spanwise – wall-normal plane (figure 4.6b). The discrepancies between the streamwise – wall-normal and the spanwise – wall-normal structure (figure 4.6a,b) may reflect an artifact of phase binning, or with the restricted simulation domain (approximately 2δ) in the spanwise direction, and are a topic of on-going work. In (figure 4.6c,d), the small-scale streamwise velocity intensity is seen to be strong and concentrated near the wall in the presence of a large-scale positive velocity structure, and lifted away from the wall in the presence of a large-scale negative velocity structure. The intensity is observed to be less concentrated at the highlighted isocontour than what was seen in the PIV results. The wall-normal small-scale intensity (figure 4.6e) appears to be bounded from above by the highlighted large-scale isocontour, showing good agreement with the PIV results of figure 4.4(c). The spanwise small-scale velocity field is observed to be most concentrated near the wall, where it is strongest in the presence of a large-scale positive structure and weakest in the presence of a large-scale negative structure. Far from the wall, some evidence of height variation is also observed, in which the small-scale spanwise intensity appears to roughly follow the behavior of the isocontour $< u >_{P,LSM} + \bar{U} = 0.8U_\infty$. The total number of 2D planes used

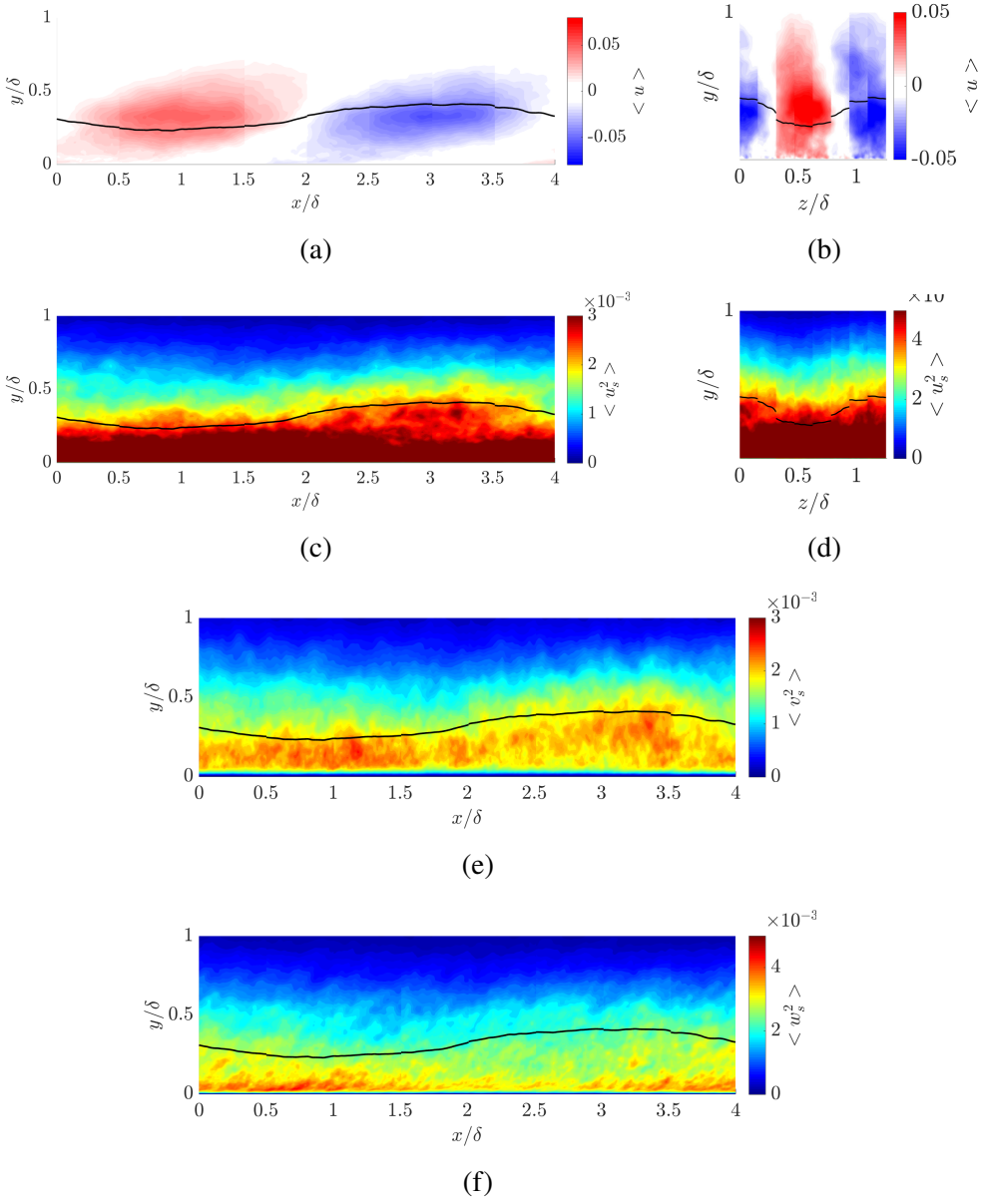

Figure 4.6: Conditional averaging results for LSMs in DNS. Large (a,b) and small (c,d) scales are shown for the streamwise velocity field in the streamwise – wall-normal (a,c) and spanwise – wall-normal (b,d) planes. The small scales of the wall-normal velocity field (e) and those of the spanwise velocity field (f) are shown in the streamwise – wall-normal plane. The black line in all panels indicates $< u >_{P,LSM} + \bar{U} = 0.8U_\infty$, the assumed convection velocity of the LSMs.

for averaging for figure 4.6 is shown in table 4.1, while the number of 2D planes associated with each estimated phase γ^* is shown in table 4.4.

	1	2	3	4	5	6	7	8
N $x-y$ planes	1180	1119	772	953	1271	891	976	1001
N $z-y$ planes	4659	2384	1948	4142	4558	4607	3880	3882
% $x-y$ planes	8	7	5	6	8	6	7	7
% $z-y$ planes	15	8	6	14	15	15	13	13

Table 4.4: The number of frames associated with each estimated phase γ^* for the P_{1D} conditional averaging method applied to DNS data with an LSM model, associated with figure 4.6. The numeric label corresponds to the index of $\gamma^* \in \Gamma^*$, with $\Gamma^* = [0, 2\pi)$ in intervals of $\pi/4$.

The organization of small scales about VLSMs

The relationship between a VLSM and the surrounding near-wall small scales was examined using the same projection, conditional averaging technique with a 1D VLSM model. The DNS data was exclusively used to study the behavior, due to its improved resolution near the wall. The assumed parameters of the VLSMs were $\lambda_x/\delta = 6$, $\lambda_z/\delta = 1.3$, and $c/U_\infty = 0.6$. As with the LSMs, the streamwise and temporal characteristics were the same as those described in chapter 3, while the spanwise wavenumber was modified slightly to be an integer of the spanwise extent of the simulation.

Figures 4.7 and 4.8 show the results of this analysis with linear and logarithmic wall-normal scales respectively. Each figure shows the streamwise velocity field (figures 4.7a,b and 4.8a,b), representing

$$< u >_{P,VLSM,}(x,y) = \frac{1}{\tilde{n}} \sum_{\tilde{t}} \sum_{\tilde{z}} \left(\frac{1}{N} \sum_{t_i} \sum_{z_j} u(x,y,z_j,t_i) \right.$$
$$\left. \forall z_j, t_i \text{ s.t. } \left(\frac{u(x,y_c,z_j,t_i) \cdot \tilde{u}_{VLSM}(x,y_c,\tilde{z},\tilde{t})}{|u(x,y_c,z_j,t_i)||\tilde{u}_{VLSM}(x,y_c,\tilde{z},\tilde{t})|} \right) = R^* > R_{th} \right) \tag{4.19}$$

and

$$< u >_{P,VLSM}(z,y) = \frac{1}{\tilde{n}} \sum_{\tilde{t}} \sum_{\tilde{x}} \left(\frac{1}{N} \sum_{t_i} \sum_{x_j} u(x_j,y,z,t_i) \right.$$
$$\left. \forall x_j, t_i \text{ s.t. } \left(\frac{u(x_j,y_c,z,t_i) \cdot \tilde{u}_{VLSM}(\tilde{x},y_c,z,\tilde{t})}{|u(x_j,y_c,z,t_i)||\tilde{u}_{VLSM}(\tilde{x},y_c,z,\tilde{t})|} \right) = R^* > R_{th} \right). \tag{4.20}$$

They also show the small-scale streamwise intensity fields in the streamwise – wall-

normal and spanwise – wall-normal planes (figures 4.7c,d and 4.8c,d), representing

$$< u_s^2 >_{P,VLSM}(x,y) = \frac{1}{\tilde{n}} \sum_{\tilde{t}} \sum_{\tilde{z}} \left(\frac{1}{N} \sum_{t_i} \sum_{z_j} u_s^2(x,y,z_j,t_i) \right.$$
$$\left. \forall z_j, t_i \text{ s.t. } \left(\frac{u(x,y_c,z_j,t_i) \cdot \tilde{u}_{VLSM}(x,y_c,\tilde{z},\tilde{t})}{|u(x,y_c,z_j,t_i)||\tilde{u}_{VLSM}(x,y_c,\tilde{z},\tilde{t})|} \right) = R^* > R_{th} \right) \tag{4.21}$$

and

$$< u_s^2 >_{P,VLSM}(z,y) = \frac{1}{\tilde{n}} \sum_{\tilde{t}} \sum_{\tilde{x}} \left(\frac{1}{N} \sum_{t_i} \sum_{x_j} u_s^2(x_j,y,z,t_i) \right.$$
$$\left. \forall x_j, t_i \text{ s.t. } \left(\frac{u(x_j,y_c,z,t_i) \cdot \tilde{u}_{VLSM}(\tilde{x},y_c,z,\tilde{t})}{|u(x_j,y_c,z,t_i)||\tilde{u}_{VLSM}(\tilde{x},y_c,z,\tilde{t})|} \right) = R^* > R_{th} \right) \tag{4.22}$$

and the small-scale wall-normal (figures 4.7e and 4.8e) and spanwise (figures 4.7f and 4.8f) intensity fields in the streamwise – wall-normal plane, representing

$$< v_s^2 >_{P,VLSM}(x,y) = \frac{1}{\tilde{n}} \sum_{\tilde{t}} \sum_{\tilde{z}} \left(\frac{1}{N} \sum_{t_i} \sum_{z_j} v_s^2(x,y,z_j,t_i) \right.$$
$$\left. \forall z_j, t_i \text{ s.t. } \left(\frac{u(x,y_c,z_j,t_i) \cdot \tilde{u}_{VLSM}(x,y_c,\tilde{z},\tilde{t})}{|u(x,y_c,z_j,t_i)||\tilde{u}_{VLSM}(x,y_c,\tilde{z},\tilde{t})|} \right) = R^* > R_{th} \right) \tag{4.23}$$

and

$$< w_s^2 >_{P,VLSM}(x,y) = \frac{1}{\tilde{n}} \sum_{\tilde{t}} \sum_{\tilde{z}} \left(\frac{1}{N} \sum_{t_i} \sum_{z_j} v_s^2(x,y,z_j,t_i) \right.$$
$$\left. \forall z_j, t_i \text{ s.t. } \left(\frac{u(x,y_c,z_j,t_i) \cdot \tilde{u}_{VLSM}(x,y_c,\tilde{z},\tilde{t})}{|u(x,y_c,z_j,t_i)||\tilde{u}_{VLSM}(x,y_c,\tilde{z},\tilde{t})|} \right) = R^* > R_{th} \right) \tag{4.24}$$

respectively. The black curve in all panels represents the isocontour $< u >_{P,VLSM} + \bar{U} = 0.6U_\infty$.

In figure 4.7, long inclined structures can be observed in the averaged fluctuating velocity field (figure 4.7a). The spanwise – wall-normal plane again shows slightly taller features (figure 4.7b), the analysis of which is a topic of on-going work. The streamwise and spanwise small scales are observed to be highly localized near the wall, while the wall-normal small-scale velocity field shows activity farther from the wall. Away from the wall, the streamwise small-scale intensity (c,d) is observed

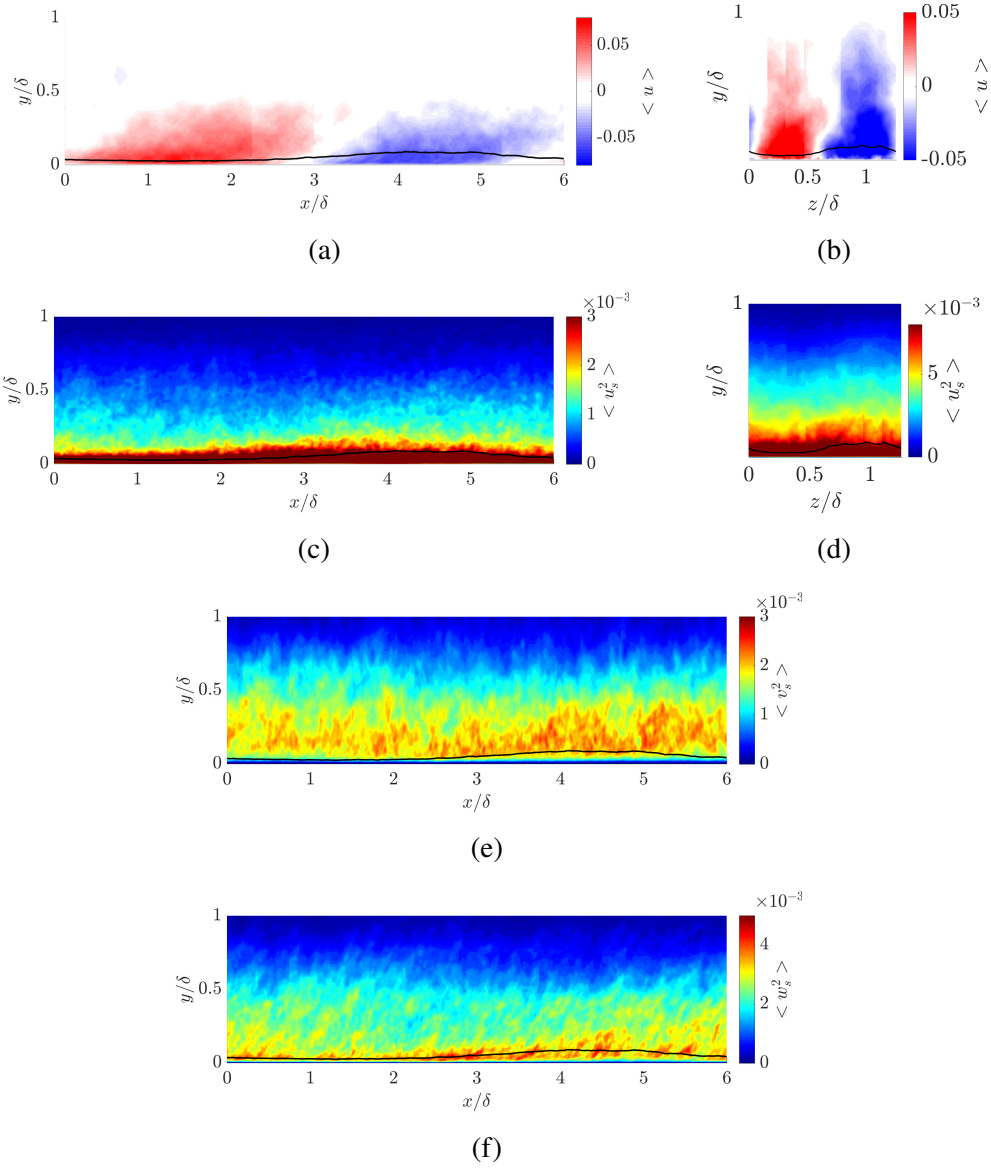

Figure 4.7: Conditional averaging results for VLSMs in DNS with a linear wall-normal scale. Large (a,b) and small (c-f) scales are shown for the streamwise velocity field (a-d), wall-normal velocity field (e), and spanwise velocity field (f) in the streamwise – wall-normal (a,c,e,f) and spanwise – wall-normal (b,d) planes. The black line in all panels indicates $< u >_{P,VLSM} + \bar{U} = 0.6U_\infty$, the assumed convection velocity of the VLSMs.

to show some similar trends to those of figures 4.4 and 4.6: the outer edge of the visible small-scale intensity bends nearer the wall for the positive large-scale structure, and farther from the wall for the negative large-scale structure. Near the wall, the spanwise small-scale intensity (figure 4.7f) is also observed to be stronger

at higher heights from the wall in the presence of a negative large-scale structure.

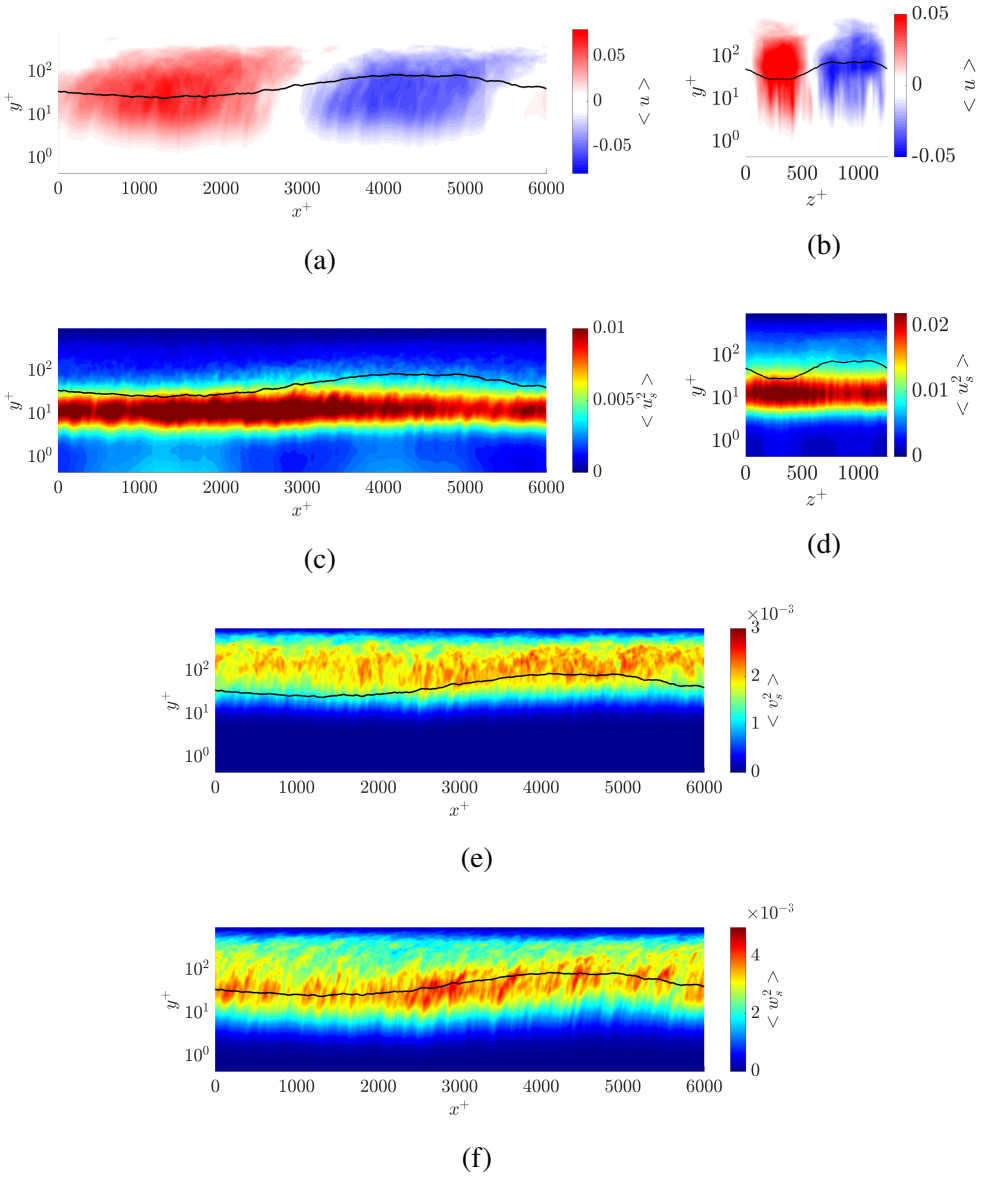

Figure 4.8: Conditional averaging results for VLSMs in DNS. Large (a,b) and small (c-f) scales are shown for the streamwise (a-d), wall-normal (e), and spanwise velocity fields (f) in the streamwise – wall-normal (a,c,e,f) and spanwise – wall-normal (b,d) planes. The black line in all panels indicates $< u >_{P,VLSM} + \bar{U} = 0.8U_\infty$, the assumed convection velocity of the VLSMs.

In figure 4.8, significantly more detail is available. The streamwise, wall-normal, and spanwise small-scale structures all show fairly different behaviors. The streamwise small-scale intensity is observed to be highly localized at one height from the wall, corresponding to the near-wall cycle. The intensity of the small scales is

observed to be highly dependent on the local sign of the large scale, consistent with previous findings (Hutchins and Marusic, 2007), in both the streamwise and spanwise directions (figure 4.8c,d). The wall-normal small-scale intensity is observed to be concentrated farther from the wall with its height fairly consistent across the large-scale phase. The amplitude of the intensity of the wall-normal small scales is observed to be strongest in the presence of a local negative large scale, consistent with its localization away from the wall (figure 4.8e). The spanwise small scales are observed to be quite localized along the highlighted isocontour, showing a spatial variation with the phase of the large scale (figure 4.8f) that is reminiscent of the behavior of the streamwise small scales about the LSM (figure 4.4b). The number of 2D planes used for averaging is shown in table 4.1 and the number of 2D planes associated with each estimated phase γ^* for the conditional averaging method with the VLSM model is shown in table 4.5.

	1	2	3	4	5	6	7	8
N $x-y$ planes	748	556	587	854	764	557	642	821
N $z-y$ planes	4879	2559	2127	2925	4503	3744	4173	5090
% $x-y$ planes	12	9	10	14	13	9	11	14
% $z-y$ planes	16	9	7	10	15	12	14	17

Table 4.5: The number of frames associated with each estimated phase γ^* for the P_{1D} conditional averaging method applied to DNS data with a VLSM model, associated with figures 4.7 and 4.8. The numeric label corresponds to the index of $\gamma^* \in \Gamma^*$, with $\Gamma^* = [0, 2\pi)$ in intervals of $\pi/4$.

The organization of small scales about NWSs

Using the DNS data and a 1D projection, the interaction of the near-wall streaks with the very small scales was studied. The assumed parameters of the near wall streaks were $\lambda_x^+ = 1000$, $\lambda_z^+ = 126$, and $c^+ = 10$. Again, the streamwise and temporal characteristics are the same as those described in chapter 3, while the spanwise wavenumber is modified slightly to be an integer of the spanwise extent of the simulation.

Figure 4.9 shows the results of the conditional averaging technique. The averaged streamwise velocity field is shown in the $x-y$ and $z-y$ planes in figures 4.9(a,b),

representing

$$< u >_{P,NWS}(x,y) = \frac{1}{\tilde{n}} \sum_{\tilde{t}} \sum_{\tilde{z}} \left(\frac{1}{N} \sum_{t_i} \sum_{z_j} u(x,y,z_j,t_i) \right.$$
$$\left. \forall z_j, t_i \text{ s.t. } \left(\frac{u(x,y_c,z_j,t_i) \cdot \tilde{u}_{NWS}(x,y_c,\tilde{z},\tilde{t})}{|u(x,y_c,z_j,t_i)||\tilde{u}_{NWS}(x,y_c,\tilde{z},\tilde{t})|} \right) = R^* > R_{th} \right) \tag{4.25}$$

and

$$< u >_{P,NWS}(z,y) = \frac{1}{\tilde{n}} \sum_{\tilde{t}} \sum_{\tilde{x}} \left(\frac{1}{N} \sum_{t_i} \sum_{x_j} u(x_j,y,z,t_i) \right.$$
$$\left. \forall x_j, t_i \text{ s.t. } \left(\frac{u(x_j,y_c,z,t_i) \cdot \tilde{u}_{NWS}(\tilde{x},y_c,z,\tilde{t})}{|u(x_j,y_c,z,t_i)||\tilde{u}_{NWS}(\tilde{x},y_c,z,\tilde{t})|} \right) = R^* > R_{th} \right). \tag{4.26}$$

The small-scale streamwise intensity fields in the streamwise – wall-normal and spanwise – wall-normal planes are shown in figures 4.9(c,d), representing

$$< u_s^2 >_{P,NWS}(x,y) = \frac{1}{\tilde{n}} \sum_{\tilde{t}} \sum_{\tilde{z}} \left(\frac{1}{N} \sum_{t_i} \sum_{z_j} u_s^2(x,y,z_j,t_i) \right.$$
$$\left. \forall z_j, t_i \text{ s.t. } \left(\frac{u(x,y_c,z_j,t_i) \cdot \tilde{u}_{NWS}(x,y_c,\tilde{z},\tilde{t})}{|u(x,y_c,z_j,t_i)||\tilde{u}_{NWS}(x,y_c,\tilde{z},\tilde{t})|} \right) = R^* > R_{th} \right) \tag{4.27}$$

and

$$< u_s^2 >_{P,NWS}(z,y) = \frac{1}{\tilde{n}} \sum_{\tilde{t}} \sum_{\tilde{x}} \left(\frac{1}{N} \sum_{t_i} \sum_{x_j} u_s^2(x_j,y,z,t_i) \right.$$
$$\left. \forall x_j, t_i \text{ s.t. } \left(\frac{u(x_j,y_c,z,t_i) \cdot \tilde{u}_{NWS}(\tilde{x},y_c,z,\tilde{t})}{|u(x_j,y_c,z,t_i)||\tilde{u}_{NWS}(\tilde{x},y_c,z,\tilde{t})|} \right) = R^* > R_{th} \right) \tag{4.28}$$

and the small-scale wall-normal (figure 4.9e) and spanwise (figure 4.9f) intensity fields are shown in the streamwise – wall-normal plane, representing

$$< v_s^2 >_{P,NWS}(x,y) = \frac{1}{\tilde{n}} \sum_{\tilde{t}} \sum_{\tilde{z}} \left(\frac{1}{N} \sum_{t_i} \sum_{z_j} v_s^2(x,y,z_j,t_i) \right.$$
$$\left. \forall z_j, t_i \text{ s.t. } \left(\frac{u(x,y_c,z_j,t_i) \cdot \tilde{u}_{NWS}(x,y_c,\tilde{z},\tilde{t})}{|u(x,y_c,z_j,t_i)||\tilde{u}_{NWS}(x,y_c,\tilde{z},\tilde{t})|} \right) = R^* > R_{th} \right) \tag{4.29}$$

and

$$< w_s^2 >_{P,NWS}(x,y) = \frac{1}{\tilde{n}} \sum_{\tilde{t}} \sum_{\tilde{z}} \left(\frac{1}{N} \sum_{t_i} \sum_{z_j} v_s^2(x,y,z_j,t_i) \right.$$
$$\left. \forall z_j, t_i \text{ s.t. } \left(\frac{u(x,y_c,z_j,t_i) \cdot \tilde{u}_{NWS}(x,y_c,\tilde{z},\tilde{t})}{|u(x,y_c,z_j,t_i)||\tilde{u}_{NWS}(x,y_c,\tilde{z},\tilde{t})|} \right) = R^* > R_{th} \right) \tag{4.30}$$

respectively. The black curve in all panels represents the isocontour $< u >_{P,NWS} + \bar{U} = 10u_\tau$.

Correlation is observed between the near-wall streaks and the small-scale streamwise and spanwise intensities in figure 4.9. Inclined structures are observed in the conditionally averaged streamwise velocity field in the $x-y$ plane (figure 4.9a). Streamwise small scales are observed to be highly localized around the isocontour $< u >_{P,NWS} + \bar{U} = 0.4U_\infty$ in both the streamwise – wall-normal and the spanwise – wall-normal planes (figure 4.9b,c). The streamwise small scales are observed to show the same spatial variation with the large-scale phase that was observed in the LSM results (figure 4.4b). The wall-normal small scales (figure 4.9e) appear to be strongest at higher heights and do not appear correlated to the near-wall streak behavior. The spanwise small scales (figure 4.9f) are observed to sit at higher heights than the isocontour $< u >_{P,NWS} + \bar{U} = 0.4U_\infty$, but do appear to be correlated to the streak behavior, showing a spatial variation across the large-scale phase. The number of 2D planes associated with each estimated phase γ^* for the conditional averaging technique with the NWS model is shown in table 4.6.

	1	2	3	4	5	6	7	8
N $x-y$ planes	137	164	115	174	165	136	167	175
N $z-y$ planes	4683	3538	3510	3401	3758	3439	3525	4146
% $x-y$ planes	2	2	1	2	2	2	2	2
% $z-y$ planes	16	12	12	11	13	11	12	14

Table 4.6: The number of frames associated with each estimated phase γ^* for the P_{1D} conditional averaging method applied to DNS data with a NWS model, associated with figure 4.9. The numeric label corresponds to the index of $\gamma^* \in \Gamma^*$, with $\Gamma^* = [0, 2\pi)$ in intervals of $\pi/4$.

4.4 Sensitivity to parameters

There are many parameters that are built into the shown analytical technique. Here, the effects of the filter size and the large-scale convection velocity will be explored; further parameter studies are intended as future work.

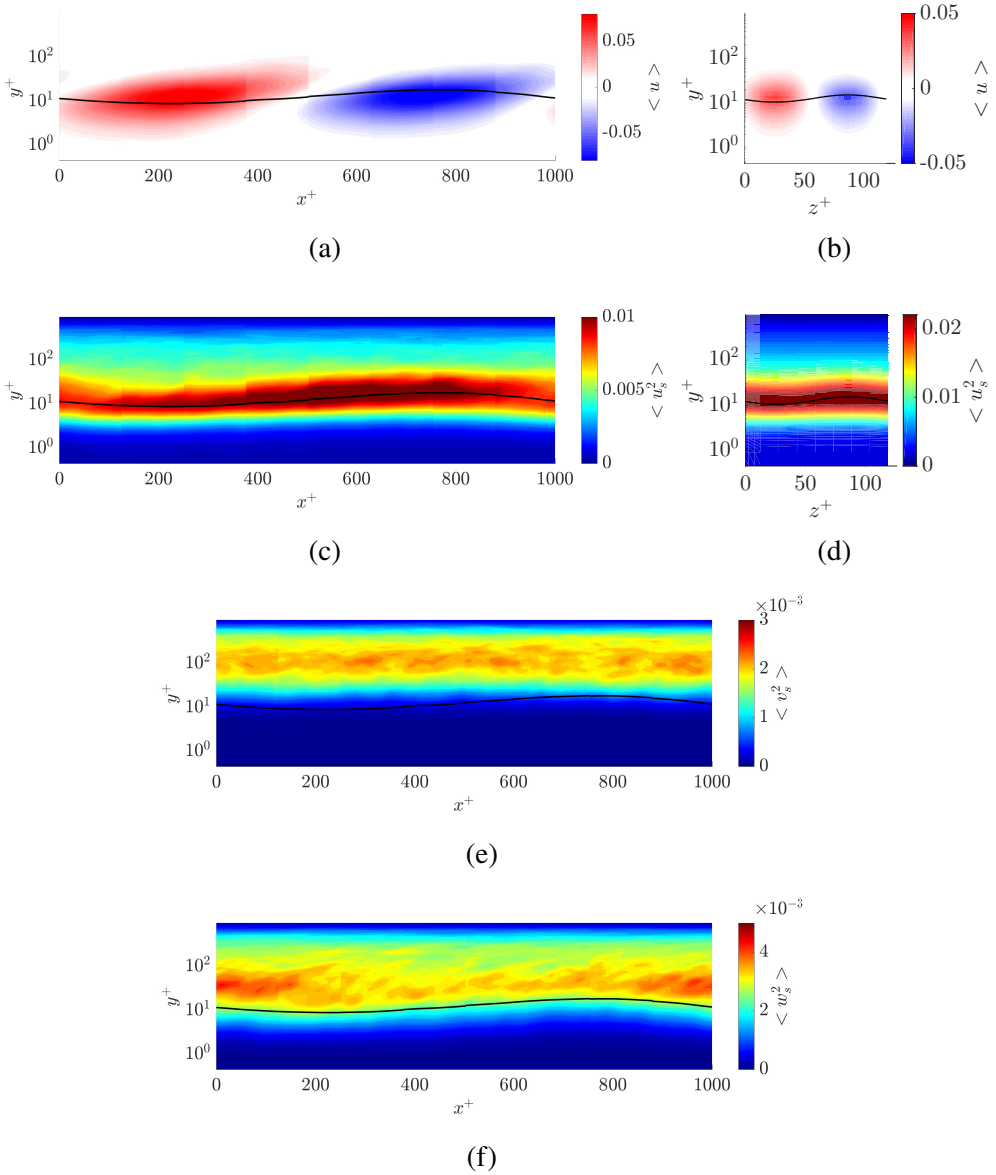

Figure 4.9: Conditional averaging results for near wall streaks in DNS. Large (a,b) and small (c,d,e,f) scales are shown for the streamwise velocity field in the streamwise – wall-normal plane (a,c,e,f) and the spanwise – wall-normal plane (b,d) for the streamwise velocity field (a-d), the wall-normal velocity field (e), and the spanwise velocity field (f). The black line in all panels indicates $< u >_{P,NWS} + \bar{U} = 0.4U_\infty$, the assumed convection velocity of the near wall streaks (equivalently $c^+ = 10$).

Filter width

One important aspect of this analysis is the definition of the small scales using a particular filter. The sensitivity of the LSM results to the width of the Gaussian filter

for the PIV results are shown in figure 4.10. These results use the 1D projection method, and the LSM, P_{1D} equations for PIV data (equations 4.7 - 4.9) hold here, with a modified definition of u_s and v_s. The equations for filtering (equations 4.1 - 4.3) hold with a new definition of σ_G. The filter width is halved to 0.25δ (figure 4.10b,c), doubled to 1δ (figure 4.10d,e), and quadrupled to 2δ (figure 4.10f,g). As the filter does not affect the conditionally averaged streamwise velocity field, it is only shown once (figure 4.10a) for reference regarding its phase. The streamwise (figure 4.10b,d,f) and wall-normal (figure 4.10c,e,g) small-scale intensities are shown for the respective filter sizes.

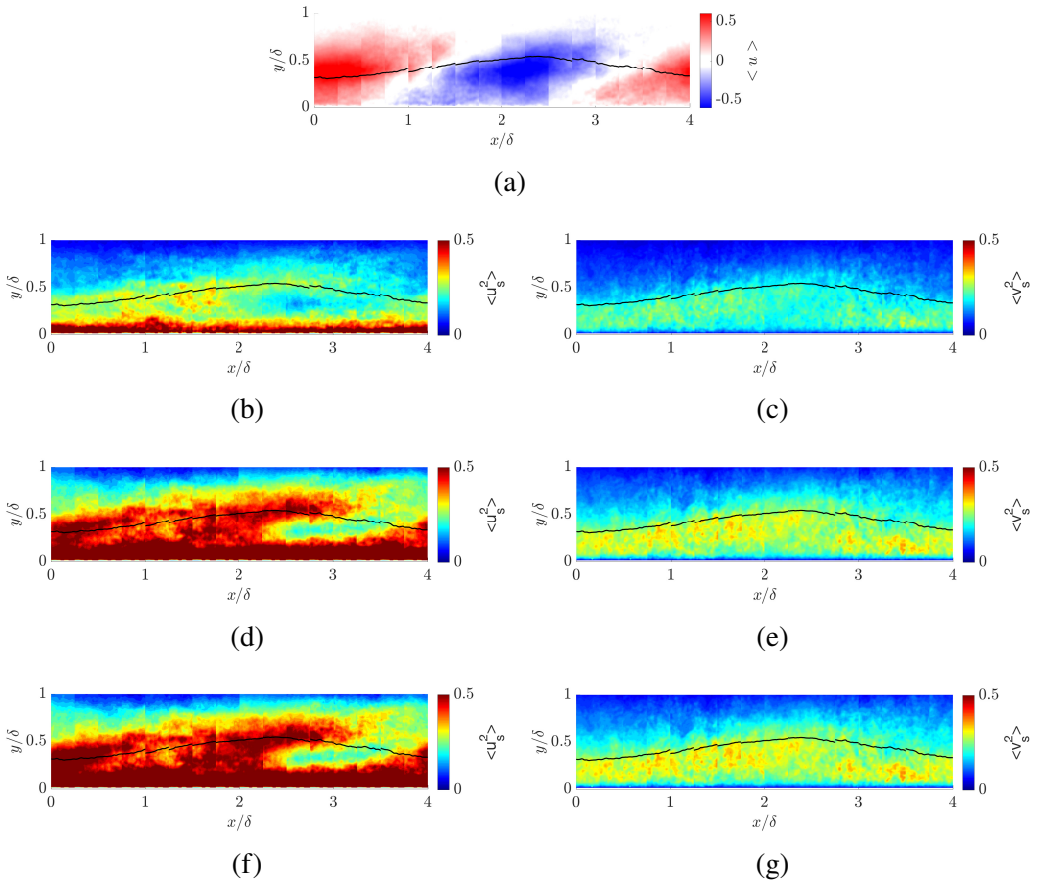

Figure 4.10: The conditionally averaged streamwise (a,b,d,f) and wall-normal (c,e,g) velocity fields are shown in the streamwise – wall-normal plane from the LSM 1D projection method applied to the PIV data. The small scales are defined using a standard deviation of 0.25δ (a,b), 1δ (c,d), and 2δ (e,f) for the Gaussian filter.

The size of the filter is observed to have a strong relationship with the magnitude of the intensity of the small scales, but does not substantially alter the overall behavior, particularly in the 0.25δ case (figure 4.10b,c). In the larger filter cases (figure

4.10d-g), the signature of the large scale shows some imprint on the streamwise small-scale intensity, observable as a larger magnitude in the region associated with the peaks of the large scale ($x/\delta \approx 0, x/\delta \approx 2$) than in the region between them ($x/\delta \approx 1$). This behavior is not observed in the case with a filter width of 0.5δ (figure 4.4), indicating a clean separation of scales. This type of contamination of the large scale in the small scale signal is not observed in the DNS data, though a systematic parameter study on the effect of filter size is identified as a necessary topic for future work.

Critical layer height of large scale

Another parameter that is built into the conditional averaging method is the assumed convection velocity of each large scale. The sensitivity to this parameter for the LSM results are explored here using the PIV data. With all other parameters held fixed, the critical layer of the large scale was considered with $c = 0.7U_\infty$ and $c = 0.9U_\infty$. In this case, the results represent

$$\begin{aligned} < u >_{P,LSM^*}(x,y) = & \frac{1}{\tilde{n}} \sum_{\tilde{t}} \left(\frac{1}{N} \sum_{t_i} u(x,y,t_i) \right. \\ & \left. \forall t_i \text{ s.t. } \left(\frac{u(x,y_c^*,t_i) \cdot \tilde{u}_{LSM^*}(x,y_c^*,\tilde{t})}{|u(x,y_c^*,t_i)||\tilde{u}_{LSM^*}(x,y_c^*,\tilde{t})|} \right) = R^* > R_{th} \right), \end{aligned} \tag{4.31}$$

where the subscript LSM^* represents that a modified LSM model is used with a changed phase speed. Here y_c^* represents the modified critical layer height corresponding to the height at which the mean velocity field is equal to the modified phase speed. The small-scale intensity is represented as

$$\begin{aligned} < u_s^2 >_{P,LSM^*}(x,y) = & \frac{1}{\tilde{n}} \sum_{\tilde{t}} \left(\frac{1}{N} \sum_{t_i} u_s^2(x,y,t_i) \right. \\ & \left. \forall t_i \text{ s.t. } \left(\frac{u(x,y_c^*,t_i) \cdot \tilde{u}_{LSM^*}(x,y_c^*,\tilde{t})}{|u(x,y_c^*,t_i)||\tilde{u}_{LSM^*}(x,y_c^*,\tilde{t})|} \right) = R^* > R_{th} \right) \end{aligned} \tag{4.32}$$

and

$$\begin{aligned} < v_s^2 >_{P,LSM^*}(x,y) = & \frac{1}{\tilde{n}} \sum_{\tilde{t}} \left(\frac{1}{N} \sum_{t_i} v_s^2(x,y,t_i) \right. \\ & \left. \forall t_i \text{ s.t. } \left(\frac{u(x,y_c^*,t_i) \cdot \tilde{u}_{LSM^*}(x,y_c^*,\tilde{t})}{|u(x,y_c^*,t_i)||\tilde{u}_{LSM^*}(x,y_c^*,\tilde{t})|} \right) = R^* > R_{th} \right). \end{aligned} \tag{4.33}$$

In figure 4.11, the streamwise velocity field (figure 4.11a,d), streamwise small-scale intensity (figure 4.11b,e) and wall-normal small-scale intensity (figure 4.11c,f) are shown for a $0.7U_\infty$ phase velocity (figure 4.11a-c) and a $0.9U_\infty$ phase velocity (figure 4.11d-f). In each panel the isocontour corresponding to $< u >_{P,LSM^*} + \bar{U} = c$ of the large scale is shown as a solid black curve, while the isocontour corresponding to $< u >_{P,LSM^*} + \bar{U} = 0.8U_\infty$ is shown in a black dashed line.

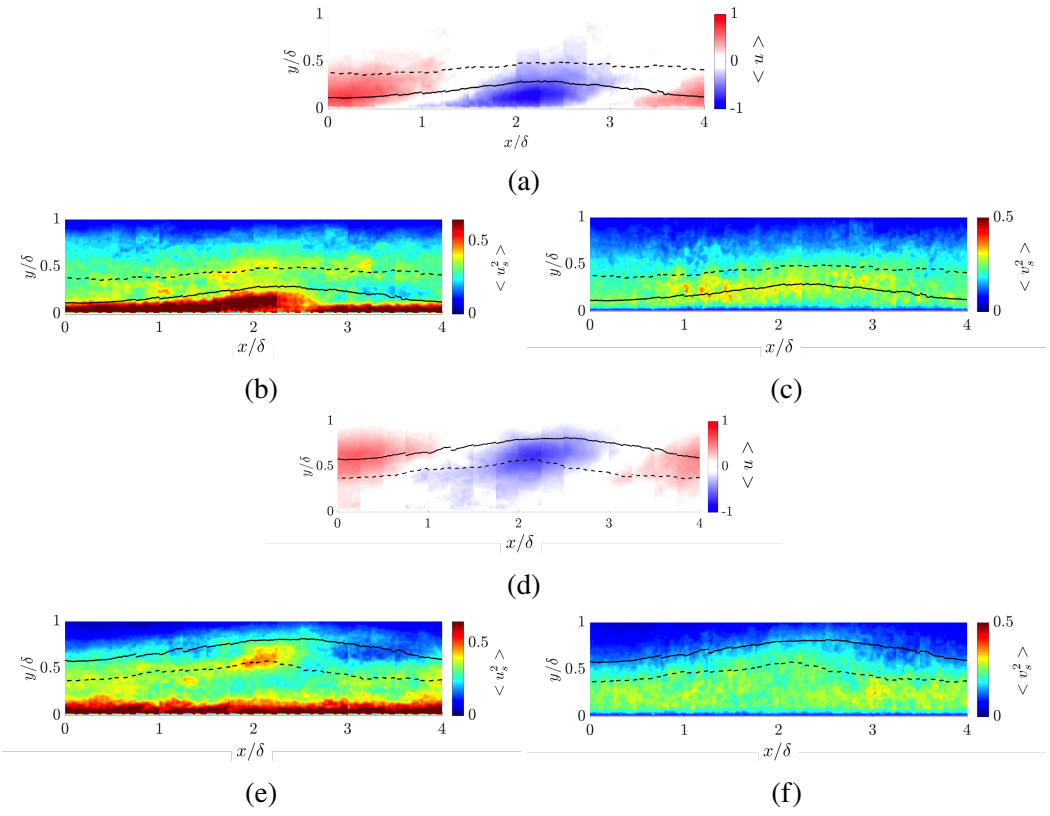

Figure 4.11: 1D projection and conditional average of PIV data with an assumed large-scale convection velocity of $0.7U_\infty$ (a-c) and $0.9U_\infty$ (d-f) . Streamwise (a,c,e,g) and wall-normal velocity fields (b,d,f,h) are shown for the full velocity field (a,b,e,f) and the small-scale intensity (c,d,g,h). The isocontour $< u >_{P,LSM^*} + \bar{U} = c$ is shown in a solid black line in each panel, while the isocontour $< u >_{P,LSM^*} + \bar{U} = 0.8U_\infty$ is shown as a dotted black line.

With the change of assumed phase velocity, the observed large scale structure is observed to shift in figure 4.11(a) and figure 4.11(d) towards and away from the wall respectively. The small scales show interesting behavior for both the $0.7U_\infty$ and $0.9U_\infty$ cases. In the $0.7U_\infty$ case, the small-scale streamwise intensity figure 4.11(b) shows an increased signature close to the wall. In the outer region of the boundary layer, a localization of streamwise small scales is still observable at the isocontour

$< u >_{P,LSM^*} + \bar{U} = 0.8U_\infty$ (dashed line). No localization of small scales is observed at the isocontour $< u >_{P,LSM^*} + \bar{U} = 0.7U_\infty$. In the $0.9U_\infty$ case, the small scale signature is significantly weaker than what was observed in figure 4.4, but is still observed to be somewhat localized near the isocontour $< u >_{P,LSM^*} + \bar{U} = 0.8U_\infty$. The wall-normal small-scale intensity is observed to be roughly bounded by the isocontour $< u >_{P,LSM^*} + \bar{U} = 0.8U_\infty$ for both cases figure 4.11(c,f). The number of frames associated with each estimated phase γ^* is shown in table 4.7.

	1	2	3	4	5	6	7	8	9	10	11	12	13	14	15	16
N frames $0.7U_\infty$	670	489	318	199	160	177	230	315	493	497	315	201	172	195	262	404
N frames $0.9U_\infty$	585	473	329	215	188	199	272	369	421	466	319	226	198	210	250	373
% frames $0.7U_\infty$	13	10	6	4	3	3	4	6	10	10	6	4	3	4	5	8
% frames $0.9U_\infty$	11	9	6	4	4	4	5	7	8	9	6	4	4	4	5	7

Table 4.7: The number of frames associated with each estimated phase γ^* for the P_{1D} conditional averaging method applied to PIV data with an LSM model with phase speeds of $0.7U_\infty$ and $0.9U_\infty$, associated with figure 4.11. The numeric label corresponds to the index of $\gamma^* \in \Gamma^*$, with $\Gamma^* = [0, 2\pi)$ in intervals of $\pi/8$.

4.5 Discussion and conclusions

Summary of the observed behavior

By leveraging the modeling of chapter 3 for a novel conditional averaging technique, a consistent pattern of spatial organization is observed between the large and small scales in both PIV and DNS data across many scales in the boundary layer. The exact nature of this organization varies across the structures considered, but many of the spatial trends are observed to agree with conditional averaging results of previous researchers (Hutchins et al., 2011; Chung and McKeon, 2010; Talluru et al., 2014; Baars, Hutchins, and Marusic, 2017), and with the conceptual drawings of Hutchins and Marusic (2007), Marusic, Mathis, and Hutchins (2010), and Baars, Hutchins, and Marusic (2017). The localization of the small scales about particular isocontours of the large-scale flow is thought to be a novel contribution to the community. As the data was presented organized by the large-scale flow field, here the full findings for each averaged field, u, u_s^2, v_s^2, and w_s^2, are summarized.

The streamwise velocity field is observed to consistently show evidence of inclined structures, even in the P_{1D} cases, in which the wall-normal coherence of the velocity field is not specified. This is consistent with many previous findings in the literature regarding the average shape of the large-scale fluctuating streamwise velocity field. The features are observed to be fairly tall: the large-scale motions, for example,

show coherence from very near the wall to approximately $y = 0.7\delta$. This average height could reflect the physical height of the structures, but could also indicate that structures that sit at multiple heights are averaged together in this process. Any large-scale structure with sufficient strength at the height where the projection is evaluated, y_c, can be included in the result, even if its centerline height is above or below y_c. Thus, a larger average height of the structure may be derived from this method than would be observed instantaneously.

The streamwise small scales are observed to be highly localized along a particular isocontour of the large-scale streamwise velocity field when conditionally averaged on both the presence of LSMs and of NWSs (figures 4.4 and 4.9). In each case, the isocontour where small scales were localized corresponded to the convection velocity of the large scale: $c/U_\infty = 0.8$ and $c^+ = 10$. The phenomenon is observed in both the streamwise and spanwise directions. It should be noted that this localization was less apparent in the streamwise small scales of the LSM in the DNS results than in the PIV results. This is hypothesized to be a result of a lack of convergence of the DNS results due to a lack of independent realizations used for averaging; further study of this discrepancy is planned as future work.

The streamwise small scales do not show the same localization behavior about the isocontour corresponding to the phase speed of the VLSMs (figure 4.8). Instead, the small scales are observed to be strongest at height at $c^+ = 10$, where the near-wall cycle sits, but are observed to be modulated in amplitude depending on the presence of the VLSM. This phenomenon is observed in both the streamwise – wall-normal and spanwise – wall-normal planes and is consistent with many previous findings described in chapter 1, which identified amplitude modulation and consistent phase relationships between the VLSMs and the near wall cycle (Mathis, Hutchins, and Marusic, 2009; Jacobi and McKeon, 2011; Talluru et al., 2014; Baars, Hutchins, and Marusic, 2017)

The spatial organization of the wall-normal small scales appears to be most strongly correlated to the LSMs (figures 4.3, 4.4, and 4.6). In the outer region of the boundary layer, the wall-normal small scales appear to be bounded by the isocontour corresponding to the phase speed of the LSMs. The VLSMs show some amplitude modulation trends with the wall-normal small scales, but no height variation is observable. No correlation is identified between the wall-normal small scales and the NWSs.

The spatial organization of the spanwise velocity small scales is correlated to the

phase of both the VLSMs and NWSs. A spatial localization along the isocontour corresponding to the phase speed of the VLSMs is observed for the spanwise small-scale velocity features (figure 4.8), in a manner reminiscent of the findings for the streamwise small scales in the LSM and NWS cases. The small-scale spanwise intensity also shows spatial variation with the NWSs, but is localized at a higher height than the NWS phase velocity (figure 4.9). The LSMs show some evidence of amplitude modulation effects on the spanwise small scales near the wall, and some mild spatial variation is observed in the outer region of the boundary layer (figure 4.6).

There is evidence that the height at which the small-scale intensity is observed to be strongest is not an artifact of the assumed convection velocity of the large scale that is built into the condition. This is perhaps most clear for the scales near the wall. The streamwise small scales are consistently localized at the isocontour $< u >_P + \bar{U} = 0.4U_\infty$ in both the VLSM and NWS results, while the spanwise small scales are consistently localized at the isocontour $< u >_P + \bar{U} = 0.6U_\infty$. However, this consistency of small-scale intensity height is also observable in the outer boundary layer in figure 4.11. If the large scale is assumed to have a phase speed of $0.7U_\infty$ or $0.9U_\infty$, the streamwise small scales still show some localization at a height of $0.8U_\infty$ and no clear localization at $0.7U_\infty$ or $0.9U_\infty$.

Hypotheses on the mechanisms underlying the results

The mechanisms for the large-scale – small-scale relationships observed in this chapter are, to the author's knowledge, not yet known. A hypothesis for at least one relevant mechanism is that of a critical layer. The concept of a critical layer comes from stability theory, in which one has a formal base flow that is a solution to the Navier-Stokes equations. The critical layer of the mean velocity profile also plays an important role in the modeled representations of the large scales shown in chapter 3 (McKeon and Sharma, 2010). Here, it is possible that the superposition of the mean and a large-scale structure may act as a pseudo-base flow, such that 'perturbations' or, in the case of fully developed turbulence, persistent small scales are strongest along isocontours where their phase speed is equal to the pseudo-base flow. Thus, if the pseudo-base flow is a function of space and time, then the height at which small scales are strongest will also be a function of space and time. 3D critical layers have previously been considered in wall-bounded turbulent flows in the context of self-sustaining mechanisms in the near wall cycle (Schoppa and Hussain, 2002), and in self-sustaining, exact solutions to the Navier-Stokes equations (Wang, Gibson, and

Waleffe, 2007; Hall and Sherwin, 2010; Park and Graham, 2015). The 3D critical layers considered in previous works have included spanwise variations in the base and pseudo-base flows, leading to spanwise-varying critical layers. They have not included streamwise or temporal variations in the base or pseudo-base flows, which are observed to be relevant in the results shown in this chapter. The physical and mathematical implications of a streamwise-varying and temporally-varying critical layer in the context of turbulent flows are, to the authors knowledge, not yet fully understood, offering an opportunity for future work.

A key component of the critical layer hypothesis is that the phase speed of the small scales, c_s, defines the height relative to the pseudo-base flow at which they are strongest. The heights of strong small-scale intensity are observed in figure 4.11 to be robust to changing the assumed phase speed of the large scales, which is compatible with the critical layer hypothesis. It also suggests that there may be dominant small scales in the boundary layer that have preferential phase speeds. In the streamwise velocity field, those small scales appear to preferentially sit at the height where $< u >_P + \bar{U} = 0.8U_\infty = 22u_\tau$ and $< u >_P + \bar{U} = 0.4U_\infty = 10u_\tau$, but in the spanwise velocity field they appear fairly localized at $< u >_P + \bar{U} = 0.6U_\infty = 17u_\tau$. These findings call for more study to better understand the existence and phase speed of dominant small scales in wall-bounded turbulent flows.

Number of frames used for conditional averaging

The number of frames used for conditional averaging was observed to vary substantially depending on the projection length used. This is most notable in the NWS results, where the projection length for the streamwise – wall-normal results was 20δ. For these results, the percentage of results used was less than 2%, rather than approximately 100% that passed the threshold for many of the other scales. The types of results observed appear to be quite robust across these drastic ranges of included frames, but these findings certainly suggest the need for further study to understand the sensitivity to projection length.

In addition, for the P_{1D} conditional averaging results for both the PIV and the DNS data, the number of instances of each estimated large scale phase, γ^* is found to be larger for values near 0 and π than for those near $\pi/2$ and $3\pi/2$. This aligns with the phase distribution observed in chapter 2 for cases where larger wavelengths are being considered than the model assumes. The distribution is observed to be least uniform for PIV cases and for the $z-y$ plane and VLSM DNS cases, suggesting that these results in particular could be improved through better estimation of the

signal wavelength. This pattern is not observed for the P_{2D}. The analysis of this distinction in distribution given a 2D rather than 1D model is a topic of future work.

Averaging on a class of structure

As discussed in chapter 2, the projection method can act as a low-pass filter or band-pass filter, meaning that in general it conditions on the presence of a range of similarly-positioned large-scale structures rather than on a single scale. While this complicates the interpretation of the results, it is consistent with the original intent behind the models used for the projection. The models presented in chapter 3 were intended to be representative of a class of structures, defined as a set of structures with similar streamwise and spanwise wavelengths and wall-normal coherences. That the method uses these models not as an exact constraint, but as a central target about which some scatter is acceptable is therefore compatible with the original intention behind the models' construction.

Topics requiring future work

The observed small-scale behavior is rich and shows significant opportunity for further study. The distinct behavior of the u_s^2, v_s^2, and w_s^2 small scales can be tied into previous observations of both the velocity and vorticity fields in turbulent boundary layers: a strong u_s^2, w_s^2 signature near the wall may be connected to the break-down of streaks observed by previous researchers (Kline et al., 1967), while the strong u_s^2, v_s^2 signature in the outer region of the boundary layer may connect to observations of hairpin vortices (Theodorsen, 1952; Adrian, Meinhart, and Tomkins, 2000).

The sensitivity of these results to the parameters used to acquire them is a topic that requires further study. Some key parameters that require further study are the projection length, model parameters ($\tilde{\lambda}$ and c), the filter width, and the filter type. Studies of the effects of these parameters are part of ongoing work. Additionally, the results shown here were for 2D planes of data in which the phase of only one of the two wall-parallel spatial variables was considered. Averaging on both the streamwise and spanwise phases could aid in the interpretation of the results and could lead to a useful three-dimensional view of the small scale intensity in physical space.

Finally, the average difference between the streamwise velocity field, u, and the model, $\tilde{u}$, could provide insight into the accuracy of the model in representing the large-scale flow field and the strength of the projection condition. As an example,

this residual would be calculated for the P_{2D} case with an LSM model as

$$< u_r >_{P_{2D},LSM}(x,y) = \frac{1}{\tilde{n}} \sum_{\tilde{t}} \left(\frac{1}{N} \sum_{t_i} \left(u(x,y,t_i) - \tilde{u}_{LSM}(x,y,\tilde{t}) \right) \right. \\ \left. \forall t_i \text{ s.t. } \left(\frac{u(x,y,t_i) \cdot \tilde{u}_{LSM}(x,y,\tilde{t})}{|u(x,y,t_i)||\tilde{u}_{LSM}(x,y,\tilde{t})|} \right) = R^* > R_{th} \right) \tag{4.34}$$

The calculation of the residual from the projection is topic of current and on-going work.

Chapter 5

PASSIVE SCALAR TRANSPORT

5.1 The aero-optic problem

One application in which turbulent structures and their interactions have detrimental effects is the field of aero-optics. When an optical beam passes through a variable-density turbulent boundary layer, the beam may become distorted and 'jitter', meaning that the beam path itself becomes a function of time. The final focus of this thesis was to probe whether velocity structures and their interactions were correlated to this deflection, and if so, to use that correlation to illuminate basic physics regarding the relationship between coherent structures and the transport of scalars in turbulent boundary layers. In particular, it was of interest to evaluate whether the energetic structures modeled in chapter 3 and the interaction of those structures with the small scales in the manner identified in chapter 4 were relevant to the deflection of the optical beam.[1]

While the aero-optic problem is generally studied in compressible turbulent boundary layers, the problem explored in this thesis focuses on an incompressible, heated turbulent boundary layer. The lower flow speeds of this set up allow for higher-resolution PIV studies of the turbulent velocity field. Details of the set up are given in chapter 2. While the physics of incompressible, heated flows and compressible flows have important distinctions, the deflection of an optical beam is observed to share similar characteristics in the two flows. In particular, a normalized spectrum of the root mean squared (RMS) of the deflection angle of the Malley probe was calculated in the incompressible, heated case and a number of compressible cases. The normalized spectrum was defined as

$$\hat{\phi}_{norm}(St_\delta) = \frac{\hat{\phi}(f)}{\frac{\rho_a}{\rho_{SL}}\frac{\delta^*}{U_\infty}\left(M^2 + D_1\frac{\Delta T}{T_\infty},\right)} \tag{5.1}$$

where ρ_{SL} is the density of air at sea level and standard conditions, δ^* is the displacement thickness, M is the Mach number of the flow ΔT is the difference in

[1]The deflection angle spectrum results were published as part of Smith et al. (2014), some instantaneous visualizations related to this work were published as part of Gordeyev et al. (2015), the results of the MP conditional averaging technique were published as part of Saxton-Fox et al. (2015), and the results of the MP / P_{1D} conditional averaging technique, as well as the models of the velocity field, were published as part of Saxton-Fox and McKeon (2017b).

temperature between the plate and the free stream, T_∞ is the temperature in the free stream, and St is the Strouhal number, defined here as $St_\delta = \frac{f\delta}{U_\infty}$ (Cress, 2010). Hat symbols indicate that Welch's power spectral density estimate has been applied. The value of D_1 is experimentally identified such that the peak amplitude of the spectrum is a constant value across experiments and was observed by Cress (2010) to be a function of the Mach number. Figure 5.1 shows the deflection angle spectra for a wide range of Reynolds and Mach numbers, normalized by the peak value identified at a Strouhal number near 0.8. The Mach numbers range from 0.03 in the present set up, to 0.41 at the highest noted Reynolds number. The blue curve in figure 5.1 corresponds to the present data, while the other curves come from work done by in the group of a collaborator, Professor Stanislav Gordeyev at the University of Notre Dame.

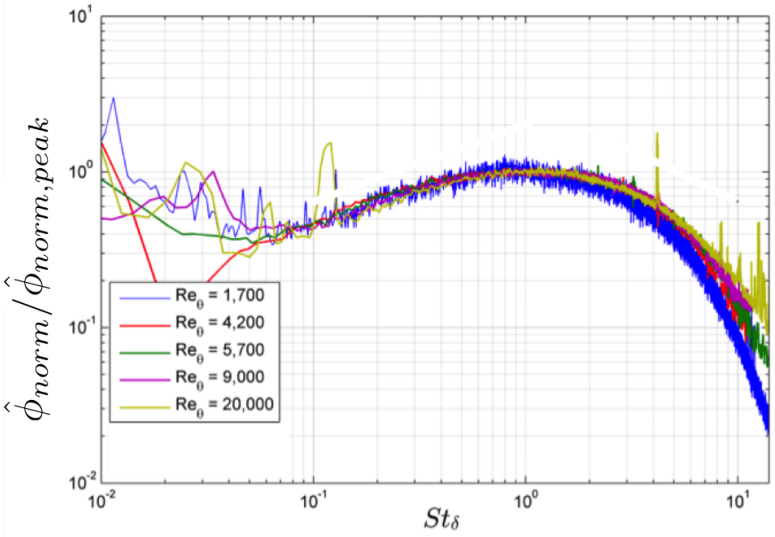

Figure 5.1: Spectra of the Malley probe signal over a large range in Reynolds and Mach numbers. The Mach number varies between 0.03 and 0.41 across the cases shown. The collapse of the spectra highlights the relevance of the incompressible, heated experiments to the compressible deflection behavior. Present data shown in blue, while other data comes from the University of Notre Dame.

The spectra are observed to collapse well outside of the highest frequencies, which show some drop off at lower Reynolds numbers. This suggests a consistency in the dominant scales that affect the Malley probe deflection. The first evidence that particular turbulent structures affect the Malley probe came from a deflection convection velocity (Malley, Sutton, and Kincheloe, 1992). The Malley probe consists of two beams aligned in the streamwise direction, allowing a convection velocity to be identified as the deflections occur in each beam in sequence. This

convection velocity was identified as $0.83U_\infty$ in this flow (consistent within 5% across a wide range of Reynolds numbers identified by other researchers (Gordeyev et al., 2014)), placing the critical flow events in the outer region of the flow. Thus, the outer region behavior will be of focus in this chapter, making the LSM model of chapter 3 and the $P1_{1D}$ conditional averaging with an LSM model of chapter 4 particularly relevant. Because only the LSM model will be considered in this chapter, the specification of the model will be dropped and the method will be referred to simply as the P_{1D} conditional average.

As highlighted in chapter 2, the deflection of the Malley probe beam can be seen as an integral measurement of the streamwise gradient of density. This effort aims to first identify the velocity features that are directly correlated to deflections in the Malley probe beam, and then use those flow features to approximate the local density field. Towards this end, conditional averages will be used both to relate the Malley probe signal to the velocity field, but also to determine the effect of the scale interaction behavior observed in chapter 4 on the Malley probe signal. Modeling will then be used to represent both the velocity and scalar fields. The LSM model of chapter 4 will be relevant, and new small-scale models will be proposed based upon experimental data.

5.2 Correlation between velocity field and aero-optic distortion

Conditional averaging velocity field on scalar signal

As described in chapter 2, a heated turbulent boundary layer was studied with sufficiently mild heating that the temperature could be considered a passive scalar. The Prandtl number of the flow was 0.7, which suggested that the behavior of the streamwise velocity field and scalar field would be fairly similar. The Malley probe sensor outputted an integral measure of the streamwise density gradients in the flow, as derived in chapter 2

$$\phi(t) \approx \frac{K_{GD}}{1 + K_{GD} n_a} \int_{y_i}^{y_f} \frac{\partial \rho}{\partial x}(x_0, y, z_0, t) dy. \tag{5.2}$$

The velocity field was conditionally averaged on $\phi < -0.5\sigma$ (figure 5.2a,b) and $\phi > 0.5\sigma$ (figure 5.2c,d) where σ is the standard deviation of $\phi(t)$ (9.5 μrad). The streamwise velocity field was averaged on these two conditions such that

$$< u >_{MP}^{-} = \frac{1}{N} \sum_{t_i} u(x, y, t_i) \qquad \forall t_i \text{ s.t. } \phi(t_i) < -0.5\sigma \tag{5.3}$$

and

$$< u >^{+}_{MP} = \frac{1}{N} \sum_{t_i} u(x, y, t_i) \qquad \forall t_i \text{ s.t. } \phi(t_i) > 0.5\sigma. \tag{5.4}$$

The same procedure was used on the wall-normal velocity field such that

$$< v >^{-}_{MP} = \frac{1}{N} \sum_{t_i} v(x, y, t_i) \qquad \forall t_i \text{ s.t. } \phi(t_i) < -0.5\sigma \tag{5.5}$$

and

$$< v >^{+}_{MP} = \frac{1}{N} \sum_{t_i} v(x, y, t_i) \qquad \forall t_i \text{ s.t. } \phi(t_i) > 0.5\sigma \tag{5.6}$$

where N is the number of frames that satisfied the condition and the superscripts $-$ and $+$ indicate upstream and downstream deflections respectively. These conditions isolated velocity structures that appeared simultaneously with moderately-large upstream (figure 5.3a,b) and downstream (figure 5.3c,d) deflections of the Malley probe beam path. This is equivalent to moderately-large negative (figure 5.3a,b) and positive (figure 5.3c,d) streamwise density gradients, integrated along the beam path. The Malley probe passes through the flow at $x/\delta = 0$.

Gradients are observed in the velocity fields seen in figure 5.2 at the point where the Malley probe passes through the flow. For upstream deflections of the Malley probe, which are associated with negative streamwise density gradients, a negative streamwise gradient is observed in the streamwise velocity field in figure 5.2(a), while a positive streamwise gradient is observed in the wall-normal velocity field in figure 5.2(b). For downstream deflections, associated with positive streamwise density gradients, a positive streamwise gradient of the streamwise velocity field is observed in figure 5.2(c) and a negative streamwise gradient of the wall-normal velocity field is observed in figure 5.2(d). These findings suggest that, on average, $\partial\rho/\partial x \sim \partial u/\partial x$ and $\partial\rho/\partial x \sim -\partial v/\partial x$. Note that the shape of the gradients observed in the averaged velocity fields in figure 5.2 would not be expected to be observed instantaneously. The vertically aligned streamwise gradients reflect the integral nature of the Malley probe measurement: gradient events anywhere along the beam path can lead to a beam deflection and are therefore averaged together.

The averaged velocity fields in figure 5.2 show some suggestion that multiple structures may be relevant to the Malley probe deflection. Near $x/\delta = 0$, localization is observed in the wall-normal fields, but some coherence extends outside of the field of view for both the streamwise and wall-normal fields. It is therefore of interest to consider filtering the result into large and small scales.

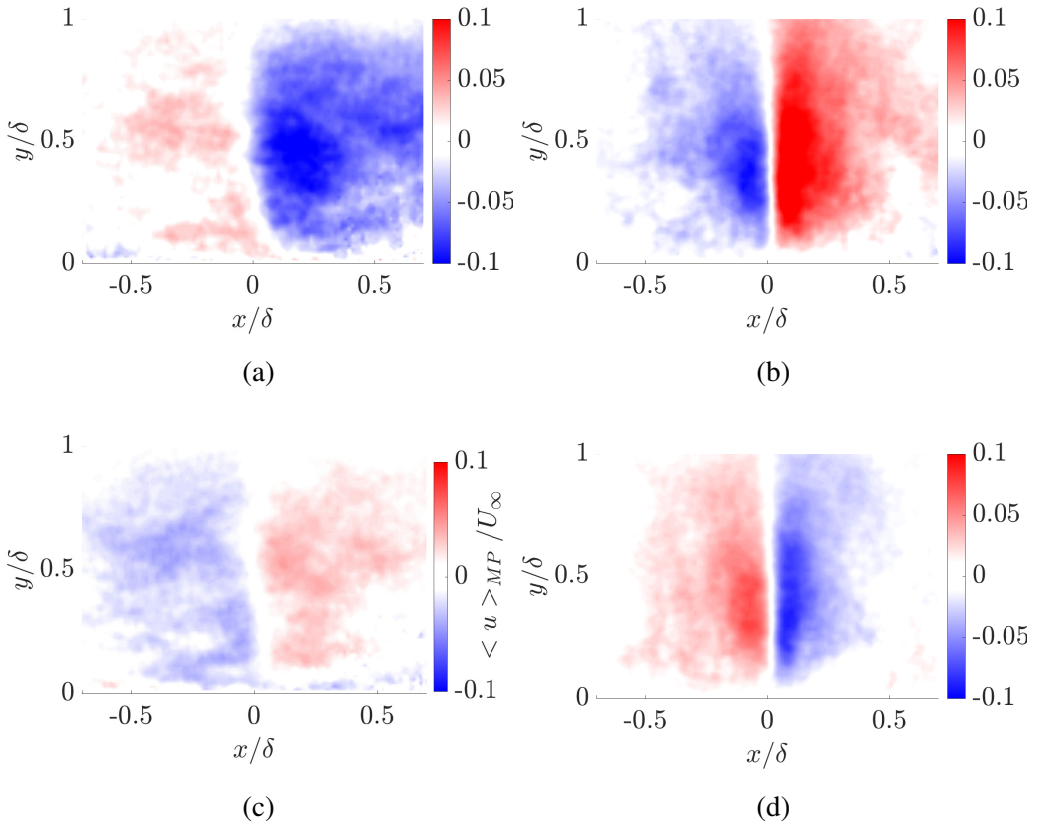

Figure 5.2: Conditional averages of (a,c) the streamwise velocity fluctuations $< u > /U_\infty$ and (b,d) the wall-normal velocity fluctuations $< v > /U_\infty$ given $\phi < -0.5\sigma$ (a,b) and $\phi > 0.5\sigma$, respectively corresponding to a moderately-large negative and positive streamwise gradient of density along the line $x = 0$. Distinct scales are observed of a large-scale nature in the streamwise velocity field and a small-scale nature in the wall-normal velocity field.

A high-pass Butterworth filter was implemented on the Malley probe temporal signal with a cutoff frequency of 300 Hz, or equivalently an approximate cutoff streamwise wavelength of $\lambda_x = 1$, chosen to match previous work by Mathis, Hutchins, and Marusic (2009), who used a spectral filter with a cutoff wavelength of 1δ to separate large and small scales. Future work includes testing the sensitivity of the results to the specific cut-off frequency chosen, and testing other filter types, including the Gaussian filter used throughout the rest of the thesis. The high-pass filtered Malley probe signal was defined as $\phi_s(t)$ and the new conditional averages were defined as

$$< u >_{MP_s} = \frac{1}{N} \sum_{t_i} u(x, y, t_i) \qquad \forall t_i \text{ s.t. } \phi_s(t_i) < -0.5\sigma(\phi_s) \tag{5.7}$$

and

$$< u >^{+}_{MP_s} = \frac{1}{N} \sum_{t_i} u(x, y, t_i) \qquad \forall t_i \text{ s.t. } \phi_s(t_i) > 0.5\sigma(\phi_s) \tag{5.8}$$

for the streamwise velocity field and

$$< v >^{-}_{MP_s} = \frac{1}{N} \sum_{t_i} v(x, y, t_i) \qquad \forall t_i \text{ s.t. } \phi_s(t_i) < -0.5\sigma(\phi_s) \tag{5.9}$$

and

$$< v >^{+}_{MP_s} = \frac{1}{N} \sum_{t_i} v(x, y, t_i) \qquad \forall t_i \text{ s.t. } \phi_s(t_i) > 0.5\sigma(\phi_s) \tag{5.10}$$

for the wall-normal velocity field. In figure 5.3, the conditionally-averaged, filtered results are shown for upstream deflections of the Malley probe (figures 5.3a,b) and downstream deflections of the Malley probe (figures 5.3c,d) for both the streamwise velocity field (figure 5.3a,c) and the wall-normal velocity field (figure 5.3b,c).

The gradients that were observed under the full Malley probe average in figure 5.2 remain clear in the wall-normal field with the high-pass filtered Malley probe (figure 5.3b,d), but disappear in the streamwise field (figure 5.3a,c). This suggests that small scales are associated with this gradient in the wall-normal field, while perhaps larger scales are associated with the gradient observed in the streamwise velocity field in figure 5.2(a,c). In figure 5.3(a), the streamwise velocity field is observed to be dominated by a tall region of low-momentum fluid. In figure 5.3(c), there is some evidence of alternating positive and negative inclined features in the streamwise velocity field, with a shear layer occurring at roughly $x/\delta = 0$ and $y/\delta = 0.3$. In the wall-normal velocity field, a structure with a distinct streamwise length scale is observed to be correlated to both negative (figure 5.3b) and positive (figure 5.3d) streamwise density gradients. Fourier transforms along a streamwise cut of both figure 5.3(b) and figure 5.3(d) identify a dominant streamwise wavelength of 0.36δ. The height of the structure is observed to span the full boundary layer thickness. The phase of this scale is distinct in figure 5.3(b) and figure 5.3(d), such that positive streamwise gradients in the wall-normal velocity field are associated with negative streamwise gradients in the density field, and vice versa. While the features in figure 5.3(d) are slightly weaker in amplitude than those in figure 5.3(b), they are observed to be equally coherent, a distinction from the streamwise velocity field.

Conditional averaging velocity field on both scale interaction and scalar signal

The presence of multiple velocity scales in the conditionally averaged flow fields in figure 5.3 suggested that the scale interaction phenomenon described in chapter

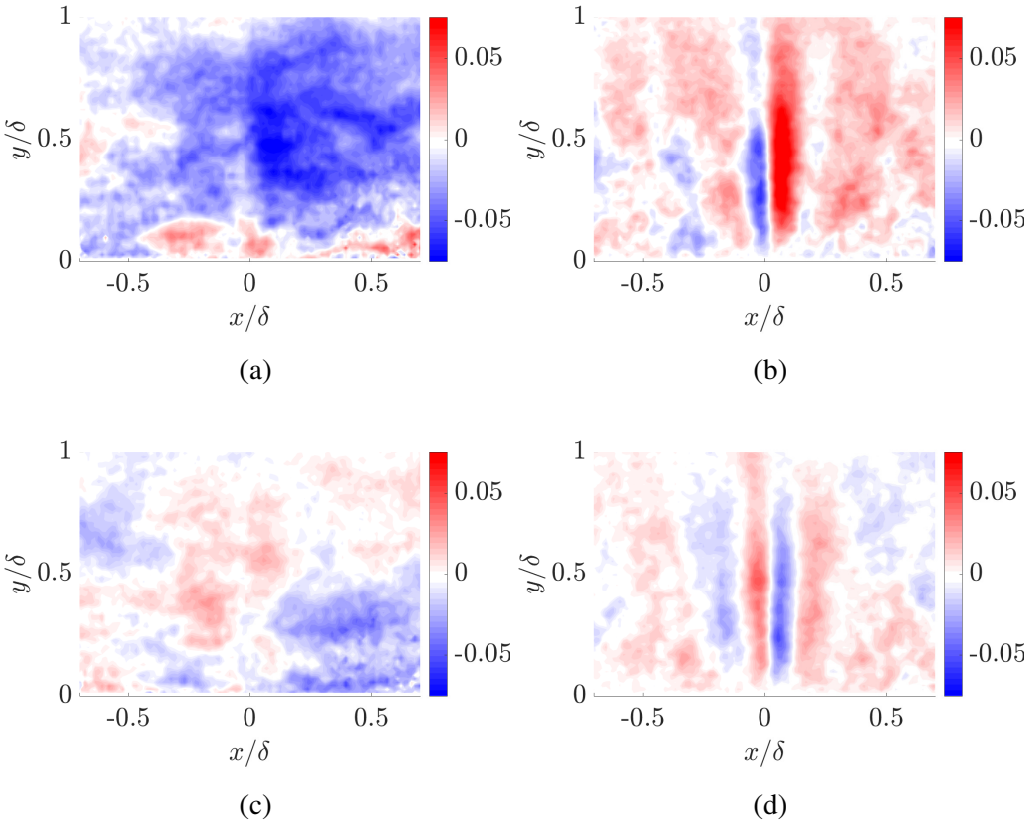

Figure 5.3: Conditional averages of (a,c) the streamwise velocity fluctuations $< u >_{MP_s} /U_\infty$ and (b,d) the wall-normal velocity fluctuations $< v >_{MP_s} /U_\infty$ given $\phi_s < -0.5\sigma$ (a,b) and $\phi_s > 0.5\sigma$, respectively corresponding to a moderately-large negative and positive streamwise gradient of density along the line $x = 0$. Distinct scales are observed of a large-scale nature in the streamwise velocity field and a small-scale nature in the wall-normal velocity field.

4 could be relevant to this problem. To explore this connection, the MP / P_{1D} conditional averaging technique described in chapter 2 was used, simultaneously conditioning on both the Malley probe deflection and the projection of the data onto a 1D model of an LSM. The results for an upstream deflection are given by

$$< u >_{MP,P}^{-}(x,y) = \frac{1}{\tilde{n}} \sum_{\tilde{t}} \left(\frac{1}{N} \sum_{t_i} u(x,y,t_i) \right.$$
$$\left. \forall t_i \text{ s.t. } \phi_s(t_i) < -0.5\sigma \text{ and } \left(\frac{u(x,y_c,t_i) \cdot \tilde{u}(x,y_c,\tilde{t})}{|u(x,y_c,t_i)||\tilde{u}(x,y_c,\tilde{t})|} \right) = R^* > R_{th} \right) \tag{5.11}$$

and

$$< v >^{-}_{MP,P}(x,y) = \frac{1}{\tilde{n}} \sum_{\tilde{t}} \left(\frac{1}{N} \sum_{t_i} v(x,y,t_i) \right.$$
$$\left. \forall t_i \text{ s.t. } \phi_s(t_i) < -0.5\sigma \text{ and } \left(\frac{u(x,y_c,t_i) \cdot \tilde{u}(x,y_c,\tilde{t})}{|u(x,y_c,t_i)||\tilde{u}(x,y_c,\tilde{t})|} \right) = R^* > R_{th} \right) \tag{5.12}$$

for the streamwise and wall-normal velocity fields respectively. The velocity fields were additionally filtered using the spatial Gaussian filter described in chapters 2 and 4. These small-scale velocity fields were averaged as

$$< u_s >^{-}_{MP,P}(x,y) = \frac{1}{\tilde{n}} \sum_{\tilde{t}} \left(\frac{1}{N} \sum_{t_i} u_s(x,y,t_i) \right.$$
$$\left. \forall t_i \text{ s.t. } \phi_s(t_i) < -0.5\sigma \text{ and } \left(\frac{u(x,y_c,t_i) \cdot \tilde{u}(x,y_c,\tilde{t})}{|u(x,y_c,t_i)||\tilde{u}(x,y_c,\tilde{t})|} \right) = R^* > R_{th} \right), \tag{5.13}$$

and

$$< v_s >^{-}_{MP,P}(x,y) = \frac{1}{\tilde{n}} \sum_{\tilde{t}} \left(\frac{1}{N} \sum_{t_i} v_s(x,y,t_i) \right.$$
$$\left. \forall t_i \text{ s.t. } \phi_s(t_i) < -0.5\sigma \text{ and } \left(\frac{u(x,y_c,t_i) \cdot \tilde{u}(x,y_c,\tilde{t})}{|u(x,y_c,t_i)||\tilde{u}(x,y_c,\tilde{t})|} \right) = R^* > R_{th} \right). \tag{5.14}$$

Note that, unlike in chapter 4, the small-scale fields are not squared before averaging. The equations for a downstream deflection are not shown here, but differ from equations 5.11 to 5.14 simply by the condition $\phi_s(t_i) > 0.5\sigma$.

Figures 5.4 and 5.5 show a compilation of eight conditionally averaged fields using the MP / P_{1D} conditional averaging technique with a negative and positive Malley probe deflection angle respectively. The black line in all frames represents an isocontour of the conditionally averaged streamwise velocity field in the laboratory frame $< u >_{MP/P_{1D}} + \bar{U} = 0.8U_\infty$, where $\bar{U}$ is the mean streamwise velocity field. The dashed lines in figures 5.4(c,d) and 5.5(c,d) show the location of the Malley probe relative to the velocity field for each panel.

Figures 5.4 and 5.5 show evidence that the scales observed in figure 5.3 interact. The P_{1D} projection method returns the large-scale streamwise and wall-normal scales, paneled by phase, in figures 5.4(a,b) and 5.5(a,b). In figures 5.4(c,d) and 5.5(c,d), the small-scale streamwise and wall-normal velocity fields are shown.

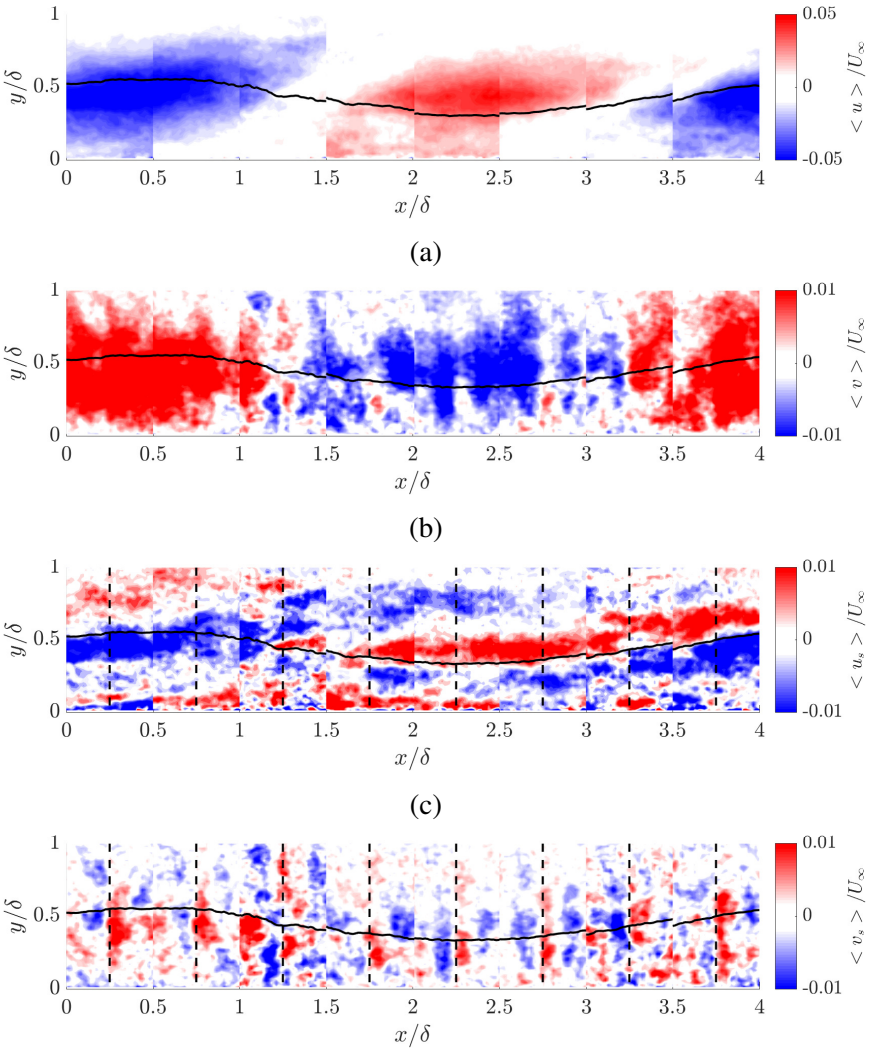

Figure 5.4: Conditional averages of (a) the streamwise velocity field $< u >_{MP/P_{1D}} /U_\infty$, (b) the wall-normal velocity field $< v >_{MP/P_{1D}} /U_\infty$, (c) the small-scale streamwise velocity field $< u_s >_{MP/P_{1D}} /U_\infty$ and (d) the small scale wall-normal velocity field $< v_s >_{MP/P_{1D}} /U_\infty$ given two conditions. The first condition is $\phi_s < -0.5\sigma$ at the x locations highlighted with dashed black lines. The second is the P_{1D} condition described in chapter 2 and 4 for an LSM model. The projection and conditional averaging are done over eight phases of the model and the eight panels are shown stitched together. The black line in all panels represents $< u >_{MP/P1D} + \bar{U} = 0.8U_\infty$.

The small scale observed in figure 5.3(b,d) is still observed in figures 5.4(d) and 5.5(d), but rather than being extended through the height of the boundary layer, it is observed to be more compact in the wall-normal direction. Additionally, it is observed to sit at a different height from the wall depending on the phase of the

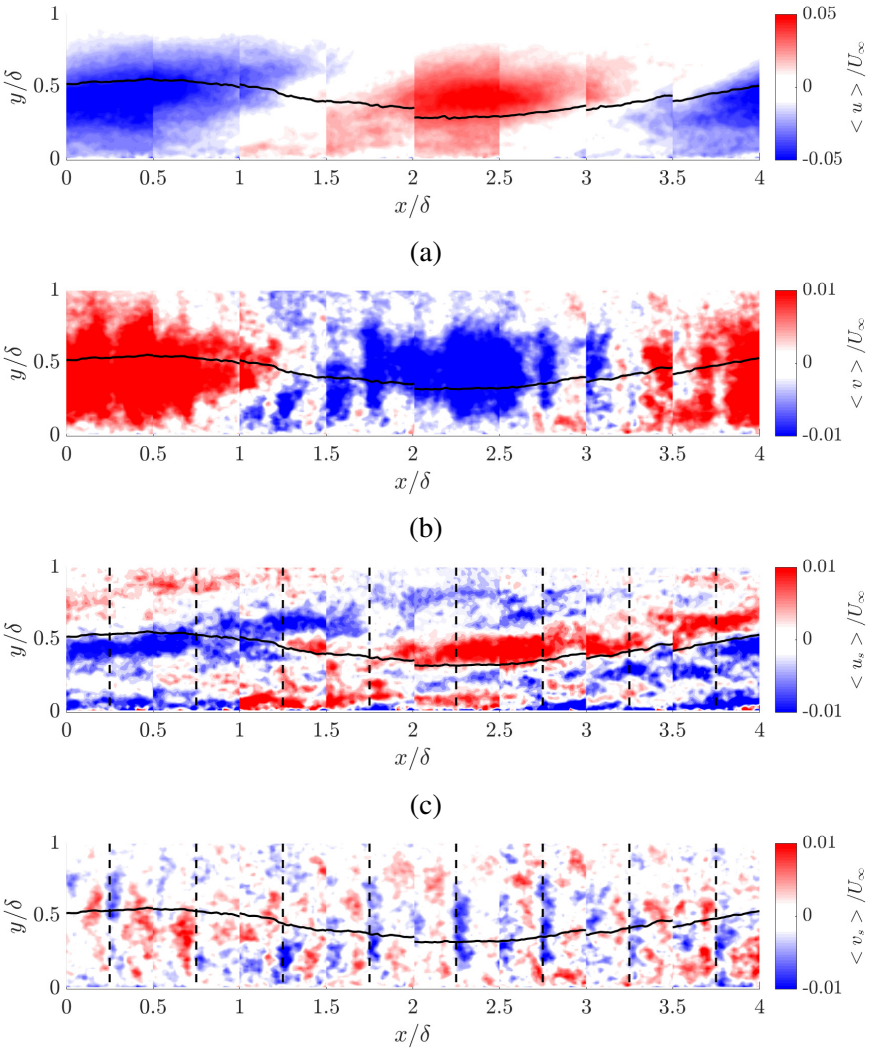

Figure 5.5: Conditional averages of (a) the streamwise velocity field $< u >_{MP/P_{1D}} /U_\infty$, (b) the wall-normal velocity field $< v >_{MP/P_{1D}} /U_\infty$, (c) the small-scale streamwise velocity field $< u_s >_{MP/P_{1D}} /U_\infty$ and (d) the small scale wall-normal velocity field $< v_s >_{MP/P_{1D}} /U_\infty$ given two conditions. The first condition is $\phi_s > 0.5\sigma$ at the x locations highlighted with dashed black lines. The second is the P_{1D} condition described in chapter 2 and 4 for an LSM model. The projection and conditional averaging are done over eight phases of the model and the eight panels are shown stitched together. The black line in all panels represents $< u >_{MP/P_{1D}} + \bar{U} = 0.8U_\infty$.

large scale velocity field (figures 5.4a and 5.5a). It appears to approximately follow the isocontour $< u >_{MP/P_{1D}} + \bar{U} = 0.8U_\infty$, supporting the critical layer hypothesis outlined in chapter 4. The only significant difference between figures 5.4 and 5.5 is in the small-scale wall-normal velocity fields (figures 5.4d and 5.5d), where

the orientation of the small-scale wall-normal structure reverses surrounding the Malley probe location. The streamwise gradient of the wall-normal velocity field is observed to be positive at the Malley probe location for figure 5.4(d) and negative at the Malley probe location for figure 5.5(d). This is shown more clearly in figure 5.6, where the conditional average of the streamwise gradient of the wall-normal velocity field is shown for each sense of ϕ.

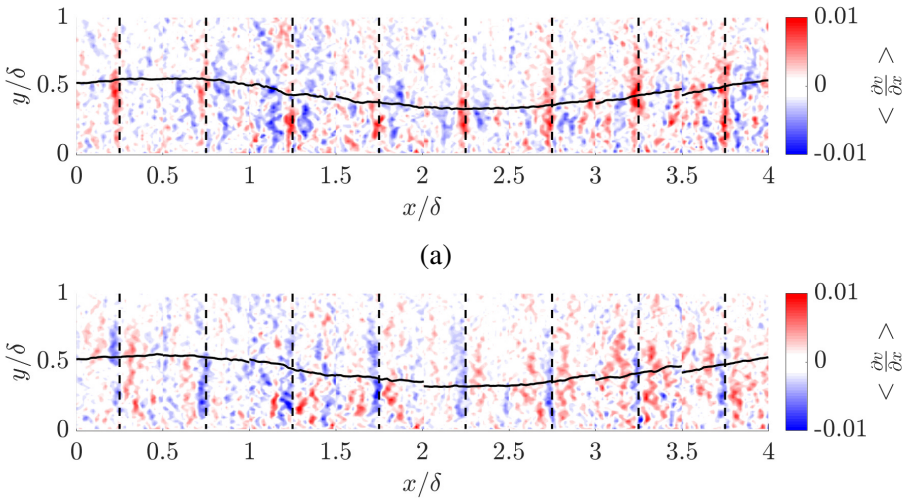

(a)

(b)

Figure 5.6: The conditional average of the streamwise derivative of the wall-normal velocity field for $\phi_s < -0.5\sigma$ (a) and $\phi_s > 0.5\sigma$ (b).

Table 5.1 lists the number of PIV frames that went into making figures 5.4 and 5.5, as well as the percentage of total frames that this represents. Approximately 30% of frames were identified as meeting the conditions. Table 5.2 provides the number of frames associated with each estimated phase γ^* for figures 5.4 and 5.5.

	$\phi_s < -0.5\sigma$	$\phi_s > 0.5\sigma$
N frames	1420	1637
% frames	28	32

Table 5.1: Number and percentage of frames used for the MP / P_{1D} conditionally-averaged results of figures 5.4 and 5.5.

The variable height of the small scales places them coincident with strong shear layers in the streamwise velocity field (see figure 3.1 in chapter 3). The localization of the small-scale coherence in v on the strong shear layer suggests that it may be the interaction between a gradient in u and a gradient in v that is ultimately most correlated to strong gradients in the density field. The overlap of the u and

	1	2	3	4	5	6	7	8
N frames $\phi_s < -0.5\sigma$:	271	188	119	120	282	208	104	128
N frames $\phi_s > 0.5\sigma$:	315	220	123	172	303	218	119	166
% frames $\phi_s < -0.5\sigma$	5	4	2	2	6	4	2	2
% frames $\phi_s < -0.5\sigma$	5	4	2	2	6	4	2	2

Table 5.2: The number of frames associated with each estimated phase γ^* for the MP / P_{1D} conditional-averaging method applied to PIV data with an LSM model, associated with figures 5.4 and 5.5. The numeric label corresponds to the index of γ^*, with $\gamma^* = [0, 2\pi)$ in increments of $\pi/4$.

v gradients also strengthens the hypothesis that a single strong gradient event is dominating the Malley probe signal, allowing the integral measurement to behave similarly to a point measurement.

As mentioned above, the small-scale wall-normal velocity structures in figures 5.4(d) and 5.5(d) are significantly more compact in the wall-normal direction than those in figure 5.3(b,d). The large wall-normal extent of the structure observed in figure 5.3(b,d) is hypothesized to be the result of averaging the compact structures observed in figures 5.4(d) and 5.5(d) at many heights in the boundary layer, effectively smearing the small scale in y such that it appears much taller in average than it would instantaneously. This process is schematically shown in figure 5.7.

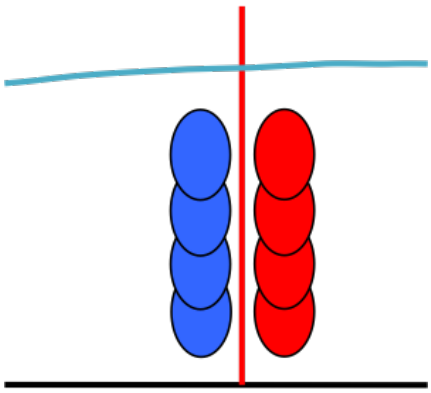

Figure 5.7: A schematic of the smearing of several compact small scale velocity structures into one tall averaged structure when the phase of the large scale is not accounted for. The red line represents the Malley probe, the black line shows the wall, the blue curve represents the edge of the boundary layer, and the red and blue ovals represent high-speed and low-speed wall-normal velocity structures. Each pair of structures is assumed to occur at a different instant, and their superposition here is associated with a smearing on average.

5.3 Modeling using resolvent analysis

Modeling individual velocity scales

Resolvent analysis was used to model the wall-normal coherence of the two velocity features in figure 5.3(a,b,d). The feature in the streamwise velocity field (figure 5.3a) was estimated as having a wavelength of 4δ based upon the structure observed in figure 5.3(a), characteristics of bulges from Kovasznay, Kibens, and Blackwelder, 1970, and statistical features of large scale motions described by Monty et al., 2009. The structure is assumed to be the same LSM described in chapters 3 and 4. The scale observed in the wall-normal velocity field of figure 5.3(b,d) was estimated as having a streamwise wavelength of 0.36δ (from the Fourier transform performed on figure 5.3b,d). Its spanwise wavelength was estimated to be equal to its streamwise wavelength, based upon some preliminary results using a 2D optical sensor called a Shack Hartmann sensor.[2] A convection velocity of the small scale was selected to be $0.8U_\infty$ for consistency with the results shown in chapter 4, where isocontours of $0.8U_\infty$ were observed to align with strong small-scale activity. However, as the convection velocity measured by the Malley probe was $0.83U_\infty$, fine-tuning of the assumed convection velocity may be considered in future work to improve the estimation. The amplitude of the large scale mode, χ_{LSM} was here set such that the amplitude of the large-scale streamwise velocity field matched that of the conditionally averaged result of figure 5.4(a). The choice of the amplitude of the small scale, χ_s, will be explained in the following subsection.

Figure 5.8 shows a streamwise – wall-normal cut of the model for the LSM (figure 5.8a,b) and the small scale (figure 5.8c,d) in the streamwise velocity field (figure 5.8a,c), and in the wall-normal velocity field (figure 5.8b,d). The models of both scales are more compact in the wall-normal direction than the Malley probe conditionally averaged result of figure 5.3, but they appear reasonably similar in the size of their wall-normal coherence to the results of conditionally averaging on both the LSM projection and on the Malley probe deflection, in figures 5.4 and 5.5.

Modeling the interaction of the identified scales

The scale interaction shown in figures 5.4 and 5.5 was modeled using multiple resolvent modes and phase information derived from amplitude modulation observations discussed at a high level in chapter 1 (Mathis, Hutchins, and Marusic, 2009; Jacobi

[2] This measurement and analysis was done at Caltech in the Merrill wind tunnel in collaboration with Stanislav Gordeyev and Nicholas DeLuca at the University of Notre Dame. The results mentioned were identified within private communication between the collaborators.

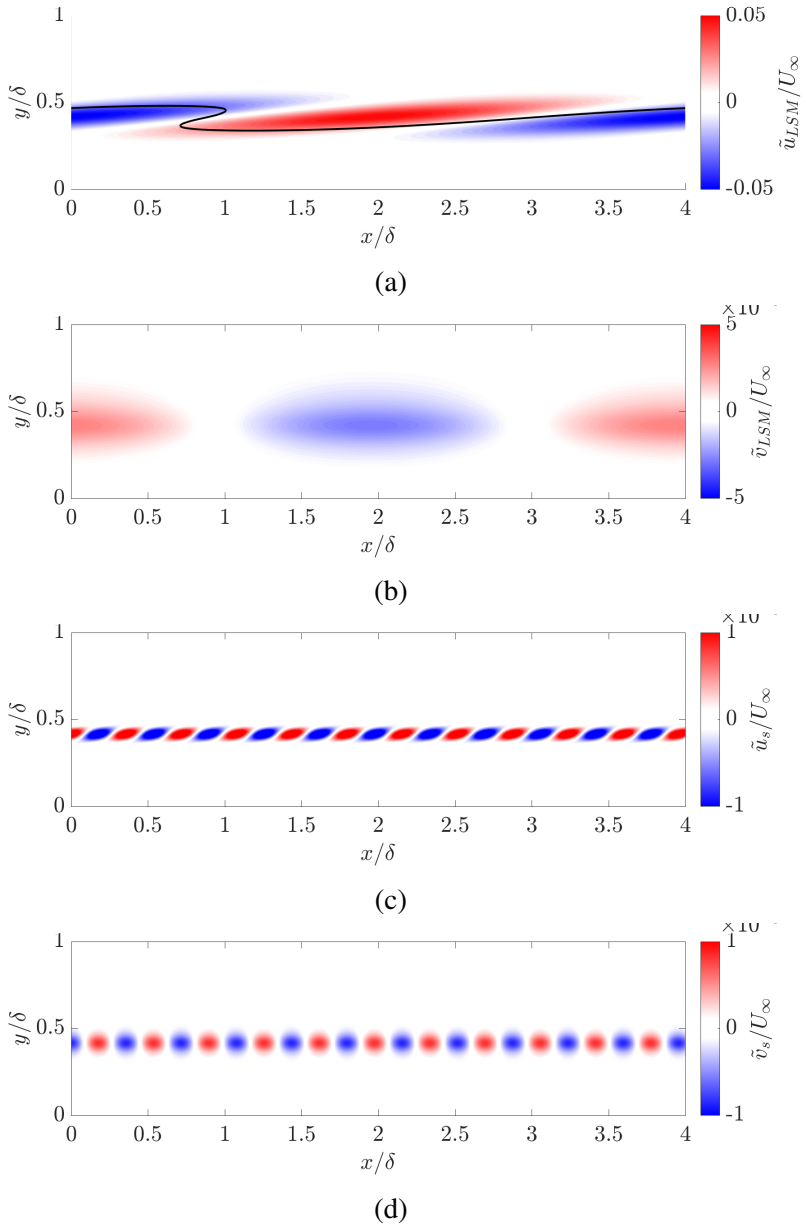

Figure 5.8: Models of the LSM (a,b) and small-scale (c,d) fluctuating velocity structures observed in figure 5.3, shown in the wall-normal – streamwise plane. Streamwise (a,c) and wall-normal (b) velocity fields are shown. Resolvent analysis is used to identify the wall-normal coherence of the models. The black line in (a) indicates $\tilde{u}_{LSM} + \bar{U} = 0.8U_\infty$ where $\tilde{u}_{LSM}$ is the fluctuating streamwise velocity field of the large scale resolvent mode.

and McKeon, 2013). A total of seven resolvent modes were used, with three values of k_x and k_z. The modes consisted of three 'triads', sets of modes in which two of the wavenumbers sum to the third. Triads allow for direct comparison to amplitude modulation statistics, as discussed by Duvvuri and McKeon (2015). All three triads

consist of the same large scale, called mode 1, with an additional two small-scale modes, called modes 2 and 3. The wavenumbers, phase velocities, temporal frequencies, and phases of the modes are shown in table 5.3. The modes are listed in terms of the wavenumbers rather than wavelengths to better see their triadic relationship, but that mode 2 at a wavespeed of $0.8U_\infty$ corresponds to the small-scale model shown in 5.8(c). The phase, γ, is here not defined as $\gamma = -\omega t$ but is instead considered separately from the temporal term, in order to match temporally-constant phase relationships observed in the literature.

Mode	$k_x\delta$	$k_z\delta$	c/U_∞	$\omega\delta/U_\infty$	γ
1	$\pi/2$	2π	0.800	32.5	π
2	5.56π	5.56π	0.780	352.0	0
			0.800	360.9	
			0.820	370.0	
3	5.06π	3.56π	0.778	319.4	π
			0.800	328.5	$3\pi/2$
			0.822	337.5	2π

Table 5.3: Set of wavenumbers for three triads of resolvent modes used to model the scale interaction observed in figures 5.4 and 5.5. Modes 2 and 3 each have three different wavenumbers considered, allowing them to be observable at different heights from the wall.

All three triads have modes with the same spatial wavenumbers. The distinction between the three triads comes from the temporal frequencies, ω, of modes 2 and 3, and in the phases of mode 3. The phase speed, c, of mode 2 was set to range from $0.78U_\infty$ to $0.82U_\infty$ in increments of $0.02U_\infty$. This set the temporal frequencies of mode 2 through the relation $\omega = ck_x$. The temporal frequencies of mode 3 were set such that $\omega_3 = \omega_2 - \omega_1$. The phase of mode 1 was set to π and the phase of mode 2 was set to 0 for all convection velocities. The phase of mode 3 was set to vary such that the sum of phases 2 and 3 was in phase with mode 1 at their slowest convection velocity and out of phase with mode 2 at their fastest convection velocity. The amplitude of each small-scale mode was set to be equal, and the sum of the small scales was set such that the amplitude of the summed small-scale wall-normal velocity field matched the amplitude of the small-scale wall-normal velocity field

of figure 5.4(d). The sum of the streamwise modeled small scales is given by

$$\begin{aligned}\Sigma\tilde{u}_s = &\sum_{i=1}^{3}\left(\mathrm{Re}[\hat{u}_{2,i}(y)(e^{i(k_{x,2}x+k_{z,2}z-\omega_{2,i}t+\gamma_2)}+e^{i(k_{x,2}x-k_{z,2}z-\omega_{2,i}t+\gamma_2)}]\right)\\ &+\sum_{i=1}^{3}\left(\mathrm{Re}[\hat{u}_{3,i}(y)(e^{i(k_{x,3}x+k_{z,3}z-\omega_{3,i}t+\gamma_{3,i})}+e^{i(k_{x,3}x-k_{z,3}z-\omega_{3,i}t+\gamma_{3,i})}]\right).\end{aligned} \tag{5.15}$$

For the wall-normal small scales, the sum is given by

$$\begin{aligned}\Sigma\tilde{v}_s = &\sum_{i=1}^{3}\left(\mathrm{Re}[\hat{v}_{2,i}(y)(e^{i(k_{x,2}x+k_{z,2}z-\omega_{2,i}t+\gamma_2)}+e^{i(k_{x,2}x-k_{z,2}z-\omega_{2,i}t+\gamma_2)}]\right)\\ &+\sum_{i=1}^{3}\left(\mathrm{Re}[\hat{v}_{3,i}(y)(e^{i(k_{x,3}x+k_{z,3}z-\omega_{3,i}t+\gamma_{3,i})}+e^{i(k_{x,3}x-k_{z,3}z-\omega_{3,i}t+\gamma_{3,i})}]\right).\end{aligned} \tag{5.16}$$

Figure 5.9 shows the streamwise fluctuating velocity field for mode 1, which is equivalent to the LSM model described in chapter 3. Figure 5.9(b,c) shows the streamwise ($\Sigma\tilde{u}_s$) and wall-normal ($\Sigma\tilde{v}_s$) velocity fields that are the result of the superposition of the six small scale modes. The wall-normal small scales in (c) are observed to appear to have a variation in their height as a function of the large-scale phase, as is observed in figures 5.4 and 5.5. The envelope of the structures seen in figure 5.9(b,c) will stay coherent in time because, though the individual small scale modes have differing phase speeds, the sum of mode 2 and mode 3 has the same phase speed as mode 1.

In figure 5.10, the large and small scales are summed to examine the full flow field in the streamwise (figure 5.10a,b) and wall-normal (figure 5.10c) velocity fields. The sum of the fluctuating streamwise velocity modes is defined as

$$\begin{aligned}\tilde{u} = &\mathrm{Re}\left[\hat{u}_1(y)(e^{i(k_{x,1}x+k_{z,1}z-\omega_1t+\gamma_1)}+e^{i(k_{x,1}x-k_{z,1}z-\omega_1t+\gamma_1)}\right]\\ &+\sum_{i=1}^{3}\left(\mathrm{Re}\left[\hat{u}_{2,i}(y)(e^{i(k_{x,2}x+k_{z,2}z-\omega_{2,i}t+\gamma_2)}+e^{i(k_{x,2}x-k_{z,2}z-\omega_{2,i}t+\gamma_2)}\right]\right)\\ &+\sum_{i=1}^{3}\left(\mathrm{Re}\left[\hat{u}_{3,i}(y)(e^{i(k_{x,3}x+k_{z,3}z-\omega_{3,i}t+\gamma_{3,i})}+e^{i(k_{x,3}x-k_{z,3}z-\omega_{3,i}t+\gamma_{3,i})}\right]\right)\end{aligned} \tag{5.17}$$

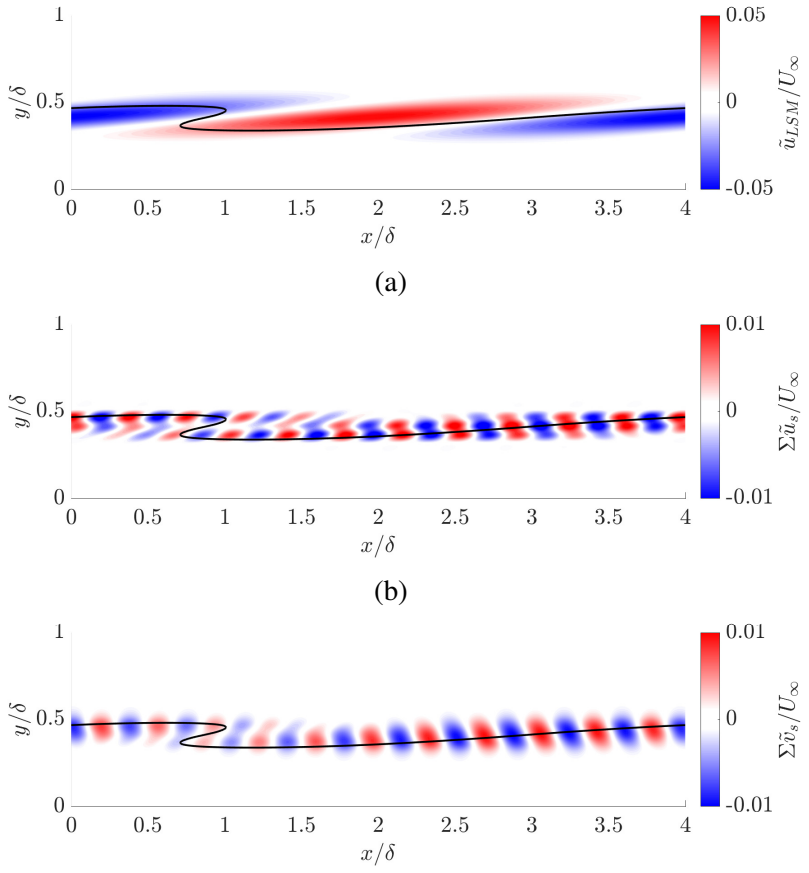

Figure 5.9: The interaction of the large and small scale velocity structures, shown in figures 5.4 and 5.5, is modeled using seven resolvent modes. The model of the large scale streamwise velocity mode is shown in (a) for reference, while (b,c) represent the streamwise and wall-normal fluctuating velocity fields, obtained from the superposition of six small scale resolvent modes with phases set from amplitude modulation statistics. Reasonable agreement is seen with figures 5.4 and 5.5.

while the streamwise sum including the mean is defined as

$$\begin{aligned}\tilde{U} =&\bar{U}(y) + \mathrm{Re}\left[\hat{u}_1(y)(e^{i(k_{x,1}x+k_{z,1}z-\omega_1 t+\gamma_1)} + e^{i(k_{x,1}x-k_{z,1}z-\omega_1 t+\gamma_1)}\right] \\ &+ \sum_{i=1}^{3}\left(\mathrm{Re}\left[\hat{u}_{2,i}(y)(e^{i(k_{x,2}x+k_{z,2}z-\omega_{2,i}t+\gamma_2)} + e^{i(k_{x,2}x-k_{z,2}z-\omega_{2,i}t+\gamma_2)}\right]\right) \\ &+ \sum_{i=1}^{3}\left(\mathrm{Re}\left[\hat{u}_{3,i}(y)(e^{i(k_{x,3}x+k_{z,3}z-\omega_{3,i}t+\gamma_{3,i})} + e^{i(k_{x,3}x-k_{z,3}z-\omega_{3,i}t+\gamma_{3,i})}\right]\right).\end{aligned} \tag{5.18}$$

For the wall-normal velocity field, the full sum is given by

$$\begin{aligned}\tilde{v} =& \mathrm{Re}\left[\hat{v}_1(y)(e^{i(k_{x,1}x+k_{z,1}z-\omega_1 t+\gamma_1)} + e^{i(k_{x,1}x-k_{z,1}z-\omega_1 t+\gamma_1)}\right] \\ &+ \sum_{i=1}^{3}\left(\mathrm{Re}\left[\hat{v}_{2,i}(y)(e^{i(k_{x,2}x+k_{z,2}z-\omega_{2,i}t+\gamma_2)} + e^{i(k_{x,2}x-k_{z,2}z-\omega_{2,i}t+\gamma_2)}\right]\right) \\ &+ \sum_{i=1}^{3}\left(\mathrm{Re}\left[\hat{v}_{3,i}(y)(e^{i(k_{x,3}x+k_{z,3}z-\omega_{3,i}t+\gamma_{3,i})} + e^{i(k_{x,3}x-k_{z,3}z-\omega_{3,i}t+\gamma_{3,i})}\right]\right).\end{aligned} \tag{5.19}$$

The large-scale streamwise feature is still observable in (figure 5.10a,b) (compared to figure 3.2 in chapter 3, for example), but the edges of the large scale feature are observed to be corrugated. More corrugation is observed in figure 5.10(a) in the region of positive fluctuating shear ($x/\delta \approx 2-4$) than in the region of negative fluctuating shear ($x/\delta \approx 0-2$). This occurs due to the phase relationship between the large and small scales that was derived from amplitude modulation statistics. The observation of strong small scales at shear layers in the model is compatible with observations of Baars, Hutchins, and Marusic (2017) in fully-turbulent, experimental flows. The large-scale wall-normal velocity feature is also observable, but the small scales are observed to be easily distinguishable through the large scale mode.

Modeling the scalar field

To obtain an approximation of the scalar field corresponding to the deflection of the Malley probe, a passive scalar resolvent model was utilized. As discussed in chapter 2, the Navier-Stokes and passive scalar equations were reformulated in a resolvent framework, allowing for scalar modes to be computed alongside velocity modes. The Prandtl number was set at 0.7 and the boundary conditions of the scalar were set to correspond to the largest value of heating at the wall, with a decaying mean temperature profile as one reached the free stream.

The mean temperature field used for formulating the scalar resolvent is given in chapter 2. In the present work, the fully heated profile of Antonia, Danh, and Prabhu (1977) was used, as it was at the appropriate Reynolds number and represented a canonical passive scalar transport flow, leading to a generalizable result. However, future work will consider the experimental mean at the measurement location, which includes the cool internal layer. The two profiles match in the region of the flow considered, suggesting that the final result should be similar, but the influence of a change in the mean on the final scalar modes warrants further study. The mean profile came from a flow with a Prandtl number of 0.7.

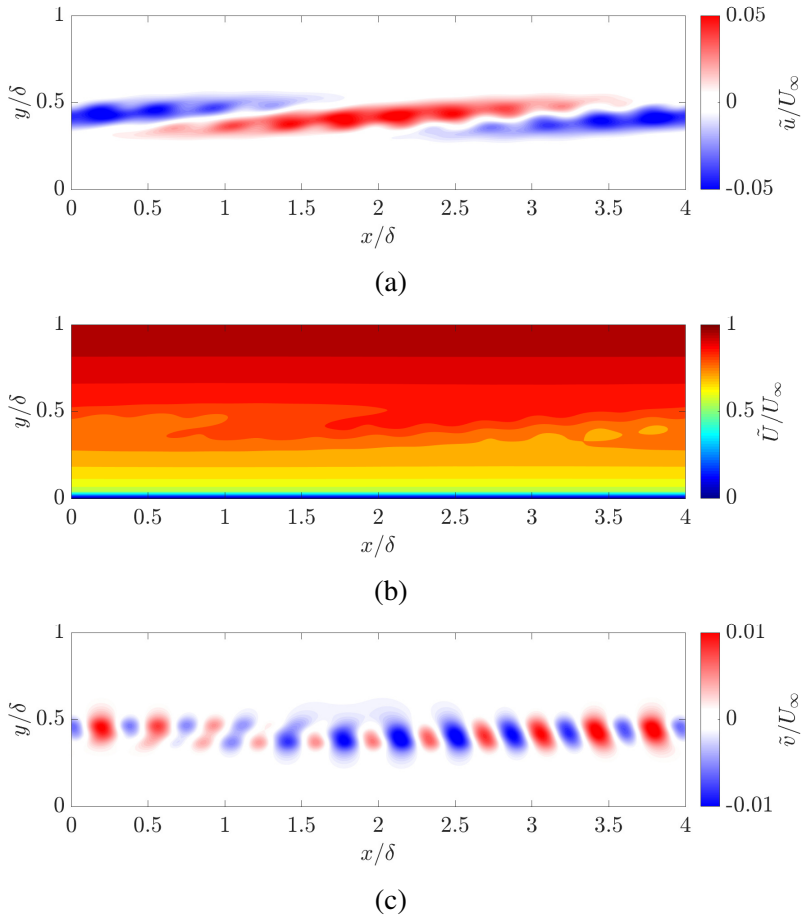

Figure 5.10: The sum of the large and small scale velocity fields of figure 5.9 is shown for the streamwise velocity field (a,b) and the wall-normal velocity field (c). The mean velocity field is included in (b).

The set of modes and phases used for figures 5.9 and 5.10 were used to identify the corresponding scalar field, given by

$$\begin{aligned}\tilde{T}' =& \mathrm{Re}\left[\hat{T}_1(y)(e^{i(k_{x,1}x+k_{z,1}z-\omega_1 t+\gamma_1)} + e^{i(k_{x,1}x-k_{z,1}z-\omega_1 t+\gamma_1)}\right] \\ &+ \sum_{i=1}^{3}\left(\mathrm{Re}\left[\hat{T}_{2,i}(y)(e^{i(k_{x,2}x+k_{z,2}z-\omega_{2,i}t+\gamma_2)} + e^{i(k_{x,2}x-k_{z,2}z-\omega_{2,i}t+\gamma_2)}\right]\right) \\ &+ \sum_{i=1}^{3}\left(\mathrm{Re}\left[\hat{T}_{3,i}(y)(e^{i(k_{x,3}x+k_{z,3}z-\omega_{3,i}t+\gamma_{3,i})} + e^{i(k_{x,3}x-k_{z,3}z-\omega_{3,i}t+\gamma_{3,i})}\right]\right),\end{aligned} \tag{5.20}$$

shown in figure 5.11(c). The sum of the fluctuating model with the mean temperature

profile gives

$$\begin{aligned}\tilde{T} =&\bar{T}(y) + \mathrm{Re}\left[\hat{T}_1(y)(e^{i(k_{x,1}x+k_{z,1}z-\omega_1 t+\gamma_1)} + e^{i(k_{x,1}x-k_{z,1}z-\omega_1 t+\gamma_1)}\right] \\ &+ \sum_{i=1}^{3}\left(\mathrm{Re}\left[\hat{T}_{2,i}(y)(e^{i(k_{x,2}x+k_{z,2}z-\omega_{2,i}t+\gamma_2)} + e^{i(k_{x,2}x-k_{z,2}z-\omega_{2,i}t+\gamma_2)}\right]\right) \\ &+ \sum_{i=1}^{3}\left(\mathrm{Re}\left[\hat{T}_{3,i}(y)(e^{i(k_{x,3}x+k_{z,3}z-\omega_{3,i}t+\gamma_{3,i})} + e^{i(k_{x,3}x-k_{z,3}z-\omega_{3,i}t+\gamma_{3,i})}\right]\right),\end{aligned} \tag{5.21}$$

shown in figure 5.11(b). The same ratio of weights is used for the scalar field as was used for the streamwise velocity field. Due to the sum of the large and small scales, the scalar field is observed to be corrugated. The scalar gradient, shown in figure 5.11(c) is therefore wavy, leading to streamwise density gradients that can deflect the Malley probe.

A similarity is observed between the streamwise velocity field and the scalar field. Because of the opposite boundary conditions on U and T (slowest and warmest near the wall, fastest and coldest away from the wall), the streamwise velocity and temperature fluctuating modes in figure 5.9 and 5.11 have opposite phase. When summed with the mean profiles of U and T, coincident bulges of low momentum and high temperature are observed. These bulges correspond to both uniform momentum and temperature zones with gradients of both velocity and temperature along their backs. This is compatible with the ramp-cliff observations made using cold wires by Chen and Blackwelder (1978). Understanding the similarity between the streamwise velocity field and the scalar field within the context of the resolvent operator and the resolvent forcing is a topic of future work.

Simulating Malley probe measurement from model

Using this model of the scalar field, the effect of a Malley probe was simulated using equation 5.2, derived in chapter 2. The fluctuating and averaged density fields were approximated from the modeled temperature field using the ideal gas law.

$$\begin{aligned}\rho &= \frac{P}{RT} \\ (\overline{\rho} + \rho') &= \frac{(\overline{P} + P')}{R(\overline{T} + T')} \\ \overline{\rho} &= \frac{\overline{P}}{R\overline{T}}\end{aligned} \tag{5.22}$$

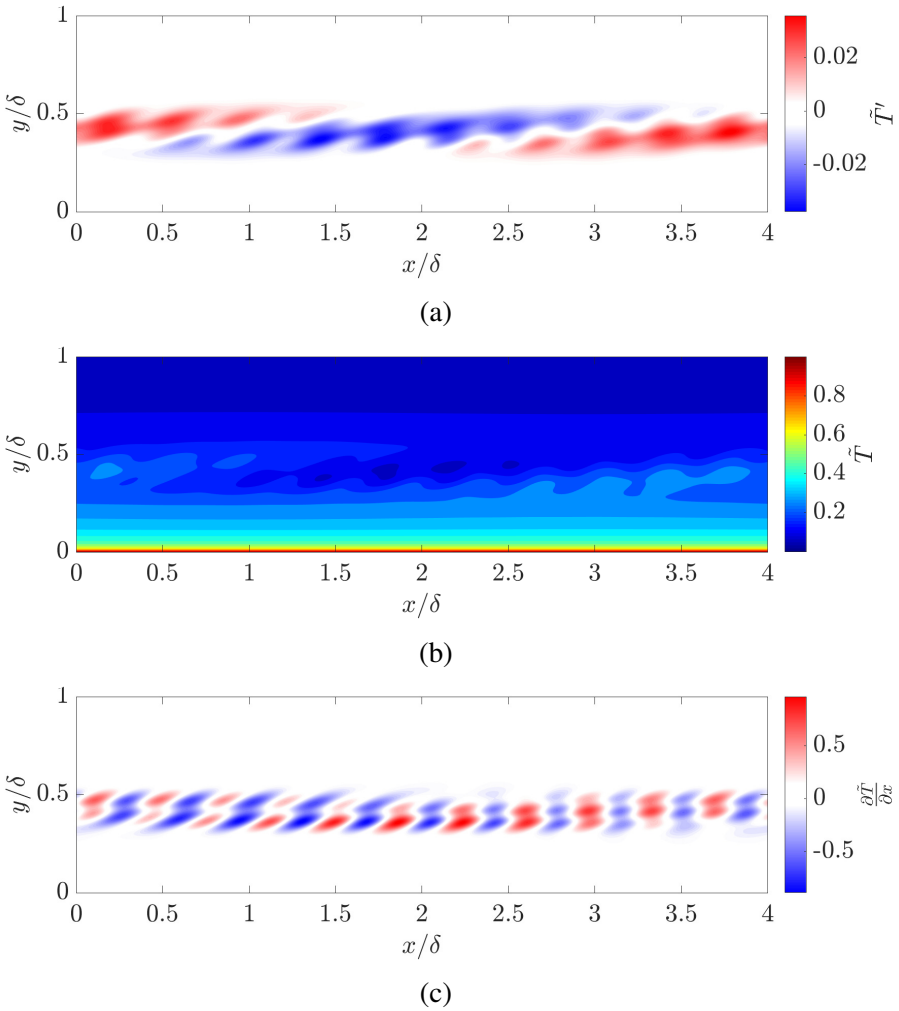

Figure 5.11: A model composed of scalar resolvent modes shows the temperature field in the $x-y$ plane (a,b) and the streamwise derivative of the temperature field in the $x-y$ pane (c). This temperature field is associated with the velocity field seen in figure 5.10. The fluctuating temperature field is shown in (a), while the sum of the fluctuating temperature field and the mean temperature field is shown in (b).

$$\rho' = \rho - \overline{\rho} = \frac{P'\overline{T} - \overline{P}T'}{R(\overline{T}^2 + \overline{T}T')} \tag{5.23}$$

Experimentally, it was observed that Malley probe deflection did not occur without the addition of heating, suggesting that P' is small. For the duration of the work, it will be assumed that $P'\overline{T} << \overline{P}T'$, but it is recommended as part of future work to include this term in the model using the resolvent pressure model formulated by Dr. Mitul Luhar to evaluate its importance (Luhar, Sharma, and McKeon, 2014).

	Pr	σ (μrad)	skewness
Data	0.7	9.5	-0.22
Model	0.7	0.25	-0.35
Model	1	0.26	-0.34
Model	7	0.3	-0.3

Table 5.4: Comparison of the measured and modeled Malley probe statistics, including standard deviation and skewness. Three values of Prandtl number are considered in the model: $Pr = 0.7, 1$, and 7.

$$\rho' = -\frac{\overline{P}T'}{R(\overline{T}^2 + \overline{T}T')}. \tag{5.24}$$

As the temperature field used in the ideal gas law is in Kelvin, the magnitude of $\overline{T}$ is always much larger than the magnitude of fluctuations about that mean temperature. Therefore, the equation is simplified even further to

$$\rho' = -\frac{\overline{P}T'}{R\overline{T}^2}. \tag{5.25}$$

At each streamwise and spanwise location in the model, a wall-normal integral was performed on the streamwise gradient of the density field. Appropriately normalized with K_{GD} and the ambient air density, this recreated a modeled form of the Malley probe signal, which will be termed $\tilde{\phi}$.

$$\tilde{\phi}(x, z) = \frac{K_{GD}}{1 + K_{GD}\rho_a} \int \frac{\partial \tilde{\rho}}{\partial x}(x, y, z)dy \tag{5.26}$$

The standard deviation and skewness of this modeled Malley probe signal is compared to the statistics of the original signal in table 5.4. The standard deviation of the modeled signal is observed to be significantly smaller than that of the measured signal. This likely reflects a natural difference in complexity between the seven-mode model and the fully turbulent field. The skewness of the model is observed to be of the appropriate sign, but is observed to be larger in magnitude than the measured skewness.

By averaging the velocity and scalar fields in a wall-normal – streamwise plane about $\tilde{\phi}$, one can model the original conditional averaging results of figure 5.3. This

represents

$$< \tilde{q} >^{-}_{MP} (x, y) = \frac{1}{N} \sum_{x_i} \sum_{z_j} \tilde{q}(x_i - \Delta x : x_i + \Delta x, y, z_j) \qquad \forall x_i, z_j \text{ s.t. } \tilde{\phi}(x_i, z_j) < -0.5\sigma \tag{5.27}$$

and

$$< \tilde{q} >^{+}_{MP} (x, y) = \frac{1}{N} \sum_{x_i} \sum_{z_j} \tilde{q}(x_i - \Delta x : x_i + \Delta x, y, z_j) \qquad \forall x_i, z_j \text{ s.t. } \tilde{\phi}(x_i, z_j) > 0.5\sigma \tag{5.28}$$

where $\tilde{q}$ is a modeled flow quantity, including the modeled fluctuating streamwise velocity field, the modeled wall-normal velocity field, the modeled density field, and the modeled streamwise density gradient. Here Δx is chosen to be 0.5δ to approximately match the PIV results.

Figures 5.12 and 5.13 show the conditionally averaged streamwise (figures 5.12a and 5.13a) and wall-normal (figures 5.12b and 5.13b) velocity fields of the model, as well as the density field (figures 5.12c and 5.13c) and the streamwise gradient of the density field (figures 5.12d and 5.13d). Figure 5.12 models the effect of a negative (upstream) Malley probe deflection angle, $\tilde{\phi} < -0.5\sigma(\tilde{\phi})$, while figure 5.13 models the effect of a positive (downstream) Malley probe deflection angle, $\tilde{\phi} > 0.5\sigma(\tilde{\phi})$. Note that $\sigma(\tilde{\phi})$ is the standard deviation of the modeled Malley probe signal.

The appropriate sense of the gradient is observed for the streamwise and wall-normal velocity fields in figures 5.12(a,b) and 5.13(a,b) relative to the density gradient. It is seen that $\partial u/\partial x \sim \partial \rho/\partial x$ and $-\partial v/\partial x \sim \partial \rho/\partial x$, as was observed in the original averages in figure 5.2. In the wall-normal velocity field, the wall-normal coherence of the averaged model in figures 5.12(b) and 5.13(b) is taller than that of the original resolvent mode shown in figure 5.8(d). The increased height in the averaged model reflects the smearing effect shown in the schematic in figure 5.7. However, a number of qualitative differences exist between the model and the averages of the data. The streamwise velocity field is observed to have a defined wall-normal coherence in the modeled fields (figures 5.12a, 5.13a), which was not observed in the original averages (figures 5.2a,c and 5.3a,c). Additionally, the wall-normal coherence of the wall-normal velocity structures in figures 5.12(b) and 5.13(b) is observed to be shorter than that observed in figure 5.2 or 5.3, indicating that the smearing covers a smaller portion of the boundary layer than what is observed in the fully turbulent field.

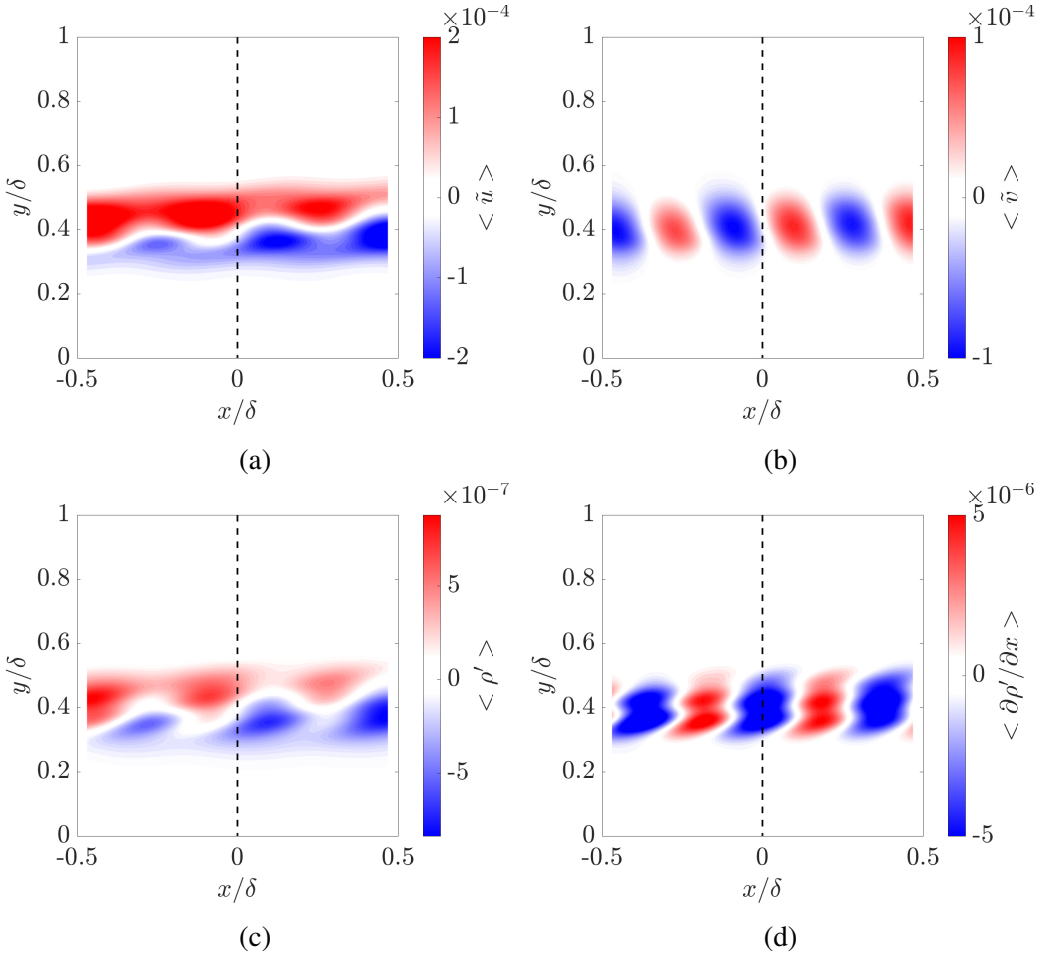

Figure 5.12: Averaging the models shown in figure 5.9 on a condition of a large negative wall-normal integral of the streamwise density gradient ($\tilde{\phi} < -0.5\sigma(\tilde{\phi})$) leads to the following fields for the fluctuating streamwise (a) and wall-normal (b) velocity fields, the fluctuating density field (c), and the streamwise gradient of fluctuating density field (d).

5.4 Effect of Prandtl number

To examine the effect of the Prandtl number, a model of the scalar field was constructed with Prandtl numbers of 1 and 7, indicating full similarity of momentum and thermal diffusivity, and the Prandtl number of water respectively. These models used the same mean temperature profile used previously, which came from a flow with a Prandtl number of 0.7. The change in Prandtl number was implemented exclusively in the resolvent operator for the scalar fluctuations. Implementing the analysis with a mean temperature profile with the accurate Prandtl number is a topic of future work. Figure 5.14 shows the temperature field in the streamwise – wall-normal plane for both simulated Prandtl numbers.

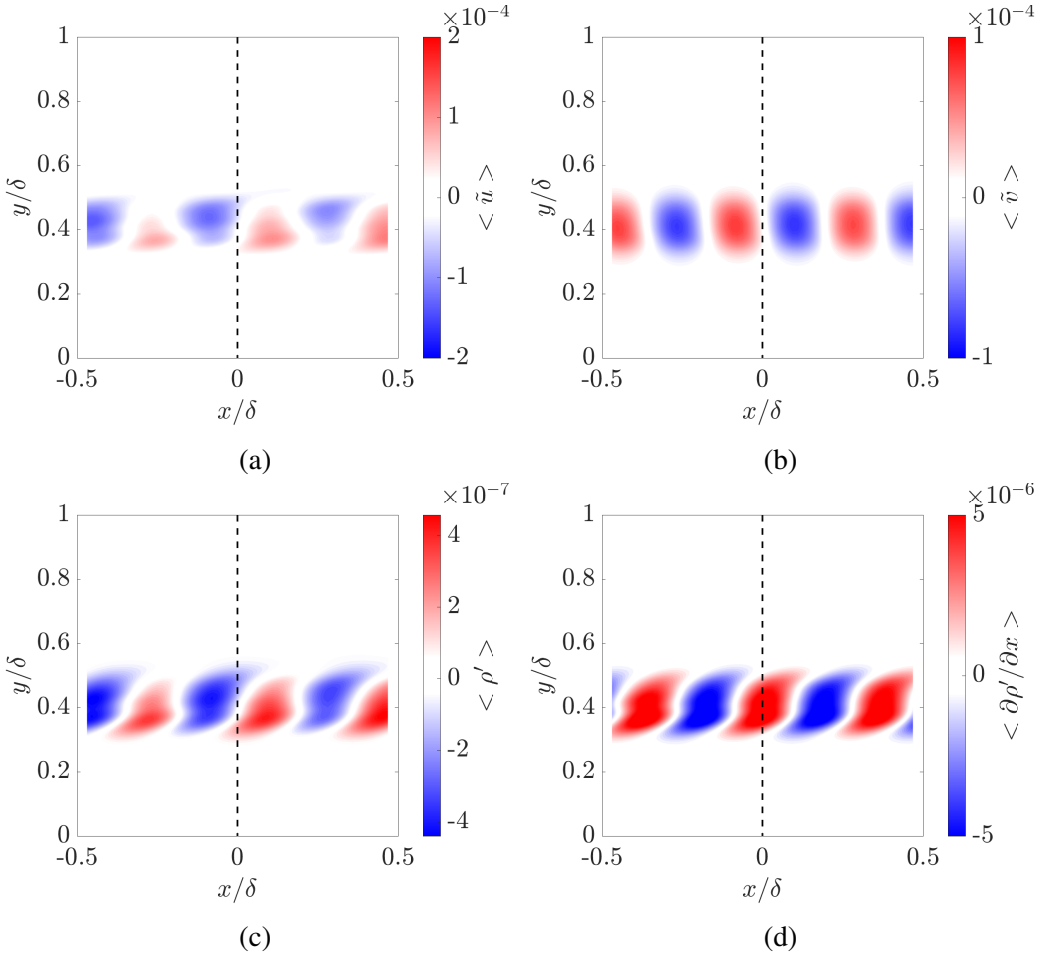

Figure 5.13: Averaging the models shown in figure 5.9 on a condition of a large positive wall-normal integral of the streamwise density gradient ($\tilde{\phi} < -0.5\sigma(\tilde{\phi})$ leads to the following fields for the fluctuating streamwise (a) and wall-normal (b) velocity fields, the fluctuating density field (c), and the streamwise gradient of fluctuating density field (d).

The temperature field for the unity Prandtl number case (figure 5.14(a,b)) is observed to be quite similar to that of the Prandtl number of 0.7. With the larger Prandtl number, however, significant changes are observed in the structure of the temperature field both in the fluctuating field (figure 5.14c) and when summed with the mean temperature field (figure 5.14d). The fluctuating structures are observed to be thinner, leading to smaller observable features in the field with the mean.

The simulated Malley probe analysis was run on the modeled fields with the new modified Prandtl numbers. Figures 5.15 and 5.16 show the modeled conditionally averaged velocity and scalar fields for a Prandtl number of 1 for the negative and positive $\tilde{\phi}$ conditions respectively, while figures 5.17 and 5.18 show the same infor-

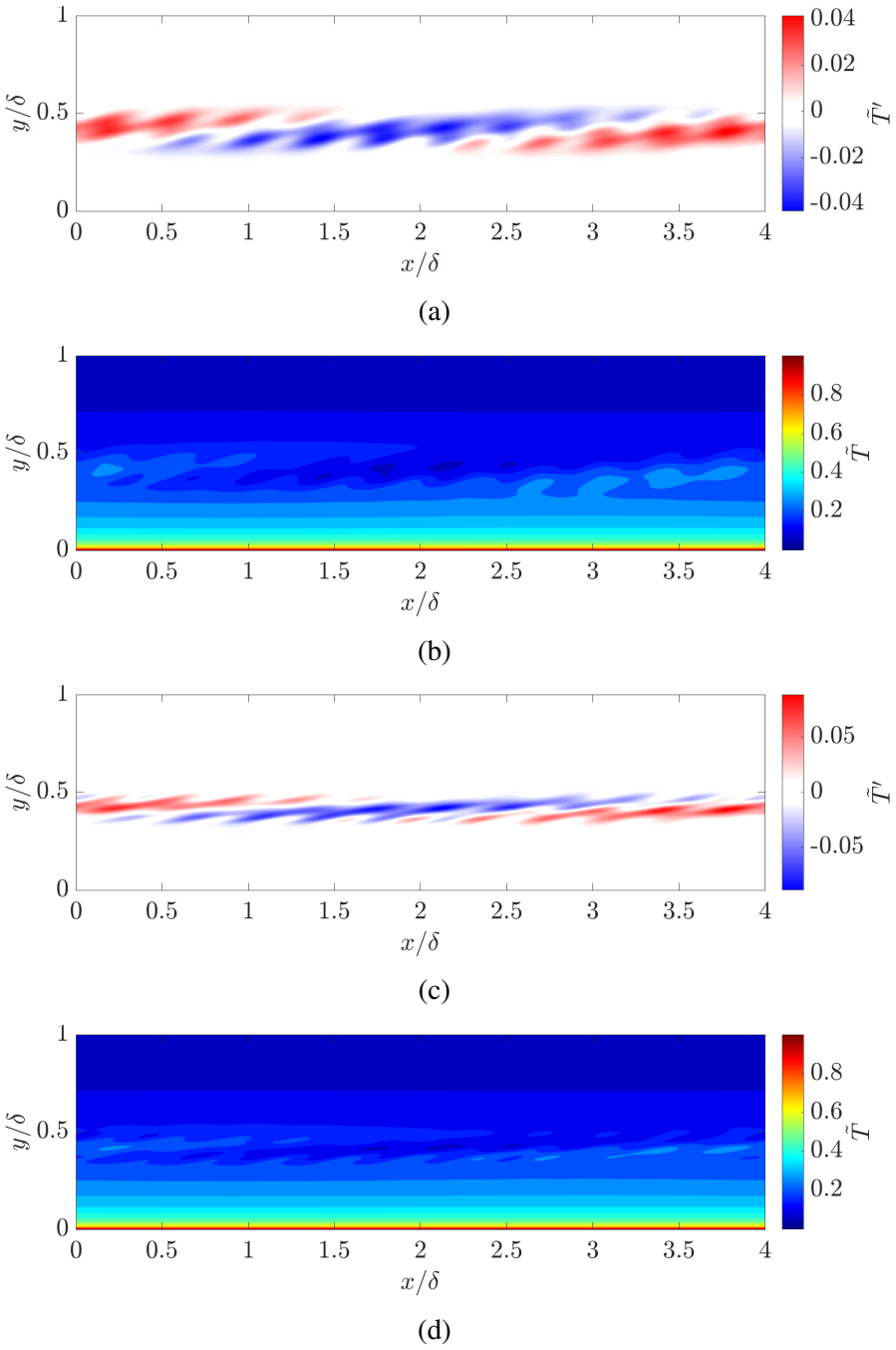

Figure 5.14: A model composed of scalar resolvent modes assuming a Prandtl number of 1 (a,b) and 7 (c,d). The temperature field is shown in the streamwise – wall-normal plane. This temperature field is associated with the velocity field seen in figure 5.10. The fluctuating temperature field is shown in (a,c), while the sum of the fluctuating temperature field and the mean temperature field is shown in (b,d).

mation for the Prandtl number of 7. As with the results of the Prantdl number of 0.7, the fluctuating streamwise and wall-normal velocity fields, the fluctuating density

field, and the streamwise gradient of the density field are shown in each figure.

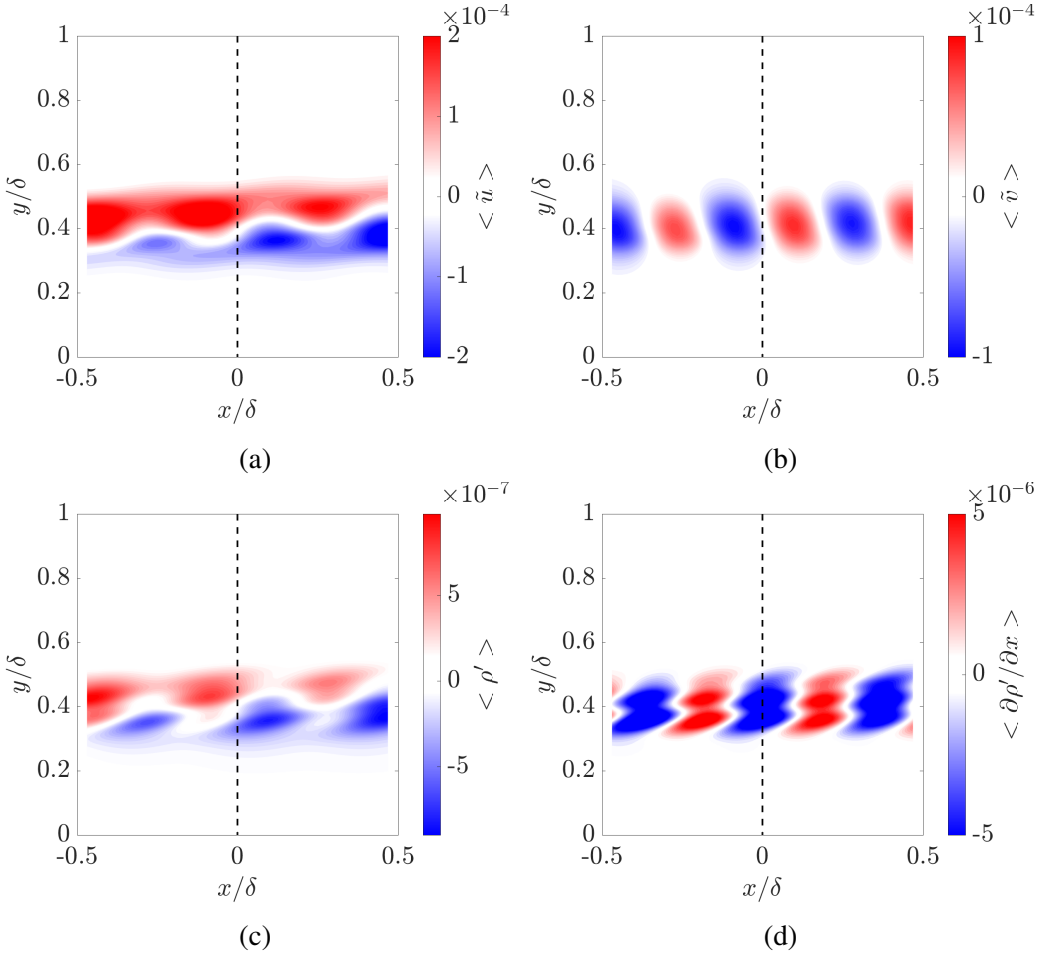

Figure 5.15: The velocity and scalar models with a Prandtl number of 1 are conditionally averaged on a modeled Malley probe signal, $\tilde{\phi} < -0.5\sigma(\tilde{\phi})$. The fluctuating streamwise and wall-normal velocity fields (a,b), the fluctuating density field (c), and the streamwise gradient of the density field (d) are shown in the streamwise – wall-normal plane.

The modeled conditionally averaged results with an increase of Prandtl number show some changes in behavior for all fields considered. For upstream angles, $\tilde{\phi} < -0.5\sigma(\tilde{\phi})$, both larger Prandtl number cases show increased observability of the large-scale wall-normal scale (figures 5.15b and 5.17b). For downstream angles, both larger Prandtl number cases show decreased large-scale coherence in the streamwise velocity field (figures 5.16a and 5.18a). For the unity Prandtl number case, the density field and streamwise density gradient remain fairly similar to those of the 0.7 Prandtl number case for both upstream and downstream angles (figures 5.15c,d and 5.16c,d). However, the results with a Prandtl number of 7

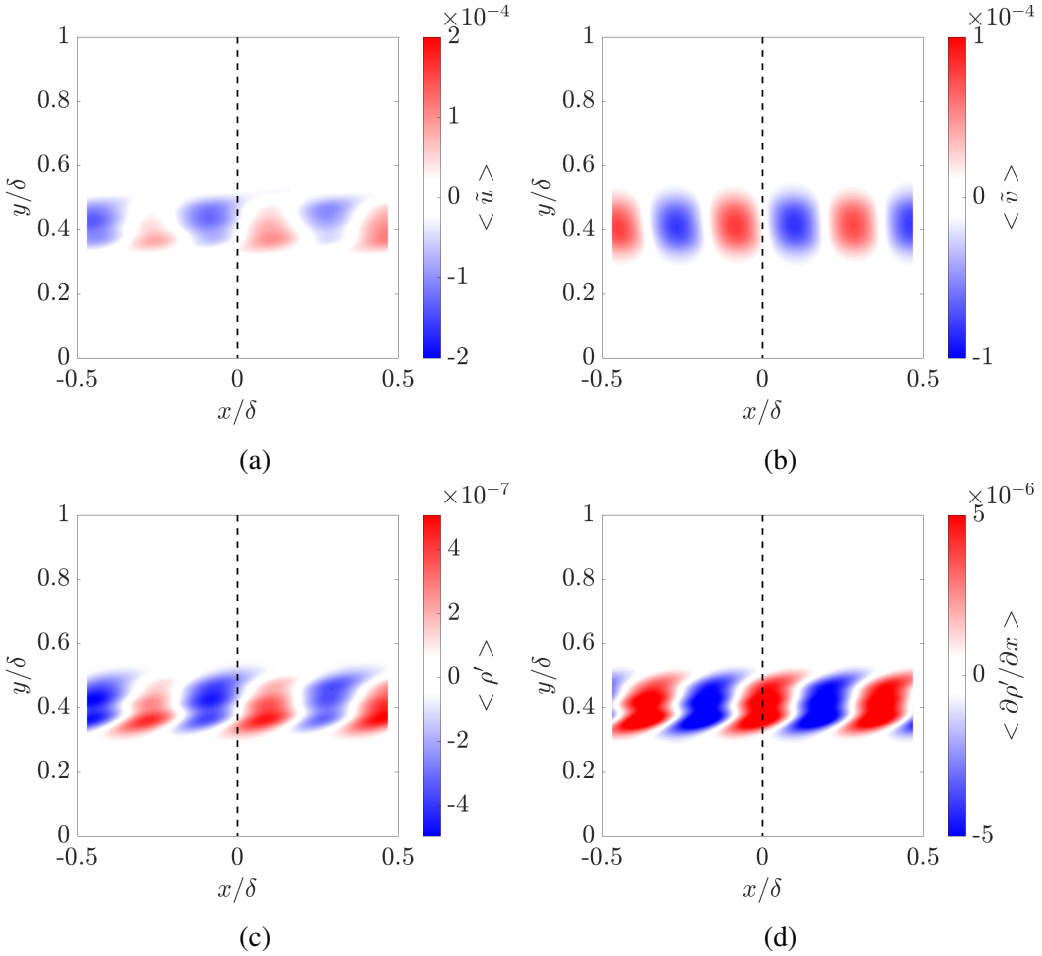

Figure 5.16: The velocity and scalar models with a Prandtl number of 1 are conditionally averaged on a modeled Malley probe signal, $\tilde{\phi} > 0.5\sigma(\tilde{\phi})$. The fluctuating streamwise and wall-normal velocity fields (a,b), the fluctuating density field (c), and the streamwise gradient of the density field (d) are shown in the streamwise – wall-normal plane.

show significant differences in the density fields. For the upstream angle, $\tilde{\phi} < -0.5\sigma(\tilde{\phi})$, the density field shows thinner structures with more defined spatial variation (figure 5.17c), and the streamwise gradient of the density field shows highly striated behavior: the contribution of each small-scale mode is observable at an independent height, rather than overlapping as was observed for the other cases (figure 5.17d). For the downstream angle, shown in figure 5.18, the density field also much appears less coherent (figure 5.18c), and striation is observable in both the density field and in the streamwise gradient of the density field (figure 5.18d).

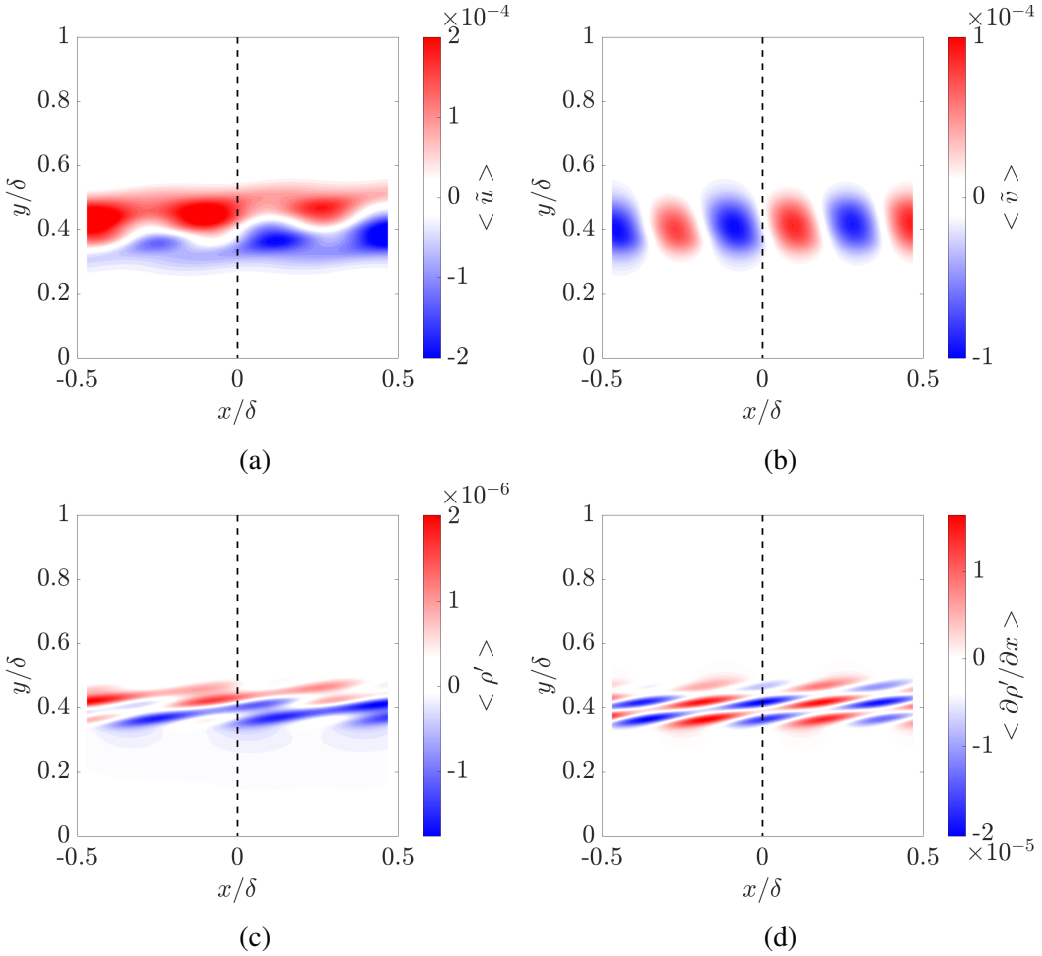

Figure 5.17: The velocity and scalar models with a Prandtl number of 7 are conditionally averaged on a modeled Malley probe signal, $\tilde{\phi} < -0.5\sigma(\tilde{\phi})$. The fluctuating streamwise and wall-normal velocity fields (a,b), the fluctuating density field (c), and the streamwise gradient of the density field (d) are shown in the streamwise – wall-normal plane.

5.5 Discussion and conclusions

Insights obtained from conditional averaging

The conditional averaging results highlighted a correlation between streamwise gradients in the density field, and streamwise gradients in the streamwise and wall-normal velocity fields (figure 5.2). The sense of these correlations was consistently $\partial u/\partial x \sim \partial\rho/\partial x$ and $\partial v/\partial x \sim -\partial\rho/\partial x$ for both upstream and downstream Malley probe deflections. When a high-pass filter was applied to the Malley probe, the correlation between $\partial v/\partial x$ and $\partial\rho/\partial x$ remained clear, but the correlation with $\partial u/\partial x$ was no longer observable (figure 5.3). This was taken as an indication that large scales may be associated with the gradient in the streamwise velocity field,

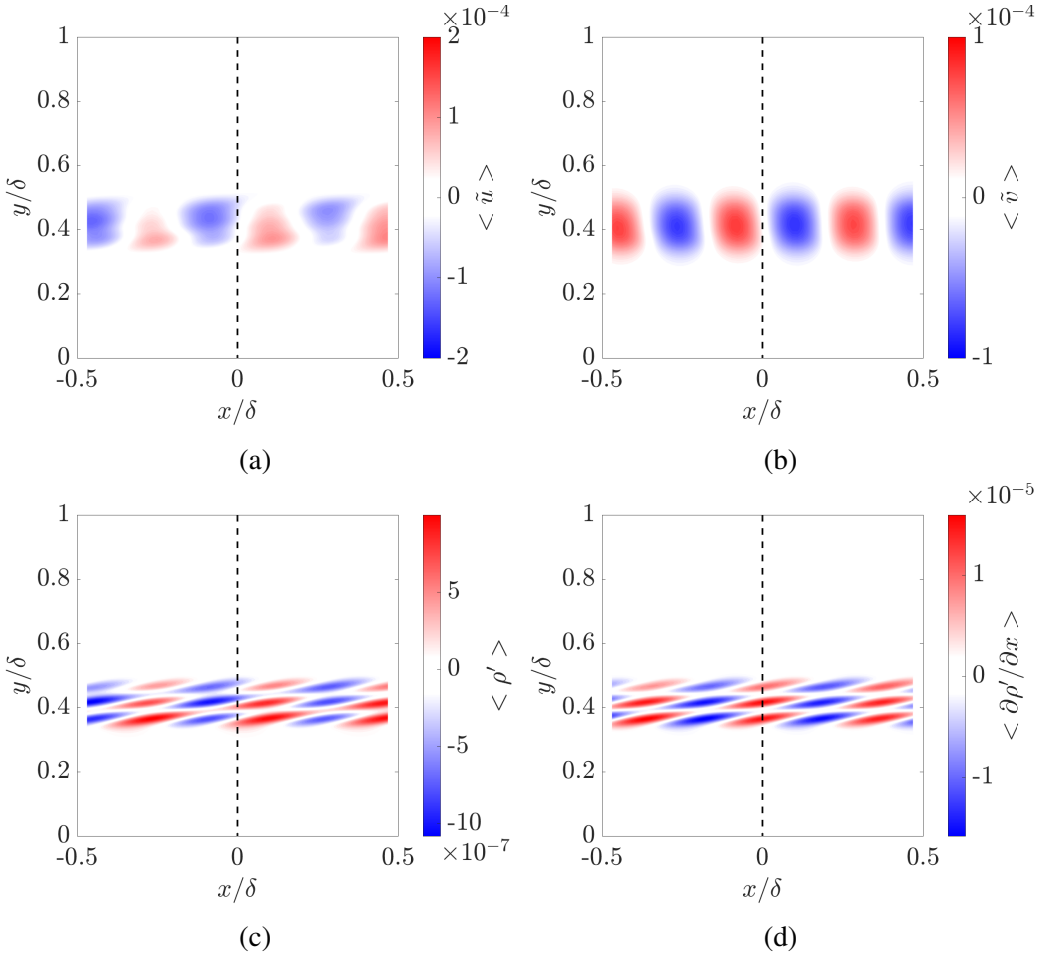

Figure 5.18: The velocity and scalar models with a Prandtl number of 7 are conditionally averaged on a modeled Malley probe signal, $\tilde{\phi} > 0.5\sigma(\tilde{\phi})$. The fluctuating streamwise and wall-normal velocity fields (a,b), the fluctuating density field (c), and the streamwise gradient of the density field (d) are shown in the streamwise – wall-normal plane.

while small scales were primarily responsible for the gradient in the wall-normal velocity field. A small-scale wall-normal feature with a streamwise wavelength of approximately $\lambda_x/\delta = 0.36$ was identified to be correlated to the deflection of the Malley probe signal.

Figure 5.3 shows evidence that the Malley probe can phase average the small-scale wall-normal structure, such that it only averages when the gradient of the wall-normal velocity field is of a specified sign. By averaging on the sign of the streamwise density gradient, the previously-mentioned correlations allow for an average on the streamwise gradients in the wall-normal velocity field as well. These gradients appear to be dominated by small scale features. This small wall-normal

velocity feature may correspond to the hairpin heads observed by other researchers, as the superposition of an alternating small-scale v with a shear layer would lead to the appearance of a vortex head with the appropriate sense of rotation (Theodorsen, 1952; Adrian, Meinhart, and Tomkins, 2000). Investigating the strength of this wall-normal small scale as a function of Reynolds number is suggested as a topic for future work, as the existence of coherent hairpin vortices at high Reynolds number is a topic of continued debate. Additionally, continued investigation of the sensitivity of the small-scale wavelength to the filtering process is a topic of ongoing work.

Finally, figures 5.4 and 5.5 suggest that this small-scale is not periodic at a constant height, but rather along a corrugated isocontour of the large scale flow. This suggests that standard hot wire techniques or wall-parallel Fourier transforms would not necessarily identify this scale as dominant: the sum of multiple wavelengths would be required to create a periodic structure that intermittently was observed at a single height. A wall-normal integral measurement like the Malley probe is able to observe this scale at any height, allowing for its identification and isolation.

Figures 5.4 and 5.5 also support the critical layer hypothesis discussed in chapter 4. In the critical layer hypothesis, a small scale would be expected to sit at a variable height depending on the local velocity of the large-scale flow. Figures 5.4 and 5.5 provide evidence that a single scale may indeed follow this expected behavior. While further work is needed to conclusively determine the validity of the hypothesis, the available data thus far is promising.

Looking back to chapter 4, the localization of small-scale intensity about particular isocontours of the large-scale flow could be due to a single small-scale, sitting at many heights from the wall, or could indicate the presence of many different small scales that each sit at a fixed height. The results of this chapter suggest the possibility that the first of those options hold in the outer region of the boundary layer. Whether this same behavior holds in other regions of the flow or at other Reynolds numbers is a topic of future work.

Along these same lines, there is a natural question of why the structures of the outer boundary layer dominate the Malley probe signal so significantly, such that the convection velocity of the Malley probe distortions is $0.83U_\infty$. Without an understanding of the nature of the small scales nearer to the wall, and their specific interaction with the VLSMs and NWSs, the answer to this question remains out of reach.

Insights obtained from modeling

By modeling the velocity and scalar fields using a resolvent analysis (McKeon and Sharma, 2010), insight was made into the instantaneous structure of the density field during a Malley probe deflection. In particular, it was observed for upstream deflections that the negative density gradient was associated with a corrugated interface between large-scale high and low density regions (figure 5.12c). These large-scale density regions were associated with similar large-scale fluctuations in the streamwise velocity field, and the corrugated interface in the density field was mirrored as a corrugated shear layer in the streamwise velocity field (figure 5.12a). The similarity in these interfaces broke down at higher Prandtl numbers, but the general trend of a corrugated large-scale interface remained. Small-scale wall-normal velocity features were found to be exactly out of phase with the corrugations in the interface in the density and streamwise velocity fields, leading to a clear relationship: $\partial v/\partial x \sim -\partial u/\partial x \sim -\partial \rho/\partial x$, which agreed with the findings of the original averages 5.2.

For downstream deflections, the average behavior was observed to be qualitatively different from that associated with upstream deflections. Large scales were no longer observable in the streamwise velocity field or the density field (figure 5.13a,c). Instead, the small scale features were significantly clearer. Because the large scales are very strong in both the streamwise velocity field and the density field (figures 5.8, 5.11), this indicates that the two senses of large scale are equally likely, allowing them to cancel. Again, the small-scale wall-normal velocity feature is out of phase with the small-scale streamwise velocity feature, such that $-\partial v/\partial x \sim \partial u/\partial x \sim \partial \rho/\partial x$.

The correlation between $\partial v/\partial x$ and $-\partial \rho/\partial x$ was observed through all Prandtl numbers considered, supporting the observation of the conditional averaging results at the Prandtl number of 0.7 and suggesting that the phase-averaging ability of the Malley probe on the wall-normal velocity field may hold in other flows, including in water channels, increasing the range of applications of the Malley probe as a turbulent sensor.

Some discrepancies were observed between the modeled conditional averages and the true conditional averages. The streamwise velocity fields appeared more coherent and more compact in the wall-normal direction in the model (figures 5.12, 5.13) than what was observed in the data (figures 5.2, 5.3). In addition, the wall-normal extent of the wall-normal structure was much shorter in the model (figures 5.12b, 5.13b) than in the data (figures 5.2b,d, 5.3b,d). These two observations taken together

suggest a possible hypothesis: that, on top of the small scale appearing at different heights, the large scale too is able to sit at different heights from the wall. If the entire pattern shown in the interaction of the triads of resolvent modes in figure 5.9 were able to sit at a variety of heights from the wall, the smearing behavior schematically shown in figure 5.7 would do two things. First, it would smear the wall-normal structure such that it appeared to have a larger wall-normal extent. Second, the smearing of the streamwise field would lead to less coherence, as the inclination of the shear layer would be smeared out, leading to the observation of a vertical shear, as was observed in figure 5.2. Further work is needed to explore this hypothesis.

The standard deviation of the model was observed to be over an order of magnitude smaller than that of the data, but the skewness was found to be of the correct sign and of an appropriate order of magnitude. More work is needed to test the sensitivity of the statistics of the modeled Malley probe to the amplitude of the resolvent modes. In addition, more insight can be derived from the modeled fields regarding the dynamics of the scalar field at different Prandtl numbers. Finally, only the streamwise and wall-normal structures have been modeled here, as they can be compared to the structures observed in the PIV data. Future work will include an investigation into the behavior of the modeled spanwise velocity field, which will allow for connections to the findings in figures 4.6(f) of chapter 4.

Chapter 6

CONCLUSIONS AND FUTURE WORK

Coherent structures of turbulent boundary layers and the interaction between them have been studied for decades (Theodorsen, 1952; Kline et al., 1967) as have the relationships between the velocity and scalar fields (Antonia, Danh, and Prabhu, 1977; Chen and Blackwelder, 1978), and yet many challenges remain. The challenges of particular interest in this thesis are:

- connecting existing descriptions of coherent structures,
- identifying mechanisms through which large scales interact with small scales,
- understanding the instantaneous relationship between the velocity and scalar fields,
- isolating the turbulent features correlated to aero-optic distortions.

This thesis contributes to these challenges through the analysis of a combination of experimental data, computational data, and reduced-order models.

Chapter 3 contributed to the first challenge by demonstrating connections between statistical and instantaneous descriptions of energetic streamwise velocity scales. A non-trivial relationship was observed between the structure and size of features in the laboratory-frame and fluctuating velocity fields, which are the common representations used by the researchers studying instantaneous and statistical phenomena respectively. Representative models of three energetic scales (the large-scale motions of the outer boundary layer, the very-large-scale motions of the logarithmic layer, and the near-wall streaks of the inner region) were used along with instantaneous visualizations of PIV data to highlight that periodic structures, consistent with statistically energetic wavelengths, could represent instantaneous complex behavior. The superposition of the three models was compared to instantaneous PIV data through the use of an instantaneous streamwise velocity histogram, a technique that is often used to study uniform momentum zone (UMZ) behavior in turbulent flows (Adrian, Meinhart, and Tomkins, 2000; de Silva, Hutchins, and Marusic, 2016). Qualitative trends were found to agree between the data and the model, suggesting

that very reduced-order, periodic models could represent instantaneous UMZ behavior. Finally, in chapter 3, the instantaneous streamwise velocity histogram technique was demonstrated to be a measure of the local shear in the flow through an analytical derivation of the probability density function of an instantaneous streamwise velocity profile.

Chapter 4 contributed to the second challenge, identifying mechanisms through which large scales interact with small scales, by applying a novel conditional averaging technique that leveraged the representative models identified in chapter 3. A projection of the data onto a model of the scale of interest was used as a conditioning criterion. This condition led to a final conditional average with smooth variation in the large-scale flow field, leading to smooth undulations in the large-scale laboratory-frame streamwise velocity isocontours through the relationship to the fluctuating field identified in chapter 3. The small-scale velocity intensity was averaged about the large scale using a phase averaging method. From this conditional averaging method, it was observed that the small-scale intensity was often localized near a single isocontour of the large-scale flow. While the trends of the small-scale behavior were consistent with many previous findings (Hutchins and Marusic, 2007; Mathis, Hutchins, and Marusic, 2009; Chung and McKeon, 2010; Ganapathisubramani et al., 2012; Talluru et al., 2014; Baars, Hutchins, and Marusic, 2017), the observation of the relation to one large-scale isocontour was new, and was likely made possible by the smooth spatial averaging condition applied to the large-scale flow. This observation suggested a hypothesis for the mechanism of interaction between the large and small scales: a critical layer. The hypothesis states that the small scales in turbulence act similarly to perturbations in a base flow with shear, showing the most growth or prominence along the isocontour of the base flow corresponding to their phase speed. This hypothesis could explain the spatial variation of the small scales with the phase of the large-scale structure, and may allow for connections to critical layer behavior observed in exact coherent solutions to the Navier-Stokes equations (Wang, Gibson, and Waleffe, 2007; Hall and Sherwin, 2010; Park and Graham, 2015).

Chapter 5 also offered a contribution to the second challenge (identifying interaction mechanisms). The Malley probe conditional average was able to phase average the small-scale structures in the outer boundary layer, due to a correlation between streamwise gradients of the wall-normal velocity field and streamwise gradients of the density field. The phase averaged small scales were observed to have a

wavelength of 0.36δ throughout the outer region of the boundary layer. When the P_{1D} conditional averaging technique of chapter 4 was combined with the Malley probe average, the small scale was observed to sit at a variety of heights depending on the phase of the large scale. This suggested that there may be a dominant small scale in the outer boundary layer at this Reynolds number, and that the small scale's height may vary, following the critical layer of the large-scale pseudo-base flow.

Chapter 5 focused largely on the third and fourth challenges, identifying relationships between the velocity and scalar fields, and isolating the turbulent dynamics correlated to Malley probe deflection. The relationship between the instantaneous velocity and scalar fields was studied through the MP conditional averaging technique and by modeling the velocity and scalar fields using a resolvent analysis, the scalar component of which was developed by Dr. Scott Dawson. This model allowed for a synthetic Malley probe signal to be generated, and offered the opportunity to study the effect of Prandtl number on the results. The MP / P1 conditional averaging technique was used to identify a nonlinear interaction between two structures in the outer boundary layer that was highly correlated to the distortion of the Malley probe, offering an answer to the fifth challenge in heated, incompressible flows, with extensions possible in compressible flows and in a three-dimensional viewpoint.

Future work and high-level perspectives

There is significant room for work to advance the findings in this thesis. The findings shown for the structure interaction analysis were confined to 2D slices, even when using DNS in which 3D data is available. The generation of a fully 3D conditionally-averaged small-scale intensity result would aid in the understanding of the distribution of the small-scale intensity in physical space. A mathematical representation of the critical layer concept, in which the superposition of the mean velocity field and a large scale that is a function of all spatial variables and time is represented as a pseudo-base flow would be useful and could illuminate the mechanisms behind the observed relationships between large and small scales. Additionally, there are interesting questions of how the small scales influence the large scale, and whether their spatial distribution affects that influence.

While a wide range of challenges were considered, the culmination of the thesis points cohesively towards a particular viewpoint and approach towards turbulence. Very few scales are considered in this thesis: three representative large scales that span the height of the boundary layer, and a single small scale in the outer boundary

layer. While this by no means indicates that these are the only relevant scales of turbulence, it is quite purposeful in its reduction of complexity. The small scales of the outer boundary layer are a prime example of the possibility of simplicity in what appears complex: a single small scale was observed to be dominant throughout the outer region of the boundary layer if one accounted for its ability to exhibit height variation. Without accounting for height variation, a much larger number of Fourier modes would be required to describe its behavior at any one height. Perhaps, by increasing the complexity of motion that scales are allowed, one can decrease the number of scales one has to consider. This perspective is both born from and influences this research, and calls for reduced dynamical systems of equations that describe the motion of these structures relative to one another. Such a model could offer a very-low-order approach to the full complexity of turbulence, and offer insights into some of the most fundamental of its mysteries: the importance of particular structures, their interaction mechanisms, and their ability to self-sustain.

Appendix A

ALGORITHMS FOR FIGURE OUTPUTS

Here algorithms are included for the creation of the figures shown in this thesis. Algorithms are included for the histograms of chapter 3 (algorithm 1), the projection conditional averaging results of chapter 4 (algorithms 2 to 6), and the Malley probe conditional averaging results and combined Malley probe, projection conditional averaging results of chapter 5 (algorithms 7 and 8). Discussion of the methods behind many of these algorithms can be found in chapter 2.

Algorithm 1: Instantaneous streamwise velocity histogram calculation

Input : Laboratory-frame streamwise velocity field, $U(x, y, t)$

Time of interest, t_0

Streamwise range, X

Number of velocity bins, n_b

Output : Instantaneous streamwise velocity histogram, $m_b(U_b^*)$

1 Define velocity range: $\Delta U = \max(U(x, y, t)) - \min(U(x, y, t))$

2 Define velocity values at center points of equally-sized velocity bins:
$U_b^* = \min(U(x, y, t)) + \frac{\Delta U}{2n_b} : \frac{\Delta U}{(n_b)} : \max(U(x, y, t)) - \frac{\Delta U}{2n_b}$

3 Extract data for histogram: $U_h = U(X, y, t_0)$

4 **for** $i = 1, n_b$ **do**

5 Define velocity bin $U_b(i) = \left[U_b^*(i) - \frac{\Delta U}{2n_b}, U_b^*(i) + \frac{\Delta U}{2n_b}\right)$

6 Count number of grid points for which the velocity value is within the bin:
$m_b(i) = \mathcal{N}\left(U_h(X, y) \in U_b(i)\right)$

7 **end**

8 Normalize m_b: $m_b = \frac{n_b}{\Delta U \sum_{i=1}^{n_b} m_b} m_b$

9 The histogram of $U(X, y, t_0)$ plots m_b against U_b^*.

Algorithm 2: Projection component of P_{2D} conditional averaging method for 2D data

Input : Fluctuating streamwise velocity field, $u(x, y, t)$
Mean streamwise velocity profile, $\bar{U}(y)$
Model streamwise wavenumber, k_x
Model spanwise wavenumber, k_z
Model temporal frequency, ω
Number of phases, n_γ

Output : Maximum value of the projection at each time $R^*(t)$
Phase that maximizes the projection at each time, $\gamma^*(t)$

Define phases considered $\Gamma = 0 : \frac{2\pi}{n_\gamma} : 2\pi - \frac{2\pi}{n_\gamma}$
Define model (here will demonstrate using resolvent analysis model):
Assume periodicity in streamwise, spanwise, and temporal variables to define a traveling wave model: $\tilde{u}(x, y, z, t) = Re[\hat{u}(y)(e^{i(k_x x + k_z z - \omega t)} + e^{i(k_x x - k_z z - \omega t)})]$
Use the resolvent analysis of McKeon and Sharma (2010) to identify $\hat{u}$ (details omitted, requires $\bar{U}(y)$)
Take slice of model at z location at which the maximum amplitude occurs: $\tilde{u}(x, y, t) = Re[\hat{u}(y)(e^{i(k_x x + k_z z_0 - \omega t)} + e^{i(k_x x - k_z z_0 - \omega t)})]$
Define $\tilde{\gamma} = -\omega t$
Perform projection:
for $t_i \leftarrow t_0 : t_f$ **do**
    for $\tilde{\gamma} \leftarrow \Gamma$ **do**
        Project flow quantity at time t_i onto model:
        $R(\tilde{\gamma}) = \left(u(x, y, t_i) \cdot \tilde{u}(x, y, \tilde{\gamma})\right) / \left(|u(x, y, t_i)||\tilde{u}(x, y, \tilde{\gamma})|\right)$
    end
    Define outputs: $R^*(t_i) = \max_{\tilde{\gamma}} R$
    $\gamma^*(t_i) = \text{argmax}_{\tilde{\gamma}} R$
end

Algorithms 2 to 6 can be made more efficient by only considering half of the possible values of Γ, and using a negative projection coefficient to identify phases larger than or equal to π. This more-efficient method is implemented for the results shown in this thesis, but is not included in the algorithm here for clarity and simplicity, as it is not needed to arrive at the final result. Note that x^* of algorithms 4 and 6 is not the same size as x, and has a maximum value of λ_x.

The outputs of either algorithm 2 or 3 can be used as an input to conditionally average a quantity of interest, q, using algorithm 4.

Algorithm 3: Projection component of P_{1D} conditional averaging method for 2D data

Input : Fluctuating streamwise velocity field $u(x, y, t)$
Mean streamwise velocity profile $\bar{U}(y)$
Model wavelength $\tilde{\lambda}_x$
Model wavespeed $\tilde{c}$
Number of phases n_γ

Output : Maximum value of the projection at each time $R^*(t)$
Phase that maximizes the projection at each time, $\gamma^*(t)$

1 Define phases considered $\Gamma = 0 : \frac{2\pi}{n_\gamma} : 2\pi - \frac{2\pi}{n_\gamma}$
2 Perform projection:
3 **for** $t_i \leftarrow t_0 : t_f$ **do**
4 **for** $\tilde{\gamma} \leftarrow \Gamma$ **do**
5 Define a model $\tilde{u} = \sin(\frac{2\pi}{\tilde{\lambda}_x} x + \tilde{\gamma})$
6 Define critical layer height y_c such that $\bar{U}(y_c) = \tilde{c}$
7 Project flow quantity at time t_i and height y_c onto model:
 $R(\tilde{\gamma}) = \left(u(x, y_c, t_i) \cdot \tilde{u}_{LSM}(x)\right) / \left(|u(x, y_c, t_i)||\tilde{u}_{LSM}(x)|\right)$
8 **end**
9 Define outputs: $R^*(t_i) = \max_{\tilde{\gamma}} R$
10 $\gamma^*(t_i) = \text{argmax}_{\tilde{\gamma}} R$
11 **end**

For the 3D projection and averaging, shown in algorithms 5 and 6, only the $x - y$ plane algorithms are shown here, but trivial changes can be made (averaging on x rather than z) to output the $z - y$ plane results.

Similarly, while only downstream deflections are shown for the Malley probe conditional averaging algorithms (algorithms 7 and 8), upstream deflections can be computed by changing the condition for the 'if' statement on line 4 of algorithm 7 to $\phi(t_i) < -0.5\sigma$.

Algorithm 4: Averaging on P condition for 2D data

Input : Flow quantity, $q(x, y, t)$
Maximum value of projection for each frame, $R^*(t)$
Phase that maximizes projection for each plane, $\gamma^*(t)$

Output : $< q >_{P_{1D}} (x, y)$

Initialize $q_{\Sigma,1} = 0$, $q_{\Sigma,2} = 0$, $\text{count}_1 = 0$, $\text{count}_2 = 0$
Define phases considered $\Gamma = 0 : \frac{2\pi}{n_\gamma} : 2\pi - \frac{2\pi}{n_\gamma}$
Sum q based upon values acquired from projection:
for $\tilde{\gamma} \leftarrow \Gamma$ **do**
  for $t_i \leftarrow t_0 : t_f$ **do**
    if $\gamma^*(t_i) = \tilde{\gamma}$ **then**
      if $R^*(t_i) > R_{th}$ **then**
        $q_{\Sigma,1}(x, y, \tilde{\gamma}) = q_{\Sigma,1}(x, y, \tilde{\gamma}) + q(x, y, t_i)$
        $\text{count}_1(\tilde{\gamma}) = \text{count}_1(\tilde{\gamma}) + 1$
      end
    end
  end
end
Combine spatial components with same phase information in $q_{\Sigma,1}$:
for $j = 1 : n_\gamma$ **do**
  for $i = 1 : n_\gamma$ **do**
    $X = \Gamma(i)\lambda_x/n_\gamma : \Gamma(i + 1)\lambda_x/n_\gamma$
    $X^* = 0 : \lambda_x/n_\gamma$
    if $min(X) > min(x)$ & $max(x) < max(x)$ **then**
      $q_{\Sigma,2}(X^*, y, \Gamma(j)) = q_{\Sigma,1}(X, y, \Gamma(j))$
      $\text{count}_2(\Gamma(j)) = \text{count}_2(\Gamma(j)) + \text{count}(\Gamma(j))$
    end
  end
  Average each phase:
  $q_{avg}(X^*, y, \Gamma(j)) = q_{\Sigma,2}(X^*, y, \Gamma(j))/\text{count}_2(\Gamma(j))$
end
Define output by concatenating q_{avg}:
$< q >_{P_{1D}} (x^*, y) = [q_{avg}(X^*, y, \Gamma(1)), ..., q_{avg}(X^*, y, \Gamma(n_\gamma))]$

Algorithm 5: Projection component of P_{1D} conditional averaging method for 3D data

Input : Fluctuating streamwise velocity field $u(x, y, z, t)$
Model wavelength $\tilde{\lambda}_x$
Model wavespeed $\tilde{c}$
Number of phases n_γ

Output : Maximum value of the projection at each time $R^*(t)$
Phase that maximizes the projection at each time, $\gamma^*(t)$

Define phases considered $\Gamma = 0 : \frac{2\pi}{n_\gamma} : 2\pi - \frac{2\pi}{n_\gamma}$
Perform projection:
for $t_i \leftarrow t_0 : t_f$ **do**
  for $z_j \leftarrow z_0 : z_f$ **do**
    for $\tilde{\gamma} \leftarrow \Gamma$ **do**
      Define a model $\tilde{u} = \sin(\frac{2\pi}{\tilde{\lambda}_x} x + \tilde{\gamma})$
      Define critical layer height y_c such that $\bar{U}(y_c) == \tilde{c}$
      Project flow quantity at time t_i and height y_c onto model:
        $R(\tilde{\gamma}) = \left(u(x, y_c, z_j, t_i) \cdot \tilde{u}(x, \tilde{\gamma})\right) / \left(|u(x, y_c, z_j, t_i)||\tilde{u}(x, \tilde{\gamma})|\right)$
    end
    Define outputs: $R^*(z_j, t_i) = \max_{\tilde{\gamma}} R$
    $\gamma^*(z_j, t_i) = \text{argmax}_{\tilde{\gamma}} R$
  end
end

Algorithm 6: Averaging on P condition for 3D data

Input : Flow quantity, $q(x, y, z, t)$
Maximum value of projection for each frame, $R^*(z, t)$
Phase that maximizes projection for each plane, $\gamma^*(z, t)$

Output : $< q >_{P_{1D}} (x, y)$

Initialize $q_{\Sigma,1} = 0$, $q_{\Sigma,2} = 0$, $\text{count}_1 = 0$, $\text{count}_2 = 0$
Define phases considered $\Gamma = 0 : \frac{2\pi}{n_\gamma} : 2\pi - \frac{2\pi}{n_\gamma}$
Sum q based upon values acquired from projection:
for $\tilde{\gamma} \leftarrow \Gamma$ **do**
  for $t_i \leftarrow t_0 : t_f$ **do**
    for $z_j \leftarrow z_0 : z_f$ **do**
      if $\gamma^*(z_j, t_i) = \tilde{\gamma}$ **then**
        if $R^*(z_j, t_i) > R_{th}$ **then**
          $q_{\Sigma,1}(x, y, \tilde{\gamma}) = q_{\Sigma,1}(x, y, \tilde{\gamma}) + q(x, y, z_j, t_i)$
          $\text{count}_1(\tilde{\gamma}) = \text{count}_1(\tilde{\gamma}) + 1$
        end
      end
    end
  end
end
Combine spatial components with same phase information in $q_{\Sigma,1}$:
for $j = 1 : n_\gamma$ **do**
  for $i = 1 : n_\gamma$ **do**
    $X = \lambda_x \Gamma(i)/n_\gamma : \lambda_x \Gamma(i + 1)/n_\gamma$
    $X^* = 0 : \lambda_x / n_\gamma$
    if $min(X) > min(x) \& max(X) < max(x)$ **then**
      $q_{\Sigma,2}(X^*, y, \Gamma(j)) = q_{\Sigma,1}(X, y, \Gamma(j))$
      $\text{count}_2(\Gamma(j)) = \text{count}_2(\Gamma(j)) + \text{count}(\Gamma(j))$
    end
  end
  Average each phase:
  $q_{avg}(X^*, y, \Gamma(j)) = q_{\Sigma,2}(X^*, y, \Gamma(j))/\text{count}_2(\Gamma(j))$
end
Define output by concatenating q_{avg}:
$< q >_{P_{1D}} (x^*, y) = [q_{avg}(X^*, y, \Gamma(1)), ..., q_{avg}(X^*, y, \Gamma(n_\gamma))]$

Algorithm 7: Conditionally averaging on downstream Malley probe deflection

Input : Fluctuating streamwise velocity field, $u(x, y, t)$
Fluctuating wall-normal velocity field, $v(x, y, t)$
Streamwise Malley probe deflection angle, $\phi(t)$

Output : $< u >_{MP} (x, y)$, $< v >_{MP} (x, y)$

```
Calculate standard deviation of φ(t): σ
Initialize u_Σ = 0, v_Σ = 0, count = 0
for t_i ← t_0 to t_f do
    if φ(t_i) > 0.5σ then
        u_Σ(x, y) = u_Σ(x, y) + u(x, y, t_i)
        v_Σ(x, y) = v_Σ(x, y) + v(x, y, t_i)
        count = count+1
    end
end
Define outputs: < u >_MP (x, y) = u_Σ(x, y)/count,
< v >_MP (x, y) = v_Σ(x, y)/count
```

Algorithm 8: Conditionally averaging on MP/P_{1D} condition for 2D data

Input : Flow quantity, $q(x, y, t)$
Maximum value of projection for each frame, $R^*(t)$
Phase that maximizes projection for each plane, $\gamma^*(t)$
Malley probe signal $\phi(t)$
Location of Malley probe in PIV frame, x_{MP}

Output : $< q >_{MP/P_{1D}} (x, y)$

Initialize $q_{\Sigma,1} = 0$, count = 0
Define phases considered $\Gamma = 0 : \frac{2\pi}{n_\gamma} : 2\pi - \frac{2\pi}{n_\gamma}$
Sum q based upon values acquired from projection:
for $\tilde{\gamma} \leftarrow \Gamma$ **do**
  for $t_i \leftarrow t_0 : t_f$ **do**
    if $\phi(t_i) > 0.25\sigma(\phi)$ **then**
      if $\gamma^*(t_i) = \tilde{\gamma}$ **then**
        if $R^*(t_i) > R_{th}$ **then**
          $q_{\Sigma,1}(x, y, \tilde{\gamma}) = q_{\Sigma,1}(x, y, \tilde{\gamma}) + q(x, y, t_i)$
          $\text{count}(\tilde{\gamma}) = \text{count}(\tilde{\gamma}) + 1$
        end
      end
    end
  end
  Crop data about Malley probe location:
  $X = x_{MP} - \lambda_x/(2n_\gamma) : x_{MP} + \lambda_x/(2n_\gamma)$
  Average each phase:
  $q_{avg}(X, y, \tilde{\gamma}) = q_{\Sigma,1}(X, y, \tilde{\gamma})/\text{count}(\tilde{\gamma})$
end
Define output by concatenating q_{avg}:
$< q >_{MP/P_{1D}} (x^*, y) = [q_{avg}(X, y, 0), ..., q_{avg}(X, y, 2\pi - \frac{2\pi}{n_\gamma})]$

BIBLIOGRAPHY

Abe, H., R. A. Antonia, and H. Kawamura (2009). "Correlation between small-scale velocity and scalar fluctuations in a turbulent channel flow". In: *Journal of Fluid Mechanics* 627, pp. 1–32.

Adrian, R. J., C. D. Meinhart, and C. D. Tomkins (2000). "Vortex organization in the outer region of the turbulent boundary layer". In: *Journal of Fluid Mechanics* 422, pp. 1–54.

Antonia, R. A., H. Abe, and H. Kawamura (2009). "Analogy between velocity and scalar fields in a turbulent channel flow". In: *Journal of Fluid Mechanics* 628, pp. 241–268.

Antonia, R. A., H. Q. Danh, and A. Prabhu (1977). "Response of a turbulent boundary layer to a step change in surface heat flux". In: *Journal of Fluid Mechanics* 80, pp. 153–177.

Baars, W. J., N. Hutchins, and I. Marusic (2017). "Reynolds number trend of hierarchies and scale interactions in turbulent boundary layers". In: *Philosophical Transactions of The Royal Society A* 375.20160077.

Bandyopadhyay, P. R. and A. K. M. F. Hussain (1984). "The coupling between scales in shear flows". In: *The Physics of Fluids* 27.9, pp. 2221–2228. DOI: 10.1063/1.864901.

Bernard, P. S. (2013). "Vortex dynamics in transitional and turbulent boundary layers". In: *AIAA Journal* 51.8, pp. 1828–1841.

Blackwelder, R. F. and H. Eckelmann (1979). "Streamwise vortices associated with the bursting phenomenon". In: *Journal of Fluid Mechanics* 94.3, pp. 577–594.

Brown, G. L. and S. W. Thomas (1977). "Large structure in a turbulent boundary layer". In: *Physics of Fluids* 20.S243.

Cantwell, B. J. (1981). "Organized motion in turbulent flow". In: *Annual Review of Fluid Mechanics* 13, pp. 457–515.

Chauhan, K. et al. (2014). "The turbulent/non-turbulent interface and entrainment in a boundary layer". In: *Journal of Fluid Mechanics* 742, pp. 119–151.

Chen, C. H. P. and R. F. Blackwelder (1978). "Large-scale motion in a turbulent boundary layer: a study using temperature contamination". In: *Journal of Fluid Mechanics* 89.1, pp. 1–31.

Chung, D. and B. J. McKeon (2010). "Large-eddy simulation of large-scale structures in long channel flow". In: *Journal of Fluid Mechanics* 661, pp. 341–364.

Chung, D. and D. I. Pullin (2009). "Large-eddy simulation and wall modelling of turbulent channel flow". In: *Journal of Fluid Mechanics* 631, pp. 281–309. DOI: 10.1017/S0022112009006867.

Cress, J. A. (2010). "Optical aberrations caused by coherent structures in a subsonic, compressible, turbulent boundary layer". Aerospace Engineering PhD Thesis. University of Notre Dame.

Davies, E. R. (2004). *Machine Vision: Theory, Algorithms, Practicalities*. Technology & Engineering. Elsevier.

de Silva, C. M., N. Hutchins, and I. Marusic (2016). "Uniform momentum zones in turbulent boundary layers". In: *Journal of Fluid Mechanics* 786, pp. 309–331.

DeGraaff, D. B. and J. K. Eaton (2000). "Reynolds-number scaling of the flat-plate turbulent boundary layer". In: *Journal of Fluid Mechanics* 422, pp. 319–346.

Del Alamo, J. and J. Jimenez (2009). "Estimation of turbulent convection velocities and corrections to Taylor's approximation". In: *Journal of Fluid Mechanics* 640, pp. 5–26.

Dimotakis, P. E., H. J. Catrakis, and D. C. Fourguette (2001). "Flow structure and optical beam propagation in high-Reynolds-number gas-phase shear layers and jets". In: *Journal of Fluid Mechanics* 433, pp. 104–134.

Duvvuri, S. and B. J. McKeon (2015). "Triadic scale interactions in a turbulent boundary layer". In: *Journal of Fluid Mechanics* 767. DOI: 10.1017/jfm.2015.79.

Duvvuri, S. and B. J. McKeon (2016). "Nonlinear interactions isolated through scale synthesis in experimental wall turbulence". In: *Physical Review Fluids* 1.032401(R).

Duvvuri, S. and B. J. McKeon (2017). "Phase relations in a forced turbulent boundary layer: implications for modelling of high Reynolds number wall turbulence". In: *Philosophical Transactions of The Royal Society A* 375.20160080.

Eisma, J. et al. (2015). "Interfaces and internal layers in a turbulent boundary layer". In: *Physics of Fluids* 27.055103.

Falco, R. E. (1977). "Coherent motions in the outer region of turbulent boundary layers". In: *Physics of Fluids* 20.

Favre, A. (1964). *The Mechanics of Turbulence*. New York: Gordon & Breach.

Ganapathisubramani, B. et al. (2012). "Amplitude and frequency modulation in wall turbulence". In: *Journal of Fluid Mechanics* 712, pp. 61–91. DOI: 10.1017/jfm.2012.398.

Gordeyev, S. et al. (2014). "Experimental studies of aero-optical properties of subsonic turbulent boundary layers". In: *Journal of Fluid Mechanics* 740, pp. 214–253.

Gordeyev, S. et al. (2015). "Studies of the large-scale structure in adiabatic and moderately-wall-heated subsonic boundary layers". In: *The Proceedings of the Symposium on Turbulence and Shear Flow Phenomena* 9.

Guezennec, Y., D. Stretch, and J. Kim (1990). "The structure of turbulent channel flow with passive scalar transport". In: *Proceedings of the Summer Program 1990, Center for Turbulence Research, Stanford* 127-138.

Hall, P. and S. Sherwin (2010). "Streamwise vortices in shear flows: harbingers of transition and the skeleton of coherent structures". In: *Journal of Fluid Mechanics* 661, pp. 178–205.

Head, M. R. and P. Bandyopadhyay (1981). "New aspects of turbulent boundary-layer structure". In: *Journal of Fluid Mechanics* 107, pp. 297–338. DOI: 10.1017/S0022112081001791.

Hussain, A. K. M. F. and W. C. Reynolds (1970). "The mechanics of an organized wave in turbulent shear flow". In: *Journal of Fluid Mechanics* 41.2, pp. 241–258.

Hutchins, N. and I. Marusic (2007). "Large-scale influences in near-wall turbulence". In: *Philosophical Transactions of The Royal Society A* 365, pp. 647–664.

Hutchins, N. et al. (2011). "Three-dimensional conditional structure of a high-Reynolds-number turbulent boundary layer". In: *Journal of Fluid Mechanics* 673, pp. 255–285.

Inoue, M. et al. (2012). "Inner-layer intensities for the flat-plate turbulent boundary layer combining a predictive wall-model with large-eddy simulations". In: *Physics of Fluids* 24.7, p. 075102. DOI: 10.1063/1.4731299.

Jacobi, I. and B. J. McKeon (2011). "Dynamic roughness perturbation of a turbulent boundary layer". In: *Journal of Fluid Mechanics* 688, pp. 258–296.

Jacobi, I. and B. J. McKeon (2013). "Phase relationships between large and small scales in the turbulent boundary layer". In: *Experiments in Fluids* 54.1481.

Jimenez, J. (2012). "Cascades in wall-bounded turbulence". In: *Annual Review of Fluid Mechanics* 44, pp. 27–45.

Jimenez, J. and P. Moin (1991). "The minimal flow unit in near-wall turbulence". In: *Journal of Fluid Mechanics* 225, pp. 213–240.

Jumper, E. J. and E. J. Fitzgerald (2001). "Recent advances in aero-optics". In: *Progress in Aerospace Sciences*, pp. 299–339.

Kim, K. C. and R. J. Adrian (1999). "Very large-scale motion in the outer layer". In: *Physics of Fluids* 11.2, pp. 417–422. DOI: 10.1063/1.869889.

Kline, S. J. et al. (1967). "The structure of turbulent boundary layers". In: *Journal of Fluid Mechanics* 30.4, pp. 741–773.

Kovasznay, L. S. G., V. Kibens, and R. F. Blackwelder (1970). "Large-scale motion in the intermittent region of a turbulent boundary layer". In: *Journal of Fluid Mechanics* 41.2, pp. 283–325.

Lindeberg, T. (1994). "Scale-space theory: a basic tool for analysing structures at different scales". In: *Journal of Applied Statistics* 21.2, pp. 225–270.

Luhar, M., A. S. Sharma, and B. J. McKeon (2014). "On the structure and origin of pressure fluctuations in wall turbulence: predictions based on the resolvent analysis". In: *Journal of Fluid Mechanics* 751, pp. 38–70.

Malley, M., G. Sutton, and N. Kincheloe (1992). "Beam-jitter measurements of turbulent aero-optical path differences". In: *Applied Optics* 31.22, pp. 4440–4443.

Marr, D. and E. Hildreth (1980). "Theory of edge detection". In: *Proceedings of the Royal Society of London. Series B* 207, pp. 187–217.

Marusic, I., R. Mathis, and N. Hutchins (2010). "Predictive Model for Wall-Bounded Turbulent Flow". In: *Science* 329.5988, pp. 193–196. ISSN: 0036-8075. DOI: 10.1126/science.1188765.

Mathis, R., N. Hutchins, and I. Marusic (2009). "Large-scale amplitude modulation of the small-scale structures in turbulent boundary layers". In: *Journal of Fluid Mechanics* 628, pp. 311–337. DOI: 10.1017/S0022112009006946.

Mathis, R., N. Hutchins, and I. Marusic (2011). "A predictive inner-outer model for streamwise turbulence statistics in wall-bounded flows". In: *Journal of Fluid Mechanics* 681, pp. 537–566.

McKeon, B. J. (2017). "The engine behind (wall) turbulence: perspectives on scale interactions". In: *Journal of Fluid Mechanics* 817. DOI: 10.1017/jfm.2017.115.

McKeon, B. J. and A. S. Sharma (2010). "A critical-layer framework for turbulent pipe flow". In: *Journal of Fluid Mechanics* 658, pp. 336–382.

Meinhart, C. D. and R. J. Adrian (1995). "On the existence of uniform momentum zones in a turbulent boundary layer". In: *Physics of Fluids* 7.694.

Moarref, R. et al. (2013). "Model-based scaling of the streamwise energy density in high-Reynolds-number turbulent channels". In: *Journal of Fluid Mechanics* 734, pp. 275–316. DOI: 10.1017/jfm.2013.457.

Moarref, R. et al. (2014). "A low-order decomposition of turbulent channel flow via resolvent analysis and convex optimization". In: *Physics of Fluids* 26.5.

Monty, J. P. et al. (2009). "A comparison of turbulent pipe, channel and boundary layer flows". In: *Journal of Fluid Mechanics* 632, pp. 431–442.

Morrill-Winter, C. and J. Klewicki (2013). "Influences of boundary layer scale separation on the vorticity transport contribution to turbulent inertia". In: *Physics of Fluids* 25.1, p. 015108. DOI: 10.1063/1.4775361.

Park, G. I. and P. Moin (2016). "Wall-modeled LES: Recent applications to complex flow". In: *Center for Turbulence Research: Annual Research Briefs*, pp. 39–50.

Park, J. S. and M. D. Graham (2015). "Exact coherent states and connections to turbulent dynamics in minimal channel flow". In: *Journal of Fluid Mechanics* 782, pp. 430–454. DOI: 10.1017/jfm.2015.554.

Perry, A. E. and M. S. Chong (1982). "On the mechanism of wall turbulence". In: *Journal of Fluid Mechanics* 119, pp. 173–217. DOI: 10.1017/S0022112082001311.

Rao, K. N., R. Narasimha, and M. A. B. Narayanan (1971). "The 'bursting' phenomenon in a turbulent boundary layer". In: *Journal of Fluid Mechanics* 48.2, pp. 339–352. DOI: 10.1017/S0022112071001605.

Robinson, S. K. (1991). "Coherent motions in the turbulent boundary layer". In: *Annual Review of Fluid Mechanics* 23, pp. 601–639.

Rosenberg, B. J. et al. (2013). "Turbulence spectra in smooth- and rough-wall pipe flow at extreme Reynolds numbers". In: *Journal of Fluid Mechanics* 731, pp. 46–63. DOI: 10.1017/jfm.2013.359.

Rosenberg, K. et al. (2016). "Towards low order models of wall turbulence using resolvent analysis". In: *Proceedings of the Summer Program 2016, Center for Turbulence Research, Stanford*, pp. 305–314.

Rought, R. (2013). "Identification of thermally-tagged coherent structures in the zero pressure gradient turbulent boundary layer". Aerospace Engineer's Thesis. California Institute of Technology.

Saxton-Fox, T. and B. J. McKeon (2017a). "Coherent structures, uniform momentum zones and the streamwise energy spectrum in wall-bounded turbulent flows". In: *Journal of Fluid Mechanics* 826. DOI: 10.1017/jfm.2017.493.

Saxton-Fox, T. and B. J. McKeon (2017b). "Modeling momentum and scalar transport in a wall-bounded turbulent flow". In: *Proceedings of the International Symposium of Turbulence and Shear Flow Phenomena* 10.

Saxton-Fox, T. et al. (2015). "Aero-optical distortion as a marker of turbulent structure". In: *The Proceedings of the International Symposium on Particle Image Velocimetry* 11.

Schlichting, Hermann (1979). *Boundary-Layer Theory*. 7th ed. New York, U.S.A.: McGraw Hill.

Schoppa, W. and F. Hussain (2002). "Coherent structure generation in near-wall turbulence". In: *Journal of Fluid Mechanics* 453, pp. 57–108.

Sharma, A. S. and B. J. McKeon (2013). "On coherent structure in wall turbulence". In: *Journal of Fluid Mechanics* 728, pp. 196–238.

Sillero, J. A., J. Jimenez, and R. D. Moser (2014). "Two-point statistics for turbulent boundary layers and channels at Reynolds numbers up to $\delta^+ \approx 2000$". In: *Physics of Fluids* 26.105109.

Smith, A. E. et al. (2014). "Subsonic boundary-layer wavefront spectra for a range of Reynolds numbers". In: *AIAA Aviation and Aeronautics Forum and Exposition* 2014-2491.

Spina, E. F., A. J. Smits, and S. K. Robinson (1994). "The physics of supersonic turbulent boundary layers". In: *Annual Review of Fluid Mechanics* 26, pp. 287–319.

Sreenivasan, K. R. (1991). "On local isotropy of passive scalars in turbulent shear flows". In: *Proceedings: Mathematical and Physical Sciences* 434.1890, pp. 165–182. ISSN: 09628444. URL: http://www.jstor.org/stable/51992.

Talluru, K. M. et al. (2014). "Amplitude modulation of all three velocity components in turbulent boundary layers". In: *Journal of Fluid Mechanics* 746. DOI: 10.1017/jfm.2014.132.

Tennekes, H. and J. L. Lumley (1972). *A First Course in Turbulence*. Cambridge, MA: MIT Press.

Theodorsen, T. (1952). "Mechanism of turbulence". In: *Proceedings of the Midwestern Conference on Fluid Mechanics*. Ohio State University, Columbus, OH.

Townsend, A. A. (1976). *The Structure of Turbulent Shear Flow*. 2nd. Cambridge University Press.

Wang, J., J. Gibson, and F. Waleffe (2007). "Lower branch coherent states in shear flows: transition and control". In: *Phys. Rev. Lett.* 98 (20), p. 204501. DOI: 10.1103/PhysRevLett.98.204501.

Warhaft, Z. (2000). "Passive scalars in turbulent flows". In: *Annual Review of Fluid Mechanics* 32, pp. 203–240.

Wu, X., P. Moin, and J-P Hickey (2014). "Boundary layer bypass transition". In: *Physics of Fluids* 26.

Wu, X. et al. (2017). "Transitional-turbulent spots and turbulent-turbulent spots in boundary layers". In: *Proceedings of the National Academy of Sciences of the United States of America*, E5292–E5299.

Wyckham, C. and A. Smits (2009). "Aero-optic distortion in transonic and hypersonic turbulent boundary layers". In: *AIAA Journal* 47.9.

Zaman, K. B. M. Q. and A. K. M. F. Hussain (1981). "Taylor hypothesis and large-scale coherent structures". In: *Journal of Fluid Mechanics* 112, pp. 379–396.